Design, synthesis, characterization and testing of materials for biomedical applications

Orsolya Karácsony

Carnegie Mellon University

Department of Chemistry

May 2015

In partial fulfillment of the requirements for the Ph.D. degree in Chemistry

ABSTRACT

In an era when antiobiotics and sanitizers are readily available, but running out of fossil fuel is not an immediate danger yet, the lengthening of lifetime and the increasement of life quality became mostly dependent on our ability to replace body parts lost by illness or accident, which places biomimetic and antifouling materials in the spotlight of the first half of the 21st century. In this thesis, step-growth polymerization (SGP) and atom transfer radical polymerization (ATRP) were utilized in the design of synthetic polymers to create biomimetic and antifouling materials, with control over structure and functionality. Biomimetic conjugates were prepared using SGP by a "click" reaction between a genetically engineered green fluorescent protein (GFP) bearing two azides and a dialkyne poly(ethylene glycol) (PEO). SGP and thermosensitive, coating forming hyaluronic acid (HA) - poly(di(ethylene glycol) methyl ether methacrylate) (P($(MEO)_2$MA)) conjugates were prepared by synthesizing the thermoresponsive polymer by ATRP using an aminated initiator, then coupling it to the carboxylic acid froups of the activated HA. The HA-P($(MEO)_2$MA) conjugates were tested for their antifouling property. Then, these conjugates were synthesized with different grafting densities (GD) and P($(MEO)_2$MA) side chain length values, in order to find the ideal parameters for an antifouling coating material and to elucidate the mechanism of coating formation. Over the course of the characterization of both types of materials, intriguing physical behavior was encountered. The GFP-PEO behaves like a wooden snake and the HA- P($(MEO)_2$MA) conjugates show an intriguing mechanism of film formation. Both behaviors were explored using various physical characterization techniques, among which atomic force microscopy (AFM) was crucial. As an important technique, AFM as a technique is isolated

for study. As part of my work, the dependence of average tip-sample forces on imaging conditions such as set-point ratio and operating frequency were explored. First, the derivation of an analytical expression for the average tip-sample force will be presented. Its predictions will be then shown to be in excellent agreement with the results of numerical simulations using a single degree of freedom, driven damped harmonic oscillator model of tapping mode AFM. In multi-frequency tapping-mode AFM (TM-AFM) experiments, quantifying the tip-sample force may be essential in understanding the nature of contrast in imaging soft materials such as block copolymers or novel complex macromolecular architectures, such as the conjugates described in this thesis.

ACKNOWLEDGEMENTS

I must first acknowledge the significant contributions of my advisor, Professor Newell Washburn. I could not have asked for a more dedicated advisor; I appreciate his constant support and encouragement, and I feel blessed to have been a part of his group. He also taught me a great amount of information related to biomedical engineering, with especial regard to characterization.

Many of the exciting results obtained in this thesis were born through working with Professor Robert Tilton, Professor Anna Balazs, Professor Tomasz Kowalewski and Professor Krzysztof Matyjaszewski; I appreciate the time they spent on our discussions and that they opened their facilities and resources to me.

In addition to these collaborations, I would also like to acknowledge useful discussions with Professor Bruce Armitage, the chair of my doctoral committee, especially regarding my work on coatings.

It was a pleasure to work with Mohamed Ramadan and Gunnar Dunér on the coating project. Chin Min Hui showed me how to run an ATRP reaction, explained all the basic principles, and kindly helped conducting experiments in the Matyjaszewski lab. Professor Susana Steppan was an invaluable help when collecting data in the Chemical Engineering Department.

I cannot thank enough to Doctor Rebecca Freeland for her help with integrating my non-traditional background into chemical research.

Finally, I would like to say thank you to my grandfather, to my friends, and to all my teachers and mentors who influenced my thinking and from whom I got inspiration and faith.

PREFACE

In this thesis, my doctoral work's largest projects are covered, the central topic of which is biologically inspired /bioactive systems, capable of the formation of one- or two-dimensional supramolecular constructs. These systems can be built using a combination of controlled radical polymerization and biology, by making use of permanent covalent, ionic, hydrogen bonding or hydrophobic interactions. Different combinations of these chemical/physical bonds serve as a means of connecting the building block, giving them potential applications in tissue engineering. In the case of the HA-conjugates, this means adhesivity, and in the case of the entropic springs comprised of objects of different lengths and permanence, this means forming objects with exciting physical properties.

My work involved synthesis and methods to study these materials. Among these methods, AFM is a central technique, and in AFM, for the study of mechanical behavior, understanding the magnitude of forces is crucial, especially for soft biomaterials, where contrast is more informative than in the case of rigid surfaces.

Herein, a brief overview of these projects is given, and the most important results are summarized, focusing on my own contribution. Topics discussed in this report include:

1) **Chapter I: Hyaluronic Acid Films for use as Antifouling Coatings**

   Collaborators: Tilton Group.

   Pulished in Langmuir.

   Contribution: Sample preparation for AFM imaging, image collection and processing, participation in quartz crystal microbalance measurements and manuscript writing. The

rest of the work (and the major part of the writing) was started by Joseph E. Prata and finished by Mohamed Ramadan.

2) **Chapter II: Reducing Protein Adsorption with Polymer-Grafted Hyaluronic Acid Coatings: Optimization of Material Properties and a Study on Coating Mechanism**

   Collaborators: Tilton Group.

   Target journal: in Langmuir.

   An extension of the project described in Chapter I and investigations of the mechanism of layer formation. A manuscript is being written based on this chapter.

3) **Chapter III: Self-assembly of Covalently bonded Fibers by Zipper-like Driven Aggregation**

   Under the guidance of Professor Matyjaszewski and Professor Kowalewski; collaborators: Balazs Group (U. Pitt.)

   Pulished in Angewandte Chemie (Communication).

   Contribution:Sample preparation for AFM imaging; image collection and processing, analysis and processing of the confocal microscopy images, performing calculations based on these images, creation of a 3D model of the modified GFP and visualization of its surface electrostatics, writing of the paper, organizing meetings with the collaborators and helping them with suggestions. Syntheis and DLS was done by Saadyah E. Averick, modeling was completed by the Balazs Group.

4) **Chapter IV: Quantification of tip-sample forces on and below resonance in tapping mode atomic force microscopy**

   Under the guidance of Professor Kowalewski.

   Target journal: Physical Review B.

Contribution: coding the simulation in Matlab and building the Simulink model, processing the data in Mathematica, and manuscript writing. To this, a considerable amount of help was received from Professor Kowalewski. A former member of the group, Brian Cusick, had also been working on this project, but my work is independent from his research.

The remaining part of the thesis is structured as the following: the first chapter gives a brief overview of technological applications of biomimetic type materials and functional macromolecules, focusing on chemical strategies and physical characterization methods. Chapters II-VI contain the technical description of the projects outlined above. The thesis is wrapped up with a brief conclusion part.

TABLE OF CONTENTS

LIST OF ABBREVIATIONS

AFM	Atomic Force Microscopy
ATRP	atom transfer radical polymerization
bpy	2,2'-bipyridine
BSA	Bovine serumabumin
DMAP	*4*-(dimethylamino)pyridine
DP	degree of polymerization
EBiB	ethyl 2-bromoisobutyrate
EO	Ethylene oxide
eqv.	equivalent
et al.	*et alii, et alia*
GD	grafting density
GFP	green fluorescent protein
GPC	Gel permeation chromatography
HA	hyaluronic acid
i.e.	*id est*
LbL	Layer by Layer
LCST	lower critical solution temperature
MW	molecular weight
MWD	molecular weight distribution
NMR	nuclear magnetic resonance
Pa	Pascal
PDI	polydispersity index

PMDETA	*N,N,N′,N″,N″*-pentamethyldiethylenetriamine
P($(MEO)_2$MA)	poly(di(ethylene glycol) methyl ether methacrylate
ppm	parts per million
PAA	poly(acrylic acid)
PBA	poly(butyl acrylate)
PEO	poly(ethylene oxide)
PLA	poly(lactite)
RT	room temperature
SEC	size exclusion chromatography
SEM	Scanning Electron Microscopy
SGP	step-growth polymerization
TEA	triethylamine
TMAFM	tapping mode atomic force microscopy
TPMA	tris[(2-pyridyl)methyl]amine

LIST OF SCHEMES

LIST OF FIGURES

Figure 3.3.4.14: The separate dissipation changes seem to be the key to a good antifouling coverage.

Figure 4.2.1.1: Fiber synthesis. “Click” step-growth polymerization approach was used for preparing GFP-PEO fibers. Synthetic conditions: GFP2/ PEO10kdialkyne/ PMDETA/ CuSO4*5H2O/ sodium ascorbate = 7*10-4 mmol/ 7*10-4mmol/ 9.1*10-3 mmol/ 7*10-3mmol/ 7.7*10-3mmol, in 0.1M PBS buffer (pH= 7.4).

Figure 4.2.2.2.1: Monomer and fiber structure of GFP-PEO fibers prepared by the “click” step-growth polymerization of GFP-diN3 and PEO1k-dialkyne. A) GFP monomer showing the modified amino acids at positions 134 and 150 in red. Modification sites in the GFP were visualized using data from the Protein Data Bank and Pymol version 1.4.1with Python version 2.7. B) Size distribution analysis using DLS of GFP-fibers. The size distribution of the suspended fibers shows an approximate diameter of 0.658 mm and CV of 0.501. C & D) Confocal microscopic analysis of the fibers. Confocal analysis shows that the GFP retains its fluorescent properties, and fibers can be observed in the range of tens of mm in length (scale bar: 10 mm). C) Spin-casted GFP-PEO fiber (scale bar: 5 mM); length ~20 mm. D) The Z-stack analysis of the drop-casted GFP-PEO solution reveals fiber nature of the GFP-PEO (scale bar: 10 mM).

Figure 4.2.2.3.1: Atomic force microscopic images of GFP fibers cast on a substrate at a 45° angle. A) height, B) phase channel of the image of a representative site of the sample. Fibers can be seen on the order of several microns lengths and up to 0.1 mm in width (image size: 1 mm).

LIST OF TABLES

CHAPTER 1

BIOLOGICALLY INSPIRED MATERIALS AND MATERIALS FOR BIOMEDICAL APPLICATIONS

1.1. Why biomaterials science?

This thesis summarizes the most important results of my main projects from my doctoral research work in the area of technological applications of biomimetic type materials and functional macromolecules, focusing on chemical strategies and physical characterization methods. What connects the projects falling into different fields is my passion for developing a better understanding for nature, not with the purpose of vivisecting life itself, but to point out hidden underlying connections and to explore the laws governing complex processes and phenomena, with the purpose of the scholar to be able to appreciate beauty and with the purpose of the doctor to cure illnesses.

For centuries, the main threat that humankind was facing was infections. Thanks to Ignác Semmelweis,who discovered the role of hand sanitation in eliminating puerperal fever, and to that of Alexander Fleming, whose discovery of penicillin launched the era of antibiotics, by the middle of the 20th century, this ceased to be the case. A couple of years before the discovery of the "savior of mothers", the idea of the computer was conceived by Charles Babbage (his "analytical engine" was built posthumously, but turned out to be functional - Figure), and, around the same time when penicillin was discovered, the first computer was built by Konrad Zuse, based on Alan Turing's paper. With the work of Carother, Flory, and Kuhn, polymer chemistry was born. Science was ready to answer new questions, and the new field of Computer Science and polymer chemistry even profited from history's disgraceful events. In natural sciences, the next big step forward was the famous Photo 51 (Figure1.1.1) taken by Raymond Gosling in Rosalind Franklin's lab in the middle of the century.

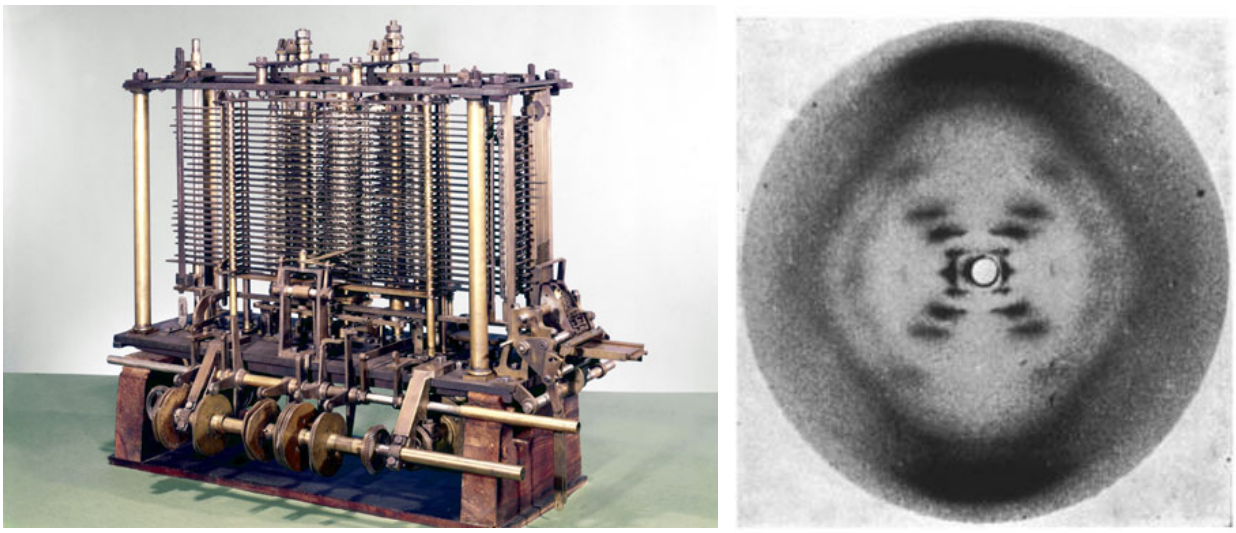

Figure1.1.1: The first computer and Photo 51 of DNA.

This started a new era of DNA-fever the climax of which was the conclusion of the Human Genome Project (HGP). Computing machines in the background were quietly but steadily following Moore's law.

In the first half of the 21st century, we struggle with an even greater depression than the one a century ago, with 3rd world problems and with decreasing resources for science. However, research cannot stop, just like it did not stop back then. HGP and cloning technology brought some results, but did not help us to cure every human disease as promised at the start. There are some similarly grandiose suggestions for exploring the human metabolome and connectome, but, considering the results of the HGP and the tight financial situation, these projects are unlikely to reach the same scale as HGP did.

The near future is probably those of small-budget integrative projects. In the era of the Internet and affordable electronic devices, the value of lexical knowledge became greatly diminished. The vast amount of information that is readily available for no more than a click increases the value of

analytical thinking and an interdisciplinary mindset. The scientist of the 21st century has to become a polyhistor before being able to contribute to science, and for this can get inspiration from Aristotle who was looking for numbers behind all natural phenomena. Because there are still questions out there, such as how to cure cancer, and we should aim for answering these questions, by looking for little pieces of gold in the white water of information.

1.2. What is biomaterials science?

Biomaterials science is the study of the application of materials to problems in biology and medicine.[10] Hence, it lies in the intersection of medicine, chemistry, materials science, and, as part of all of these, in the form of biophysics, physical chemistry, polymer physics, statics and mechanics: physics. It encompasses both theoretical and experimental work, latter one including simulations and laroratory experiments as well. Some work aims directly material development, and some focuses on improving methodology such as synthesis and characterization methods. Material development research has two main goals, one being the development of biologically inspired materials for non-biological applications (e.g. making use of the adhesivity of mussel materials, the physics of gecko feet – Figure1.2.1 - or the strength of the spider web) and the other one being biomedical engineering: the application of all of our engineering knowledge to help the recovery of the human organism when something goes wrong (e.g. development of diagnostic tools and aiding wound healing).

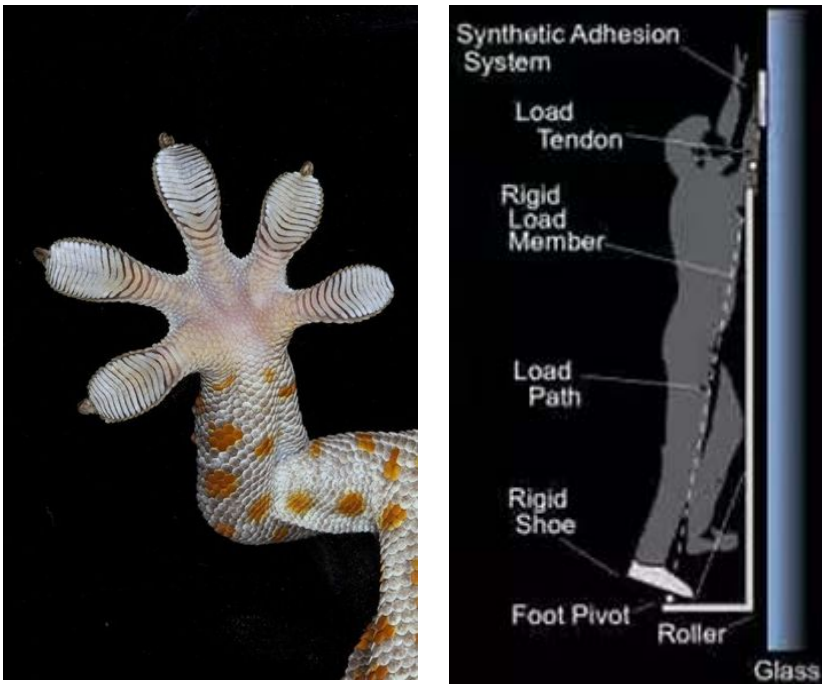

Figure1.2.1: The way a gecko does it (A) and the human way – plenty of space for improvement on our part…

1.3. Current trends in biomaterials science

Among biologically inspired materials, the two probably most important trends are 1) the development of intelligent materials and 2) the biological approaches to harvesting energy. The first cathegory includes constructs with the capability of adjusting their structure or physical properties to that of their environment (adaptive, often biomimetic materials) and those whose properties can be changed intentionally but independently from their environment (programmable materials). The second cathegory includes bioelectronics and light-harvesting photonic materials that mimic photosynthesis. Since adaptive materials have not only been in the spotlight over the last decade but are also the closest group to my work, in section 1.3.1 I will review the most promisising subset of these.

In biomedical engineering, the currently most popular topics include 1) signaling/imaging, 2) protein adsorption and 3) tissue engineering. Since 1) is not really interdisciplinary in nature, it will not be discussed here in detail. It has to be noted, however, that this topic will be reoccurring throughout this thesis in the form of atomic force microscopy, which will be covered in Chapter IV. Similarly, for a discussion on 2) the reader is referred to Chapters I and II. The materials aspect of 3) deals with the development of materials for drug delivery or facilitating tissue and organ recovery (wound healing). This latest category is reviewed below in section 1.3.2.

1.3.1. Self-healing materials

Self-healing materials are a class of adaptive materials that are capable of restoring their original structure and functionality after damage. The restorative action usually requires a trigger, but the ultimate goal in designing these materials is autonomous recovery. Examples include rubbery materials[1], epoxides and even hydrogels[2]. The aim of the current work is to give a brief, what systematic overview of how work in this area is done and evaluated in general.

Polymeric materials exhibit visco-elasto-plastic behavior**.** This means that when subjecting a polymeric material to an external force, the resulting deformation is composed of three terms, weighed by different factors (depending on the given material): elastic deformation, viscous response, and plastic flow. The elastic deformation is related to the stored energy, can be used to recover the original state of the material from the deformed one. The viscous response contributes to healing via its memory effect. Plastic flow does not contribute to structural-functional recovery.

Thermoplastics exhibit viscoelastic flow and re-flow behavior, depending on how much of the energy that was given to the system gets dissipated, and how much is the residual stress; the macroscopic shape of the material is also influenced by surface tension, which keeps the surface

area small. Thermosets, on the other hand, undergo elastic deformation until they eventually crack. In the first phase, energy put into the system is stored; if the deforming force is abolished before rupture, then the stored energy is released *via* elastic re-bounce; in the opposite case, by fracturing (Figure 1.3.1.1).

The ideal self-healing material should exhibit an optimal mixture of these responses, ensuring reversible deformability and sufficient toughness at the same time.

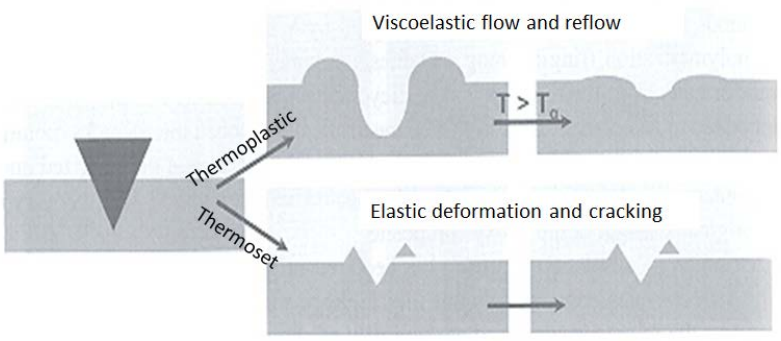

Figure 1.3.1.1: The two extreme cases of a polymer's response to mechanical deformation: viscoelastic flow and elastic deformation.

Self-healing materials can be classified as autonomously healing composites and materials capable of only stimulus-dependent recovery. In the latter case, the stimulus can be mechanical[3], thermal[4], electrical[5], photo[6]- or chemical (redox[7] or pH). It has to be noted, however, that, in the case of photo- or mechanical stimulus, the repeatability of the healing phenomenon is usually poor, even if the fracture of tensile test shows good efficiency.[3a, 3b, 6]

Over the past few years, the trend in the design of self-healing materials has been to build systems of interpenetrating networks (Figure 1.3.1.2); these networks can consist of two (or more) different structures or two different types of bonds (allowing for the case of both). Healing happens via non-

covalent (e. g. hydrogen, ionic) or covalent bonds that can be broken and formed again by a physical or chemical trigger (see above).

In the case of two different structures, one is usually “hard”, possessing the properties of thermosets, which ensures elasticity, and one is a “soft” thermoplastic, accounting for the viscoelastic response for deformations. If the material mainly consists of one type of monomer, then the self-healing behavior is achieved by the incorporation of end functionalities that are capable of reversible bond formation. The reversibility of the bond formation is mostly, but not exclusively, realized by weak (usually hydrogen) bonds.[8] Exceptions include disulfide and ester bonds[7a, 9] – both of which is important in biological systems.

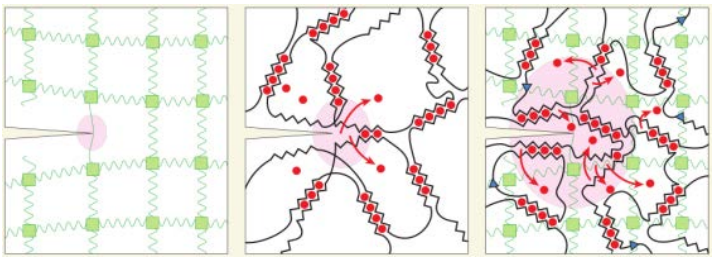

Figure 1.3.1.2: The current trend in the design and synthesis of self-healing materials is preparing composites of polymers, each of which has one of the required properties, this way aiming for reaching ideal mechanical behavior by tuning the chemical composition.[2b]

Hydrogen bonding is made use of, for example, in a recent work of Hentschel et al (Figure 1.3.1.3), where in a complex system, composed of poly-(*n*-butyl acrylate) (PBA) and polystyrene (PS) blocks, the ends of the PBA chains were functionalized with 2-ureido-4-pyrimidinone (UPy).[8] UPy is known to be able to dimerize by forming quadruple hydrogen bonds between the pairs, and since the UPy units were covalently linked to the main chains of the polymer, these bonds were broken

first when the material was exposed to mechanical (pulling) stress. Then, when being brought into each other's close proximity again (by pressing the broken ends against each other), these units could re-establish their connections. This served as a basis of self-healing capacity; it has to be noted however, that the composition of the backbone of the material also played an important role in ensuring the necessary mechanical properties, by containing two blocks, one of which was soft (PBA), and the other one hard (PS).

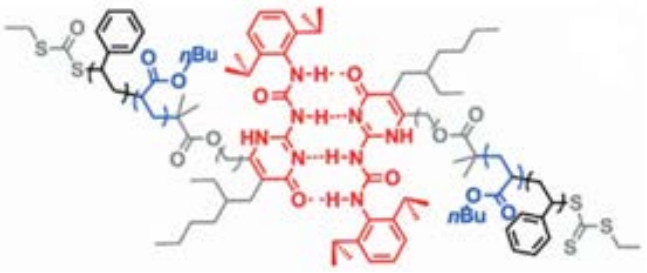

Figure 1.3.1.3: Hydrogen bonds between two UPy units anchored to the chain ends of a PS-PBA block copolymer.[8]

An example of self-healing realized by the reversible (re)formation of *covalent* bonds can be found in the Leibler group's work, who prepared so-called vitrimers, which exhibit a glass transition, but, unlike glass, are soft and elastic at room temperature.[9] This behavior is ensured by trans-esterification reactions (Figure 1.3.1.4).

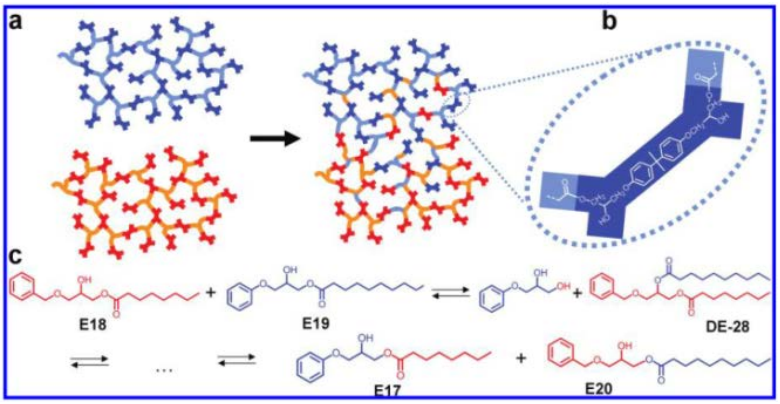

Figure 1.3.1.4: Structure and healing mechanism of the vitrimers – a) cartoon of the structure, b) chemical structure, c) rearrangement by trans-esterification.[9]

However, this rearrangement requires elevated temperatures; in this regard, the Matyjaszwski groups thiol-functionalized star polymers are superior to the vitrimers.[7a] These polymers also have two different types of components: their core consists of poly(ethylene glycol diacrylate) (PEGDA), and the arms are composed of PBA. The thiol end-functionalities are introduced by reaction with **disulphide** dimethacrylate (DSDMA) (Figure 1.3.1.5).

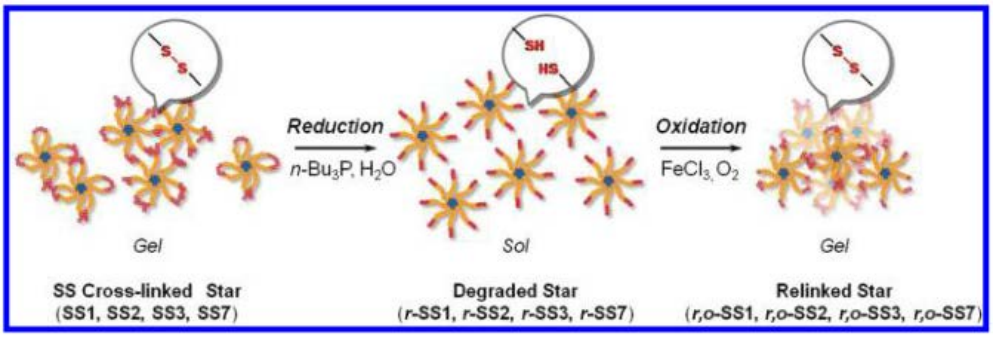

Figure 1.5: Polymeric stars with PEGDA core and PBA arms exhibit self-healing capability due to the presence of thiol end-functionalities. These groups are capable of forming disulfide bonds in an oxidative environment; the formed bridges break up upon reduction.[7a]

Inter-arm bonds are formed in the presence of an oxidizing agent (e. g. iodine) and broken upon reduction (e. g. by tri-n-butyl phosphine, $^{n}Bu_3P$). Since the necessary redox chemistry does not require heating, and similar reactions (catalyzed by enzymes) take place even *in vivo*, this material has probably more potential in practical applications then the Leibler group's vitrimers. A possible drawback of the disulfide bonding, however, is that this is a homogenous bond, allowing for bond formation between PBA arms belonging to the same particle. From the point of view of self-

healing, this intraparticular bond formation is improductive at the best, but can also contribute to aging of the material and other unwanted phenomena.

1.3.2 Tissue engineering: materials for organ recovery

The goal of tissue engineering is to help the human body to rebuild its structural, functional parts when it is not capable of doing so on its own, applying the principles of engineering and the life sciences. Common purposes of introducing foreign materials to the human body include the acceleration of wound healing, organ regeneration after surgery, and functional repair after autoimmun diseases (e.g. failure of beta-cells in type I diabetes mellitus).

Constructs developed for tissue engineering applications can be evaluated based on the ease of their production and applicability, the degree of control over physical and chemical properties, biocompatibility, biodegradibility, stability, and performance compared to existing alternatives. Materials used in regenerative medicine generally fall into one of the following categories: 1) inorganic materials, 2) synthetic polymers and 3) biopolymers. Inorganic compounds are mainly used as bone substitutes:stainless steel’s excellent mechanical propertiesare, unfortunately, accompanied by a high tendency to corrode, for which there is a much lower chance in the case of titanium, which, in term, has a weaker fatigue resistance. For soft tissue replacement, we have a choice between 2) and 3). Synthetic polymers are functionalizable, which, along with controlling the size and architecture, leads to tuneable chemical and mechanical properties, but, unfortunately, usually results in unnatural degradation products. Also, more complicated constructs tend to have nonlinear degradation profiles, and even slight deviations from linearity can lead to immune reaction weeks or even months after implantation. For the same reason, materials that undergo surface degradation are preferred for applications in regeneartive medicine over the ones with bulk

degradation. Degradation type depends on monomer type and implant size. The chief advantage of bioplymers is their high biocopatibility and biodegradibility; however, they often don't result in much improvement compaed to the control, and what's more: peptide-based polymers tend to be highly immunogenic. Therefore, the best answer to our needs might be hybrid materials, falling into the intersection of the above three categories.

An especially promising group of materials is the one of peptide amphiphiles made famous by the Stupp group at Northwestern University. They are also worth of our attention because of their resemblance to the fibers discussed in Chapter III. Peptide amphiphiles are bioactive molecular filaments sharing some properties with synthetic materials, being themselves synthetic. These attributes include tuneable chemical properties, with the resulting capability for undergoing self-assembly on demand and for exhibiting high and tuneaable epitope concentration. Additionally, due to their highly organized structures, they have good and improveable mechanical properties, can be readily combined with othe materials and their synthesis is automated. Moreover, being peptide-based, they also show similarities with biomaterials, including biocompatibility and biodegradibility.

The individual molecules consist of fur regions: a hydrophobic tail, a beta-sheet region, a highly polar region containing charged amino acids, and an optional signaling epitope (Figure 1.3.2.1A).

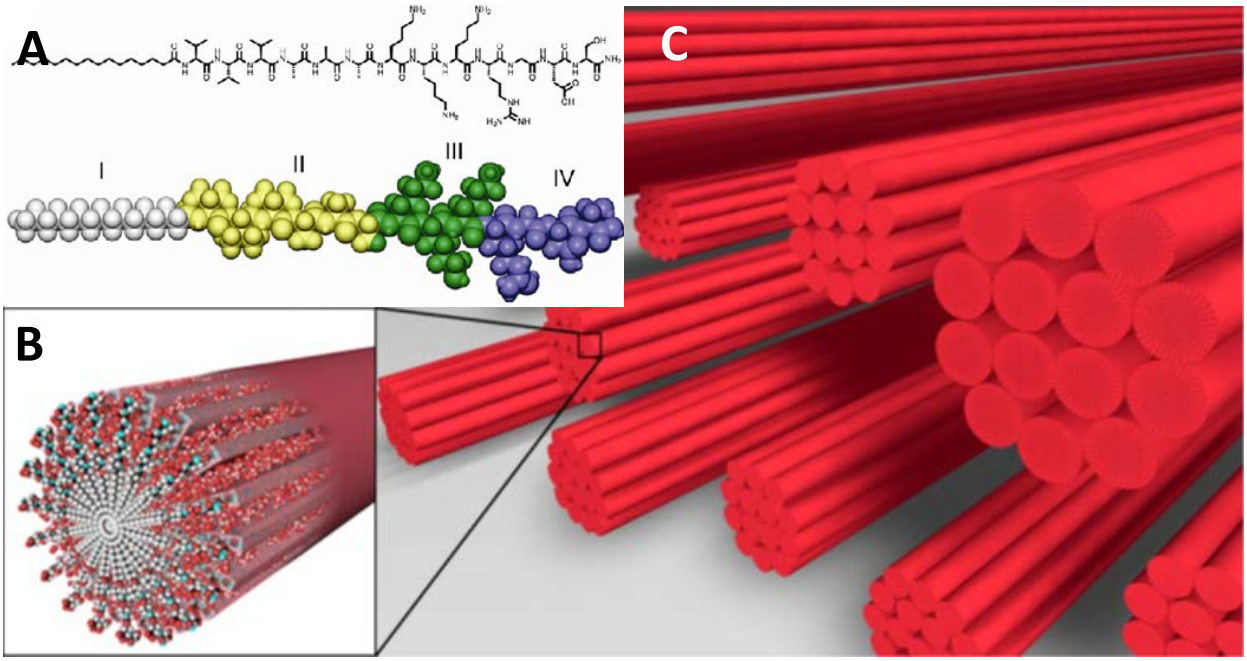

Figure 1.3.2.1: Thestructure of peptide amphiphils. [11,12]

In an aqueous environment, the peptides form cylinders with the hydrophobic tales in connecting end-on to the cylinder's axis, presenting the epitopes on the cylinder's surface (Figure 1.3.2.1 B). One might be wondering why aren't the resulting structures spherical micelles or vesicles consisting of flexible bilayers, which may seem energetically more favorable; however, structure is determinded by the ratio of the base area and height of the geometrical shape best fitting the individual molecules. In the case of peptide amphiphiles, the value of this parameter falls between one-third and half, corresponding to a truncated cone, which explains the formation of cylindrical micelles (Figure 1.3.2.2). The cylinders are then arranged into parallel running bundles (Figure 1.3.2.1 C).

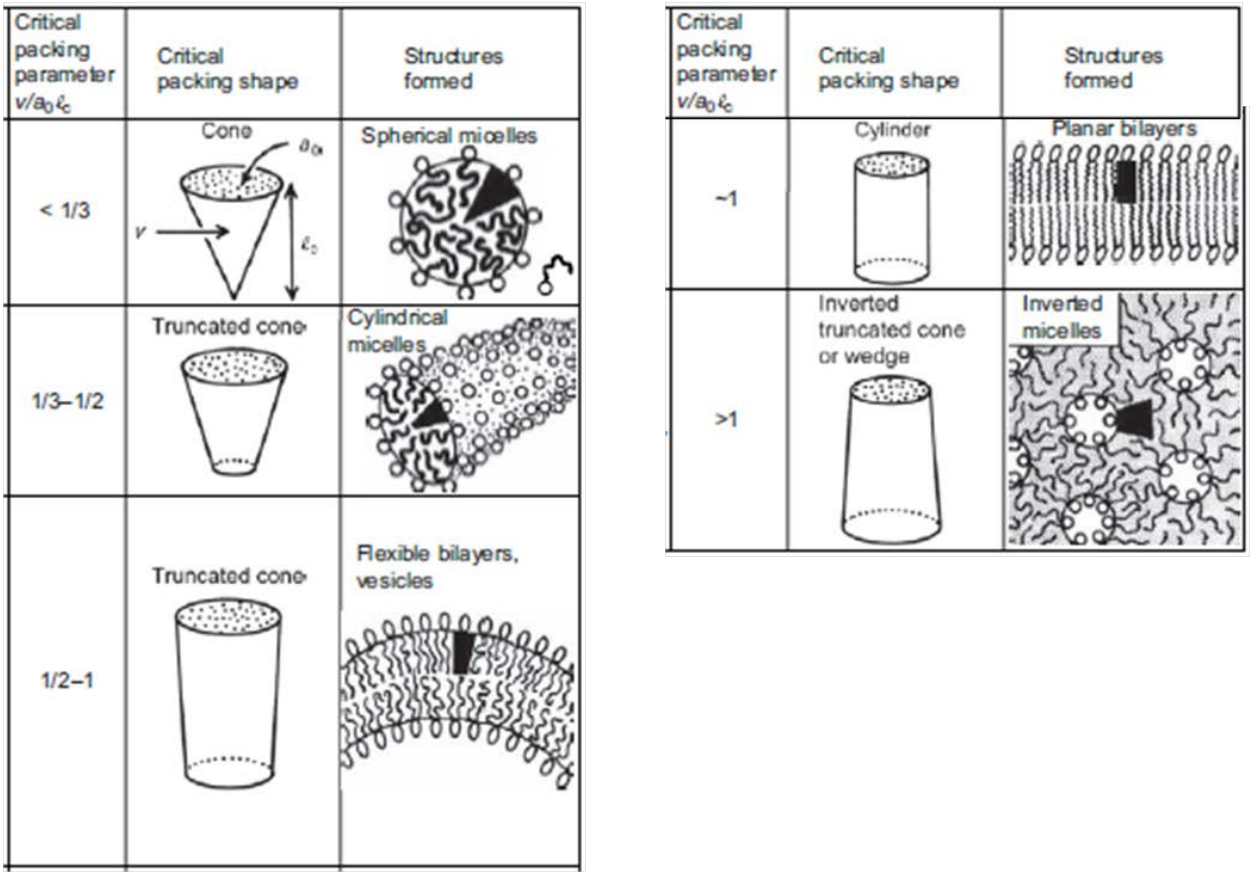

Figure 1.3.2.2: The physics behind the shapes of micelles.[13]

Self-assembly is initiated by change in the environment's pH or ionic strength; the crucal pH or pI is dependent (and therefore can be controlled by) the amino acid sequence.

1.4. Placing recent and current work

My doctoral research mainly falls into the area of biomedical engineering.

First, in blood diagnostics, protein adsorption is a big issue that should be targeted and can be potentially solved by applying antifouling coatings to the equipment surface.

Second, a biocompatible and biodegradable polymer with remarkable physical properties that can undergo self-assembly, driven by strong secondary interactions in a reversible and controllable manner, has great potential in tissue engineering.

Third, the strength of the AFM in the characterization of biological samples and soft polymers lies in its capability to collect information about the sample's various physical properties including depth and compressibility, without destroying the sample, and even under varying (including physiological) conditions, in real time, as opposed to electron microscopy, wich is capable of none of the above. These capabilities therefore make the AFM a unique tool in characterizing biological samples on the nanoscale, and the instrument's performance can be enhanced even more to get optimal contrals when applying the correct choice of cantilever and adequate settings of frequency, amplitude in tapping mode.

1.5 Summary

In this chapter, a brief overview of the research areas related to the topic of this thesis was presented, giving an insight into relevant current trends, with the goal of placing the work to be introduced in the following four chapters both with respect to trends at the time and to modern science over the long term. This background information was felt necessary to explain the context of the diverse and yet connected and in many ways intervowen projects discussed in the rest of the thesis.

1.6 References

1. Zhang, R.; Yan, T.; Lechner, B.-D.; Schröter, K.; Liang, Y.; Li, B.; Furtado, F.; Sun, P.; Saalwachter, K., Heterogeneity, Segmental and Hydrogen Bond Dynamics, and Aging of

Supramolecular Self-Healing Rubber. Macromolecules 2013. *Macromolecules* **2013,** *46* (5), 1841-1850.

2. (a) Sun, J.-Y.; Zhao, X.; Illeperuma, W. R. K.; Chaudhuri, O.; Oh, K. H.; Mooney, D. J.; Vlassak, J. J.; Suo, Z., Highly stretchable and tough hydrogels. *Nature* **2012,** *489,* 133–136; (b) Shull, K. R., A hard concept in soft matter. *Nature* **2012,** *489* (7414), 36-37.

3. (a) White, S. R. S., N. R.; Geubelle, P. H.; Moore, J. S.; Kessler, M. R.; Sriram, S. R.; Brown, E. N.; Viswanathan, S. , Autonomic healing of polymer composites. *Nature* **2001,** *409* (6822), 794; (b) Toohey, K. S.; Sottos, N. R.; Lewis, J. A.; Moore, J. S.; White, S. R., Self-healing materials with microvascular networks. *Nature Materials* **2007,** *6.* (8), 581-585; (c) Cordier, P.; Tournilhac, F.; Soulie-Ziakovic, C.; Leibler, L., Self-healing and thermoreversible rubber from supramolecular assembly. *Nature* **2008,** *451* (7181), 977-980.

4. Zhang, Y.; Broekhuis, A. A.; Picchioni, F., Thermally Self-Healing Polymeric Materials: The Next Step to Recycling Thermoset Polymers? *Macromolecules* **2009,** *42* (6), 1906-1912.

5. Williams, K. A.; Boydston, A. J.; Bielawski, C. W., Towards electrically conductive, self-healing materials. *Journal of the Royal Society, Interface* **2007,** *4* (13), 359-362.

6. Ghosh, B.; Urban, M. W., Self-Repairing Oxetane-Substituted Chitosan Polyurethane Networks. *Science* **2009,** *323* (5920), 1458-1460.

7. (a) Kamada, J.; Koynov, K.; Corten, C.; Juhari, A.; Yoon, J. A.; Urban, M. W.; Balazs, A. C.; Matyjaszewski, K., Redox Responsive Behavior of Thiol/Disulfide-Functionalized Star Polymers Synthesized via Atom Transfer Radical Polymerization. *Macromolecules* **2010,** *43,* 4133–4139; (b) Yoon, J. A.; Kamada, J.; Koynov, K.; Mohin, J.; Nicolay, R.; Zhang, Y.; Balazs,

A. C.; Kowalewski, T.; Matyjaszewski, K., Self-Healing Polymer Films Based on Thiol-Disulfide Exchange Reactions and Self-Healing Kinetics Measured Using Atomic Force Microscopy. *Macromolecules* **2012,** *45*, 142–149.

8. Hentschel, J.; Kushner, A. M.; Ziller, J.; Guan, Z., Self-Healing Supramolecular Block Copolymers. *Angew. Chem., Int. Ed.* **2012,** *51* (42), 10561-10565.

9. Capelot, M.; Montarnal, D.; Tournilhac, F.; Leibler, L., Metal-Catalyzed Transesterification for Healing and Assembling of Thermosets. *J. Am. Chem. Soc.* **2012,** *134*, 7664−7667.

10. Ratner, B.D. Biomaterials Science: An Interdisciplinary Endeavor. In Biomaterials science- An introduction to materials and medicine; Ratner, B. D., Hoffman, E.S., Schoen, F. J., Lemons, J.E., Ed. 1; Academic Press: San Diego,CA, Unidted States, 1996; pp 1. 11. Hartgerink JD, Beniash E, Stupp SI. Proc. Natl. Acad. Sci. 2002; 99:5133–8.

12. Angeloni, N. L. B., C. W.; Tang, Y.; Harrington, D. A.; Zhang, S.; Stupp, S. I.; McKenna, K. E.; Podlasek, C. A. Biomaterials 2011, 32 1091.

13. J. N. Israelachvili, Intermolecular and Surface Forces (Academic Press, London, 1992).

Note

This thesis consists of the work I did during my Ph.D. studies and some of the chapters are already published. A footer was placed at the first page of each relevant chapter showing the reference to the published study. Below is the list of the publications I coauthored during my presence at Carnegie Mellon University.

1. Averick, S.; Karácsony, O.; Mohin, J.; Yong X.; Moellers, N. M.; Woodman, B. F.; Zhu, W.; Mehl R. A.; Balazs A. C.; Kowalewski, T.; Matyjaszewski, K Cooperative, Reversible Self-assembly of Covalently Pre-linked Proteins into Giant Fibrous Structures. Angew. Chem., Int. Ed. **2014**, *53* (31), 8050-8055.
2. Ramadan, M. H.; Prata, J.E.; Karácsony, O.; Dunér, G., Washburn, N. R., Reducing Protein Adsorption with Polymer-Grafted Hyaluronic Acid Coatings. Langmuir. **2014**, *30* (25), 7485-95.

CHAPTER 2

REDUCING PROTEIN ADSORPTION WITH POLYMER-GRAFTED HYALURONIC ACID COATINGS

2.1. Introduction

Adsorption of serum proteins onto the surfaces of implanted biomaterials initiates a cascade of biological events that can lead to deleterious host responses, often resulting in formation of a fibrous capsule or the development of chronic inflammation. The Vroman effect describes the time-dependent microenvironment surrounding the implant characterized by complex dynamics of protein binding and denaturation resulting in formation of a coating that presents cell adhesion peptides or epitopes that activate immune responses.[1-2] Within seconds of implantation, smaller, abundant proteins, such as albumin, adsorb onto nonpolar surfaces due to their high concentration and rapid diffusion in blood. Subsequently, surface rearrangement takes place via desorption of the hydrophilic, low molecular weight proteins and the adsorption of higher molecular weight proteins, such as fibrinogen, on the surface. This process leads to changes of the construct surface properties that can provoke intense host responses despite the construct's biocompatibility. Being in an aqueous environment, protein adsorption on nonpolar surfaces leads to conformational changes and the exposure of once shielded hydrophobic groups. Upon denaturation, protein epitopes can be presented to the microenvironment causing activation of the immune system, and chronic inflammation can be provoked. Preventing or minimizing protein adsorption to the surface of implants becomes an important design criterion, and strategies have focused on reducing protein adsorption on biomaterial interfaces.[1]

* The work presented in the section was reformatted from a previous publication: Ramadan, M. H.; Prata, J.E.; Karácsony, O.; Dunér, G., Washburn, N. R., Reducing Protein Adsorption with Polymer-Grafted Hyaluronic Acid Coatings. Langmuir. **2014**, *30* (25), 7485-95.

Numerous strategies have been developed to tune the properties of biomaterial surfaces in order to inhibit protein adsorption.[2-7] One well studied approach involves increasing the hydrophilicity of the surface through incorporation of polar and charged groups. For example, ultraviolet-light treatment of alkyl silane self-assembled monolayers was used to create a gradient in substrate oxidation that resulted in a gradient in water contact angle that ranged from 30° (hydrophilic) to 80° (hydrophobic). Following exposure to a fibronectin solution, cell adhesion and spreading decreased monotonically with water contact angle, presumably due to decreased protein adsorption.[8] A separate study demonstrated that plasma treatment of poly(tetrafluoroethylene) surfaces could tune the water contact angle from 15-85°.[9] This work demonstrated that water contact angles of 20-45°, which correlated with the highest concentrations of fibronectin adsorbed from serum, were optimal for promoting the adhesion of endothelial cells but surfaces with water contact angle below 20° inhibit protein adsorption.[10-12] However, while straightforward to perform, surface ionization using light or plasma discharge is generally a line-of-sight technique, allowing for patterning using photoresist techniques but making complete passivation of complex three-dimensional objects challenging.

Steric blocking of the surface through dense grafting of poly(ethylene glycol) (PEG) is another well-established technique for reducing protein adsorption on the surface.[4] Water-soluble PEG has established biocompatibility,[4, 7, 13-14] and coating surfaces with it has been shown to significantly reduce protein adsorption.[3, 15-16] Monofunctional PEG can be reacted with the surface, providing a controlled method for grafting since unreacted PEG can be removed through washing.[4] This technique is appropriate for surface patterning and coating complex objects[4, 16] but requires highly reactive PEG end groups, such as silanes, or surface functionalization.

PEG-grafted polymers have been used as coatings to reduce protein adsorption in other studies relying on the polymer backbone to drive adsorption to the surface. PEG-grafted poly(L-lysine) (PLL) forms coatings on oxide surfaces, relying on the strong interactions between PLL and the oxide surface.[17] For oxide surfaces with isoelectric points below 7, such as TiO_2, Nb_2O_5, and Ta_2O_5, the net negative charge of the oxide surface binds the PLL chain strongly, allowing for high grafting densities of the 2 kDa PEG chains in an adherent coating. On TiO_2, the PLL-g-PEG coating reduced fibrinogen adsorption from 559 +/- 15 ng/cm^2 on the oxide to 22 +/- 12 ng/cm^2.[5, 18-19] For biomaterial surfaces with negative charge under physiological conditions, this approach provides a straightforward method for passivation against protein adsorption.[5]

An alternative to surface functionalization with PEG is grafting carboxymethyl dextran, a charged polysaccharide known for anticoagulant activities.[20] The most common protocol involves a combination of surface grafting and interchain crosslinking, resulting in the formation of a hydrogel coating with thickness *ca.* 200 nm.[21] This has been used for designing bioanalytical interfaces, such as those used in surface plasmon resonance analysis of blood samples,[21] where the high resistance to protein adsorption and high density of antibodies or other capture groups allows for sensitive analyte detection.[22] The zwitteration of dextran is obtained through a one-pot reaction with carboxybetaine and is reported to yield good antifouling properties as well as enhanced optical transparency and switchability. [23] However, utilization of the antifouling properties of many natural polysaccharides is challenging and, despite interest in these materials, several intrinsic limitations prevent their broader application in biomedical applications. QCM results show that dextran-based materials show reduced antifouling properties in contact with blood.[24] It was also demonstrated that the use of agarose derivatives in biosensors is challenged by

nonspecific binding.[25] We hypothesized that hyaluronic acid (HA) might be an ideal candidate for formation of nonfouling coatings since it is a component of most highly hydrated tissues.

Use of controlled radical polymerization is an established method for modifying the properties of polysaccharides.[26-27] In this study, HA was grafted with the thermoresponsive polymer poly(di(ethylene glycol) methyl ether methacrylate) ($PMEO_2MA$) prepared via atom transfer radical polymerization (ATRP) to make it suitable for one-step surface coating as a base for preventing protein adsorption. HA is a linear, viscous, naturally occurring, high molecular weight glycosaminoglycan (GAG) composed of a copolymer of D-glucuronic acid and N-acetyl-D-glucosamine.[18, 28-32] Unlike dextran, HA has intrinsic anti-inflammatory activities[33] and is recognized by cells through the cell surface receptors that promote a motile phenotype (CD44, RHAMM, ICAM-l), making it a potent mediator of biological processes such as metastasis, morphogenesis, inflammation and wound repair.[18, 28, 31-32] Chemical modification of HA through targeting the carboxylic acid groups, as well as other groups on the backbone, have been reported for various applications.[34-35] The thermo-responsive behavior of the polymer can be conducted to HA by grafting the polymer to the HA backbone, similar to what was reported by Tan et al. with poly(N-isopropylacrylamide) (PNIPAM) in their preparation of HA-PNIPAM scaffolds.[36] Separate studies measuring the adsorption of PNIPAM on various substrates demonstrated that hydrophobic forces keep the material bound to the substrate as long as rinse temperatures were above the LCST of the polymer.[37] The temperature described as LCST in the following chapters could be more correctly called a clouding point, but is commonly referred to as LCST. Therefore, this term will be used throughout this thesis. The challenge in preparing non-fouling HA coatings based on grafts with an LCST was in providing sufficient driving force for forming a robust coating without resulting in extensive protein adsorption to the hydrophobic components of the surface.

This work presents the preparation and characterization of these materials and is organized as follows. First, coating morphologies were characterized using atomic force microscopy, and antifouling properties of coatings based on these materials were tested using novel bio-layer interferometry (BLI) using bovine serum albumin, fibrinogen and human immunoglobulin solutions. This technique, which provides similar information as surface plasmon resonance (SPR), can run multiple samples in parallel and offers significant advantages in understanding the interfacial properties of these coatings. This label-free technology allows for real-time measurement of biomolecular interactions. By analyzing the interference patterns of white light reflected from consecutive interfaces in an end-coated fiber optic, this bio-layer interferometry is able to accurately measure changes in the optical path length of the fiber and correlate this to changes in the thickness of molecules adsorbed at the solution interface with a sensitivity reported by the manufacturer of 0.1 Å. A second validation of the antifouling properties of the coatings using quartz crystal microbalance with dissipation monitoring (QCM-D) is also presented. Finally, we demonstrate coating of a two-dimensional grid suggesting this method may be a route toward surface functionalization of more complex objects.

2.2. Preparation and Characterization of HA-P(M(EO)2MA) Conjugates

2.2.1. Materials

Di(ethylene glycol) methyl ether methacrylate ($M(EO)_2MA$), ethyl 2-bromo-2-methylpropionate (EBiB), 2,2′-bipyridine (bpy), Copper(I) bromide (CuBr), anisole, hexanes, ethylenediamine, triethylamine (TEA), 4-(dimethylamino)pyridine (4-DMAP), and hyaluronic acid (HA) derived from *Streptococcus equi* (ca. 1.6 MDa) were purchased from Sigma-Aldrich. Albumin from bovine serum (BSA) (>98%, received as a lyophilized powder) and fibrinogen (Fbg) from human

plasma and human (IgG) were purchased from Sigma-Aldrich. Propane phosphonic acid anhydride (T3P) in 50% w/w solution in N,N-dimethylformamide was obtained from Sigma-Aldrich. Monomethoxy poly(ethylene glycol) epoxide (mPEG-epoxide) of a 10 kDa molecular weight was purchased from Creative PEGWorks and used as received.

2.2.2. Synthesis of the homopolymer of P(MEO)$_2$MA by ATRP

Synthesis of PMEO$_2$MA was performed as reported[38] with minor modifications. First bpy and CuBr (0.20 mmol and 0.12 mmol, respectively) were added to a dry 25 mL Schlenk flask. The flask was deoxygenated rapidly after adding the solids *via* four consecutive vacuum-nitrogen cycles. Anisole, M(EO)$_2$MA and EBiB were dried over baked 4 Å molecular sieves and degassed with nitrogen for 30 minutes prior to reacting with the catalysts. Using the Schlenk techniques, 3.3 mL anisole, 4.9 mL of the monomer (M(EO)$_2$MA) (26.6 mmol) and 18.6 µL of EBiB (0.13 mmol) were added to the schlenk flask under nitrogen. The reaction was allowed to proceed at 60 °C using an oil bath for 6 h. The reaction was terminated by exposing it to air. The reaction mixture was then diluted in excess THF and the catalyst was removed from the mixture by passing the sample through a neutral alumina column. The solution was then precipitated in excess hexane and the precipitate was filtered. The solid product was dried under vacuum for 6 h. Polymerization reaction kinetics were monitored by periodically withdrawing samples from the reaction mixture. Composition was validated by ^{1}H NMR and end group analysis indicated an M_n value of 34,000 g/mol. Gel permeation chromatography (GPC) was used to measure M_n and M_w/M_n.

2.2.3. Modification of PMEO2MA with amine group

The procedure followed another performed by Coessens et al.[39] Following drying, PMEO$_2$MA with a terminal bromide end group was acquired. Then PMEO$_2$MA was dissolved in ethanol at a

concentration of 50 mg/mL. $PMEO_2MA$ solution was mixed with a 25X molar excess of ethylenediamine (EDA) and 1.2X molar excess of TEA to EDA. The mixture was allowed to react for 48 h in an oil bath at 60 °C then was precipitated into hexanes. The solid polymer was re-dissolved in milli-Q water and dialyzed against 2,000 MWCO membrane with repeated water changes to remove unreacted reagents. Following dialysis, the sample was frozen at -80 °C and lyophilized on a Labconco Freezeone Plus freeze-dry system. Products were characterized using ^1H NMR.

2.2.4. Synthesis of HA-PMEO2MA conjugates

HA was dissolved in Milli-Q water at a concentration of 5 mg/mL. Then carboxylic acid groups on HA were activated by 0.3 molar equivalents (relative to the number of carboxylic acid groups on HA) of T3P. To that 4-DMAP was added to the activated HA as an acylating agent in a 2:1 ratio. To the activated HA, a 1:1 molar ratio of NH_2-$PMEO_2MA$ was added. The reaction mixture was set at room temperature for 24 h. After 24 h the solution was diluted with water and dialyzed against a 100,000 MWCO dialysis membrane to remove unreacted $PMEO_2MA$. Dialyzed samples were frozen at -80 °C and lyophilized. Then ^1H NMR characterization was carried out on the solid product to confirm HA-$PMEO_2MA$ conjugation.

2.2.5. ^1H NMR characterization

NMR spectra were obtained using a Bruker Avance 300 MHz spectrometer. Deuterated chloroform ($CDCl_3$) was used as the solvent for $PMEO_2MA$ and its derivatives. Deuterium oxide (D_2O) was used as the solvent for HA and its derivatives. All samples were prepared at a concentration of 0.5% (wt/wt).

2.2.6. Gel Permeation Chromatography (GPC)

A GPC system composed of a Waters 515 HPLC Pump and Waters 2414 Refractive Index Detector using PSS columns (Styrogel 10^2, 10^3, 10^5 Å) in dimethylformamide (DMF) as an eluent at a flow rate of 1 mL/min at 50 °C was used. Samples were filtered over neutral alumina prior to analysis. The column system was calibrated with 12 poly(methyl methacrylate) (PMMA) standards.

2.2.7. Dynamic light scattering (DLS)

Dynamic light scattering (DLS) was measured using a Zetasizer Nano from Malvern Instruments, Ltd. Samples were prepared at a 0.1% (w/w) solution, and diluted in Milli-Q water. Sphere radii were taken from an average of 3 runs.

2.2.8. Tapping mode atomic force microscopy (AFM)

Experiments were carried out using a Multimode Nanoscope III system (Veeco 2 Instruments). Measurements were performed in air, using commercial silicon cantilevers with a nominal spring constant and resonance frequency respectively equal to 50 N/m and 290 kHz.

Silicon wafers with native oxide layers were cleaned with a jet of acetone, then with a jet of isopropyl alcohol, before the acetone evaporated, and blown dry with a flow of nitrogen. All samples were drop-casted on the substrates from 1 mg/mL aqueous solutions. Casting above lower-critical solution temperature (LCST) was carried out at 37 °C in a Fisher Scientific low temperature incubator.

The HA-PMEO_2MA sample was allowed to dry on a substrate at 37 °C. Coated wafers were incubated in a 10% albumin solution for up to 15 days and then imaged to assess protein adsorption on the scratched area.

2.2.9. Water contact angle measurements for modified HA films

Water contact angle was measured for films casted on Teflon surfaces using a Ramè-Hart contact angle goniometer. A 4 mg/mL solution of HA-PMEO_2MA was prepared in pure water. The modified HA solution was drop-cast over Teflon surfaces below the LCST. The discs were then incubated at 37 °C for an hour to ensure transition, uniform and tight coating over the surface. Warm water droplets (2-15 µL) were placed over the cast film and the native substrate; images were taken 30 s post water placement. The process was repeated 10 times for each volume and average measurements were reported.

2.2.10. Quartz Crystal Microbalance (QCM-D) analysis

A Q-Sense E4 system (Biolin Scientific) was used for these mesaurements. Experiments were performed using 4 SiO_2 sensors (QSX 303) mounted in QFM 401 flow modules. All experiments were performed with the sensors mounted in parallel. An external digital pump (Ismatec IPC-N 4) was used to control the flow rate of the solutions, using tubing with inner diameter of 0.64 mm. An E4 Autosampler was used for liquid handling. Before each experiment, the sensors were cleaned for 10 min using a UV/Ozone Procleaner™ (Bioforce Nanosciences) followed by immersion of the sensors in 2 wt% sodium dodecylsulfate for 30 min. The sensors were subsequently rinsed carefully with copious amounts of deionized water, and were dried under a gentle stream of nitrogen gas. Finally, the sensors were exposed to UV/ozone for 10 min before mounting in the flow modules.[40-44] After the sensors were mounted, the flow modules and tubing were filled with water and the resonance frequencies were collected at ambient temperature. The volume above the sensor is 40 µL.

The experiments were performed as follows: the temperature was set to 15 °C, and sensors 1-3 were exposed to HA (40 µL above sensor, 4 mg/mL), whereas sensor 4 was exposed to water at a

flow rate of 100 μL/min. Sensor 4 was further used as a positive control for BSA binding. Next, the temperature was set to 37 °C, and the resulting frequency and dissipation shifts, Δf and ΔD respectively, were recorded. Following baseline stabilization after the temperature increase, solutions of BSA, pre-heated to 37 °C, were injected to sensors 1, 2 and 4, and water, as a negative control, to sensor 3. Finally, the sensors were regenerated by setting the temperature to 15 °C and rinsing with pre-cooled water to remove the HA. All results are reported for the third overtone (n=3), unless otherwise stated.

2.2.11. Biolayer Interferometry (BLI) analysis

A ForteBio Octet Red (Pall Life Sciences) system was used in this study. Experiments were performed in a 96-well, polypropylene, flat-bottom, black microplate (Greiner Bio-one). Experiments were performed at 37 °C for HA-PMEO_2MA samples, with the microplate shaking at 1000 rpm. The volume of the sample in each well was 230 μL. All solutions were prepared in 1X PBS that was filtered through a 0.2 μm Acrodisc PTFE syringe filter. Sensor tips selected for these experiments were aminopropylsilane (APS). ForteBio sensor tips were hydrated in 1X PBS for a minimum of 15 minutes before beginning each experiment and the sample plate was equilibrated for 5 minutes to ensure a steady temperature. To model a moderately hydrophobic biomaterial surface, APS tips were reacted with a (3-glycidyloxypropyl)trimethoxysilane (≥98%, Aldrich) in a 25 min loading step during the ForteBio experiments. Data analysis was performed on the ForteBio data analysis software.

2.2.11.1 Control experiments with unmodified HA

Control experiments were run against unmodified HA to ensure that the polymer had no affinity to the trimethoxysilane sensor surface. APS sensor tips were submerged in a 0.5% (v/v) solution

of (3-glycidyloxypropyl)trimethoxysilane in water, with a pH adjusted to 4.3 with 0.1% (v/v) aqueous acetic acid solution for 25 minutes. The sensor tips were then submerged in a well containing 1X PBS for 60 s to rinse off any unreacted material. Tips were then moved to wells containing a 2.5 mg/mL solution of unmodified HA in 1X PBS, and submerged for 10 minutes.

2.2.11.2 Control experiments with PEG

Monomethoxy poly(ethylene glycol) epoxide (mPEG-epoxide) of a 10 kDa molecular weight was purchased from Creative PEGWorks, and was used as received. A 0.5% (w/w) solution of the epoxide in water adjusted to a pH of 3.5 with a 0.1% (v/v) aqueous acetic acid solution was prepared. The APS sensor tips were submerged in a solution of mPEG-epoxide in a loading step that lasted 30 minutes. Real-time loading of the epoxide was monitored by surface thickness changes as monitored by the Fortebio software. Following loading, the sensor tip was rinsed for 60 s in 1X PBS to remove any unreacted PEG. Functionalized sensor tips were then exposed to wells containing 0.1 mg/mL solutions of IgG, Fbg and BSA for 10 minutes.

2.2.11.3 Modified HA.

Lyophilized HA-PMEO_2MA was dissolved in 1X PBS, and was kept below its LCST before the experiment began. Sample plates were prepared with 0.2, 0.1, 0.05, 0.025, 0.0125 mg/mL concentrations of proteins BSA , Fbg and IgG. Modified HA concentrations were kept at 0.240 mg/mL for all experiments.

The experiment were performed as follows: (1) 60 s baseline in 1X PBS, (2) 25 min loading in epoxysilane, (3) 60 s wash in 1X PBS, (4) 20 min loading to modified HA, (5) 60 s rinse in 1X PBS, (6) 60 s baseline in 1X PBS, (7) 10 min association to protein, and (8) 10 min dissociation in 1X PBS.

2.2.12 Coating complex objects

Micromachined grids of poly(methyl methacrylate) having thickness 50 μm and channel width 100 μm were obtained from Laser Micromachining Limited (St. Asaph, UK) and pressed into a grid using small amounts of CH_2Cl_2 at the edges. To image the coating, HA-$PMEO_2MA$ was fluorescently labeled using a carboxyl-reactive label, Alexafluor 488 hydrazide, through a carbodiimide-mediated reaction on the carboxyl group of HA. A target of 0.1 mol% of COOH groups on HA were labeled. To the HA-$PMEO_2MA$ solution, 10 molar excess of EDC was added as a solution and mixed well. To that, 0.1 mol% of COOH groups of dye was added and let stir for 4 hours at 4 °C. the solution was then dialyzed for 48 hours against ultra-pure water through a 1,000 MWCO dialysis membranes. The fluorescently coated grids were imaged using a Zeiss LSM 700 confocal microscope.

2.3 Results and Discussion

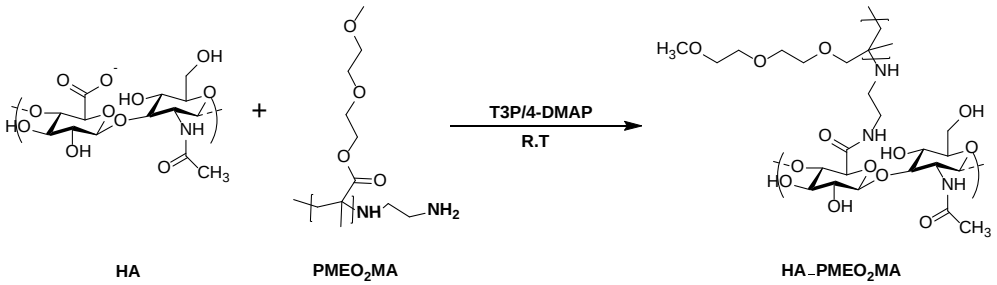

Scheme 2.3.1. The chemical composition of HA and modification route.

2.3.1. HA Modification

HA was modified with $PMEO_2MA$, as shown in Scheme 2.3.1, by grafting the thermoresponsive polymer $PMEO_2MA$ onto HA to prepare HA-$PMEO_2MA$. Characterization of the grafting density was performed using ^1H NMR with representative data shown in Figure 2.3.1.1. $PMEO_2MA$ is a biocompatible thermoresponsive polymer whose lower critical solution temperature (LCST) can be tailored to temperatures in the range of 26-52 °C depending on the number of ethylene oxide

repeat units on the side chains.[38] Once the LCST was exceeded, the polymer precipitated from solution, as the hydrophobic interactions within the polymer chains overcome those of the hydrophilic interactions between the polymer and the solvent, transitions from coil to globule and anchor the HA to surrounding surfaces.[45] This drove physical adsorption of the polymer to the surface of the substrate, binding HA to the surface with it. We hypothesized that this process would result in presentation of the hydrophilic HA from the surface of the coating, providing a means for preparing a robust biomaterial surface that resists protein adsorption.

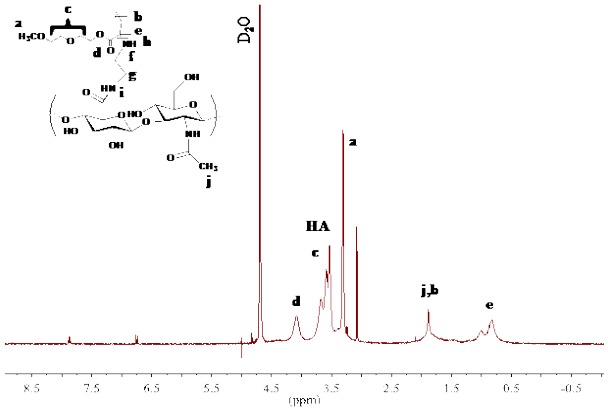

Figure 2.3.1.1. ^{1}H NMR for HA-PMEO$_2$MA coating material.

2.3.2. Proposed structure of coating

Based on these data, the structure of a single domain is proposed schematically in Figure 2.3.2.1. The schematic is depicted assuming that the driving force for adsorption is the change in polymer-graft solubility but the water contact angle and resistance to protein adsorption appear to be determined largely by the HA so the PMEO$_2$MA grafts are sequestered at the substrate and within the coating. This mechanism intrinsically leads to a highly hydrophilic surface that resists protein adsorption and adheres tightly to hydrophobic surfaces.

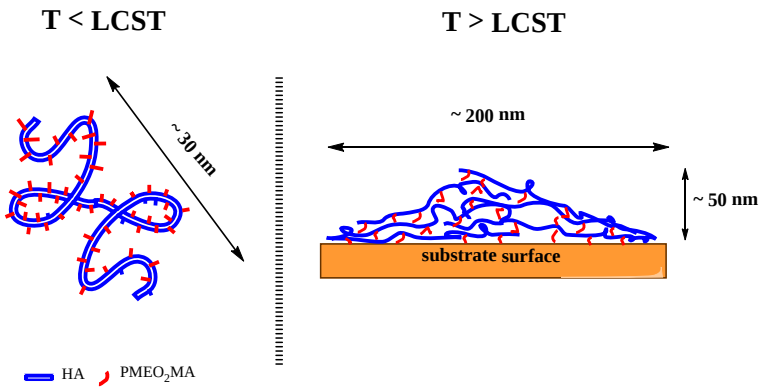

Figure 2.3.2.1. Schematic of HA-PMEO$_2$MA in solution at T < LCST (left) and the coating (T > LCST). The schematic at T > LCST illustrates a potential structure that is compatible with the AFM images but is not drawn to scale.

2.3.3. Dynamic Light Scattering

DLS was used to characterize the size of HA-PMEO$_2$MA in solution. Below the LCST, solutions of HA-PMEO$_2$MA showed particle sizes not significantly different than unmodified HA solutions, with a mean size of 30 nm, consistent with previous reports.[46] Above the LCST, HA-PMEO$_2$MA aggregates showed a particle size approaching 300 nm (Figure 2.3.3.1). This suggests that aggregates form homogenously in solutions and then precipitate onto the surface to form the coating, but further work is required to determine the exact steps of this process.

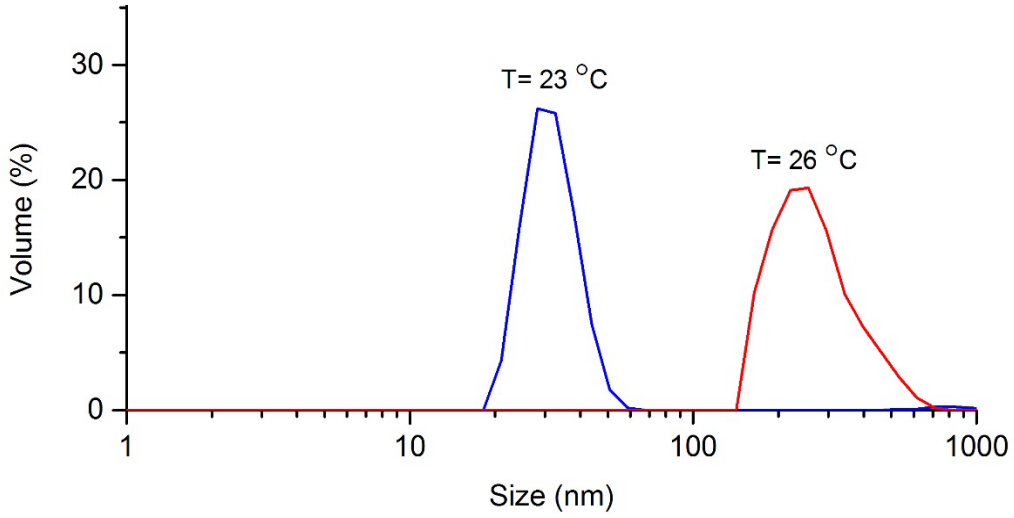

Figure 2.3.3.1. DLS data showing the distributions of diameters for HA-PMEO$_2$MA below LCST and above LCST.

2.3.4. Atomic Force Microscopy (AFM) Analysis

AFM analysis was used to compare the morphology of uncoated SiO_2 surfaces with those exposed to the HA-PMEO$_2$MA solutions. Moreover, film thickness was assessed employing a scratch test in which a scratch is created on the coated surface, creating a groove of uncoated surface. Results obtained from these experiments are shown in Figure 2.3.4.1. In these experiments, HA-PMEO$_2$MA was deposited on an SiO_2 surface cleaned by sonication in ethanol and blown dry with air. The coating was deposited by drop-casting from an aqueous solution, dried in an incubator, and rinsed with warm water. The thickness of the layer was determined by measuring the film profile following mechanical delamination with a needle. Following the scratch test, a difference in reflectivity was observed with the delaminated region reflecting ambient light much more strongly than the coated region. By comparing the change in film height using AFM, the thickness was determined to be ~50 nm. The scratch clearly exposed the SiO_2 surface, evidenced by the decrease in surface roughness (Figure 2.3.4.1D) and by the difference of the images taken inside

and outside of the scratch (Figures 2.3.4.1C). When compared to the uncoated SiO_2 surface (delaminated), the coating based on HA-$PMEO_2MA$ material showed a different morphology (Figure 2.3.4.1C). AFM analysis revealed the presence of a uniform layer of characteristic granular appearance. The average diameter of the rounded asperities was around 230 nm on average, suggesting each is composed of several HA-$PMEO_2MA$.

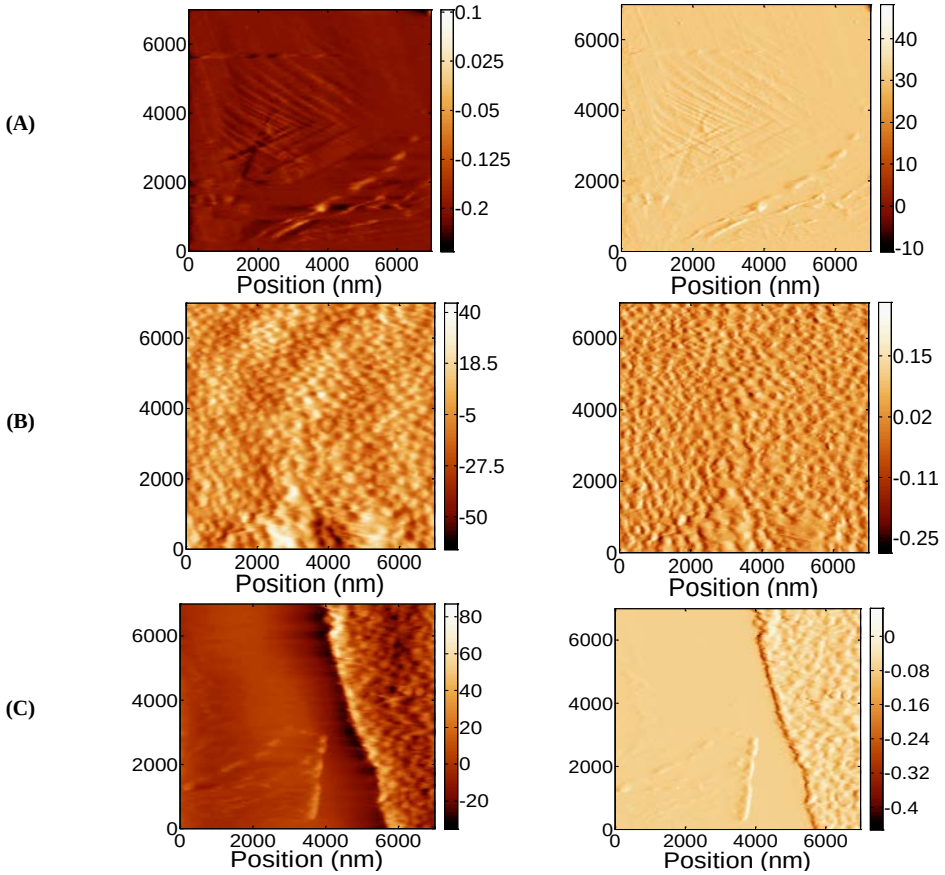

(D)

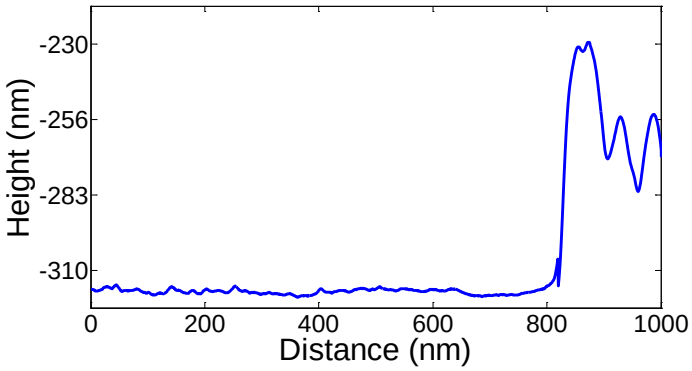

Figure 2.3.4.1. AFM images HA-PMEO$_2$MA materials. Images on the left show height (nm) while those on the right show cantilever deflection (nm). **(A**) Unmodified silica wafer surface. **(B**) HA-PMEO$_2$MA coatings. **(C)** Scratched HA-PMEO$_2$MA coatings. **(D)** Height profile of coating from scratch region to coated region

2.3.5. Water contact angle

The average of 10 measurements on films formed by the drop-casting of HA-PMEO$_2$MA materials above LCST showed that, although not completely wetting, HA-PMEO$_2$MA-coated surfaces exhibited a significant increase in hydrophilicity, changing from 98° on uncoated Teflon to 16° on HA-PMEO$_2$MA films on a Teflon substrate. This effect is attributed to the HA rather than the hydrophilic ethylene oxide domains in PMEO$_2$MA because surface-grafted PMEO$_2$MA brushes have been shown to exhibit water contact angle shifts from 40° to 102° below and above LCST, respectively.[47] Although the coating domains appeared uniform, as demonstrated by AFM measurements, a non-negligible fraction of hydrophobic PMEO$_2$MA domains could still be presented from the surface of the coating as opposed to being sequestered in the coating interior or at the Teflon surface. This could explain the less-than-complete-wetting behavior observed on coatings prepared from HA-PMEO$_2$MA materials (data not shown). However, although not completely wetting, the surface is expected to inhibit protein adsorption.[10-11] These results also

correlated well with recent theoretical and experimental work dealing with the adsorption of blood-proteins to various surfaces.[12]

2.3.6. Biolayer Interferometry (BLI) Analysis

2.3.6.1 Control experiments of protein against the surface of unmodified sensor tips

BLI technology uses interferometric detection of changes in the optical path length at a fiber optic sensor tip to measure binding kinetics. For the current work, a ForteBio Octet Red instrument was used to examine the extent of protein adsorption occurring on a coated material surface. The instrument reports shifts in units of nm, and although this cannot be taken as an absolute thickness measurement, it does provide a highly accurate kinetics measurement. Control experiments with free protein and an APS sensor tip were performed in which APS tips were reacted with 3-glycidoxypropyltrimethoxysilane to functionalize the tip as a moderately hydrophobic surface for interactions with free proteins. By reacting the amine surface with the trimethoxysilane (TMS), we also remove the charge on the sensor surface so that there is no enhancement in affinity between sensor surface and free protein due to electrostatics. Also, more control experiments were performed using PEG-based materials to assess the efficacy of the prepared HA-PMEO$_2$MA coatings.

Three separate experiments were performed where six sensor tips per experiment were modified with TMS, and introduced to 6 wells of a 96-well plate containing Fbg, BSA, and unmodified HA (all proteins were run in separate experiments). The protein-adsorption experiments were all run at concentrations of 0.2 mg/mL, 0.1 mg/mL, 0.05 mg/mL, 0.025 mg/mL, 0.0125 mg/mL, and 0 mg/mL, while unmodified HA was run at a concentration of 2.5 mg/mL.

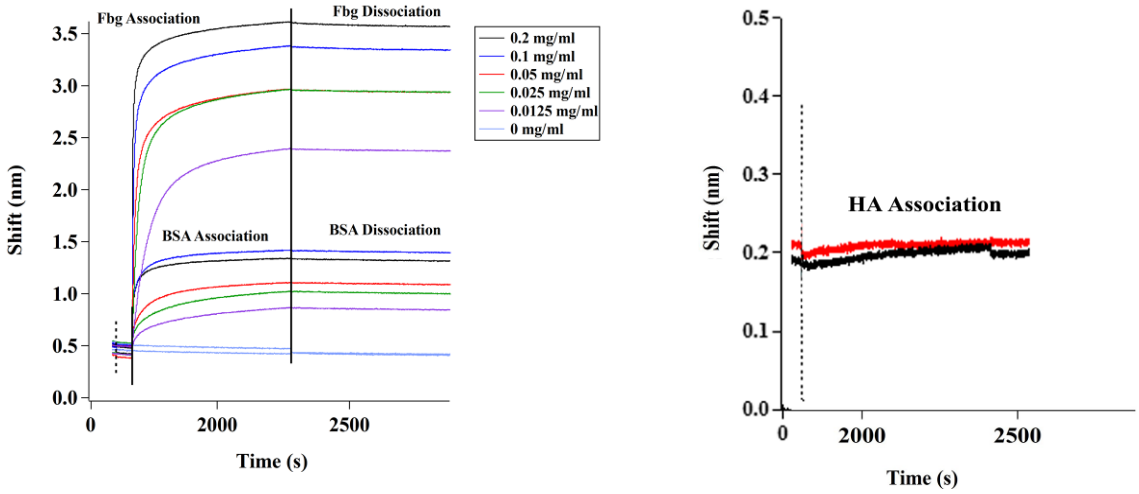

Figure 2.3.6.1.1. Binding behavior of BSA and Fbg proteins (left) and unmodified HA (right) against TMS functionalized sensor tip as measured.

Figure 2.3.6.1.1 shows representative protein and HA adsorption experiments on TMS-functionalized sensors. The Fbg protein had a change in film thickness characterized by shift values ranging from 1.9 – 3.1 nm, BSA had shift values ranging from 0.4 – 0.9 nm, consistent with relative differences in protein size. The data were fit using the ForteBio analysis software, and an average on-rate, k_{on}, for protein association, was calculated to be (5.8 ± 1.3) x 10^5 $M^{-1}s^{-1}$ for Fbg, and (2.8 ± 1.9) x 10^5 $M^{-1}s^{-1}$ for BSA. An off-rate was also estimated for this model, and for Fbg k_{off} was (3.0 ± 1.5) x 10^{-5} s^{-1}, while for BSA it was (5.2 ± 3.6) x 10^{-5} s^{-1}. Note the dissociation rate is very slow for both proteins, so the error in these measurements is relatively large. The K_D values for Fbg and BSA on the TMS-functionalized surfaces were 5.2 x 10^{-11} M and 1.9 x 10^{-10} M respectively, suggesting strong binding interactions for both serum proteins on hydrophobically modified sensor surfaces. In contrast, HA does not bind appreciably to the TMS-functionalized surfaces, as expected given its hydrophilic character.

2.3.6.2 Effect of free PEG on protein adsorption

A separate control experiment was performed to identify the effect of free PEG on protein adsorption. Here, the amine terminated sensor tips were reacted with an epoxy-terminated 10 kDa methoxyPEG. A 10 kDa molecular weight is estimated, based on the number of active sites on the sensor tips, and the radius of gyration of the 10 kDa PEG, to provide full coverage of the surface area of the sensor tip when the polymer reacted with the free amines.

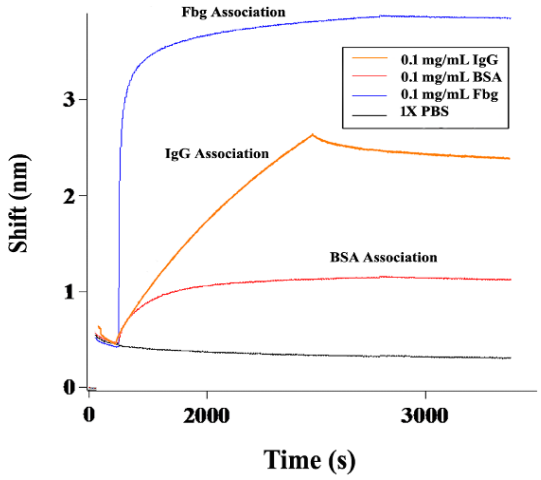

Figure 2.3.6.2.1. Protein adsorption profiles on PEG-modified sensor tips as measured by BLI against BSA, Fbg and IgG.

Figure 2.3.6.2.1 shows that the Fbg, IgG and BSA deposited with 3.4 nm, 2.5 nm and 0.7 nm change in film thickness, respectively. Despite the presence of a free PEG chain at the surface, proteins were still capable of depositing onto the sensor tip.

2.3.6.3 Modified HA materials

Protein adsorption on the HA-PMEO$_2$MA coatings was then investigated. Here, the modified sensor tips were introduced to solutions of HA-PMEO$_2$MA at a concentration of 0.240 mg/mL with an approximate HA modification degree of 10%. The experiments were run at 37 °C to

ensure that the experimental temperature exceeded the LCST temperature (26 °C) of the HA-PMEO$_2$MA materials and to simulate human physiological temperatures.

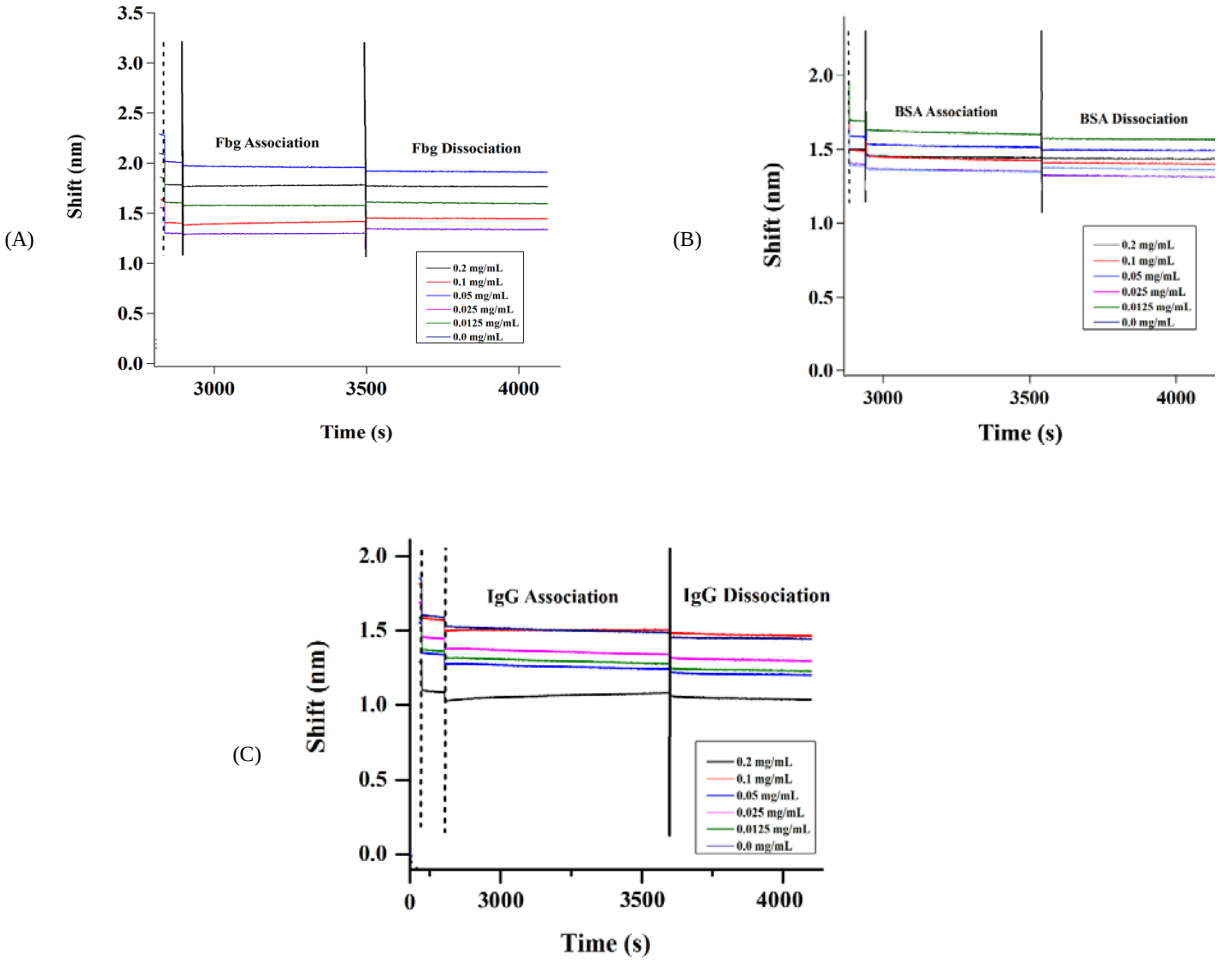

Figure 2.3.6.3.1. Protein adsorption profiles on HA-PMEO$_2$MA materials as measured using BLI. **(A**) Fbg. **(B)** BSA. IgG (**C**)

HA-PMEO$_2$MA-functionalized sensor tips were then immersed in solutions of Fbg , BSA and IgG. Figures 2.3.5.3.1A , 2.3.5.3.1B and 2.3.5.3.1C display the results of protein adsorption to the sensor tips functionalized with the HA-PMEO$_2$MA material. In the Fbg , BSA and IgG experiments, tips were immersed in the protein solution for 10 min, and showed no measurable

association for Fbg, BSA and IgG, indicating that the HA-PMEO$_2$MA polymer prevents protein adsorption to the surface of the functionalized sensor tip.

2.3.6. Quartz Crystal Microbalance with Dissipation Monitoring (QCM-D)

QCM-D measurements were performed to explore the HA-PMEO$_2$MA coatings as antifouling materials. Initial exposure of the silicon dioxide sensors to HA-PMEO$_2$MA at 15 °C, resulted in a frequency shift of -47.5±1.5 Hz and dissipation shift of 3.8±0.2 for the third overtone (n=3). Changing the temperature to 37 °C resulted in *ca.* 250 Hz net decrease of the resonance frequency for the HA coated sensors, whereas the net dissipation decrease was 10^{-6} (n=3). Thus, these results indicate a thick enough layer to fully coat the underlying substrate, and highly rigid binding of the HA-PMEO$_2$MA to the silicon dioxide surfaces. Figure 2.3.6.1 below, shows the frequency shift, Δf, as a function of time upon injection of BSA over HA-coated (HA-PMEO$_2$MA) silica and plain silica as a positive control.

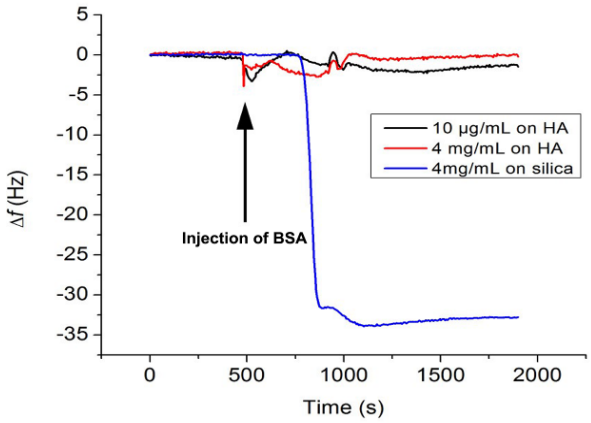

Figure 2.3.6.1. Injection of BSA over HA-coated (HA-PMEO$_2$MA) sensors and plain silicon dioxide as indicated at 37°C. For injection over HA-PMEO$_2$MA, the response of the negative control (water injected over HA-PMEO$_2$MA, not shown) was subtracted.

As can be seen in Figure 2.3.6.1, injecting BSA over the HA-coated surfaces results in negligible frequency shifts, whereas injection of BSA over plain silica, results in a frequency shift of *ca.* 32 Hz. Thus, the data presented in Figure 9 support the antifouling behavior of the HA coating.

The well-known Sauerbrey relation states that for thin, rigid and homogenous films, Δf is directly proportional to the change in mass,[48] Δm_f, of the film according to:

$$\frac{\Delta f}{n} = -\frac{f_0}{t_q \rho_q} \Delta m_f \qquad (1)$$

Where f_0 (5 MHz) is the fundamental frequency of the quartz crystal, t_q (3.3×10^{-4} m) the thickness of the quartz plate, ρ_q (2648 kg/m^3) the density of quartz and n = 3, 5, 7… the overtone number. However, under viscous damping, energy is lost during the oscillatory motion of the crystals according to

$$D = \frac{E_l}{2\pi E_s} = \frac{1}{\pi f \tau} \qquad (2)$$

where E_l and E_s are the lost and stored energies, respectively, and τ is the time constant of the amplitude decay of the oscillating crystal observed as the driving voltage over the crystal is turned off.[49] In general, thin, as well as thick and rigid layers induce low damping, whereas viscoelastic films lead to higher dissipative losses. If water couples hydrodynamically to the film, the dissipation is usually higher, which is observed in a higher $\Delta D/\Delta f$ ratio.[50-52] Thus, a net frequency shift of 250 Hz and a dissipation shift of 10^{-6} upon HA-PMEO$_2$MA binding to the silicon dioxide surfaces indicate highly rigid binding of the polymer to the silicon dioxide surfaces.

Lowering the temperature to 15 °C after BSA injection and rinsing with water at 100 µL/min resulted in the removal of the HA as seen by the large positive frequency shifts. After water

injection for 2000 s, the frequency had reversed to 90% of the starting value on average for the HA coated surfaces, suggesting the coating can be removed at temperatures below the LCST.

2.3.7. Coatings on complex objects

Figure 2.3.7.1 shows micromachined orthogonal PMMA discs incubated at 37 °C with fluorescently labeled HA grafted with $PMEO_2MA$ chains. Excellent coating coverage and stability could be observed, indicating this approach is amenable to coating complex shapes. Further investigations of this are necessary, but good coverage in conformal coating is observed at the higher solution concentrations. Figure 10D shows the same orthogonal discs after 5 minutes incubation in cold water, 4 °C. After incubation, fluorescent signals could not be detected, indicating the complete removal of the labeled HA-$PMEO_2MA$ materials, which further support the reversibility of the coating process.

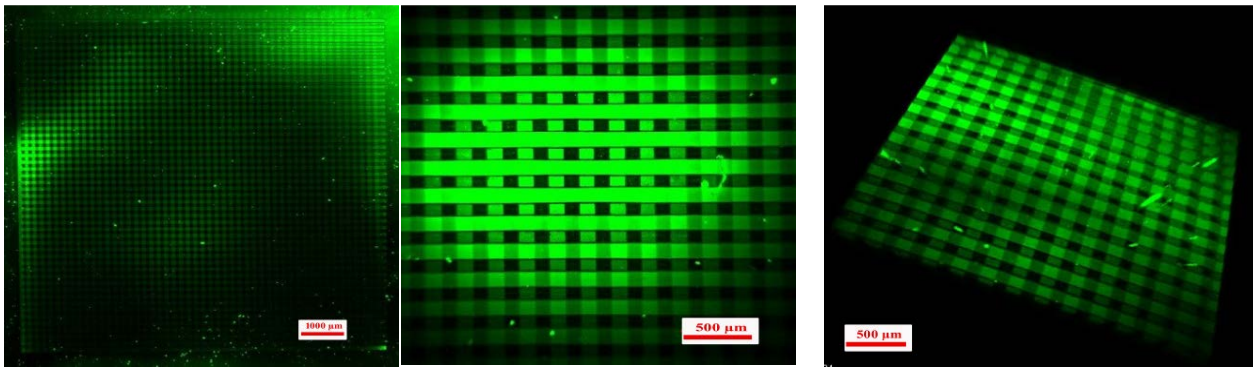

(A) **(B)** **(C)**

(D)

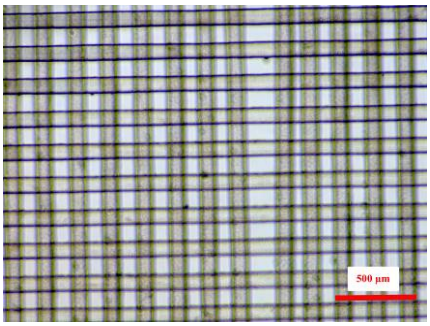

Figure 2.3.7.1. Confocal images of HA-PMEO$_2$MA-coated PMMA discs **(A)** 1X 2D view **(B)** 5X 2D, **(C)** 5X Z-stack view, **(D)** 4X optical view of PMMA discs after washing with cold water. Grids are 100 x 100 µm.

2.4 Conclusions

We have demonstrated that functionalization of HA with a polymer having an LCST can be used to prepare robust coatings that inhibit protein adsorption. The covalent attachment of PMEO$_2$MA to HA resulted in a material that became insoluble in aqueous media above 26 °C, forming robust coatings on SiO_2 and Teflon with domains based on a lateral size of *ca.* 230 nm and an average thickness of 50 nm. These coatings had a water contact angle of 16°, making them sufficiently hydrophilic to resist adsorption of BSA, Fbg and IgG as measured using optical interferometry and quartz crystal microbalance. A structural model of the adsorbed coating was proposed in which the PMEO$_2$MA grafts segregate to the substrate surface and the interior of the coating domain, presenting the HA to the solution where it imparts resistance to protein adsorption despite the high concentration of hydrophobic grafts. We propose that this approach could be the basis for the facile preparation of robust hydrophilic coatings on a range of hydrophobic surfaces.

Finally, I would like to emphasize that the work presented in this chapter was done in collaboration with Mohamed Ramadan and Gunnar Duner. I was responsible for the experiments, data analysis and writing of the part about atomic force microscopy and took part in the QCM experiments.

2.5 References

1. Vroman, L.; Adams, A. L.; Fischer, G. C.; Munoz, P. C., Interaction of high molecular weight kininogen, factor XII, and fibrinogen in plasma at interfaces. *Blood* **1980,** *55* (1), 156-9.

2. Garland, A.; Shen, L.; Zhu, X., Mobile precursor mediated protein adsorption on solid surfaces. *Progress in Surface Science* **2012,** *87* (1-4), 1-22.

3. Gombotz, W. R.; Guanghui, W.; Horbett, T. A.; Hoffman, A. S., Protein adsorption to poly(ethylene oxide) surfaces. *Journal of biomedical materials research* **1991,** *25* (12), 1547-1562.

4. Alcantar, N. A.; Aydil, E. S.; Israelachvili, J. N., Polyethylene glycol-coated biocompatible surfaces. *Journal of biomedical materials research* **2000,** *51* (3), 343-51.

5. Geelhood, S. J.; Horbett, T. A.; Ward, W. K.; Wood, M. D.; Quinn, M. J., Passivating protein coatings for implantable glucose sensors: evaluation of protein retention. *Journal of biomedical materials research. Part B, Applied biomaterials* **2007,** *81* (1), 251-60.

6. Bridges, A. W.; Garcia, A. J., Anti-inflammatory polymeric coatings for implantable biomaterials and devices. *Journal of diabetes science and technology* **2008,** *2* (6), 984-94.

7. Lee, J. H.; Lee, H. B.; Andrade, J. D., Blood compatibility of polyethylene oxide surfaces. *Progress in Polymer Science* **1995,** *20* (6), 1043-1079.

8. Kennedy, S. B.; Washburn, N. R.; Simon, C. G., Jr.; Amis, E. J., Combinatorial screen of the effect of surface energy on fibronectin-mediated osteoblast adhesion, spreading and proliferation. *Biomaterials* **2006,** *27* (20), 3817-24.

9. Dekker, A.; Reitsma, K.; Beugeling, T.; Bantjes, A.; Feijen, J.; van Aken, W. G., Adhesion of endothelial cells and adsorption of serum proteins on gas plasma-treated polytetrafluoroethylene. *Biomaterials* **1991,** *12* (2), 130-8.

10. Bumgardner, J. D.; Wiser R Fau - Elder, S. H.; Elder Sh Fau - Jouett, R.; Jouett R Fau - Yang, Y.; Yang Y Fau - Ong, J. L.; Ong, J. L., Contact angle, protein adsorption and osteoblast precursor cell attachment to chitosan coatings bonded to titanium. (0920-5063 (Print)).

11. Sigal, G. B.; Mrksich, M.; Whitesides, G. M., Effect of Surface Wettability on the Adsorption of Proteins and Detergents. *Journal of the American Chemical Society* **1998,** *120* (14), 3464-3473.

12. Vogler, E. A., Protein adsorption in three dimensions. *Biomaterials* **2012,** *33* (5), 1201-1237.

13. Zhang, M.; Desai, T.; Ferrari, M., Proteins and cells on PEG immobilized silicon surfaces. *Biomaterials* **1998,** *19* (10), 953-960.

14. Akizawa, T.; Kino, K.; Koshikawa, S.; Ikada, Y.; Kishida, A.; Yamashita, M.; Imamura, K., Efficiency and biocompatibility of a polyethylene glycol grafted cellulosic membrane during hemodialysis. *ASAIO transactions / American Society for Artificial Internal Organs* **1989,** *35* (3), 333-5.

15. Churaev, N. V.; Sergeeva, I. P.; Sobolev, V. D., Hydrodynamic Thickness and Deformation of Adsorbed Layers of Polyethylene Oxides. *Journal of Colloid and Interface Science* **1995,** *169* (2), 300-305.

16. McPherson, T.; Kidane, A.; Szleifer, I.; Park, K., Prevention of Protein Adsorption by Tethered Poly(ethylene oxide) Layers: Experiments and Single-Chain Mean-Field Analysis. *Langmuir : the ACS journal of surfaces and colloids* **1998,** *14* (1), 176-186.

17. Kenausis, G. L.; Vörös, J.; Elbert, D. L.; Huang, N.; Hofer, R.; Ruiz-Taylor, L.; Textor, M.; Hubbell, J. A.; Spencer, N. D., Poly(l-lysine)-g-Poly(ethylene glycol) Layers on Metal Oxide Surfaces: Attachment Mechanism and Effects of Polymer Architecture on Resistance to Protein Adsorption†. *The Journal of Physical Chemistry B* **2000,** *104* (14), 3298-3309.

18. Shi, J.; Xing, M. M. Q.; Zhong, W., Development of Hydrogels and Biomimetic Regulators as Tissue Engineering Scaffolds. *Membranes* **2012,** *2* (4), 70-90.

19. Huang, N.-P.; Michel, R.; Voros, J.; Textor, M.; Hofer, R.; Rossi, A.; Elbert, D. L.; Hubbell, J. A.; Spencer, N. D., Poly(l-lysine)-g-poly(ethylene glycol) Layers on Metal Oxide Surfaces: Surface-Analytical Characterization and Resistance to Serum and Fibrinogen Adsorption. *Langmuir : the ACS journal of surfaces and colloids* **2000,** *17* (2), 489-498.

20. Mauzac, M.; Jozefonvicz, J., Anticoagulant activity of dextran derivatives. Part I: Synthesis and characterization. *Biomaterials* **1984,** *5* (5), 301-4.

21. Löfås, S.; Johnsson, B., A Novel Hydrogel Matrix on Gold Surfaces in Surface Plasmon Resonance Sensors for Fast and Efficient Covalent Immobilization of Ligands. *Journal of the Chemical Society, Chemical Communications* **1990**, 1526-1528.

22. Schasfoort, R. B. M.; Tudos, A. J., *Handbook of Surface Plasmon Resonance*. 1 ed.; RSC Publishing: Cambridge, UK, 2008; p 426.

23. Cao, B.; Li, L.; Wu, H.; Tang, Q.; Sun, B.; Dong, H.; Zhe, J.; Cheng, G., Zwitteration of dextran: a facile route to integrate antifouling, switchability and optical transparency into natural polymers. *Chemical Communications* **2014,** *50* (24), 3234-3237.

24. Dubois, J.; Gaudreault, C.; Vermette, P., Biofouling of dextran-derivative layers investigated by quartz crystal microbalance. *Colloids and Surfaces B: Biointerfaces* **2009,** *71* (2), 293-299.

25. Lichty, J. J.; Malecki, J. L.; Agnew, H. D.; Michelson-Horowitz, D. J.; Tan, S., Comparison of affinity tags for protein purification. *Protein Expression and Purification* **2005,** *41* (1), 98-105.

26. Tizzotti, M.; Charlot, A.; Fleury, E.; Stenzel, M.; Bernard, J., Modification of Polysaccharides Through Controlled/Living Radical Polymerization Grafting—Towards the Generation of High Performance Hybrids. *Macromolecular Rapid Communications* **2010,** *31* (20), 1751-1772.

27. Thomas, H.; Stephanie, H.; Nico, M.; Katrin, S., Polysaccharide Derivatives for the Modification of Surfaces by Self-Assembly. In *Model Cellulosic Surfaces*, American Chemical Society: 2009; Vol. 1019, pp 195-221.

28. Segura, T.; Anderson, B. C.; Chung, P. H.; Webber, R. E.; Shull, K. R.; Shea, L. D., Crosslinked hyaluronic acid hydrogels: a strategy to functionalize and pattern. *Biomaterials* **2005,** *26* (4), 359-71.

29. Lapcik, L., Jr.; Lapcik, L.; De Smedt, S.; Demeester, J.; Chabrecek, P., Hyaluronan: Preparation, Structure, Properties, and Applications. *Chem Rev* **1998,** *98* (8), 2663-2684.

30. Kogan, G.; Soltes, L.; Stern, R.; Gemeiner, P., Hyaluronic acid: a natural biopolymer with a broad range of biomedical and industrial applications. *Biotechnology letters* **2007,** *29* (1), 17-25.

31. Stern, R.; Asari, A. A.; Sugahara, K. N., Hyaluronan fragments: an information-rich system. *European journal of cell biology* **2006,** *85* (8), 699-715.

32. Schanté, C. E.; Zuber, G.; Herlin, C.; Vandamme, T. F., Chemical modifications of hyaluronic acid for the synthesis of derivatives for a broad range of biomedical applications. *Carbohydrate Polymers* **2011,** *85* (3), 469-489.

33. Neumann, A.; Schinzel, R.; Palm, D.; Riederer, P.; Münch, G., High molecular weight hyaluronic acid inhibits advanced glycation endproduct-induced NF-κB activation and cytokine expression. *FEBS Letters* **1999,** *453* (3), 283-287.

34. Bulpitt, P.; Aeschlimann, D., New strategy for chemical modification of hyaluronic acid: Preparation of functionalized derivatives and their use in the formation of novel biocompatible hydrogels. *Journal of biomedical materials research* **1999,** *47* (2), 152-169.

35. Kuo, J. W.; Swann, D. A.; Prestwich, G. D., Chemical modification of hyaluronic acid by carbodiimides. *Bioconjugate Chemistry* **1991,** *2* (4), 232-241.

36. Tan, H.; Ramirez, C. M.; Miljkovic, N.; Li, H.; Rubin, J. P.; Marra, K. G., Thermosensitive injectable hyaluronic acid hydrogel for adipose tissue engineering. *Biomaterials* **2009,** *30* (36), 6844-53.

37. Miura, M.; Cole CA, Monji, N.; Hoffman, A. S., Temperature-dependent absorption/desorption behavior of lower critical solution temperature (LCST) polymers on various substrates. *Journal of Biomaterials Science, Polymer Edition* **1994**, *5* (6), 555-568.

38. Yamamoto, S.-I.; Pietrasik, J.; Matyjaszewski, K., The effect of structure on the thermoresponsive nature of well-defined poly(oligo(ethylene oxide) methacrylates) synthesized by ATRP. *Journal of Polymer Science Part A: Polymer Chemistry* **2008,** *46* (1), 194-202.

39. Coessens, V.; Matyjaszewski, K., Synthesis of polymers with hydroxyl end groups by atom transfer radical polymerization. *Macromolecular Rapid Communications* **1999,** *20* (3), 127-134.

40. Popova, M. V.; Chernyshev, Y. S., Self-Association of Potassium Nonanoate Molecules in Aqueous Aerosil Dispersions: 13C NMR Data. *Colloid Journal* **2004,** *66* (5), 567-574.

41. Penfold, J.; Staples, E.; Tucker, I.; Thomas, R. K., Adsorption of Mixed Anionic and Nonionic Surfactants at the Hydrophilic Silicon Surface. *Langmuir : the ACS journal of surfaces and colloids* **2002,** *18* (15), 5755-5760.

42. Harewood, K.; Wolff Iii, J. S., A rapid electrophoretic procedure for the detection of SDS-released oncorna-viral RNA using polyacrylamide-agarose gels. *Analytical Biochemistry* **1973,** *55* (2), 573-581.

43. Vig, J. R., UV/ozone cleaning of surfaces. *Journal of Vacuum Science & Technology A* **1985,** *3* (3), 1027-1034.

44. Krozer, A.; Rodahl, M., X-ray photoemission spectroscopy study of UV/ozone oxidation of Au under ultrahigh vacuum conditions. *Journal of Vacuum Science & Technology A* **1997,** *15* (3), 1704-1709.

45. Lutz, J.-F., Polymerization of oligo(ethylene glycol) (meth)acrylates: Toward new generations of smart biocompatible materials. *Journal of Polymer Science Part A: Polymer Chemistry* **2008,** *46* (11), 3459-3470.

46. Grymonpré, K. R.; Staggemeier, B. A.; Dubin, P. L.; Mattison, K. W., Identification by Integrated Computer Modeling and Light Scattering Studies of an Electrostatic Serum Albumin-Hyaluronic Acid Binding Site. *Biomacromolecules* **2001,** *2* (2), 422-429.

47. Zengin, A.; Yildirim, E.; Caykara, T., RAFT-mediated synthesis and temperature-induced responsive properties of poly(2-(2-methoxyethoxy)ethyl methacrylate) brushes. *Journal of Polymer Science Part A: Polymer Chemistry* **2013,** *51* (4), 954-962.

48. Sauerbrey, G., The use of quartz oscillators for weighing thin layers and for microweighing. *Zeitschrift fur Physik* **1959,** *155*, 206-22.

49. Rodahl, M.; Höök, F.; Krozer, A.; Brzezinski, P.; Kasemo, B., Quartz crystal microbalance setup for frequency and Q-factor measurements in gaseous and liquid environments. *Review of Scientific Instruments* **1995,** *66* (7), 3924-30.

50. Höök, F.; Kasemo, B., The QCM-D technique for probing biomacromolecular recognition reactions. *Springer Series on Chemical Sensors and Biosensors* **2007,** *5* (Piezoelectric Sensors), 425-447.

51. Larsson, C.; Rodahl, M.; Höök, F., Characterization of DNA immobilization and subsequent hybridization on a 2D arrangement of streptavidin on a biotin-modified lipid bilayer supported on SiO2. *Analytical Chemistry* **2003,** *75* (19), 5080-5087.

52. Reimhult, E.; Larsson, C.; Kasemo, B.; Höök, F., Simultaneous surface plasmon resonance and quartz crystal microbalance with dissipation monitoring measurements of biomolecular adsorption events involving structural transformations and variations in coupled water. *Analytical Chemistry* **2004,** *76* (24), 7211-7220.

CHAPTER 3

REDUCING PROTEIN ADSORPTION WITH POLYMER-GRAFTER HYALURONIC ACID COATINGS: OPTIMIZATION OF MATERIAL PROPERTIES AND A STUDY ON COATING MECHANISM

3.1. Introduction

When a sterile but foreign material is placed inside a biological environment, for example a stent or a titanium plate is implanted inside the human body, a series of events begin, commonly known as the Vroman effect. The surface attracts serum proteins in a process that first affects small proteins with high mobility and abundance, such as albumin, but these are later replaced by larger ones, typically globulin, followed fibrinogen, then fibronectin, and factor XII, which can activate factor XI once that is transferred to the surface by high molecular weight kinin. However, if the surface is hydrophobic, then, upon arrival, fibrinogen changes its tertiary structure in order to maximize surface contact with its hydrophobic amino acids. These regions are normally hidden inside due to the physiologic environment's hydrophilicity, and denaturation leads to the presentation of amino acid sequences that attract platelets or function as signals for immunological, inflammatory cascades, with consequent thrombogenesis, inflammation followed by fibrous capsule formation, and host-versus-graft reaction.[22, 23]

To prevent these pathological events, implants, stents, and medical devices exposed to body fluids, particularly to serum, need to be coated.[23-28] This study focuses on the question of creating the best coating to prevent adsorption and understand how this coating is formed. A possible strategy is increasing hydrophilicity of the contact area, since it was shown that there was a threshold in contact angle above which protein adsorption was promoted but below which it was inhibited, and this threshold value was found to be 20°.[31-33] Hydrophilicity can be increased by ionization *via* plasma treatment or irradiation by ultraviolet light, but these methods will not have an effect on shielded areas of three-dimensional objects' surface.[29, 30] However, blocking the surface with an isolating layer could solve this problem.

To create this coating, a biocompatible and hydrophilic polymer can be used. Poly(ethylene glycol) (PEG) has been widely studied from this aspect.[24, 34-35] Unfortunately, PEG does not adhere strongly enough to hydrophobic materials without chemical attachment, and anchoring with covalent bonds requires the polymer's end-functionalization, which increases production costs. Also, this approach replaces drop- or spin-casting with a synthetic step, in which PEG's functional group has to be reacted with the accordingly modified substrate (e.g. maleimide-thiol or N-hydroxyl-succinimide-amine coupling).

There were studies where PEG was grafted on poly(L-lysine) (PLL), a polymer that gets physically adsorbed to negatively charged surfaces.[36] The weakness of this conjugate as an antifouling coating is that positively charged surfaces cannot be protected with it. Therefore, attempts were made to make use of the uncharged polysaccharide carboxymethyldextran (CMD) by grafting PEG onto it, but the resulting coating was heavily crosslinked, giving an uneven interface with unadvantageous rheological properties.[37]

Hence, in our previous work, HA, another polysaccharide that is naturally present in biological systems, including the human body, was used instead of CMD, in the hope that its linear structure would allow for a smoother surface coverage than CMD, eliminate the above mentioned problem of turbulences.[3] An alternative to CMD, HA is appealing because in addition to being hydrophilic and biocompatible, it is biologically active and resorbable, but it presents challenges in developing coatings due to its high concentration of reactive hydroxyl and carboxylic acid groups. In our previous work[3], we presented a chemical modification strategy of the biopolymer HA to make it suitable for coating a broad range of substrates.

As an established method for grafting onto, atom transfer radical polymerization (ATRP) was applied.[41] The resulting polymer was conjugated to HA by anchorment to HA's carboxyl groups via the aminated ATRP initiator.[21] The thermoresponsive polymer P($(MEO)_2$MA) was grafted onto HA to create an hydrophilic but potentially bioactive material for masking implant surfaces.[3] The LCST polymer was applied with the intention of benefiting its transition above room temperature but below body temperature, which was hypothesized to help to form a strongly adsorbing layer in situ, similarly to a study involving PNIPAM.[38, 39]

Here, our previous work was taken a step further. A series of conjugates were synthesized and studied with different chemical properties to find the most effective antifouling layer, and to help elucidate the underlying mechanism (Figure 3.1.1)

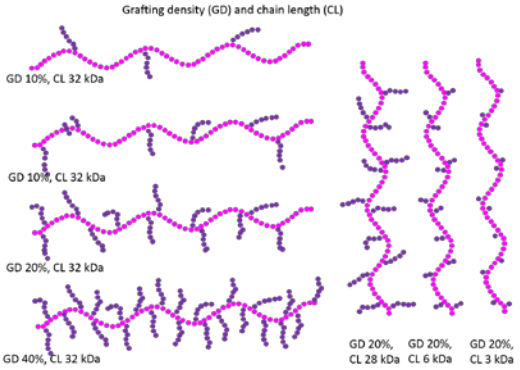

Figure 3.1.1: Conjugates with different GD and CL values

First, a series of conjugates with different GDs (5%, 10%, 20%, 40%) were prepared to find the optimal value that would allow for best prevention of protein adsorption. The materials were used to coat silica surfaces; the acquired film was visualized by atomic force microscopy (AFM), and QCM-D was applied to characterize aspects of the surface properties of the materials prepared. Results from this work indicate that surfaces coated with HA-P($(MEO)_2$MA)-GD 20% exhibited

a practically non-biofouling profile due to faster, uniform coating and a better prevention of irreversible protein adsorption.

It is hardly surprising that a grafted polymer, when prepared with different GD values, exhibits a maximum of a desirable property at a certain value. Intuitively, a minimal amount of the grafts should be necessary to add their chemical/physical properties to the "base molecule", but above a certain amount, steric hindrance can become an issue. An example for this is the incorporation of PLL into poly(ethylene glycol) diacrylate (PEGDA) for cell carrier applications, a system that is fairly similar to the ones studied in the current work. PLL-PEGDA showed optimal neural progenitor cell attachment and proliferation with 2 wt% PLL content.[40]

Therefore, in the second part of the optimization study, this particular GD value was further examined to find the minimal necessary CL. Conjugates were prepared by grafting P($(MEO)_2$MA) side chains of different length onto the HA backbone (32 kDa, 28 kDa, 6 kDa, 3 kDa). The excellent antifouling properties make the HA P($(MEO)_2$MA) conjugates with GD 10, 20 and 40% with CL 32 kDa promising materials for surface functionalization of devices exposed to a biological environment.

The second question raised by this study is pointed towards the mechanism of coating formation: how and why does it work; in relation to this, an explanation for the above samples' superior antifouling property was searched for. Based on results of DLS, QCM-D, UV-visible spectroscopy and contact angle experiments, the following trends are present. First, since both components are necessary – the polysaccharide for increasing hydrophilicity and the LCST polymer to allow for controlled deposition and consequently, for a smooth surface, which are both required to decrease contact angle – a comparable amount of the two components need to be incorporated in the

conjugates. Second, since the kinetics of deposition are heavily influenced by the value of the LCST, compositions that change this – for example, by allowing the formation of supramolecular structures – can lead to unexpected performance in terms of antifouling capabilities. The results suggest that these are the two most important factors that determine changes in energy dissipation during coating formation. Dissipation changes are important because, based on the studied samples, deposition and rearrangement being two separate events during coating formation appears to be the key to a good antifouling capability.

The rest of the chapter is organized as follows: a synthetic approach that is somewhat different from the previous one[3] is introduced, followed by the chemical and physical characterization of the materials by ^{1}H NMR, Gas Permeation Chromatography (GPC), DLS and AFM. Following this, the results of the QCM experiments are presented from the point of view of antifouling capabilities and mechanism of layer formation, further elucidated by water contact angle and UV-visible absorbance measurements. At the end of the chapter, the major results and their interpretation is summarized.

3.2 Experimental

3.2.1 Materials

Di(ethylene glycol) methyl ether methacrylate ($M(EO)_2MA$), ethyl 2-bromo-2-methylpropionate (EBiB), 2,2′-bipyridine (bpy), Copper(I) bromide (CuBr), anisole, hexanes, ethylenediamine, triethylamine (TEA), 4-(dimethylamino)pyridine (4-DMAP), and hyaluronic acid (HA) derived from Streptococcus equi (ca. 1.6 MDa) were purchased from Sigma-Aldrich at the highest purity available. Albumin from bovine serum (BSA) (> 98%, received as a lyophilized powder) and fibrinogen (Fbg) (from human plasma) were purchased from Sigma-Aldrich. Propane phosphonic

acid anhydride (T3P) in 50% w/w solution in N,N-dimethylformamide was received as a generous gift from Archimica. Also, 3-((tert-butoxycarbonyl)amino)propyl 2-bromo-2-methylpropanoate was received a gift of Saadyah E. Averick.

3.2.2 Synthesis of the homopolymer of P((MEO)$_2$MA) by ATRP (OK-1-2 and OK-1-5)

Synthesis of P((MEO)$_2$MA) was done as reported by Matyjaszewski et al.[34] with minor modifications. Bpy and CuBr (0.20 mmol and 0.12 mmol respectively) were added to a dry 25 mL Schlenk flask. The flask was deoxygenated rapidly after adding the solids via four consecutive vacuum-nitrogen cycles. Anisole, M(EO)$_2$MA and EBiB were dried over baked 4 Å molecular sieves and degassed with nitrogen for 30 minutes prior reacting with the catalysts. Using the Schlenk techniques, 3.3 mL anisole, 4.9 mL of the monomer (M(EO)$_2$MA) (26.6 mmol) and 18.6 µL of EBiB (0.13 mmol) were added to the Schlenk flask under nitrogen. The reaction was allowed to proceed at 60 °C using an oil bath for 6 hours. The polymerization process was terminated by quenching the radicals with oxygen by exposing the flask's contents to air. The reaction mixture was diluted in excess THF and the catalyst was removed from the mixture by passing the sample through a neutral alumina column. Solution was precipitated in excess hexane and the precipitate was filtered. The solid product was dried in a vacuum oven for 6 hours. Polymerization reaction kinetics was monitored by withdrawing samples from the reaction mixture at different time points. Theoretical molecular weight was determined by 1HNMR by monitoring the decrease in acrylate peaks, and it was found to be 33,991 g/mol and 33,505 g/mol for and for OK-1-2 and for OK-1-5, respectively. Yield for OK-1-2: 0.4509 g, for OK-1-5: 2.2212 g.

3.2.3 Modification of the homopolymer P((MEO)$_2$MA) with amine group (OK-1-8 and OK-1-15)

The procedure followed another performed by Coessens et al.[21] Following drying, P($(MEO)_2$MA) (in OK-1-8: OK-1-2, and in OK-1-15: OK-1-5) with a terminal bromide end group was acquired. P($(MEO)_2$MA) was dissolved in ethanol at a concentration of 50 mg/mL. P($(MEO)_2$MA) solution was mixed with a 25 molar excess of ethylenediamine (EDA) and 1.2 molar excess of TEA to EDA. The mixture was allowed to react for 48 hours in an oil bath at 60 °C. A 10 times excess hexane was used to precipitate the product following the 48 hours long reaction. The solid polymer was re-dissolved in milli-Q water and dialyzed against 2,000 MWCO membranes with repeated water changes to get rid of unreacted reagents. Following dialysis, the sample was frozen at -80 °C and lyophilized on a Labconco Freezeone Plus freeze-dry system with a collector temperature of -84 °C and a vacuum pressure of 0.040 mBar. Samples were left to lyophilize till complete dryness to yield 0.4195 g product. ^{1}H NMR characterization was done on the solid product.

3.2.4 Synthesis of the homopolymer of P($(MEO)_2$MA) by ATRP (OK-1-9)

Synthesis of P($(MEO)_2$MA) was done in a procedure based on the one reported by Matyjaszewski et al.[(34)] Bpy and CuBr (0.0944 mmol and 0.0772 mmol respectively) were added to a dry 25 mL Schlenk flask. The flask was deoxygenated rapidly after adding the solids via four consecutive vacuum-nitrogen cycles. Anisole, M$(EO)_2$MA and 3-((tert-butoxycarbonyl)amino)propyl 2-bromo-2-methylpropanoate were dried over baked 4 Å molecular sieves and degassed with nitrogen for 30 minutes prior reacting with the catalysts. Using the Schlenk techniques, 3.4 mL anisole, 3.4 mL of the monomer (M$(EO)_2$MA)(18.3 mmol) and 0.191 g of the initiator (0.0858 mmol) were added to the Schlenk flask under nitrogen. The reaction was allowed to proceed at 60 °C using an oil bath for 6 hours. The polymerization process was terminated by quenching the radicals with oxygen by exposing the flask's contents to air. The reaction mixture was diluted in excess THF and the catalyst was removed from the mixture by passing the sample through a neutral

alumina column. Solution was precipitated in excess hexane and the precipitate was filtered. The solid product was dried in a vacuum oven for 6 hours. Polymerization reaction kinetics was monitored by withdrawing samples from the reaction mixture at different time points. Theoretical molecular weight was determined by 1HNMR by monitoring the decrease in acrylate peaks, and it was found to be 27566 gm/mol:DP=147. Yield 1.6780 g.

3.2.5 Deprotection by removal of the t-Boc group (OK-1-12, 13, 14)

The P($(MEO)_2$MA) sample was dissolved in anisole and then a fivefold molar excess of CF_3COOH (with respect to the amount of the t-Boc group in the polymer) was added. The reaction mixture was stirred at room temperature for 24 hours. The polymer was precipitated from excess hexane. Traces of CF_3COOH in the polymer and solvent were removed by vacuum drying at 60 °C overnight, to yield 1.1034g, 0.3297 g, and 1.3348g polymer for OK-1-12, OK-1-13, and OK-1-14, respectively.

3.2.6 Synthesis of HA-P($(MEO)_2$MA) conjugates (OK-1-16, 17, 18, 19)

HA was dissolved in milli-Q water at a concentration of 5mg/mL. Twenty percent of the carboxylic acid groups on HA were activated by 1.5 mol excess T3P. To the activated HA, 4-DMAP was added as an acylating agent in a 2:1 ratio. To the activated HA, a stoichiometric amount of P($(MEO)_2$MA) (in OK-1-16, the product of OK-1-8, in OK-1-17, the product of OK-1-12, in OK-1-18, the product of OK-1-13, in OK-1-19, the product of OK-1-14) was added. The reaction mixture was set at room temperature for 24 hours. After 24 hours the solution was diluted with water and dialyzed against a 100,000 MWCO dialysis membrane to get rid of unreacted reagents. Dialysis continued with repeated 1 liter water changes. Dialyzed samples were frozen at -80 °C and lyophilized using a Labconco Freezone Plus freeze-dry system with a collector temperature of

-84 °C and a pressure of 0.040 mBar. Samples were lyophilized till complete dryness. Characterization by ^{1}H NMR was carried out on the solid product to confirm HA-P($(MEO)_2$MA) conjugation. Yields: 0.0710 g for OK-1-16, 0.2240 g for OK-1-17, 0.1104 g for OK-1-18, 0.9235 g for OK-1-19.

3.2.7 Characterization by ^{1}H NMR

NMR spectra were obtained using a Bruker Avance 500 MHz spectrometer. Deuterated chloroform ($CDCl_3$) was used as the solvent for P($(MEO)_2$MA) and its derivatives. Deuterium oxide (D_2O) was used as the solvent for HA and its derivatives. All samples were prepared at a concentration of 0.5% (w/w). For HA and its derivatives, spectra were collected at 296 K.

3.2.8 Gel Permeation Chromatography (GPC)

A GPC system composed of a Waters 515 HPLC pump and Waters 2414 refractive index detector using PSS columns (Styrogel 10^2, 10^3, and 10^5 Å) in dimethylformamide (DMF) as an eluent at a flow rate of 1 mL/min at 50 °C was used. Samples were filtered over neutral alumina prior to analysis. The column system was calibrated with 12 poly(methyl methacrylate) (PMMA) standards.

3.2.9 Dynamic LightScattering (DLS)

DLS was measured using a Zetasizer Nano from Malvern Instruments, Ltd. Samples were prepared at a 0.1% (w/w) solution and diluted in Milli-Q water. Sphere radii were taken from an average of three runs.

3.2.10 Atomic Force Microscopy

Tapping mode experiments were carried out using a Nanoscope V system (Veeco 2 Instruments). Measurements were performed in air, using commercial silicon cantilevers (Veeco TAP150A model) with a nominal spring constant 5 N/m and resonance frequency 308.5 kHz.

Silicon wafers were cut into 0.8 cm by 0.8 cm pieces. The rectangular pieces were cleaned first mechanically, then sonicated in ethanol three times for 2 min, then in deionized (DI) water three times. Following this, the wafers were soaked in HNO_3 at 80 °C for 15 min, then in DI water for 15 min, then rinsed with DI water, and dried under a flow of ultra high purity (UHP) nitrogen.[2]

A solution of P($(MEO)_2$MA) with MW 33000 conjugated to HA of MW of 1.6 MDa with GD 20% in Millipore water was freshly prepared with a concentration of 1 mg/mL, and 40 uL of it was drop-casted onto each wafers, and placed into a Fisher Scientific low-temperature incubator for 5 min, then thoroughly rinsed with warm water and dried in a vacuum desiccator overnight.[2]

Channels: height, phase, amplitude, amplitude error, all both in trace and retrace, data scale: 10 nm, 50°, 50 mV, respectively for the acid-treated surfaces, and 20 nm, 50°, 50 mV for the non-acidtreated ones.

Scan rate of 1 Hz, 2048 lines per images and sample points per line.

Contact mode experiments were carried out using a NT-MDT integra system. Measurements were performed in water, using commercial silicon cantilevers.

3.2.11 Water Contact Angle Measurements for Modified HA-P($(MEO)_2$MA) Films

WCA was measured for films casted on silicon surfaces using a Ramè-Hart contact angle goniometer. A 1 mg/mL solution of HA-P($(MEO)_2$MA) was prepared in pure water. The modified HA solution was drop-cast over the Si surfaces below the LCST.

The disks were then incubated at 37 °C to ensure transition, uniform, and tight coating over the surface. Incubation time for the kinetics experiments varied from 1 to 20 min. Warm water droplets (1.5–10 μL) were placed over the cast film and the native substrate; images were taken 1 min post water placement. The process was repeated 3 times for each volume, and average measurements were reported.

3.2.12 QCM-D Analysis

A Q-Sense E4 system (Biolin Scientific) was used for these measurements. Experiments were performed using four SiO_2 sensors (QSX 303) mounted in QFM 401 flow modules. All experiments were performed with the sensors mounted in parallel. An external digital pump (Ismatec IPC-N 4) was used to control the flow rate of the solutions, using tubing with inner diameter of 0.64 mm. An E4 autosampler was used for liquid handling. Before each experiment, the sensors were cleaned for 10 min using a UV/ozone Procleaner (Bioforce Nanosciences) followed by immersion of the sensors in 2 wt % sodium dodecyl sulfate for 30 min. The sensors were subsequently rinsed carefully with copious amounts of deionized water and were dried under a gentle stream of nitrogen gas. Finally, the sensors were exposed to UV/ozone for 10 min before mounting in the flow modules.[11-15] Following the mounting of the sensors, the flow modules and tubing were filled with water and the resonance frequencies were collected at ambient temperature. The volume above the sensor is 40 μL.

The experiments were performed as follows: the temperature was set to 15 °C, and sensors 1–3 were exposed to HA (40 μL above sensor, 4 mg/mL), whereas sensor 4 was exposed to water at a flow rate of 100 μL/min. Sensor 4 was further used as a positive control for BSA binding. Next, the temperature was set to 37 °C, and the resulting frequency and dissipation shifts, Δf and ΔD,

respectively, were recorded. Following baseline stabilization after the temperature increase, solutions of BSA, preheated to 37 °C, were injected to sensors 1, 2, and 4; and water, as a negative control, to sensor 3. Finally, the sensors were regenerated by setting the temperature to 15 °C and rinsing with precooled water to remove the HA. All results are reported for the third overtone (n = 3), unless otherwise stated.

3.2.13 UV-Visible Spectroscopy

Spectroscopic measurements were performed on an Agilent Cary 300 UV-Visible Spectrophotometer. The instrument's software was used to scan from 200 nm to 400 nm at temperatures ranging from 24 °C to 32 °C. UV/Visible spectra were recorded 2 min after the temperature was set. The spectra reported herein had the baseline subtracted.

3.3 Results and Discussion

3.3.1 Synthesis

HA-P((MEO)$_2$MA) conjugates were synthesized in two different ways. The first approach is described in our previous paper.[3] This involves the polymerization of (MEO)$_2$MA by ATRP, followed by amination of the initiator, which will then allow for the attachment to HA in a reaction that involves the activation of the polysaccharide's carboxyl groups. A second approach was tried since amination is challenging to quantify because the amine protons' shift in the spectrum can vary and the Kaiser-test is only qualitative. In this second approach, an amine-terminated initiator with Boc-protection (Figure 3.3.1.1) was used in the ATRP, followed by the removal of the

protecting group in a step, the success of which is easily determined by ^{1}H NMR. The amine-

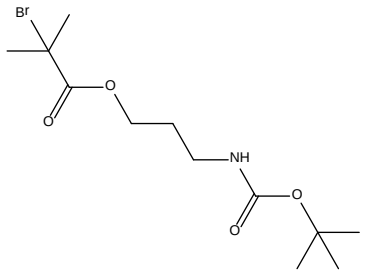

Figure 3.3.1.1: The initiator: 3-((tert-butoxycarbonyl)amino)propyl 2-bromo-2-methylpropanoate, MW=324.21.

terminated initiator was synthesized with a regular ATRP in the presence of Cu(II). The conditions were otherwise kept similar to the ones of the original approach (Scheme 3.3.1.1). For ^{1}H NMR

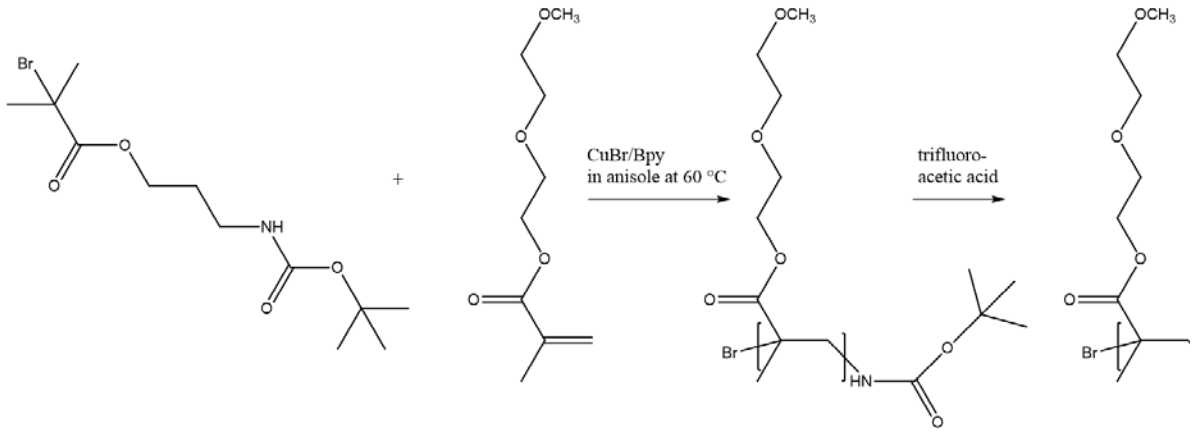

Scheme 3.3.1.1: Use of an aminated initiator eliminates the need for amination, which is hard to quantify by NMR. Instead, the Boc protecting group will have to be removed, but the yield of this reaction can be easily determined.

spectra of the initiator conjugates, please see the appendix. Based on the spectra, there is a significant impurity in the samples. (There is a small amount of acetone, which came from the NMR tubes, otherwise it would have precipitated the polymers in the vials, which did not happen.) There should be three peaks belonging to the methyl group of methacrylate, but since these are short peaks, the one with the highest ppm value is often not visible for atactic polymers.

The peak with the highest ppm value becomes more pronounced, and hence, visible, for mixtures of atactic and isotactic polymers with a ratio of close to 1:1,[4] which, based on ^{1}H NMR, seems to be the ratio for the GD 5% and GD 20% samples. The P($(MEO)_2$MA) used to synthsize these conjugates came from the same batch as those used for the other conjugates. However, since the polymers are stored dry, the amount needed for conjugation is taken from the batch instead of dissolving the whole batch. The isotactic regions probably have a tendency to come to each other's close proximity during lyophilization, and therefore, the batch is not homogenous. Nevertheless, this inhomogenicity does not seem to affect LCST, since the LCST for 5% was the same as for 10% and 40%.

Target GD values were confirmed by integration of the peaks belonging to the aminocarbonyl methyl and P($(MEO)_2$MA) backbone (1.9 ppm), and methacrylate peaks (0.5 - 1.5 ppm) (see the Appendix for more details).

For GPC, 5 mg sample was dissolved in 1 mL DMF containing 50 mM LiBr and one drop of toluene-DPE for calibration (Figure 3.3.2).

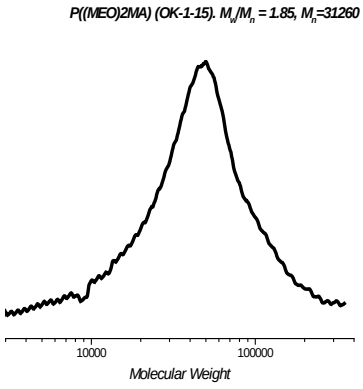

Figure 3.3.1.2: GPC curve of the polymer that was conjugated to HA with different GDs.

3.3.2 Dynamic Light Scattering

DLS was used to characterize the size of HA-P((MEO)$_2$MA) in solution. We would like to note that - based on our earlier results - these are not composite LCST values, because HA does not have an LCST and with the grafted architecture, there is very little overlap between the side chains.[3] Graphs showing the hydrodynamic diameter values at 23 °C and at LCST are included in the Appendix. Below LCST, solutions of the conjugate showed a mean size of 5 nm. The hydrodynamic diameter was measured in the lack of extra salt, which accounts for the almost one order of magnitude difference between the values reported herein and those described in previous reports,[7] where DLS measurements were run in 0.5 M NaCl solution, according to the increase of hydrodynamic radius upon the increase of ionic strength of the solution.[8]

Above the LCST, HA-PMEO$_2$MA aggregates showed a particle size above 1000 nm (Figure

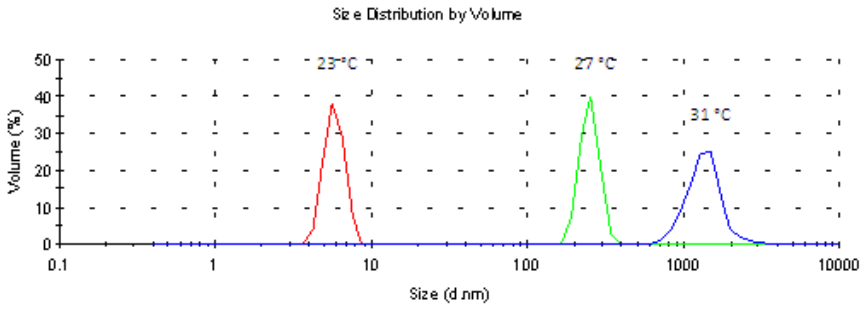

Figure 3.3.2.1: DLS data showing the distributions of diameters for HA-P((MEO)$_2$MA) below LCST and above LCST.

3.3.2.1). GD 0.3, 5, 10, and 40% samples with P((MEO)$_2$MA) of molecular weight higher than 30 kDa transition at 25 °C, but the GD 20% sample at transitions at 31 °C. This latter sample also exhibits a mean size increase of more than an order of magnitude at 27 °C, above which the hydrodynamic diameter decreases again. Other P((MEO)$_2$MA) lengths were also examined. With 28 kDa P((MEO)$_2$MA), no size change was seen at 27 °C, but the LCST is still 31 °C. When

attaching even shorter 6 kDa polymer side chains to the HA backbone, there is a size change at 31 °C, but this does not persist upon temperature increase, and with 3 kDa side chains, even this temperature-sensitive increase in size disappears.

In order to see if the state of the GD 20% sample at 27 °C is thermodynamically stable, it was kept

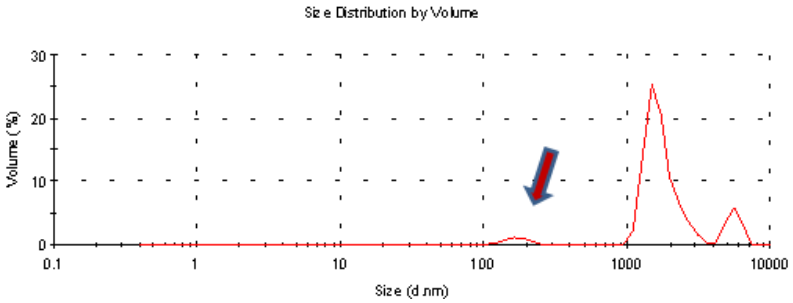

Figure 3.3.2.2: DLS data showing the distributions of diameters for HA-P($(MEO)_2$MA) with GD 20% after keeping the sample at 27 °C for 2 days. The arrow shows the peak corresponding the non-aggregated particles.

at 27 °C for 2 days, after which the DLS measurement was repeated (Figure 3.3.2.2). The structures do not fall apart, evidenced by the lack of a peak below 10 nm, and some of them persist, but most of them aggregate.

3.3.3 Atomic Force Microscopy

HA-P($(MEO)_2$MA) with GD 20% was drop-casted on silicon wafers as described in section 3.2.10 and studied by tapping mode AFM (TM-AFM). After 5 min of incubation at 37 °C, a smooth coverage could be seen by what appeared to be a thin layer of individual particles of height of a couple of nm, and diameter around the resolution limit (30 nm) (Figure 3.3.3.1).

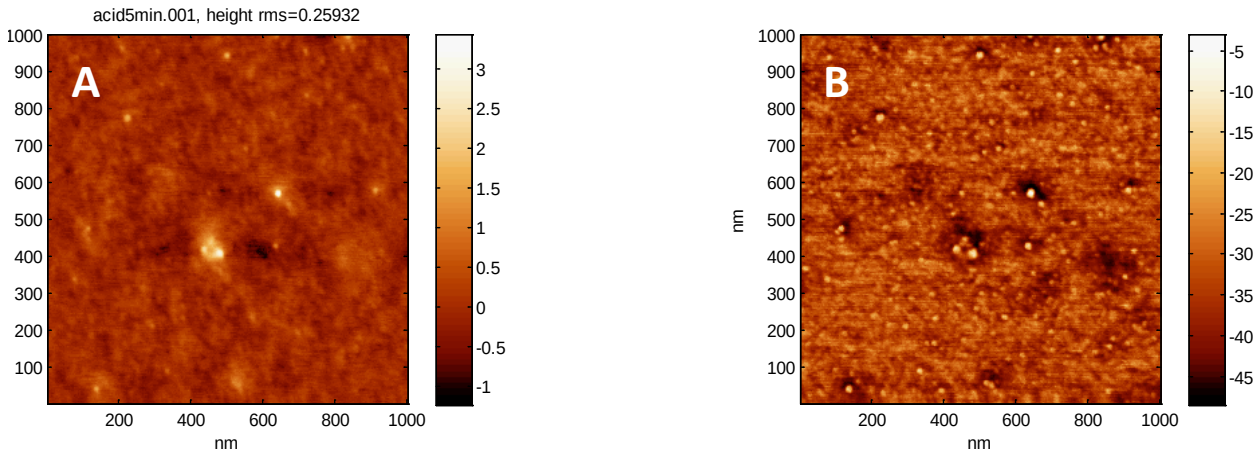

Figure 3.3.3.1: Height (A) and phase (B) TM-AFM images of a layer formed from HA-P($(MEO)_2$MA) with GD 20% after 5 min at 37 °C. The phase images reveal individual particles.

In order to measure the thickness of the casted film, a cut was made in the deposited layer by scratching the surface with a needle (Figure 3.3.3.2). The surface was scanned in contact mode in

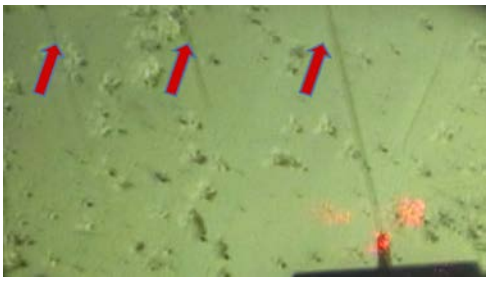

Figure 3.3.3.2: The surface under light microscope, showing the three parallel cuts made with the needle. The rightmost cut was used to measure film thickness.

water. The thickness was determined to be approximately 50 nm, but definitely below 80 nm, similar to what had been measured earlier (Figure 3.3.3.3). Compared to the height of the individual particles, this thickness shows that the coating consisted of several layers already after 5 minutes, implying that deposition of the surface happens within a few minutes.

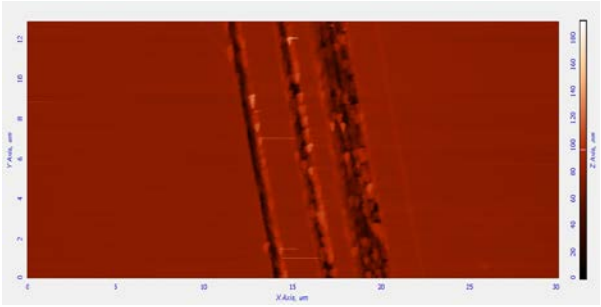

Figure 3.3.3.3: The coated surface under water, showing the three needle-cut grooves.

3.3.4 Quartz Crystal Micrometry

QCM-D measurements were performed to study the HA-P($(MEO)_2$MA) conjugates as antifouling coatings and to understand the mechanism of layer formation. In every experiment, four silicon dioxide surfaces were used, following cleaning by the standard procedure.[3] Three of the surfaces were exposed to an aqueous solution of HA-P($(MEO)_2$MA and one to deionized water. The concentration of the coating solution was the same as the one of the more concentrated protein solution used in the subsequent antifouling tests: 4mg/mL. The fourth sample served as a control and the signal collected on this channel was subtracted from the signals of the other three channels.

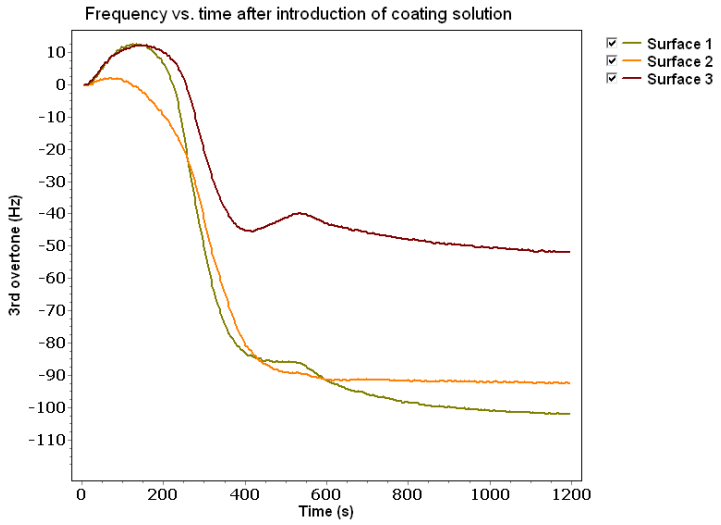

Figure 3.3.4.1: Frequency changes were used to calculate the mass of the material present on the surface.

Frequency and energy dissipation data for the third overtone were collected. An example for frequency change as a function of time is shown on Fig. 3.3.4.1; in the rest of the chapter, the mass changes calculated from the frequency changes based on the Sauerbrey equation will be shown.

According to the Sauerbrey equation, for thin, rigid, and homogeneous films, Δf is directly proportional to the change in mass, Δm_f, of the film[16]

$$\frac{\Delta f}{n} = -\frac{f_0}{t_q \rho_q} \Delta m_f \qquad (1)$$

where n = 3, 5, 7, ... the overtone number, f_0 (5 MHz) is the crystal's fundamental frequency, t_q (3.3×10^{-4} m) the plate's thickness, and ρ_q (2648 kg/m^3) the density of quartz. Due to viscous damping, some energy is lost during the crystals' oscillations. The resulting dissipation is given by

$$D = \frac{E_l}{2\pi E_s} = \frac{1}{\pi f \tau} \qquad (2)$$

where E_l and E_s are the lost and stored energies, respectively, and τ is the time constant of the amplitude decay of the oscillation in the lack of sustained drive.[17]

In kinetic experiments, by definition, we are interested in changes of certain variables over time, and this is true for our protein deposition experiments, because these were run at constant temperature (37 °C). In the case of coating deposition, we are more interested in the change as a function of temperature, but first these changes are also plotted as a function of time, for consistency, but, more importantly, because temperature was not a monotonic function of time for

the whole course of all experiments (Fig.3.3.4.2). For the reader's convenience, graphs belonging

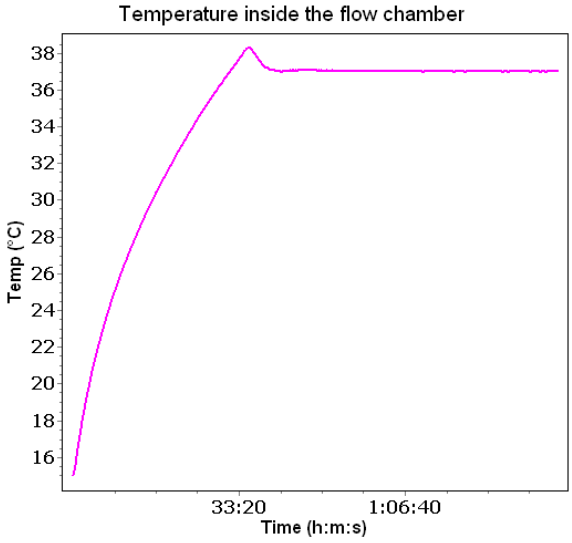

Figure 3.3.4.2: To study coating deposition and to protect the tubing of the instrument from polymer deposition, cold solution was injected, then the flow stopped and the temperature set to 37°C (see the increasing part of the curve). For antifouling test, the temperature was kept at a constant 37 °C. Note that the actual temperature is following the set temperature closely, but not exactly.

to changing-temperature experiments are also plotted as a function of temperature (Fig.3.3.4.3). Here we have five samples: GD 20%, CL 28 kDa (A), GD 20%, CL 32 kDa (B), GD 40%, CL 32% kDa (C), GD 10%, CL 32 kDa (D), GD 5%, CL 32 kDa (E). All samples were dissolved in water with a concentration of 4 mg/mL, and this coating solution was introduced to three silicon dioxide surfaces inside the QCM chambers. In the first column, we show the areal mass as a function of temperature; in the second, as a function of time. LCST is indicated by a red line, the GD 20%, CL 32 kDa sample's pre-transition by a bright blue line. We start our analysis with the plot belonging to the GD 20%, CL 28 kDa sample, because this is the closest to the ideal sigmoid curve that we would expect when depositing at a narrow temperature range. The most important thing to note about this curve is that deposition does not happen *around* but *below* LCST, which for this sample (for all samples with side chains of at least 6 kDa) is 31 °C (indicated by a red line in Fig.3.3.4.3 A). This effect will be discussed later.

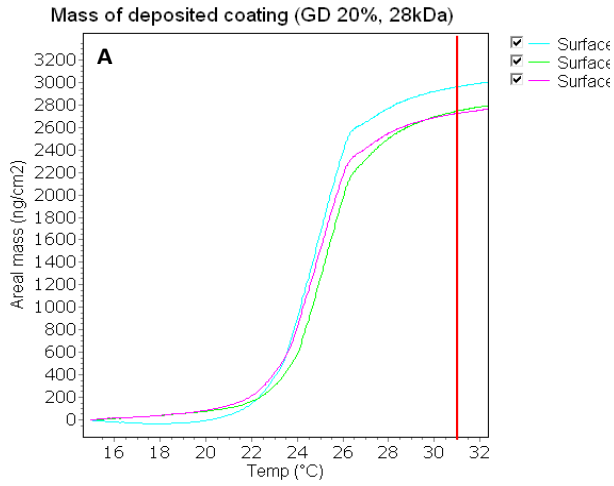
Mass of deposited coating (GD 20%, 28kDa)
A
Areal mass (ng/cm2)
Temp (°C)
Surface
Surface
Surface

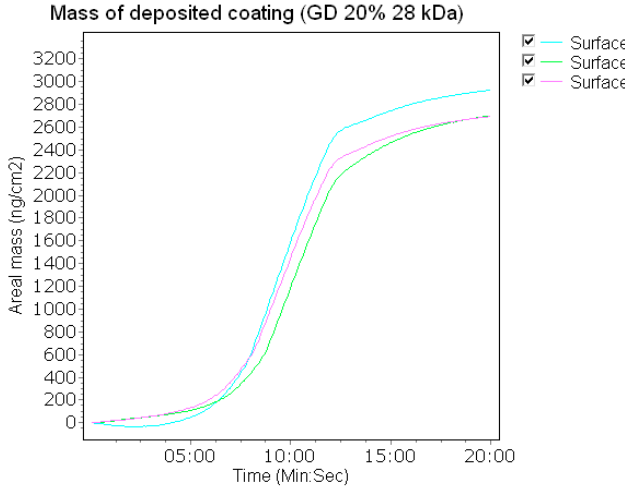
Mass of deposited coating (GD 20% 28 kDa)
Areal mass (ng/cm2)
Time (Min:Sec)
Surface
Surface
Surface

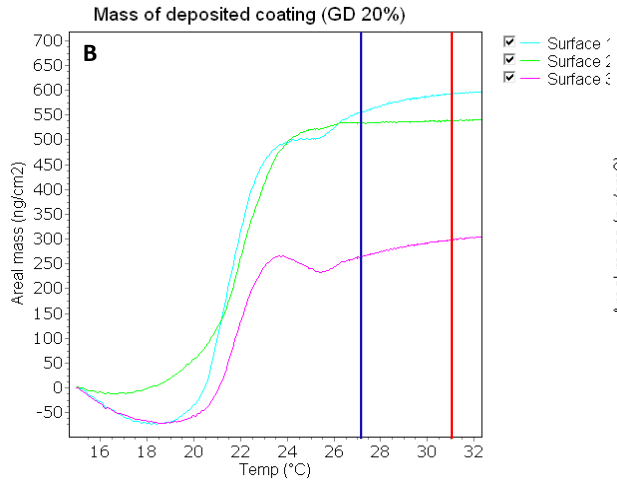
Mass of deposited coating (GD 20%)
B
Areal mass (ng/cm2)
Temp (°C)
Surface 1
Surface 2
Surface 3

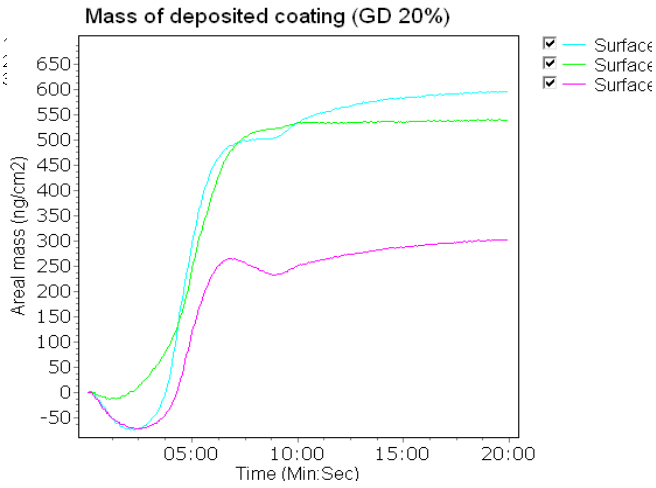
Mass of deposited coating (GD 20%)
Areal mass (ng/cm2)
Time (Min:Sec)
Surface
Surface
Surface

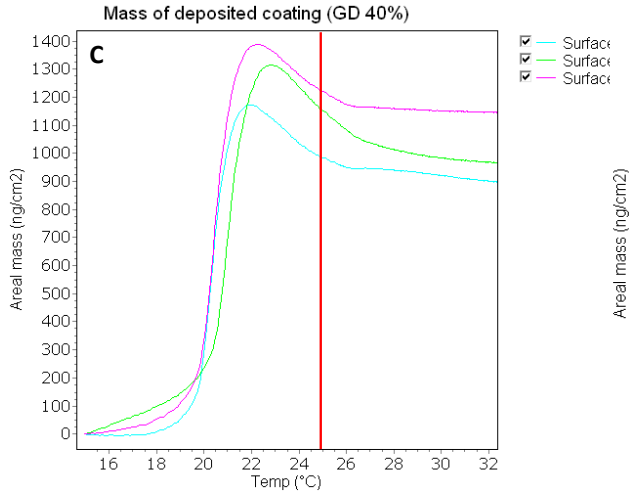
Mass of deposited coating (GD 40%)
C
Areal mass (ng/cm2)
Temp (°C)
Surface
Surface
Surface

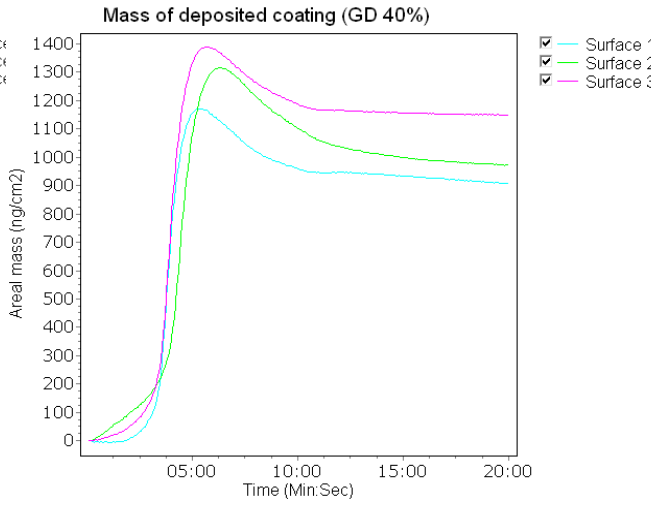
Mass of deposited coating (GD 40%)
Areal mass (ng/cm2)
Time (Min:Sec)
Surface 1
Surface 2
Surface 3

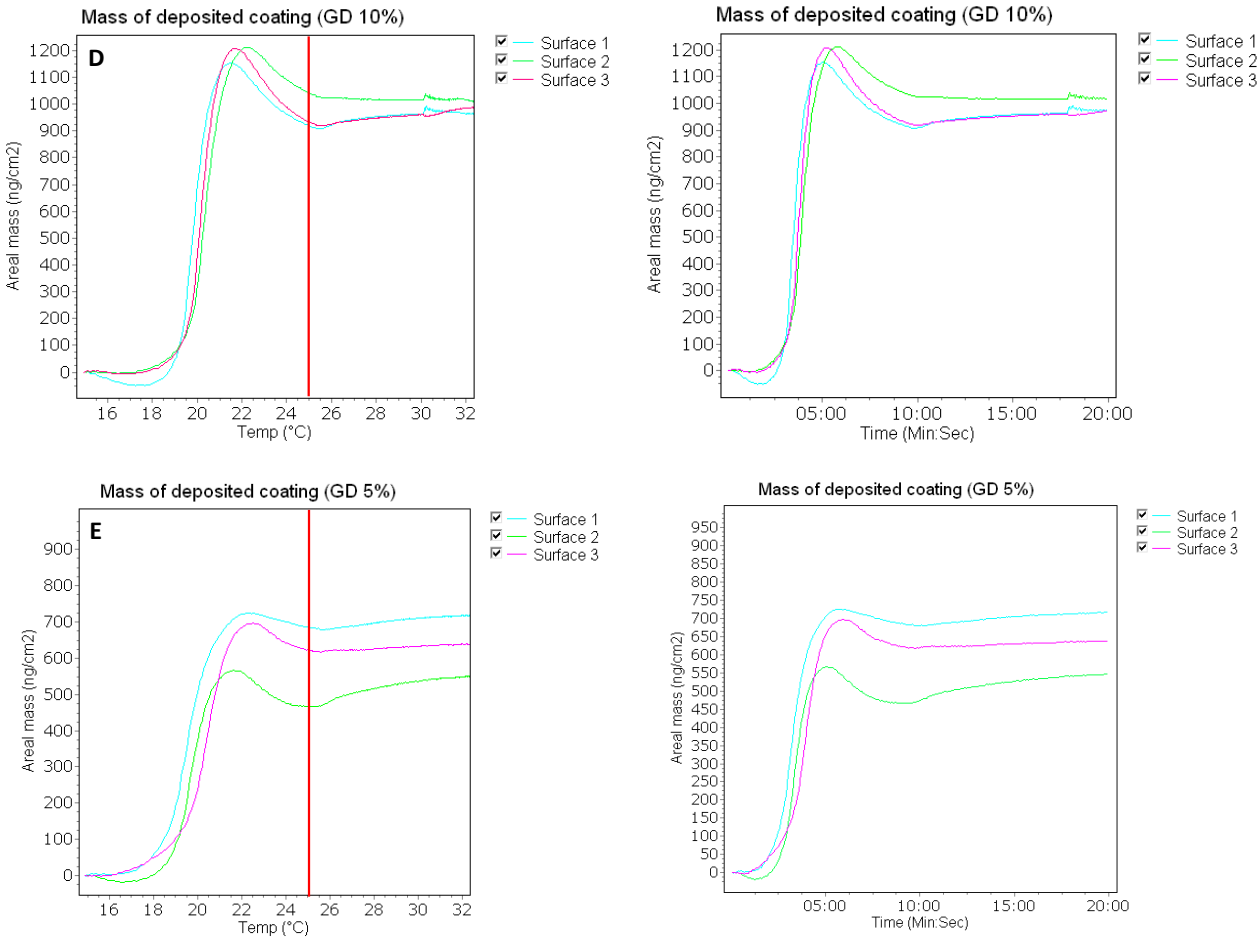

Figure 3.3.4.3: Kinetic study of coating for A: GD 20%, CL 28 kDa, B: GD 20%, CL 32 kDa, C: GD:40%, CL 32% kDa, D:GD 10%, CL 32 kDa, E: GD 5%, CL 32 kDa. LCST is indicated by a red line, pre-transition by a blue line.

On Fig.3.3.4.3 B we can see all three potentially interesting deviations from the expected sigmoid curve. Fig.3.3.4.3 C – D show one or more of these.

The first deviation is an initial dip on the plot. This is caused by a perceived mass decrease and was present in our experiments several times. The possible reason for this is the sudden change from room temperature to 15 °C when the chamber is flooded by the cold solution, and probably does not have a significant influence on the outcome of the experiments.

The second deviation is a discrepancy in the value of the areal mass in the second part of the graph. This discrepancy means that there are differences between masses deposited on the three surfaces among identical conditions, which might influence the antifouling property. Therefore, this effect was further investigated. We will discuss this effect before moving on to the third deviation.

To better understand the effect, we approached it analytically. The rate of deposition was calculated by taking the derivative of the mass as a function of time with respect to time (Fig.3.3.4.4).

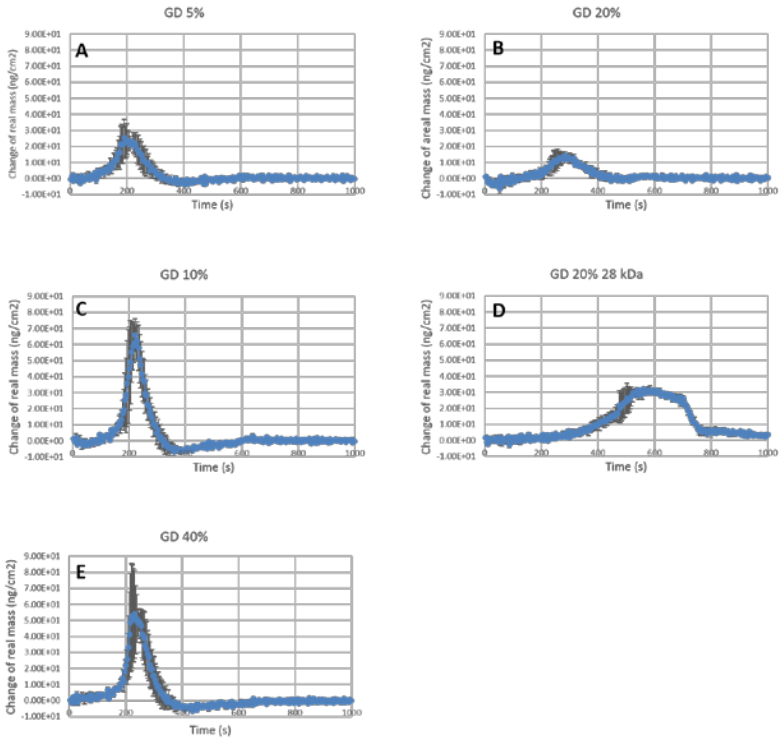

Figure 3.3.4.4: The rate of coating deposition as a function of time. A: GD 5%, CL 32 kDa, B: GD 20%, CL 32 kDa, C: GD: 10%, CL 32% kDa, D:GD 20%, CL 28 kDa, E: GD 40%, CL 32 kDa.

These graphs show that the deviation is always largest before the maximum. This is when we are depositing fast, and a change is about to happen: the most vulnerable point of the system, when even the smallest change will have a consequence. And there must be a change, since something will cause deposition to slow down soon. Just like in a motorbike race: most accidents happen at

the beginning of turns. In Fig. 3.3.4.5, the blue dots correspond to the temperature values at which standard deviation for a given sample is maximal, and the red dots correspond to the temperature at which the rate of deposition is maximal. As we can see, the blue dots are right below the red ones, with one exception.

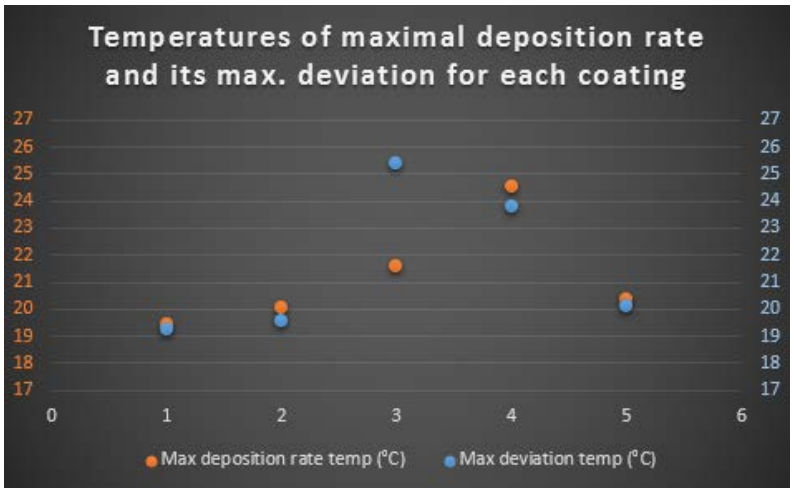

Figure 3.3.4.5: The deviation between surfaces under identical conditions is probably the result of a general effect. 1: GD 5%, CL 32 kDa, 2: GD 10%, CL 32 kDa, 3: GD: 20%, CL 32% kDa, 4: GD 20%, CL 28 kDa, 5: GD 40%, CL 32 kDa.

Now that we have a plausible explanation for the second deviation, we will examine its significance. The importance of the deviation between surfaces coated with the same sample can be judged by the correlation between the maximum of the deviation and the antifouling property. In this study, correlation is not meant as a mathematical term but to describe a similar trend. In this particular case, we are looking for a trend in protein deposition (Fig.3.3.4.6, red dots) and the

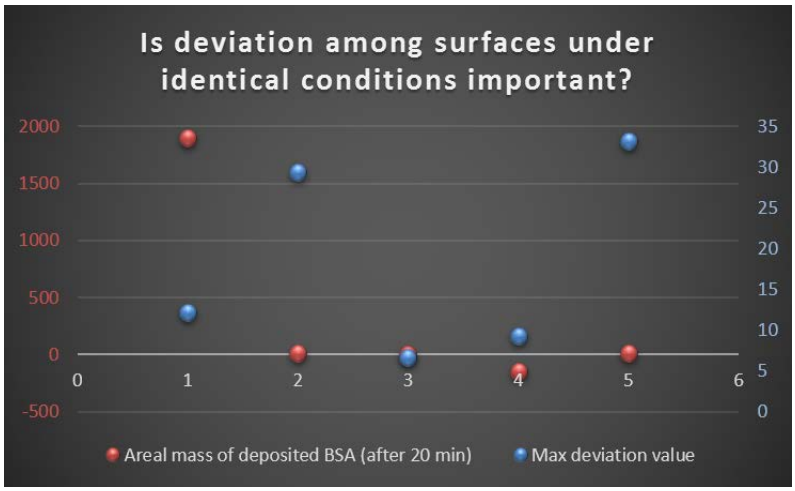

Figure 3.3.4.6: Increase in deviation does not seem to increase protein adsorption on the coated surfaces. 1: GD 5%, CL 32 kDa, 2: GD 10%, CL 32 kDa, 3: GD: 20%, CL 32% kDa, 4: GD 20%, CL 28 kDa, 5: GD 40%, CL 32 kDa.

maximal values of standard deviation for each sample (blue dots). In the sense used in this study, increase in deviation does not seem to correlate with increase in protein adsorption on the coated surfaces.

Before moving on to the third deviation on the coating deposition plots that we want to analyze, we must pause to consider a few observations about the rate plots for further references.

We can observe that the shape and mode of the GD 20% samples are different from that of the others, which are very similar in shape and in their mode (and we have just concluded that other differences do not matter). In terms of both quantities, the CL 32 kDa sample falls in between the CL 28 kDa sample and the rest, similarly to its composition. The maxima vary, but this will be discussed later.

To return to the third deviation in Fig. 3.3.4.3, this phenomenon is a dip on the deposition curves after reaching the maximum. This means that after deposition is completed, some of the material leaves the surface. The property that we are examining here is the value of minimal deposition rate following the maximum but before deposition is complete and is shown in blue in Fig. 3.3.4.7. Protein adsorption is shown in yellow, similarly to the previous graphs. The deviation is present in the case of those samples for which the blue dot falls below the zero line. After the elimination of the outlier GD 5% sample (see the justification later), we can say that this deviation is present in the case of the samples with good antifouling property and only in the case of these, and

therefore seems to be advantageous. Probably the top layers that are weakly adsorbed come off and this helps to form a more solid, more protein resistant coating.

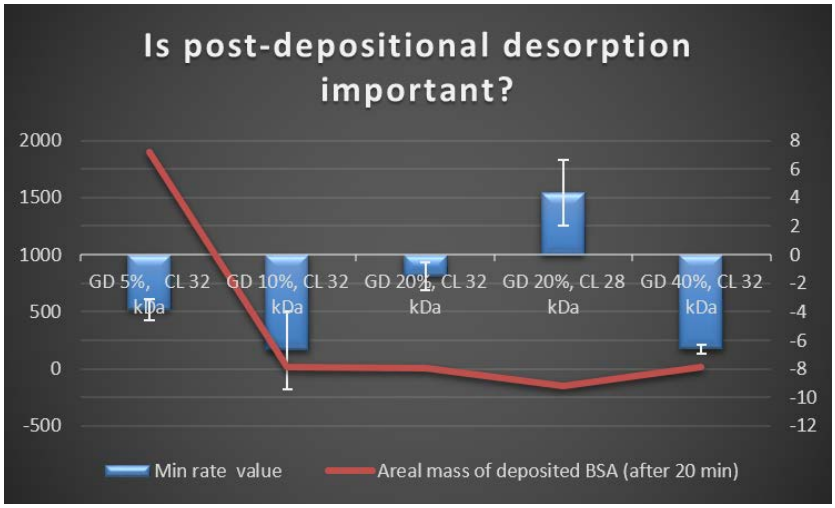

Figure 3.3.4.7: Post-depositional desorption seems to be beneficial. 1: GD 5%, CL 32 kDa, 2: GD 10%, CL 32 kDa, 3: GD: 20%, CL 32% kDa, 4: GD 20%, CL 28 kDa, 5: GD 40%, CL 32 kDa.

Now let us return to our observations about deposition rate changes (Fig. 3.3.4.4), namely that the shape and mode of the GD 20%, 28kDa sample is different from others, the GD 20%, 32 kDa sample is in between, and the maxima vary.

The maxima means the amount of deposited coating, which is shown in blue in Fig. 3.3.4.8; the amount of deposited protein is, again, shown in red. There is no clear correlation, but samples with good antifouling property (GD 10%, CL 32 kDa; GD: 20%, CL 32% kDa; GD 40%, CL 32 kDa) were deposited in a moderate amount (500-1500 ng/cm2). Based on this, it seems that in terms of coating thickness more is not necessarily better - for example, it might get desorbed in the presence of a hydrophobic protein such as BSA.

The modes in Fig. 3.3.4.4 mean the temperatures for each sample at which deposition rate is maximal. This is what we plot next together with protein adsorption (Fig. 3.3.4.9, in blue and in red), and, once again, eliminate the outlier GD5%. We can notice that a) samples with good

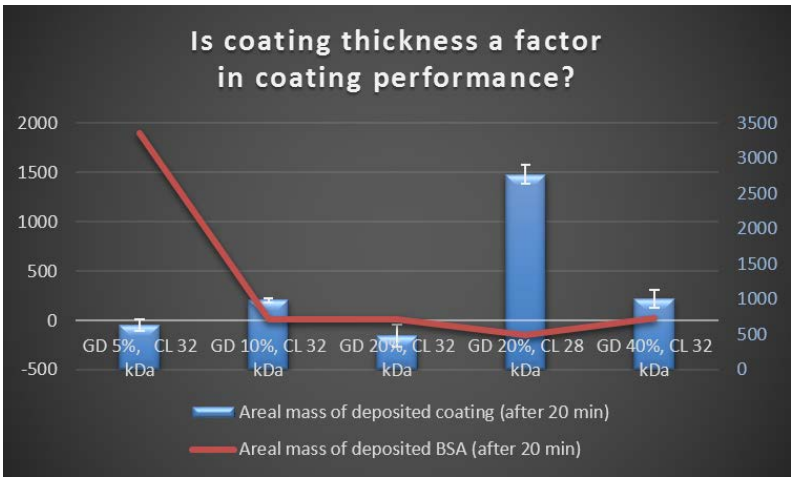

Figure 3.3.4.8: A moderate coating thickness seems to be optimal. 1: GD 5%, CL 32 kDa, 2: GD 10%, CL 32 kDa, 3: GD: 20%, CL 32% kDa. 4: GD 20%. CL 28 kDa. 5: GD 40%. CL 32 kDa.

antifouling property (samples 2, 3, 5) get deposited in the narrow range of 20-22 °C, b) the poorer sample (sample 4) gets deposited around 24 °C and c) the two samples with almost identical antifouling property (samples 2 and 5) get deposited at almost the same temperature. It seems that with this we have found the most important factor that influences the antifouling property. (Notice that we had to eliminate an outlier, meaning that there will be at least one other factor – see later.).

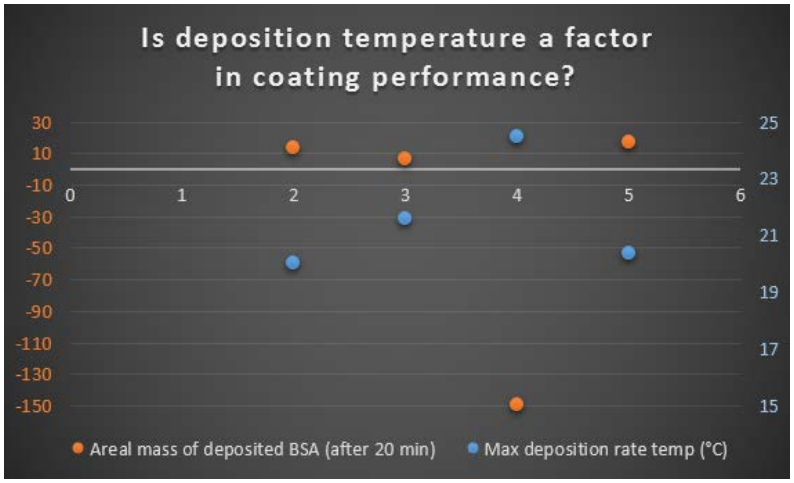

Figure 3.3.4.9: There is an inverse relationship between deposition temperature and the antifouling property. The poorest antifouling coating formed from the CL28 kDa sample. 1: GD 5%, CL 32 kDa, 2: GD 10%, CL 32 kDa, 3: GD: 20%, CL 32% kDa, 4: GD 20%, CL 28 kDa, 5: GD 40%, CL 32 kDa.

To see the reason for this, we plotted deposition rates as a function of temperature, once again, until 37 C, this time showing all samples in one graph Fig. (3.3.4.10). For the poorest antifouling (CL 28kDa) sample, we were expecting to see a curve that is very different from the others. And

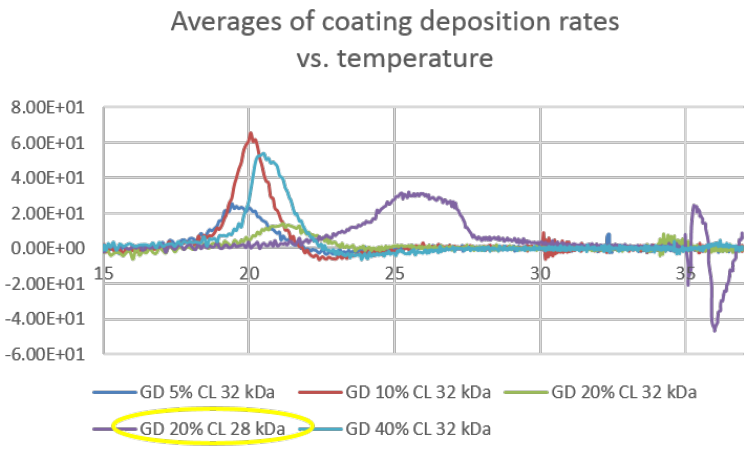

Figure 3.3.4.10: The poorest coating formed from the CL28 kDa sample (circled in yellow) starts to leave the surface before body temp. For standard deviation (here omitted for clarity), see Fig.3.3.4.4.

indeed: this sample is deposited at significantly higher temperatures than the others; moreover, as it is visible on by the great dip at the end: the coating starts to get desorbed even before we reach body temperature! The effect is shown schematically in Figure 3.3.4.11 B.

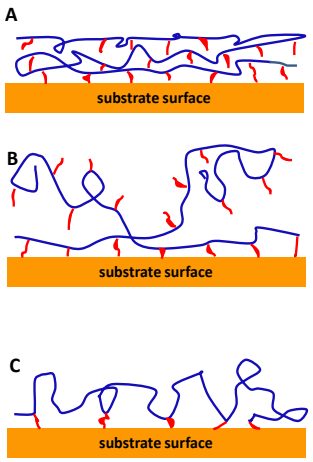

Figure 3.3.4.11: Schematic figures of coatings formed using different compositions: moderate GD with a long enough CL to allow for a transition below body temperature (A), too high LCST (B) and too low GD (C).

The promised explanation for the poor antifouling property of the GD5% sample probably does not come as a surprise after taking a look at Fig. 3.1.1.1 and after the note in the introduction about a balanced ratio of the two components: with such a low GD, there is simply not enough LCST polymer present to anchor the hydrophilic HA to the hydrophobic silicon dioxide surface in aqueous environment. Bauer et al. have found that trifluoroethylamine capping increased or maintained the performance of HA coatings[42], but we can also approach the question from the other end. Specifically, it is possible that low GD might not only be insufficient to decrease protein adsorption, but could even facilitate that, by leading to uneven coverage and a consequently increased surface roughness (Fig. 3.3.4.11 C, as opposed to Fig. 3.3.4.11 A, showing the hypothesized structure of coatings with good antifouling property). Increased surface roughness

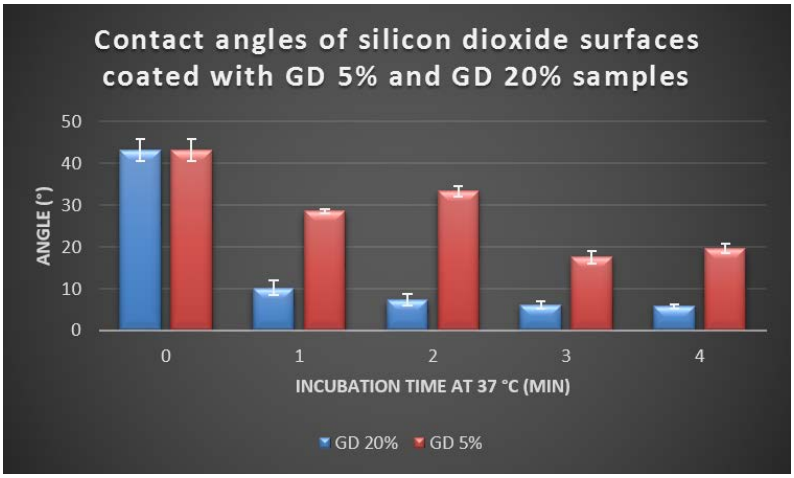

Figure 3.3.4.12: The reason for the poor antifouling property of the GD 5% sample is probably the lack of sufficient amount of anchoring LCST polymer. 1: GD 5%, CL 32 kDa, 2: GD 10%, CL 32 kDa, 3: GD: 20%, CL 32% kDa, 4: GD 20%, CL 28 kDa, 5: GD 40%, CL 32 kDa.

was also implied by high contact angle values, especially compared to those of other samples. In Fig. 3.3.4.12, contact angle values are shown after 0,1, 2, 3 and 4 minutes of incubation time for the GD 5% sample (in red) and for a sample with good antifouling property (in blue). We can see that the angles are decreasing fast for the sample with good antifouling property but for GD 5%,

the angles are and stay above 20°, which is too high a value to prevent protein adsorption. This result is in agreement with the findings of Morra and Cassineli.[43] They have valuated the anti-adhesive properties of surfaces covered by HA by XPS analysis and water contact angle measurements and discussed the results in terms of the surface fractional coverage by the polysaccharide, and found that HA could exert its effect only if completely hiding the underlying substrate.[43] On a more positive note, Palumbo et al., who grafted oligomethacrylate chains on partially aminated HA with 37% GD have found that the hydrogel formed from the material decreased the extent of BSA adsorption at about the same extent as our material with GD 40% (and GD 10%).[44]

Finally, there is one quantity that seems to be able to predict the net result of all the effects analyzed above, and this is energy dissipation. Deposition will naturally change the viscosity and consequently the dissipation of the surface, but so will the rearrangement of the deposited coating. The plots of energy dissipation relative to water are included in the Appendix, for all samples. When plotting the number of time/temperature intervals when dissipation changes occur (Fig.

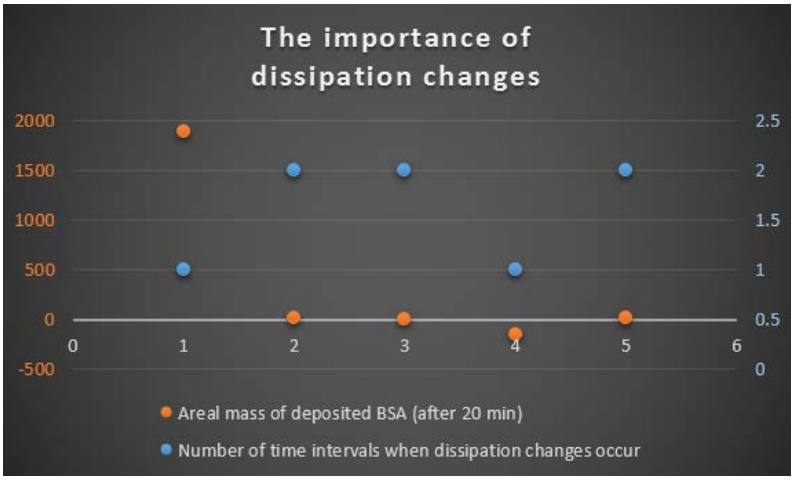

Figure 3.3.4.13: The separate dissipation changes seem to be the key to a good antifouling coverage. 1: GD 5%, CL 32 kDa, 2: GD 10%, CL 32 kDa, 3: GD: 20%, CL 32% kDa, 4: GD 20%, CL 28 kDa, 5: GD 40%, CL 32 kDa.

3.3.4.13, in blue), we can see that the value of two is assigned to and only to the samples with good antifouling property, and the value of one is assigned to the poor samples. Based on this, it seems that the key to good antifouling coverage is the clear separation of these dissipation changes in time. An everyday example for this kind of effect would be the melting of ice cream in the cone after you left the air-conditioned store (smooth surface) vs. spooning already molten pieces into a cone after power outage at home (chunks and melt).

The last note of this chapter is on the mechanism of coating formation. In our earlier work,[3] we hypothesized that the coating material is crushed out of solution around LCST. In this study, it was found that deposition rate is maximal (plotted in red in Fig. 3.3.4.14 A) on average at least 5 °C below LCST (plotted in blue in Fig. 3.3.4.14 A) and is competed (plotted in grey in Fig. 3.3.4.14 A) around LCST; probably a consequence of gradually decreasing solubility upon approaching LCST, observed by UV-visible spectroscopy. Based on the spectra in Fig. 3.3.4.14 C, the effect is shown quantitatively for the GD 20%, CL32 kDa sample in Fig. 3.3.4.14 B. Here we plotted absorbance and wavelength as a function of temperature. In the case of both quantities, the increase

happens between 26 °C and 29 °C, after which there does not seem to be a significant increase. This suggests that the change in solubility happens below LCST (for this sample, 31 °C), in correlation with the deposition.

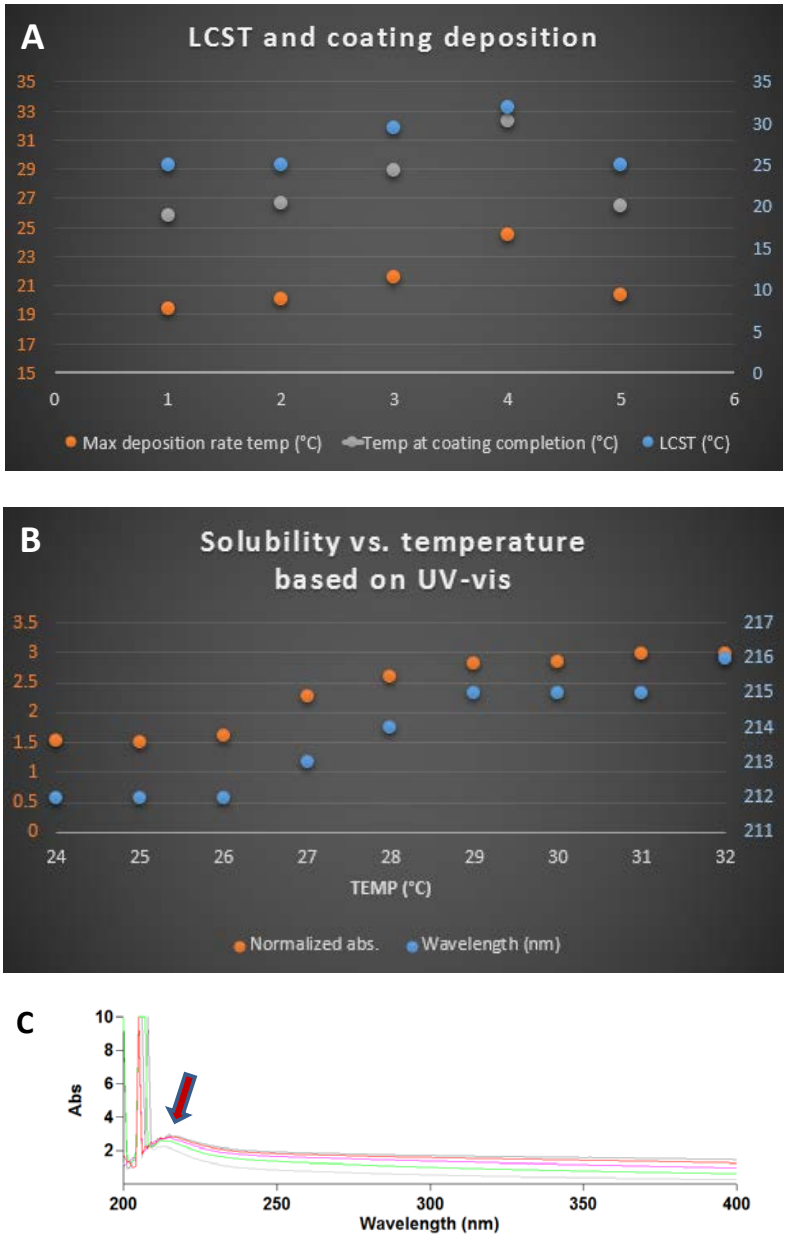

Figure 3.3.4.14: The separate dissipation changes seem to be the key to a good antifouling coverage. 1: GD 5%, CL 32 kDa, 2: GD 10%, CL 32 kDa, 3: GD: 20%, CL 32% kDa, 4: GD 20%, CL 28 kDa, 5: GD 40%, CL 32 kDa.

Based on the strong correlation between LCST, maximal deposition temperature and layer completion temperature in Fig. 3.3.4.14, we can conclude that deposition happens in an LCST-dependent fashion. On the other hand, we have to note that most of the coating is deposited at temperatures significantly (but consistently) lower the clouding point. Taking these trends into account, along with the amphiphilic nature of the coating material - HA being the hydrophilic part and the side chains the hydrophobic part - we suggest that deposition process is started by concurrent homogenous nucleation in the solution, followed by layer formation. Because of HA's high hygroscopicity which property is also preserved in the conjugate, we do not find crystallization to be likely to affect the deposition process.

3.4 Conclusions

P((MEO)$_2$MA) side chains were conjugated to HA backbone with different GD values. DLS shows that all but the GD 20% samples have LCST at 25 °C; provided that the side chain is long enough, the GD 20% samples have LCST at 31 °C. Since the 6 kDa P((MEO)$_2$MA) exhibits a more than tenfold increase in the hydrodynamic diameter at 31 °C, but upon further increase these globuli collapse again, these chains are probably not much shorter than the minimum necessary length to realize LCST. The excellent antifouling properties make the HA P((MEO)$_2$MA) conjugates with GD 10, 20 and 40% with CL 32 kDa promising materials for surface functionalization of devices exposed to a biological environment.

The second question raised by this study was pointed towards the mechanism of coating formation: how and why does it work; in relation to this, an explanation for the above samples' superior antifouling property was searched for. Based on results of DLS, QCM-D, UV-visible spectroscopy and contact angle experiments, the following trends are present. First, since both components are necessary – the polysaccharide for increasing hydrophilicity and the LCST polymer to allow for

controlled deposition and consequently, for a smooth surface, which are both required to decrease contact angle - a comparable amount of the two components need to be incorporated in the conjugates. Second, since the kinetics of deposition are heavily influenced by the value of the LCST, compositions that change this – for example, by allowing the formation of supramolecular structures – can lead to unexpected behavior in terms of antifouling capabilities. The results suggest that these are the two most important factors that determine changes in energy dissipation during coating formation. Dissipation changes are important because, based on the studied samples, deposition and rearrangement being two separate events during coating formation appears to be the key to a good antifouling capability.

3.5 References

1. Komatsu, T.; Nakagawa, A.; Curry, S. *et al.,* The role of an amino acid triad at the entrance of the heme pocket in human serum albumin for O(2) and CO binding to iron protoporphyrin IX. *Org. Biomol. Chem.* **2009**, *7 (18)*, 3836–41.
2. Guhathakurta, S. and Subramanian, A., Effect of Hydrofluoric Acid in Oxidizing Acid Mixtures on the Hydroxylation of Silicon Surface. *J. Electrochem. Soc.*, **2007**, *154 (11)*, 136-146.
3. Ramadan, M. H.; Prata, J.E.; Karácsony, O.; Dunér, G., Washburn, N. R., Reducing Protein Adsorption with Polymer-Grafted Hyaluronic Acid Coatings. *Langmuir*. **2014**, *30 (25)*, 7485-95.
4. Franco, L., Tacticity Determination of Poly (methyl Methacrylate) (PMMA) by High-Resolution NMR. *J. Pol. Sci.: Pol. Lett.*, **1982**, *20*, 525-529.
5. Kikuchi, H. et al., Fast Electro-Optical Switching in Polymer-Stabilized Liquid Crystalline Blue Phases for Display Application, SID07 Digest, 1737-1740.

6. http://ciks.cbt.nist.gov/~garbocz/SP946/node5.htm
7. Grymonpre, Kristopher R.; Staggemeier, Bethany A.; Dubin, Paul L.; Mattison, Kevin W., Identification by Integrated Computer Modeling and Light Scattering Studies of an Electrostatic Serum Albumin-Hyaluronic Acid Binding Site. *Biomacromolecules*, **2001**, *2 (2)*, 422-429.
8. Horkay, F.; Falus, P.; Hecht, A.-M.; Geissler, E., Length scale dependence of the dynamic properties of hyaluronic acid solutions in the presence of salt. *J. Phys. Chem. B* . **2010**; *114 (47)*, 15445-50.
9. Hu, Z.; Cai, T.; Chi, C., Thermoresponsive oligo(ethylene glycol)-methacrylate- based polymers and microgels. *Soft Matter* **2010**, *6*, 2115–212.
10. Okabe et al., Heat-Induced Self-Assembling of Thermosensitive Block Copolymer. 1. Small-Angle Neutron Scattering Study. *Macromolecules*, **2002**, *35 (21)*, 8139-8146.
11. Popova, M. V.; Chernyshev, Y. S. Self-association of potassium nonanoate molecules in aqueous aerosil dispersions: 13C NMR data *Colloid J.* **2004**, *66 (5)*, 567– 574.
12. Penfold, J.; Staples, E.; Tucker, I.; Thomas, R. K. Adsorption of mixed anionic and nonionic surfactants at the hydrophilic silicon surface *Langmuir* **2002**, *18 (15)*, 5755–5760.
13. Harewood, K.; Wolff Iii, J. S. A rapid electrophoretic procedure for the detection of SDS-released oncorna-viral RNA using polyacrylamide-agarose gels *Anal. Biochem.* **1973**, *55, (2)*, 573– 581.
14. Vig, J. R. UV/ozone cleaning of surfaces *J. Vac. Sci. Technol., A* **1985**, *3 (3)*, 1027– 1034.
15. Krozer, A.; Rodahl, M. X-ray photoemission spectroscopy study of UV/ozone oxidation of Au under ultrahigh vacuum conditions *J. Vac. Sci. Technol., A* **1997**, *15 (3)*, 1704– 1709.

16. Sauerbrey, G. The use of quartz oscillators for weighing thin layers and for microweighing *Z. Phys.* **1959**, *155*, 206– 22.
17. Rodahl, M.; Höök, F.; Krozer, A.; Brzezinski, P.; Kasemo, B. Quartz crystal microbalance setup for frequency and Q-factor measurements in gaseous and liquid environments *Rev. Sci. Instrum.* **1995**, *66 (7)*, 3924– 30.
18. Höök, F.; Kasemo, B. The QCM-D technique for probing biomacromolecular recognition reactions *Springer Ser. Chem. Sens. Biosens.* **2007**, *5*, 425– 447.
19. Larsson, C.; Rodahl, M.; Höök, F. Characterization of DNA immobilization and subsequent hybridization on a 2D arrangement of streptavidin on a biotin-modified lipid bilayer supported on SiO_2 *Anal. Chem.* **2003**, *75 (19)*, 5080– 5087.
20. Reimhult, E.; Larsson, C.; Kasemo, B.; Höök, F. Simultaneous surface plasmon resonance and quartz crystal microbalance with dissipation monitoring measurements of biomolecular adsorption events involving structural transformations and variations in coupled water *Anal. Chem.* **2004**, *76 (24)*, 7211– 7220.
21. Coessens, V.; Matyjaszewski, K. Synthesis of polymers with hydroxyl end groups by atom transfer radical polymerization *Macromol. Rapid Commun.* **1999**, *20 (3)*, 127– 134.
22. Vroman, L.; Adams, A. L.; Fischer, G. C.; Munoz, P. C. Interaction of high molecular weight kininogen, factor XII, and fibrinogen in plasma at interfaces **1980**, *55 (1)*, 156– 159.
23. Garland, A.; Shen, L.; Zhu, X. Mobile precursor mediated protein adsorption on solid surfaces *Prog. Surf. Sci.* **2012**, *87 (1-4)*, 1– 22.
24. Gombotz, W. R.; Guanghui, W.; Horbett, T. A.; Hoffman, A. S. Protein adsorption to poly(ethylene oxide) surfaces *J. Biomed. Mater. Res.* **1991**, *25 (12)*, 1547– 1562.

25. Alcantar, N. A.; Aydil, E. S.; Israelachvili, J. N. Polyethylene glycol-coated biocompatible surfaces *J. Biomed. Mater. Res.* **2000**, *51 (3)*, 343– 51.

26. Geelhood, S. J.; Horbett, T. A.; Ward, W. K.; Wood, M. D.; Quinn, M. J. Passivating protein coatings for implantable glucose sensors: evaluation of protein retention *J. Biomed. Mater. Res., Part B* **2007**, *81 (1)*, 251– 60.

27. Bridges, A. W.; Garcia, A. J. Anti-inflammatory polymeric coatings for implantable biomaterials and devices J. Diabetes Sci. Technol. **2008**, *2 (6)*, 984– 94.

28. Lee, J. H.; Lee, H. B.; Andrade, J. D. Blood compatibility of polyethylene oxide surfaces *Prog. Polym. Sci.* **1995**, *20 (6)*, 1043– 1079.

29. Kennedy, S. B.; Washburn, N. R.; Simon, C. G., Jr.; Amis, E. J. Combinatorial screen of the effect of surface energy on fibronectin-mediated osteoblast adhesion, spreading and proliferation *Biomaterials* **2006**, *27 (20)*, 3817– 24.

30. Dekker, A.; Reitsma, K.; Beugeling, T.; Bantjes, A.; Feijen, J.; van Aken, W. G. Adhesion of endothelial cells and adsorption of serum proteins on gas plasma-treated polytetrafluoroethylene *Biomaterials* **1991**, *12 (2)*, 130– 8.

31. Bumgardner, J. D.; Wiser R Fau - Elder, S. H.; Elder Sh Fau - Jouett, R.; Jouett R Fau - Yang, Y.; Yang Y Fau - Ong, J. L.; Ong, J. L. Contact angle, protein adsorption and osteoblast precursor cell attachment to chitosan coatings bonded to titanium (0920-5063 (print)).

32. Sigal, G. B.; Mrksich, M.; Whitesides, G. M.Effect of surface wettability on the adsorption of proteins and detergents *J. Am. Chem. Soc.* **1998**, *120 (14)*, 3464– 3473.

33. Vogler, E. A.Protein adsorption in three dimensions *Biomaterials* **2012**, *33 (5)*, 1201– 1237.

34. Churaev, N. V.; Sergeeva, I. P.; Sobolev, V. D.Hydrodynamic thickness and deformation of adsorbed layers of polyethylene oxides *J. Colloid Interface Sci.* **1995**, *169 (2)*, 300– 305.

35. McPherson, T.; Kidane, A.; Szleifer, I.; Park, K.Prevention of protein adsorption by tethered poly(ethylene oxide) layers: Experiments and single-chain mean-field analysis *Langmuir* **1998**, *14 (1)*, 176– 186.

36. Kenausis, G. L.; Vörös, J.; Elbert, D. L.; Huang, N.; Hofer, R.; Ruiz-Taylor, L.; Textor, M.; Hubbell, J. A.; Spencer, N. D. Poly(l-lysine)-g-poly(ethylene glycol) layers on metal oxide surfaces: Attachment mechanism and effects of polymer architecture on resistance to protein adsorption *J. Phys. Chem. B* **2000**, *104 (14)*, 3298– 3309.

37. Dubois, J.; Gaudreault, C.; Vermette, P. Biofouling of dextran-derivative layers investigated by quartz crystal microbalance Colloids Surf., B **2009**, *71 (2)*, 293– 299.

38. Tan, H.; Ramirez, C. M.; Miljkovic, N.; Li, H.; Rubin, J. P.; Marra, K. G. Thermosensitive injectable hyaluronic acid hydrogel for adipose tissue engineering *Biomaterials* **2009**, *30 (36)*, 6844– 53.

39. Miura, M.; Cole, CA; Monji, N.; Hoffman, A. S. Temperature-dependent absorption/desorption behavior of lower critical solution temperature (LCST) polymers on various substrates *J. Biomater. Sci., Polym. Ed.* **1994**, *5 (6)*, 555– 568.

40. Cai L.; Lu, J.; Sheen,V.; Wang, S. Optimal Poly(l-lysine) Grafting Density in Hydrogels for Promoting Neural Progenitor Cell Functions *Biomacromolecules*. **2012**, *13(5)*, 1663– 1674.

41. Tizzotti, M.; Charlot, A.; Fleury, E.; Stenzel, M.; Bernard, J.Modification of polysaccharides through controlled/living radical polymerization grafting—towards the

generation of high performance hybrids *Macromol. Rapid Commun.* **2010**, *31 (20)*, 1751–1772.

42. Bauer Stella; Arpa-Sancet Maria Pilar; Finlay John A; Callow Maureen E; Callow James A; Rosenhahn Axel. Langmuir, **2013**, *29(12)*, 4039-47.
43. Morra, Marco; Cassineli, Clara. J. Biomat. Sci., Pol. Ed. **1999**, *10(10)*, 1107-1124.
44. Palumbo, Fabio Salvatore; Volpe Bavuso, Antonella; Cusimano, Maria Grazia; Pitarresi, Giovanna; Giammona, Gaetano; Schillaci, Domenico. Int. J. Pharm. **2015**, *478(1)*, 70-77.

CHAPTER 4

SELF-ASSEMBLY OF COVALENTLY BONDED FIBERS BY ZIPPER-LIKE DRUVEB AGGREGATION

4.1. Introduction

Protein-polymer hybrids (PPHs) are generally prepared by coupling polymers to individual proteins by "grafting from" or "grafting to" methods.[1-8] These materials have gained wide interest in the fields of drug delivery,[9-14] imaging[15] and sensing.[16, 17] Recently, non-canonical amino acids were genetically engineered into proteins[18] and PPHs were gained by conjugating polymers to this incorporated functionality. Coupling polymers to non-canonical amino acids allows for the use of bio-orthogonal coupling reactions and residue-specific modification of proteins without compromising the structural integrity, stability and bioactivity of the proteins.[19, 20]

Protein fibers have been designed and synthesized for tissue engineering applications, e. g. for preparing biocompatible artificial surfaces or matrices. The biocompatibility and physicochemical properties of these surfaces and matrixes has a crucial effect on the contacting/embedded cells' viability. Furthermore, these biocompatible synthetic materials can incorporate and elute therapeutics (i.e. small molecules/proteins/nucleic acids), and promote tissue growth and remodeling in vivo.[21, 22]

Current technology of the preparation of bioartificial surfaces or matrices focuses on protein-fibers with a large number of amino acid repeat units, by the electro-spinning of protein solutions to directly produce protein fibers[23-25] and protein-amphiphiles**.** [27] There are practical limitations to the art of electro-spinning of protein solutions, that arise, for example, from the required high

* Some of this work was published along with other results in Averick, S.; Karácsony, O.; Mohin, J.; Yong X.; Moellers, N. M.; Woodman, B. F.; Zhu, W.; Mehl R. A.; Balazs A. C.; Kowalewski, T.; Matyjaszewski, K Cooperative, Reversible Self-assembly of Covalently Pre-linked Proteins into Giant Fibrous Structures. Angew. Chem., Int. Ed. 2014, 53 (31), 8050-8055..

temperature and current fluctuations, because these can change a protein's tertiary structure, which is likely hamper the bioactivity of the synthesized fibers.[28]

Protein-polymer amphiphiles are remarkable materials, due to their ability to assemble into macroscopic structures, but in some applications, their non-covalent nature can be a drawback. These include cases when they are applied in an environment where significant fluctuations in pH or ionic strength might occur, leading to the breaking of their physical bonds and forming new ones, for example between the hydrophobic parts of the protein and the polymer. Furthermore, controlling the architecture of the conjugates to form fibers is challenging and several undesired structures can be formed.[6, 7, 29, 30]

Due to the current limitations of protein-fibre synthesis, it is desirable to design new routes to their preparation. Therefore, in this work we addressed this important issue and report herein the synthesis of a PPH via a novel methodology, characterization of the fibers, theoretical considerations and simulations that confirm the microscopic structure and physical behavior. Synthesis and chemical characterization was conducted by Saadyah E. Averick, a graduate student in the Matyjaszewski group, and modeling by Frank Yong, a postdoctoral fellow and Nicholas Moellers, an undergraduate student, both members the Balazs group at the University of Pittsburgh.

4.2 Results and Discussion

4.2.1 Preparation of a Protein-Polymer Fibre via Click Step-Growth Polymerization

It was envisioned that a protein could be polymerized using step-growth polymerization to directly form protein fibers under mild synthetic conditions. This direct copolymerization of proteins and biocompatible polymers is not possible with the current bioconjugation technology, due to the

inability of modifying a protein's amino acid residues with a high enough selectivity, which leads to the formation of a mixture of proteins with different modified amino acid residues.[2] This heterogeneous modification of the amino acids in the protein will lead to the formation of a cross-linked protein network, rather than fibers.

To overcome traditional limitations associated with the direct polymerization method, we propose a combination of genetic engineering and click chemistry. The incorporation of an unnatural amino acid into a protein at known positions introduces a precise number of reactive sites at specific locations. This genetically engineered protein can then be expanded by "click" step growth polymerization, to form PPH, taking advantage of the mild reaction conditions. Scheme 1 depicts the method used to prepare protein fibres by direct step-growth polymerization of diazide proteins with dialkyne poly(ethylene glycol).[31, 32] Copper-catalyzed azide-alkyne cycloaddition ("click") chemistry was selected because of the bio-orthogonality and low temperature requirements of this reaction.[33-37] "Click" chemistry has been used to prepare a wide range of biomaterials including bionanoparticles [38, 39]and drug delivery systems.[40, 41] Since the reactive groups in the "click" reaction are bio-orthogonal, these reactive moieties have been incorporated into unnatural amino acids (UAAs) and expressed in proteins using amber codon suppression technology for a wide range of applications *in vitro* and *in vivo*. [42-44]

To achieve the goal of preparing protein fibers (i.e. regular chain extended multimeric protein-polymer hybrids), a well-defined protein, bearing exactly two reacting moieties was required to facilitate the step-growth polymerization. GFP was selected as a model protein, because of its fluorescent properties that facilitated visualization and characterization of the resulting PPH fiber. Amber codon suppression technology was employed to incorporate two unnatural amino acids (codon: UAA) containing azide functionality at surface-exposed residues (amino acid residues134

and 150) of GFP (Figure 4.2.1.1A). A *Methanococcus jannaschii* (*Mj*) tyrosyl-tRNA synthetase (RS)/$tRNA_{CUA}$ pair was used for the co-translational and site-specific incorporation of p-azidophenylalanine (pN_3F) into GFP.[45] The resulting protein was used for direct copolymerization with poly (ethylene oxide) (PEO) under mild aqueous reaction conditions, thereby circumventing the previously mentioned issues associated with other protein-fiber synthesis techniques. Furthermore, by preparing covalently linked protein-fibers, a stable hybrid structure that would provide superior protein stability in bioengineering applications, is realized.

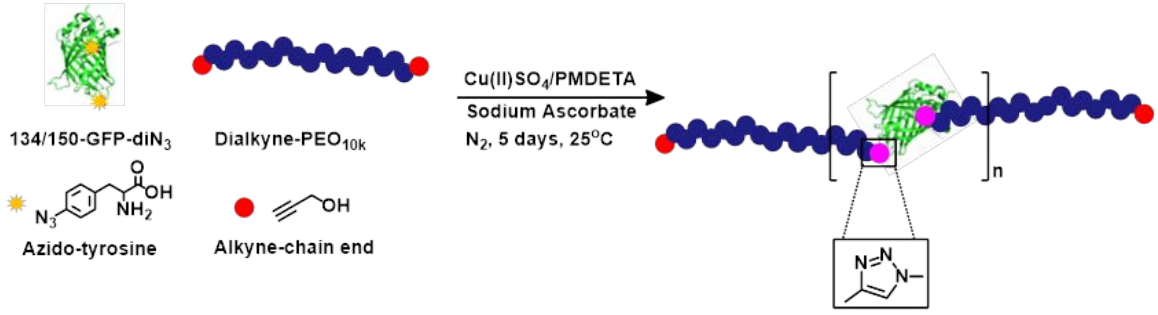

Figure 4.2.1.1: Fiber synthesis. "Click" step-growth polymerization approach was used for preparing GFP-PEO fibers. Synthetic conditions: GFP_2/ PEO_{10k}dialkyne/ PMDETA/ $CuSO_4*5H_2O$/ sodium ascorbate = $7*10^{-4}$ mmol/ $7*10^{-4}$mmol/ $9.1*10^{-3}$ mmol/ $7*10^{-3}$mmol/ $7.7*10^{-3}$mmol, in 0.1M PBS buffer (pH= 7.4).

The "click" step growth polymerization was conducted by dissolving dialkyne-PEO, $CuSO_4$-$5H_2O$, and PMDETA in water followed by dropwise addition of a solution containing GFP-diN_3 in phosphate buffer saline (1x PBS, pH= 7.4). The reaction mixture was protected from light, and sodium ascorbate was added to produce Cu(I) *in situ*. The reaction was stirred for 5 days,

centrifuged, and the supernatant discarded. The GFP-PEO fibers were suspended again and centrifuged two additional times with PBS, to remove the catalyst and any unreacted GFP.

4.2.2 Characterization

4.2.2.1 Dynamic light scattering

The size distribution of the GFP-PEO fibers was determined using dynamic light scattering (DLS); the fibres were visualized by atomic force microscopy (AFM) and confocal microscopy. For DLS, a 0.1 mg/mL solution of the GFP-PEO was vortex mixed for 5 minutes, to disperse the fibers. Figure 1B shows the volume distribution, as determined by dynamic light scattering (DLS). The DLS volume distribution results indicated relatively well-defined particles with a diameter of approximately 0.658 μm with a PDI of 0.501. DLS analysis of a control, where the sodium ascorbate was not added to the reaction mixture and no "click" chain extension occurred, shows particles of 5 nm (cf. SI Fig1). This size matches that of native GFP and indicates that indeed a "click"-mediated step-growth polymerization occurred after the addition of sodium ascorbate.

4.2.2.2 Confocal microscopy

Since the mild conditions used to prepare the GFP-PEO fibers allowed the GFP molecules to retain their tertiary structure, confocal microscopy analysis could be employed to study the morphology of the fibers. Two surfaces were prepared for analysis: on the first one, a 0.01 μg/mL solution of GFP-PEO was spin-casted at 2000 rotations per minute (r.p.m.) (Figure 4.2.2.2.1C); for the second one, a (1 μg/mL solution was drop-casted onto a glass cover slip (Figure 4.2.2.2.1D). , Based on the acquired images of the spin-casted sample the length of an isolated fiber is ~20 μm (Figure 2C). ; in the drop-casted sample elongated fluorescent fibers of approximately 10 μm in length

were seen (Figure 4.2.2.2.1D). Images were collected with 130 nm per pixel, and with this resolution, the fluorescence along the fibers appears to be evenly strong.

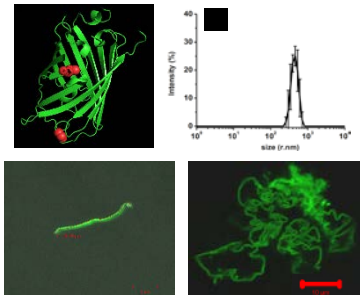

Figure 4.2.2.2.1: Monomer and fiber structure of GFP-PEO fibers prepared by the "click" step-growth polymerization of GFP-diN_3 and PEO_{1k}-dialkyne. A) GFP monomer showing the modified amino acids at positions 134 and 150 in red. Modification sites in the GFP were visualized using data from the Protein Data Bank and Pymol version 1.4.1with Python version 2.7. B) Size distribution analysis using DLS of GFP-fibers. The size distribution of the suspended fibers shows an approximate diameter of 0.658 μm and CV of 0.501. C & D) Confocal microscopic analysis of the fibers. Confocal analysis shows that the GFP retains its fluorescent properties, and fibers can be observed in the range of tens of μm in length (scale bar: 10 μm). C) Spin-casted GFP-PEO fiber (scale bar: 5 μM); length ~20 μm. D) The Z-stack analysis of the drop-casted GFP-PEO solution reveals fiber nature of the GFP-PEO (scale bar: 10 μM).

4.2.2.3.Atomic Force Microscopy

Atomic Force Microscopy (AFM) analysis was conducted to ascertain fiber morphology. A well-dispersed solution (1 μg/mL fiber, 2 nM $CaCl_2$) was cast at a 45° angle first on a freshly cleaved mica surface (SI Figure 2), where fibers of 1 μm length were observed, but in the presence of a significant amount of impurities, most probably unreacted PEO molecules and small molecular weight chains from the reaction, because in a step-growth polymerization process, typically a broad range of molecular weights and thus fiber sizes are obtained.[47] Since GFP has a total negative charge (isoelectric point ~5), a small amount of $CaCl_2$ was added to the solution of the fibers. When casted on highly ordered pyrolytic graphite (HOPG) substrate, we serendipitously obtained much clearer images (Figure 4.2.2.3.1). This can be explained by the fact that from the strongly hydrophobic surface of HOPG, the fiber solution could be allowed to drop off the surface instead of letting evaporating, like in the case of mica, and consequently, most of the small molecular weight water-soluble impurities were not retained on the surface. The vertical traces observable on the phase images are caused by the small amount of low molecular weight deposits that still remained on the surface and were dragged along with the probe. The fact that fibers were not destroyed by the probe show their mechanical strength. Again, the fibers were found to be several microns in length and up to 0.1 μm in width, in agreement with the confocal microscopy data. The height was found to be up to 10 nm (see color bar in Figure 4.2.2.3.1), which is slightly larger than the height of two GFP barrels (2*4 nm, Figure 4.2.2.4.1); the difference is most probably caused by the presence of PEO. Because of this and the double helical structure observed in the AFM images (Figure 4.2.2.3.1), it is hypothesized that the fibers present on the images are in fact two chains wrapping around each other.

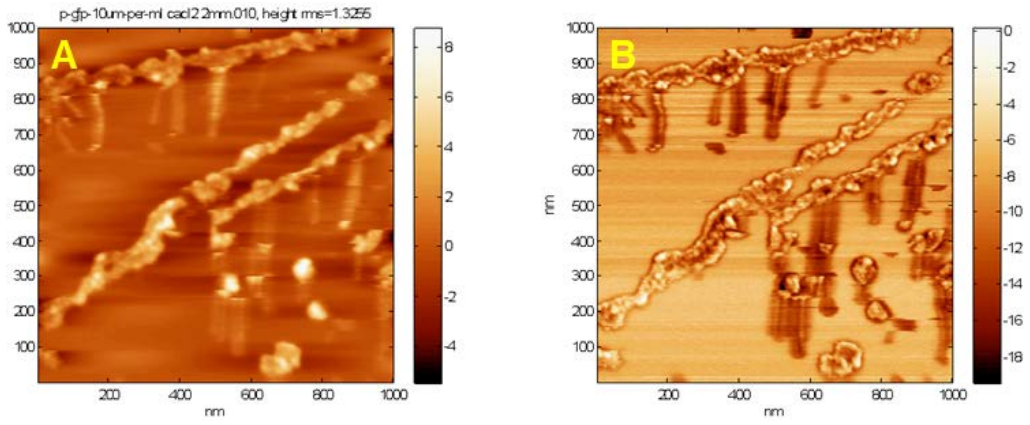

Figure 4.2.2.3.1: Atomic force microscopic images of GFP fibers cast on a substrate at a 45° angle. A) height, B) phase channel of the image of a representative site of the sample. Fibers can be seen on the order of several microns lengths and up to 0.1 μm in width (image size: 1 μm).

4.2.2.4 Physical and biological properties

4.2.2.4.1 Dimerization

The entropy of PEO chains would drive them to coil, but by covalently linking GFP molecules to them, the local concentration of these is increased to a value at which the hydrophobic interaction between them becomes important (Figure 4.2.2.4.1.1), turning them into a special (non-spherical) form of Janus particles. Consequently, entire chains can be dimerized with a remarkably long persistence length (about 2.5 μm, with 100-120 segments per persistence length, see SI), which makes them stable over an extended period of time, shown by the fact that samples could be imaged two years after synthesis without a loss of integrity. The fibers' mechanical stability is proven by their survival of tapping on a strongly hydrophobic surface, over the course of which small fragments were moved by the probe along its track. The double helical structure and persistence

length make these fibers similar to DNA. However, their building blocks are not nucleotides but amino acids (besides of the connecting PEO), and the strains are not held together by hydrogen bonds, but by hydrophobic interactions, like in the case of pore-forming proteins, e. g. ion channels.

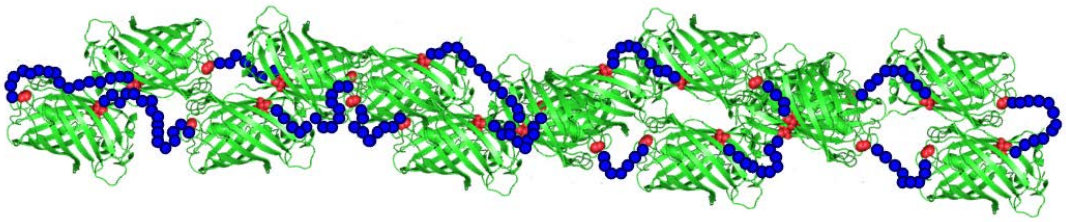

Figure 4.2.2.4.1.1: Cartoon showing the helical structure of the fibers.

4.2.2.4.2 Biodegradability

For potential biomedical applications, the fibers' biodegradability is an important property. Therefore, a 0.1 mg/mL solution of the fibers was treated with 2.5% of trypsin for 4 days at 37°C, and vortex mixing before the measurement, to assure suspension. The sample was measured before and after the trypsinic digestion. After 4 days, the volume distribution decreased to ~10 nm, indicating successful enzymatic degradation (Figure 4.2.2.4.2.1).

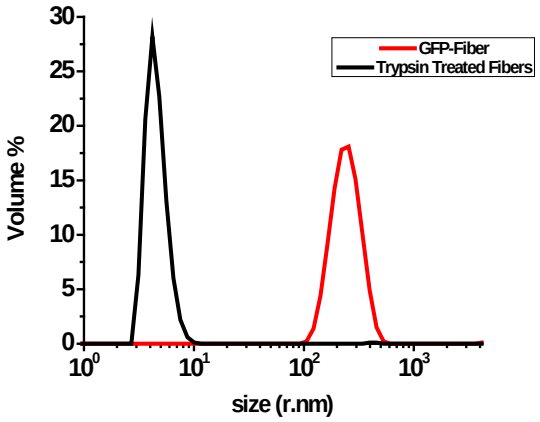

Figure 4.2.2.4.2.1: Enzymatic degradation of GFP-PEO fibers using 2.5% trypsin for 4 days at 37°C. The graph shows the volume distribution of the fibers before and after enzymatic degradation was measured by dynamic light scattering.

4.2.2.4.3 Reversibility of self-assembly

To demonstrate the dynamic nature of the self-assembly, the fibers were ultrasonicated for 180 s with 1 s intervals, at 25 °C. The samples were then transferred to a DLS cuvette and the intensity of the transmitted light measured at various time points after ultrasonication to determine time required for fiber reformation at 25 °C. The fibers were minimally disturbed (i.e. removal from DLS measurement chamber) between measurements (Figure 4.2.2.4.3.1). As the graphs show, the fibers were perfectly recovered after 2 days.

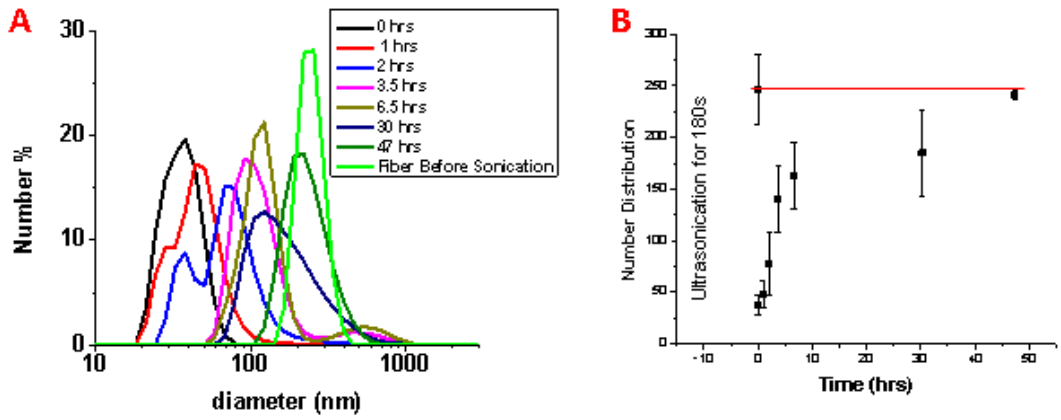

Figure 4.2.2.4.3.1: Reversibility of self-assembly. A: size distribution, B: change in average diameter over time. Ultrasonication disrupts the fibers, but they fully recover in two days.

4.2.3 The Physics of the Chains

4.2.3.1 The Equivalent Freely Jointed Chain Model

The general behavior of flexible polymers is described by the equivalent freely jointed chain model. This equivalent chain has the same maximum and root-mean square end-to-end distance as the real polymer, but can be divided into freely jointed effective bonds of equal length. These effective bonds are called Kuhn segments. The root-mean-square end-to-end distance (R_{rms}) of the polymer chain is given by Eq. 4.2.3.1.1:

$$\mathrm{Rrms} = B^{1/5} l\, Kuhn^{2/5} \mathrm{NN}^{3/5} \qquad 4.2.3.1.1$$

where B is the second virial coefficient, l Kuhn stands for the Kuhn segment length, and NN for the number of Kuhn segments within a chain.

The segment persistence length (sp) is the scale at which local correlations between bond vectors decay;[50] in other words, the intersegmental distance above which the movement of one segment of the chain doesn't influence the position of another segment. In our case, there is no restriction on torque angle (the angle with which one segment rotates out of the plane of the two previous segments), the fibers can be considered as freely rotating chains (FRC). Therefore, sp can be calculated according to the FRC model, using Eq. 4.2.3.1.2:

$$\mathrm{sp} = -\frac{1}{\log(\cos(\theta))} \qquad 4.2.3.1.2$$

where θ is the angle between two adjacent segments of the equivalent chain and

$$< \cos(\theta_{i,j}) >= \cos(\theta)^{\mathrm{Abs}[i-j]} = \cos(\theta)^{k} = e^{-\frac{k}{\mathrm{sp}}} \qquad 4.2.3.1.3$$

where $\theta_{i,j}$ is the rotational angle between segment i and j, and k=|i-j|.[50] Equations 4.2.3.1.2 and 4.2.3.1.3 were used to calculate the values of the persistence length and Kuhn length, in order to get a quantitative assessment of chain behavior.

4.2.4 Quantitative evaluation of chain behavior

The chains were tracked on the longest possible path in two dimensions, using Mathematica's image processing toolbox (SI Table 2). Three dimensional tracking was not possible because images were taken with a slice width of 5 µm, which does not make k3D reconstruction possible. The expected value of the distance that the chains reach is the same in all directions; compared to the sample size, the results are in reasonable agreement with this expectation (Figure 4.2.4.1).

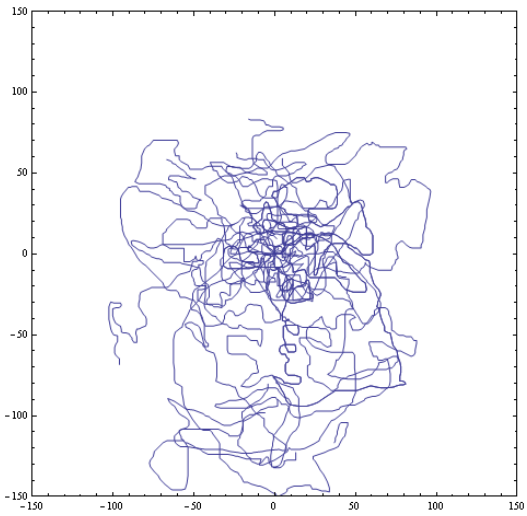

Figure 4.2.4.1: Superimposition of the chains after moving their first points to the origin.

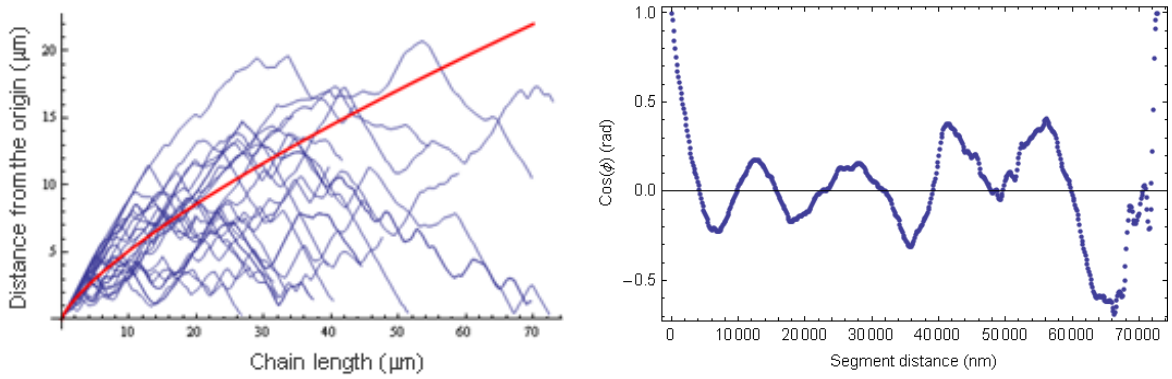

Figure 4.2.4.2: Left: Distance of each point from the origin of the slice, for each slice. The red line shows the prediction of this value for a self-avoiding random walk in 3 dimensions. Right: dependence of Cos(Φ) on segment distance.

Based on tracking 27 slices, the following values were calculated:

l_{Kuhn} = 0.912 (std. dev: 0.188)

α = 0.749 (std. dev: 0.138)

The calculated value for Kuhn length is about one third of the persistence length. For comparison, this ratio for a worm-like chain would be equal to 3.

Figure 4.2.4.3: A wooden snake as a model of the chains. The energy barrier between the folded and extended conformation is low enough for a pulling force to overcome it and fold the chain while turning a GFP monomer, which now would lose its preference for staying in the close vicinity of the neighboring monomer that has the same orientation - like in a wooden snake toy.

Over long distances, the agreement gets better, but over short distances, these chains are much straighter than what would be expected for a Gaussian chain. The other important fact to notice is that the chains that are originally rigid, tend to fold back after reach a certain distance of their origin (these are the local maxima in the distance curves, see Figure 4.2.4.2). It is worth noting that the slopes of both the approaching and withdrawing parts are fairly constant, manifesting in triangular shapes on the curves.

4.2.5 Quantification of periodicity in the fibers

In an attempt to quantify the observed periodicity on the height images, that we hypothesize to be attributable to the janusoid GFP monomers trying to maximize contact with each other, the volume profile of the image was calculated (Figure, left) and transformed into frequency space by applying a Fourier transform (Figure 4.2.5.1, right).

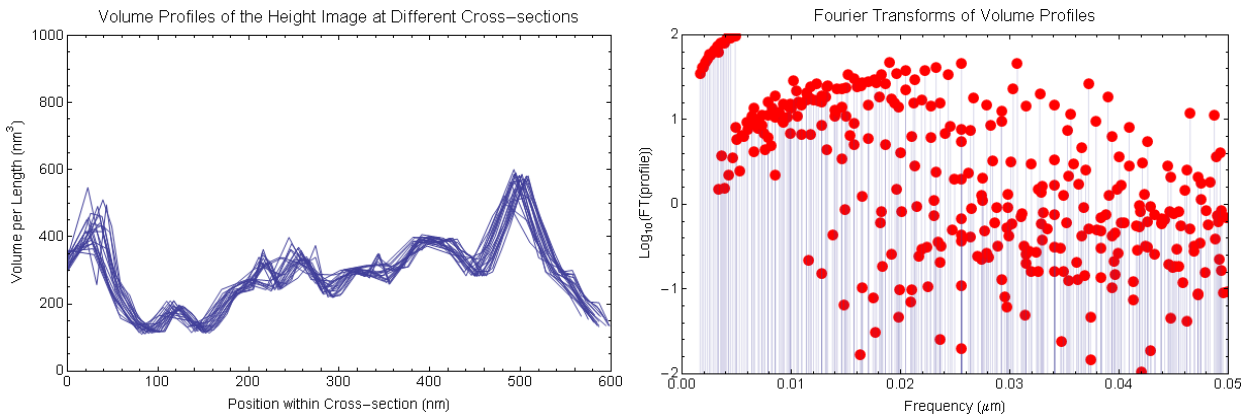

Figure 4.2.5.1: Volume profile (left) and Fourier transform (right) of the height images.

On the Fourier transform graph, we can suspect a local maximum at 30 nm, which would correspond to the expectations (Figure 4.2.2.3.1, with an average PEO length of 10 nm), but the individual transformations (SI Table 3) show the local maxima around 30 nm better.

4.2.6 The roles of PEO –

4.2.6.1 Entropic elasticity

This means that the PEO does more than simply holding the GFP monomers close together. The anthropic elasticity of the PEO chains pulls the monomeric proteins together, but the height of the energy barrier between the folded and extended conformation is low enough for a pulling force to overcome it and fold the chain while turning a monomer, which now would lose its preference for staying in the close vicinity of the neighboring monomer that has the same orientation - just like in a wooden snake toy (Figure 2.7). (Note: for this reason, this simple and catchy but representative model could be a good starting point for the graphical abstract.) During stirring, shear flow is

applied, which explains why we see mostly circular objects in the fluorescent images (Figures Figure 4.2.2.2.1, 4.2.4.1).

The above reasoning mean that in the form of these fibers, we have bistable nanoscale objects with both high persistence length and high pliability. Their importance lies in combining these usually mutually exclusive concepts. Apart from scientific novelty, the advantageous physicochemical properties make these PEO-GFP conjugates interesting from the point of view of applicability as well. The fibers are strong yet flexible, giving them the potential of being used as nanoscale ropes. This, combined with their fluorescence, which makes them easy to visualize, opens up a number of ways to proceed with their study. This would include developing methods to control their self-assembly, starting with checking the effect of reversible changes in pH and ionic strength of the medium. Furthermore, due to their biodegradability, they have potential uses in tissue engineering and other medical applications. (Note: connecting synthetic Janus particles by PEO chains would be an interesting project, and the product might even have an industrial potential. For example, polyethylene terephthalate was shown to become water-repellent when coated with amphiphilic particles.[3])

4.2.6.2 Switching on the Janus properties of GFP

GFP monomers, if their local concentration in the solution is high enough (5 mM and above), which in this case is assured by binding them together by PEO chains, behave as Janus-particles. The driving force behind this pairing is discussed in the next section.

4.2.7 The Force behind the Self-assembly: Hydrophobic Interactions

The crystallographic contacts among monomers are all rather tenuous, consisting of a few amino acids' side chains for each. The non-crystallographic symmetry is maintained by extensive

contacts and thus is likely to be the source of the dimerization seen in solution studies[48] (Figure 4.2.7.1).

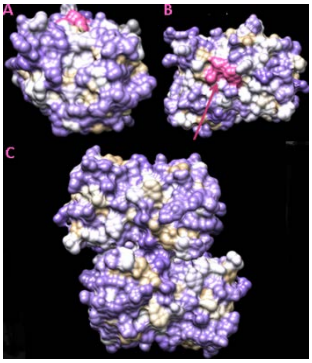

Figure 4.2.7.1: End-on view of the monomer (A), **t**op view of the dimer contact face (B), hydrophobic interface in the GFP dimer (C). K-D hydrophobicity (see Table 3.3.1) color scale: the most polar residues are medium purple, the most hydrophobic ones are tan, and white corresponds to neutral ones (0 on the K-D scale). The hydrophobic cluster consisting of Ala[206], Leu[221], and Phe[223] is shown in hot pink.

Residue Type	kdHydrophobicity[a]	wwHydrophobicity[b]	hhHydrophobicity[c]
Ile	4.5	0.31	-0.60
Val	4.2	-0.07	-0.31
Leu	3.8	0.56	-0.55
Phe	2.8	1.13	-0.32
Cys	2.5	0.24	-0.13
Met	1.9	0.23	-0.10
Ala	1.8	-0.17	0.11
Gly	-0.4	-0.01	0.74
Thr	-0.7	-0.14	0.52
Ser	-0.8	-0.13	0.84
Trp	-0.9	1.85	0.30
Tyr	-1.3	0.94	0.68
Pro	-1.6	-0.45	2.23
His	-3.2	-0.96	2.06
Glu	-3.5	-2.02	2.68
Gln	-3.5	-0.58	2.36
Asp	-3.5	-1.23	3.49
Asn	-3.5	-0.42	2.05
Lys	-3.9	-0.99	2.71
Arg	-4.5	-0.81	2.58

Table 4.2.7.1: Hydrophobicity scale of amino acid residues.[49]

The dimer contacts are fairly tight and consist of a core of hydrophobic side chains from Ala[206], Leu[221], and Phe[223] from each of the two monomers and a wealth of hydrophilic contacts(Table 3.3.1), including Tyr[39], Glu[142], Asn[144], Asn[146], Ser[147], Asn[149], Tyr[151], Arg[168], Asn[170], Glu[172], Tyr[200], Ser[202], Gln[204], and Ser[208].. Contacts with other crystallographic molecules are not extensive, and the salt-dependence of this dimer interface and/or the loose contacts with neighboring molecules may explain the difficulties with isomorphism in initial heavy atom phasing studies.[48]

Figure 4.2.7.2 shows the hydrophobic cluster's location and the PEO attachment sites on the ribbon-model of the GFP dimer.

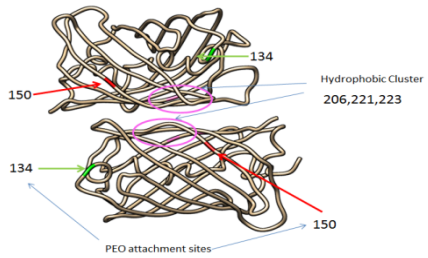

Figure 4.2.7.2: Ribbon-model of the GFP dimer.

4.2.8 The nature of self-assembly

Based on the above results, we conclude that the fibers exhibit self-assembly induced by pairing, where the pairs are held together by hydrophobic interaction. The resulting aggregates are extended to linearity, but in the same time also obey Gaussian statistics, which ensures high flexibility (quantified by their high Kuhn length values, calculated by Equation 2.1. This is realized by the PEO chains, which behave as entropic springs, ensuring the necessary distance between the

janusoid GFP units, and also being able to bend without breaking. A helical structure allows for tighter packing and thus maximizes the contact between the GFP units (Figure 2.1).

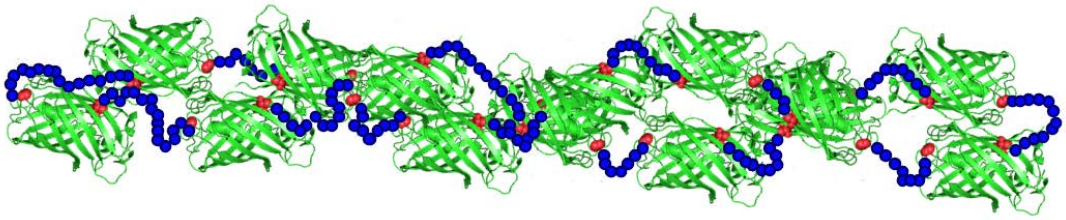

Figure 4.2.8.1: Cartoon showing the helical structure of the fibers.

This is a new form of self-assembly, and the significance of this structure is that other fibers of this persistence length (calculated by equations 2.2 and 2.3, dependence shown in SI Table 1) break upon bending.

Furthermore, due to having hydrophobic interaction as the driving force behind their self-assembly, these fibers are much easier to disassembly and reassembly than peptide amphiphiles that are held together by H-bonds (see section Reversibility of self-assembly).

4.3 In the Seek for a Good Computational model

Based on the dimensions of the GFP monomer, the length of the PEO chains, and the following considerations of the reasons behind dimerization, the following model was used as a basis for the repeat units in the simulations (Figure 4.3.1).

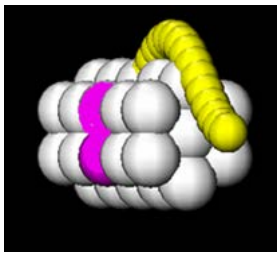

Figure 4.3.1: Suggested model for the repeat unit in the next round of simulations.

4.3.1 Quantification of the Results

Experiments were run with a hydrophobic cluster consisting of one (1), three (A, B) and four beads (C). A and B differed in the orientations of the beads. Run 1 served as control. Run B and C had a row of hydrophobic beads running down the long side of the cylinder, whereas run A's hydrophobic patch was perpendicular to rows B and C (A had a vertical row, B and C had horizontal rows). What this means is that the three hydrophobic beads in run A had two particles touching the edge of the face, whereas particles in run B and C had all of their beads in the center of a face. As expected, dimers formed in run 1 were sparse and unstable, because of the weak attractive force between these small hydrophobic portions (Figure 4.3.1.1, 1).

The difference in orientation between A and B had a remarquable effect on dimer formation. Run A was very similar to run 1: Dimer formation was very low, usually just one dimer at a time, and very unstable (Figure 4.3.1.1, A). However, B had very stable dimer formation, with fully half of the monomers forming dimers at times (Figure 4.3.1.1, B). This huge difference in dimer formation came exclusively from the change in the orientation of hydrophobic particles on the surface of the GFP monomers.

In run C, there was a moment where every single particle was in the form of a dimer, and no trimers were ever formed (Figure 4.3.1.1, C).

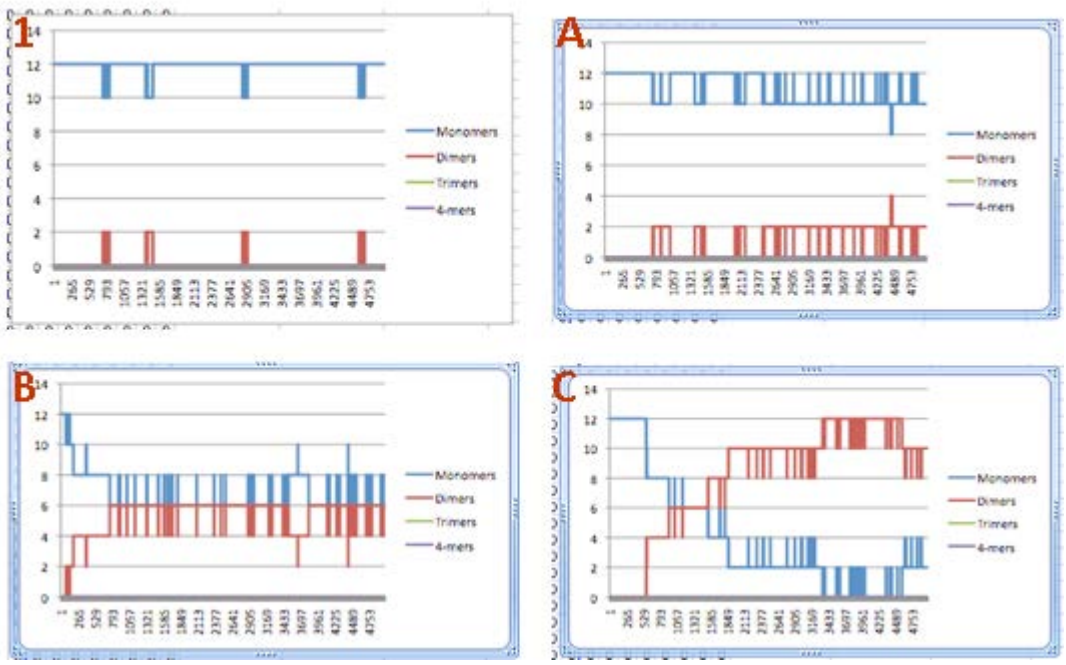

Figure 4.3.1.1: The dynamics of aggregate formation in runs 1, A, B, and C.

4.3.2 Graphical results

The visualization of the best model (the one with four hydrophobic beads, top left) shows that it was very energetically unfavorable for these particles to rotate with respect to each other, indicated by the fact that we see rotations only rarely, much less commonly than in any other run.

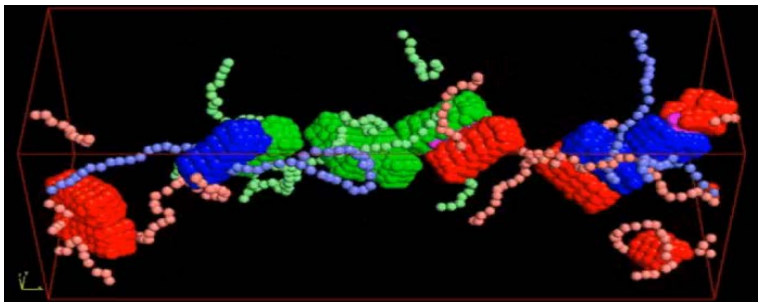

Figure 4.3.2.1: The best model seems to be the one with four hydrophobic beads as hydrophobic cluster on the GFP monomers.

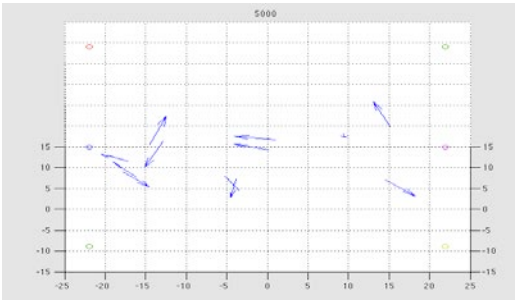

Figure 4.3.2.2: Vector field representation of the fibers.

For the quantitative assessment of the overall topology of the aggregates, a vector field comprised of vectors corresponding to the long axes of monomer particles was implemented (top right).

Defining the box of the simulation with periodic boundary conditions leads to crosslinking (Figure 4.3.2.3). To remove this artifact, this boundary was replaced by a hard reflecting wall with short-range potential. The second issue with this implementation of the box was its extremely small size, which led to a concentration about an order of magnitude higher than in the solution used for

imaging (10 mg/mL or 1%). Since high concentration also facilitates aggregation, the box size was increased. Furthermore, since in an ideal solution, the 2nd virial coefficient is equal to zero, the 3-body interactions were removed from the model.

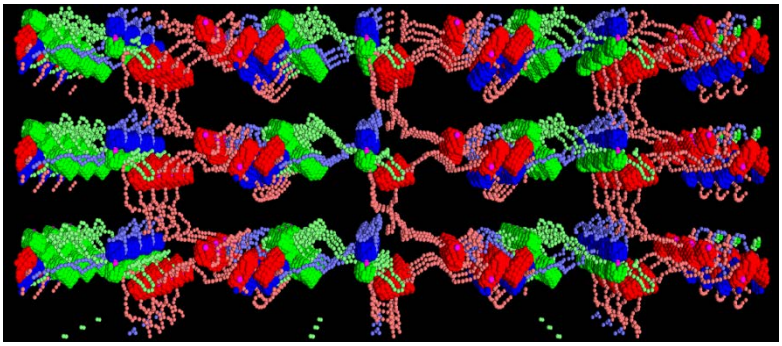

Figure 4.3.2.3: Network formation as a result of the use of a periodic boundary condition.

Having identified the configuration strength/topology necessary for robust dimerization, the next step would be exploring the role of PEO linkages in terms of length and stiffness. As for the length, DP=2000, implying $l_{fully\ extended}$ = 15 nm. (Note that for an ideal chain, $l_{end\text{-}to\text{-}end}^2 = l_{contour}$.) A shortening of the chain from 30 beads to 20 has led to the formation of a cluster that looks very much like a fiber. Furthermore, this cluster did not appear to bond with other clusters, neither in the x, y, nor z directions (Figure 4.3.2.4).

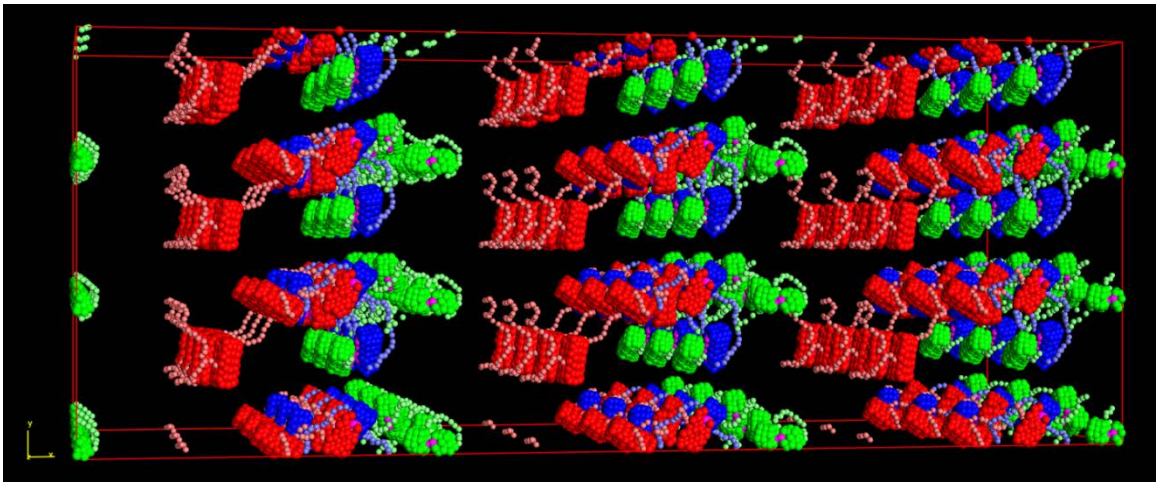

Figure 4.3.2.4: Fiber formation with PEO chains implemented with 20 beads.

When the PEO chains are within a reasonable agreement with the ideal chain model (perfect agreement is impossible because of the repulsion), the network formation is dependent on the length of the PEO linkers. So far simulations were run with linkers consisting of 10, 20, 30, 40, 50 beads. 40 and 50 gave the most significant network formation, 30 moderate, and 10 and 20 limited amount of crosslinking.

It has to be noted, however, that dimerization of the chains with PEO linkers consisting of 10 or 20 beads is mostly intramolecular (Figure 4.3.2.5). For this reason, in the next round of simulations, the attraction between the hydrophobic patches will be removed in order to allow the chains to relax, and switched on only after this.

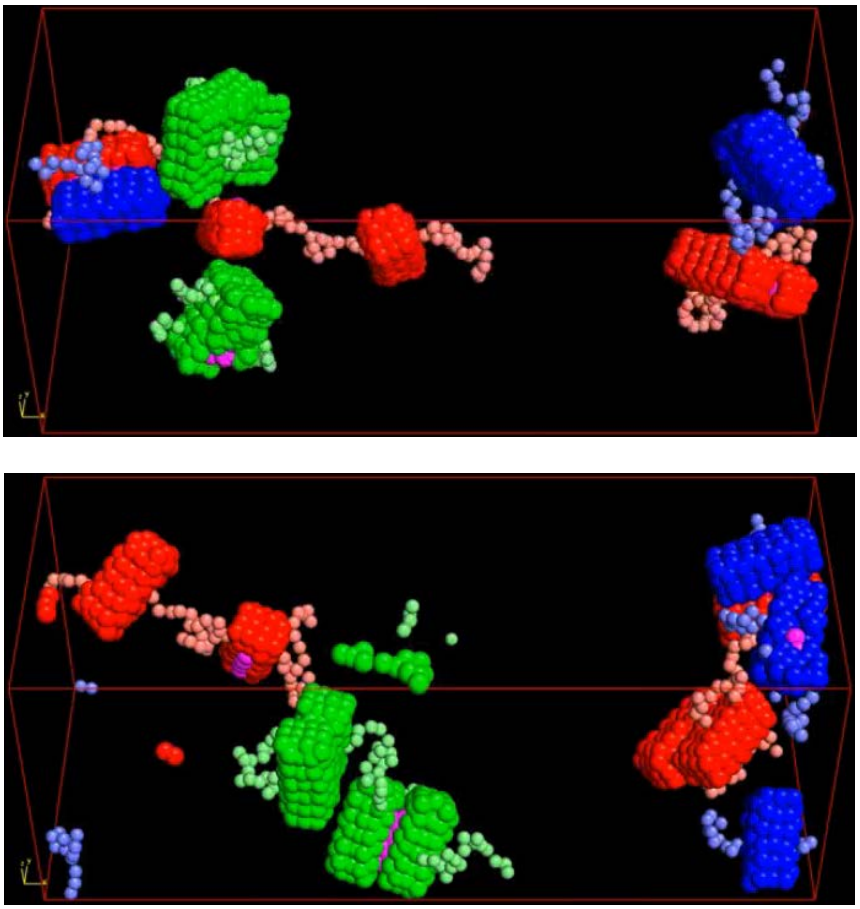

Figure 4.3.2.5: Intramolecular dimer formation with PEO chains consisting of 20 beads.

4.4 Conclusions

A facile synthetic strategy was developed for the direct step-growth polymerization of precisely defined protein-polymer constructs. The method uses a protein that was genetically engineered to have two azide functionalities at the desired locations, and a polymer with alkyne chain endings. Direct polymerization is realized by the “click” reaction of the azide and alkyne functionalities. This is the first demonstration of the application of step-growth polymerization methods to chain-extend site specifically functionalized proteins. The results clearly demonstrate that this novel, broadly applicable step-growth polymerization technique can be used for the synthesis of well-defined protein fibers. Due to the relative ease of encoding the amber codon into a wide

range of proteins and the mild conditions required for click chain extension reactions, we expect that this step-growth polymerization method can be employed to prepare a wide range of protein-polymer fibers for cell and tissue culture substrates.

As a proof of concept, we applied this method to polymerize diazide-GFP with dialkyne-PEO. The fibers retained GFP's fluorescent properties, as proven by confocal microscopy. AFM analysis showed that the fluorescent polymeric fibers are several micrometers in length and ~0.1 micrometers in width.

The presented results show that the GFP-PEO fibers exhibit self-assembly based on pairing, where the pairs are held together by hydrophobic interaction. The resulting aggregates are extended to linearity, but at the same time also obey Gaussian statistics, which ensures high flexibility. This is realized by the PEO chains, which behave as entropic springs, ensuring the necessary distance between the Janus-like GFP units, and also being able to bend without breaking. A helical structure allows for tighter packing and thus maximizes the contact between the GFP units. The asymmetry of the PEO attachment sites on the GFP monomers represent the chirality in the structure necessary for double helix formation.

This is a new form of self-assembly, and the significance of this structure is that other fibers of this persistence length break upon bending. Furthermore, due to having hydrophobic interaction as the driving force behind their self-assembly, these fibers are much easier to disassembly and reassembly than other, protein-based structures that are held together by H-bonds (e. g. peptide amphiphiles).

Furthermore, these results suggest that this zipper-like driven aggregation could be extended to other Janus-like particles held together by polymeric chains behaving as entropic springs.

Due to the biocompatibility of both building blocks, combined with GFP's easily detectable signal, the construct has potential applications in biomedical engineering. We envision that the fibers synthesized by this novel approach can be printed or weaved into, well-defined bio-articifical surfaces and matrices for tissue engineering applications. A pure aqueous solution could be injected at the site of an injury, where fibers could be formed *in situ*, as a result of the presence of Ca^{2+} in the extracellular matrix. The *in situ* formed fibers could facilitate the recovery of the damaged tissue, for example by guiding the growing capillaries during revascularization, or the axons of neural cells. As a consequence of GFP's fluorescence, formation of the fibers and their degradation could be followed *in vivo*.

4.5 References

1.Abuchowski, A.; McCoy, J. R.; Palczuk, N. C.; van Es, T.; Davis, F. F. (1977) Effect of covalent attachment of polyethylene glycol on immunogenicity and circulating life of bovine liver catalase. J. Biol Chem. 252, 3582-3586.

2.Hermanson, G. T., *Bioconjugate techniques*. Academic Press: San Diego, 1996; p xxv, 785 p.

3.Lele, B. S.; Murata, H.; Matyjaszewski, K.; Russell, A. J. (2005) Synthesis of uniform protein-polymer conjugates. Biomacromolecules 6, 3380-3387.

4.Lutz, J.-F.; Boerner, H. G. (2008) Modern trends in polymer bio-conjugates design. Prog. Polym. Sci. 33, 1-39.

5.Le Droumaguet, B.; Nicolas, J. (2010) Recent advances in the design of bioconjugates from controlled/living radical polymerization. Polymer Chemistry 1, 563-598.

6.Velonia, K. (2010) Protein-polymer amphiphilic chimeras: recent advances and future challenges. Polymer Chemistry 1, 944-952.

7.Bulmus, V. (2011) RAFT polymerization mediated bioconjugation strategies. Polymer Chemistry 2, 1463-1472.

8.Averick, S. E.; Magenau, A. J. D.; Simakova, A.; Woodman, B. F.; Seong, A.; Mehl, R. A.; Matyjaszewski, K. (2011) Covalently incorporated protein-nanogels using AGET ATRP in an inverse miniemulsion. Polymer Chemistry 2, 1476-1478.

9.Molineux, G. (2002) Pegylation: engineering improved pharmaceuticals for enhanced therapy. Cancer Treat. Rev. 28, 13-16.

10.Duncan, R. (2003) The dawning era of polymer therapeutics. Nat. Rev. Drug Discovery 2, 347-360.

11.Parveen, S.; Sahoo, S. K. (2006) Nanomedicine - Clinical applications of polyethylene glycol conjugated proteins and drugs. Clinical Pharmacokinetics 45, 965-988.

12.Jain, A.; Jain, S. K. (2008) PEGylation: An approach for drug delivery. A review. Crit. Rev. Ther. Drug Carrier Syst. 25, 403-447.

13.Finn, M. G.; Pokorski, J. K.; Breitenkamp, K.; Liepold, L. O.; Qazi, S. (2011) Functional Virus-Based Polymer-Protein Nanoparticles by Atom Transfer Radical Polymerization. J. Am. Chem. Soc. 133, 9242-9245.

14.Zhang, J. J.; Lei, Y. G.; Dhaliwal, A.; Ng, Q. K. T.; Du, J. J.; Yan, M.; Lu, Y. F.; Segura, T. (2011) Protein-Polymer Nanoparticles for Nonviral Gene Delivery. Biomacromolecules 12, 1006-1014.

15.Shi, W.; Dolai, S.; Averick, S.; Fernando, S. S.; Saltos, J. A.; L'Amoreaux, W.; Banerjee, P.; Raja, K. (2009) A General Methodology Toward Drug/Dye Incorporated Living Copolymer-Protein Hybrids: (NIRF Dye-Glucose) Copolymer-Avidin/BSA Conjugates as Prototypes. Bioconjugate Chemistry 20, 1595-1601.

16.Qian, H.; He, L. (2009) Detection of Protein Binding Using Activator Generated by Electron Transfer for Atom Transfer Radical Polymerization. Analytical Chemistry 81, 9824-9827.

17.Liu, Y.; Dong, Y.; Jauw, J.; Linman, M. J.; Cheng, Q. (2010) Highly Sensitive Detection of Protein Toxins by Surface Plasmon Resonance with Biotinylation-Based Inline Atom Transfer Radical Polymerization Amplification. Analytical Chemistry 82, 3679-3685.

i18.Schultz, P. G.; Chin, J. W.; Cropp, T. A.; Anderson, J. C.; Mukherji, M.; Zhang, Z. W. (2003) An expanded eukaryotic genetic code. Science 301, 964-967.

19.Schultz, P. G.; Deiters, A.; Cropp, T. A.; Summerer, D.; Mukherji, M. (2004) Site-specific PEGylation of proteins containing unnatural amino acids. Bioorg. Med. Chem. Lett. 14, 5743-5745.

20.Cho, H.; Daniel, T.; Buechler, Y. J.; Litzinger, D. C.; Maio, Z. W.; Putnam, A. M. H.; Kraynov, V. S.; Sim, B. C.; Bussell, S.; Javahishvili, T.; Kaphle, S.; Viramontes, G.; Ong, M.; Chu, S.; Becky, G. C.; Lieu, R.; Knudsen, N.; Castiglioni, P.; Norman, T. C.; Axelrod, D. W.; Hoffman, A. R.; Schultz, P. G.; DiMarchi, R. D.; Kimmel, B. E. (2011) Optimized clinical performance of growth hormone with an expanded genetic code. Proc. Natl. Acad. Sci. U. S. A. 108, 9060-9065.

21.Chen, C. S.; Mrksich, M.; Huang, S.; Whitesides, G. M.; Ingber, D. E. (1998) Micropatterned surfaces for control of cell shape, position, and function. Biotechnology Progress 14, 356-363.

22.Vasita, R.; Katti, D. S. (2006) Nanofibers and their applications in tissue engineering. International Journal of Nanomedicine 1, 15-30.

23.Li, M. Y.; Mondrinos, M. J.; Gandhi, M. R.; Ko, F. K.; Weiss, A. S.; Lelkes, P. I. (2005) Electrospun protein fibers as matrices for tissue engineering. Biomaterials 26, 5999-6008.

24.Rho, K. S.; Jeong, L.; Lee, G.; Seo, B. M.; Park, Y. J.; Hong, S. D.; Roh, S.; Cho, J. J.; Park, W. H.; Min, B. M. (2006) Electrospinning of collagen nanofibers: Effects on the behavior of normal human keratinocytes and early-stage wound healing. Biomaterials 27, 1452-1461.

25.Greiner, A.; Wendorff, J. H. (2007) Electrospinning: A fascinating method for the preparation of ultrathin fibres. Angewandte Chemie-International Edition 46, 5670-5703.

26.Le Droumaguet, B.; Velonia, K. (2008) In Situ ATRP-Mediated Hierarchical Formation of Giant Amphiphile Bionanoreactors. Angew. Chem., Int. Ed. 47, 6263-6266.

27.Lavigueur, C.; Garcia, J. G.; Hendriks, L.; Hoogenboom, R.; Cornelissen, J. J. L. M.; Nolte, R. J. M. (2011) Thermoresponsive giant biohybrid amphiphiles. Polymer Chemistry 2, 333-340.

28.Liu, T.; Teng, W. K.; Chan, B. P.; Chew, S. Y. (2010) Photochemical crosslinked electrospun collagen nanofibers: Synthesis, characterization and neural stem cell interactions. Journal of Biomedical Materials Research Part A 95A, 276-282.

29.Delaittre, G.; Reynhout, I. C.; Cornelissen, J. J. L. M.; Nolte, R. J. M. (2009) Cascade Reactions in an All-Enzyme Nanoreactor. Chemistry-a European Journal 15, 12600-12603.

30.Reynhout, I. C.; Cornelissen, J. J. L. M.; Nolte, R. J. M. (2009) Synthesis of Polymer-Biohybrids: From Small to Giant Surfactants. Accounts of Chemical Research 42, 681-692.

31.Golas, P. L.; Matyjaszewski, K. (2007) Click chemistry and ATRP: a beneficial union for the preparation of functional materials. QSAR Comb. Sci. 26, 1116-1134.

32.Golas, P. L.; Matyjaszewski, K. (2010) Marrying click chemistry with polymerization: expanding the scope of polymeric materials. Chem. Soc. Rev. 39, 1338-1354.

33.Averick, S.; Paredes, E.; Li, W.; Matyjaszewski, K.; Das, S. R. Direct DNA Conjugation to Star Polymers for Controlled Reversible Assemblies. Bioconjugate Chem., ACS ASAP.

34.Agut, W.; Taton, D.; Lecommandoux, S. (2007) A versatile synthetic approach to polypeptide based rod-coil block copolymers by click chemistry. Macromolecules 40, 5653-5661.

35.Siegwart, D. J.; Oh, J. K.; Gao, H. F.; Bencherif, S. A.; Perineau, F.; Bohaty, A. K.; Hollinger, J. O.; Matyjaszewski, K. (2008) Biotin-, Pyrene-, and GRGDS-Functionalized Polymers and Nanogels via ATRP and End Group Modification. Macromolecular Chemistry and Physics 209, 2180-2193.

36.Skwarczynski, M.; Zaman, M.; Urbani, C. N.; Lin, I. C.; Jia, Z. F.; Batzloff, M. R.; Good, M. F.; Monteiro, M. F.; Toth, I. (2010) Polyacrylate Dendrimer Nanoparticles: A Self-Adjuvanting Vaccine Delivery System. Angewandte Chemie-International Edition 49, 5742-5745.

37.Kolb, H. C.; Finn, M. G.; Sharpless, K. B. (2001) Click chemistry: Diverse chemical function from a few good reactions. Angewandte Chemie-International Edition 40, 2004-2021.

38.Raja, K. S.; Wang, Q.; Gonzalez, M. J.; Manchester, M.; Johnson, J. E.; Finn, M. G. (2003) Hybrid virus-polymer materials. 1. Synthesis and properties of PEG-decorated cowpea mosaic virus. Biomacromolecules 4, 472-476.

39.Sen Gupta, S.; Raja, K. S.; Kaltgrad, E.; Strable, E.; Finn, M. G. (2005) Virus-glycopolymer conjugates by copper(I) catalysis of atom transfer radical polymerization and azide-alkyne cycloaddition. Chemical Communications, 4315-4317.

40.Shi, W.; Dolai, S.; Rizk, S.; Hussain, A.; Tariq, H.; Averick, S.; L'Amoreaux, W.; El Ldrissi, A.; Banerjee, P.; Raja, K. (2007) Synthesis of monofunctional curcumin derivatives, clicked curcumin dimer, and a PAMAM dendrimer curcumin conjugate for therapeutic applications. Organic Letters 9, 5461-5464.

41.Dolai, S.; Shi, W.; Corbo, C.; Sun, C.; Averick, S.; Obeysekera, D.; Farid, M.; Alonso, A.; Banerjee, P.; Raja, K. (2011) “Clicked” Sugar–Curcumin Conjugate: Modulator of Amyloid-β and Tau Peptide Aggregation at Ultra low Concentrations. ACS Chemical Neuroscience.

42.de Graaf, A. J.; Kooijman, M.; Hennink, W. E.; Mastrobattista, E. (2009) Nonnatural Amino Acids for Site-Specific Protein Conjugation. Bioconjugate Chemistry 20, 1281-1295.

43.Greiss, S.; Chin, J. W. (2011) Expanding the Genetic Code of an Animal. Journal of the American Chemical Society 133, 14196-14199.

44.Neumann, H.; Wang, K. H.; Davis, L.; Garcia-Alai, M.; Chin, J. W. (2010) Encoding multiple unnatural amino acids via evolution of a quadruplet-decoding ribosome. Nature 464, 441-444.

45.Miyake-Stoner, S. J.; Miller, A. M.; Hammill, J. T.; Peeler, J. C.; Hess, K. R.; Mehl, R. A.; Brewer, S. H. (2009) Probing protein folding using site-specifically encoded unnatural amino acids as FRET donors with tryptophan. Biochem. 48, 5953-5962.

46.Bontempo, D.; Heredia, K. L.; Fish, B. A.; Maynard, H. D. (2004) Cysteine-reactive polymers synthesized by atom transfer radical polymerization for conjugation to proteins. Journal of the American Chemical Society 126, 15372-15373.

47.Golas, P. L.; Tsarevsky, N. V.; Sumerlin, B. S.; Walker, L. M.; Matyjaszewski, K. (2007) Multisegmented block copolymers by 'click' coupling of polymers prepared by ATRP. Australian Journal of Chemistry 60, 400-404.

48.http://www-bioc.rice.edu/Bioch/Phillips/Papers/gfpbio.html

49. Kyte J, Doolittle, R. F. *J Mol Biol.* **1982**, *157*(1), 105-32.

50. Rubinstein, M. and Colby, R. H. Polymer Physics, 3rd ed.; Oxford University Press: New York, 2005.

CHAPTER 5

QUANTIFICATION OF TIP - SAMPLE FORCES ON AND BELOW RESONANCE IN TAPPING-MODE ATOMIC FORCE MICROSCOPY

5.1 Introduction

Over the last two decades, tapping mode imaging has become a powerful tool to map the topography and mechanical properties of soft systems such as polymers, fragile nanostructures and biological samples [1]. Although the force in tapping mode is relatively low compared to other AFM operation modes, even this force is high enough to produce mechanical artifacts [2-7]. Under certain circumstances, these artifacts could be used to produce additional contrast, e.g. compliance contrast [8] [9] [10]. A better understanding of tip-sample forces may also help in the elimination of undesirable artifacts.

To date, the question of the dependence of tip-sample force on AFM imaging conditions has been addressed only to a limited degree, most notably in the work by Garcia and co-workers, who have derived the expression for the average tip-sample force for on-resonance operation [11] [1]. There is also a mention of "empirical" relationship for operation below resonance in the paper co-authored by one of us [9]. The purpose of the present study was to provide a full description of how the aforementioned relationship between tip-sample force and imaging conditions can be inferred from computer simulations, and to demonstrate its general validity through the derivation of an analytical solution. The expression for the average tip-sample force given in Eq. 3 was also presented in the thesis of Brian Cusick, former graduate student in the Kowalewski group, but the derivation presented herein was done independently from his work.

5.2 The physical model of the system

The model used throughout this study treats the oscillating cantilever as a single degree of freedom system, described by the tip position *z(t)*, which also corresponds to the distance of the tip from the surface (Figure 1). The cantilever is attached to the base positioned at the average height z_o

above the surface, and its oscillatory motion is sustained by vertical harmonic oscillation of the base around z_o with amplitude a_o and angular frequency ω. The tip interacts with the surface with force $F_{ts}(z(t))$. The primary objective of this study was to determine the dependence of this force on key parameters relevant to tapping mode AFM imaging conditions, such as tip oscillation amplitude and frequency. The motion of the tip in the presence of force F_{ts} is described by the familiar driven damped harmonic oscillator equation:

$$mz''(t) + bz'(t) + k\{z(t) - [z_o + a_o\cos(\omega t)]\} = F_{\mathrm{ts}}(z(t)) \qquad (1)$$

where the effective mass of the cantilever $m = \frac{k}{\omega_o^2}$, k is the cantilever spring constant, ω_o is the natural frequency of the cantilever, the damping factor $b = \frac{k}{Q\omega_o}$, and Q is the quality factor. The driving force needed to sustain the oscillation is incorporated into the model in the third term on the left hand side of Equation 1, which corresponds to the elastic force arising from the difference between the tip position and base position.

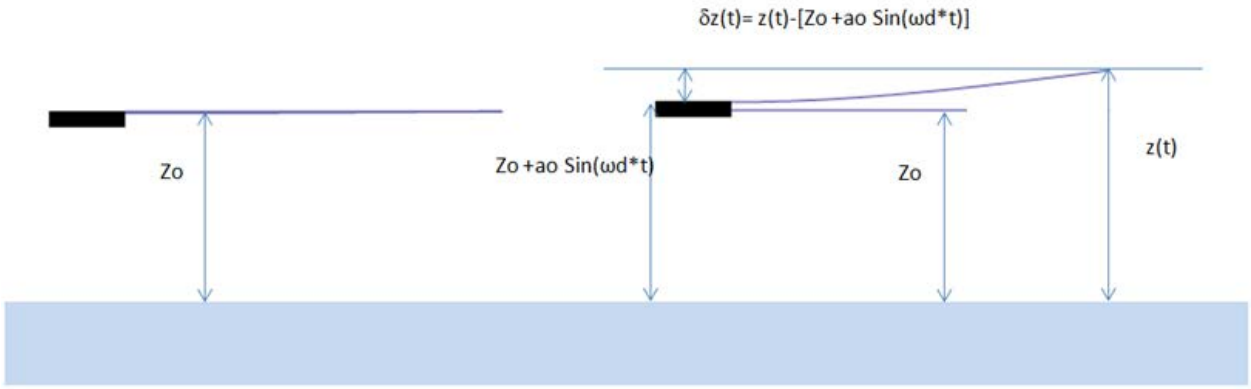

Figure 5.2.1: Piezo-actuated AFM cantilever modeled as driven damped harmonic oscillator.

5.3 Results

5.3.1 Analytical model

In seeking analytical expression for the average tip –sample force $<F_{ts}>$, as a point of departure we will use the single-mode, single degree of freedom driven damped harmonic oscillator model which will be explored in the next section through the numerical solution of equation 1. Far away from the surface, (i.e. under conditions when F_{ts}=0, the position of the tip would be described by the familiar solution

$$z(t) = z_o + A\cos(\omega t + \phi) \tag{5}$$

Simple inspection shows immediately that the solution in this form is inappropriate in the presence of tip-sample interaction, since it would imply that the average of tip sample force over each oscillation cycle equals to zero. It can be easily shown that the physically meaningful harmonic approximation of the solution can be obtained by switching from the laboratory frame of reference to a frame with origin at the current base position, in which the coordinate *q(t)* corresponds to the deflection of the cantilever.

$$q(t) = z(t) - (z_o + a_o\cos(\omega t) \tag{6}$$

with the anticipated solution given in the form

$$q(t) = q_o + A_d\cos(\omega t + \phi) \tag{7}$$

It can be now checked that substituting Equations 6 and 7 into the left hand side of the equation of motion (Equation 1) gives the time-dependent tip-sample force.

$$F_{\mathrm{ts}} = -2m\gamma\omega[a_o\sin(\omega t) + A_d\sin(\omega t + \phi)] + \tag{8}$$

$$k[A_d\cos(\omega t+\phi)+q_o]$$

$$-\frac{k\omega^2[a_o\cos(\omega t)+A_d\cos(\omega t+\phi)]}{\omega_o^2}$$

The fact that the harmonic oscillation within the oscillating base frame (Equation 8) is indeed appropriate for non-vanishing tip-sample forces, becomes apparent after computing the average value of the tip-sample force over one oscillation period $(\tau, \tau+\frac{2\pi}{\omega})$:

$$< F_{\text{ts}} >= \frac{1}{\frac{2\pi}{\omega}}\int_{\tau}^{\tau+\frac{2\pi}{\omega}} RHS\, dt = k\, q_o \tag{9}$$

In addition to providing the physically meaningful form of harmonic solution of the cantilever tip motion, the use of the cantilever deflection as a coordinate describing its motion offers another advantage. Namely, this allows one to immediately connect the obtained solutions to the physical measurements performed with the typical AFM set-up, in which the cantilever motion is monitored by measuring its deflection. In particular, the cantilever deflection amplitude A_d can now be directly related to the oscillation amplitude, used in tapping mode AFM as a surface tracking signal.

Since integration of the RHS of Equation 8 plugged into Equation 1 gives only the average cantilever deflection q_o, one needs to consider additional physics to find the equation describing dependence of q_o on oscillation frequency and amplitude, which would yield the information similar to one inferred from computer simulations in the previous section. This dependency will be sought using the combination of virial equation and energy conservation, analogous to one described in the past in seminal papers by Cleveland et al. [15] and Garcia et.al [11].

At this point it should be emphasized that the description of the harmonic oscillation of the cantilever in terms of its deflection rather than position (Equation 1) is equivalent to the use of a non-inertial frame of

reference (harmonically oscillating cantilever base). This gives rise to the appearance of inertial forces, which need to be included in rigorous virial and energy balance analysis, and were not always accounted for in the earlier harmonic models of AFM described in literature. To avoid this problem, all calculations described from this point on will be performed by transforming back to the fixed laboratory frame using relationships between *q(t)* and *z(t)* given by Equations 6 and 7. For a single degree of freedom periodically oscillating system such as the one considered here, the virial equation [16], which relates the average kinetic energy $<E_k>$ to the average work performed by all the external forces *F(t)* over some path *z(t)* can be written the form

$$\langle E_k \rangle = -\frac{1}{2}\langle F\ (t) z(t) \rangle \tag{10}$$

[11], with the averaging indicated by <> brackets performed over one oscillation cycle. Inspection of the main equation of motion (Equation 1) indicates that the external forces which need to be considered are given by the sum:

$$F(t) = -bz'(t) - k(z(t) - (\mathrm{zo} + a_o \cos(\omega t))) + F_{\mathrm{ts}}(t) \tag{11}$$

The average kinetic energy, described in the laboratory frame, is then given by

$$\langle E_{kin} \rangle = \langle \frac{mz'(t)^2}{2} \rangle \tag{12}$$

which after substituting the harmonic deflection solution transformed to laboratory frame (Equation 6) and performing the integration gives

$$\langle E_{kin} \rangle = \frac{ka_o^2\omega^2}{4\omega_o^2} + \frac{ka_o A_d \cos(\phi)\omega^2}{2\omega_o^2} + \frac{kA_d^2\omega^2}{4\omega_o^2} \tag{13}$$

It can be easily shown that, for a high quality factor *Q* system such as a tapping mode cantilever, $A_d >> a_o$, and thus the first two terms in Equation 13 can be ignored, leading to the approximation

$$\langle E_{kin} \rangle \approx \frac{1}{4} m A_d^2 \omega^2 \tag{14}$$

The virial term can be determined in a similar manner by substituting the solution for the cantilever deflection into Equation 12 and performing the integration, yielding

$$Evirial = \tag{15}$$

$$-\frac{1}{2} k a_o A_d \cos(\phi) - \frac{k A_d^2}{2} - k q_o^2 - k q_o z_o + < F_{\mathrm{ts}}(t) z(t) >$$

Combining Equations 10, 14 and 15 and solving for $\cos(\phi)$, one then gets

$$\cos(\phi) = \frac{2 < F_{\mathrm{ts}}(t) z(t) >}{k a_o A_d} - \frac{A_d}{a_o} - \frac{2 q_o^2}{a_o A_d} - \frac{2 q_o z_o}{a_o A_d} + \frac{A_d \omega^2}{a_o \omega_o^2} \tag{16}$$

We now note that, given the fact that tip sample force F_{ts} is nonzero only over a small portion of the oscillation cycle, when the cantilever is in the vicinity of the sample (see Figure 8), the integral describing the work performed by the tip-sample force can be approximated as

$$< F_{\mathrm{ts}}(t) z(t) > = < F_{\mathrm{ts}} > z_{\min} \tag{17}$$

where z_{min} is equal to the value of position during tip-sample encounter, i.e. at the bottom of the oscillation cycle

$$z_{\min} = \mathrm{Min}[a_o \cos(\omega t) + A_d \cos(\omega t + \phi) + q_o + z_o] \tag{18}$$

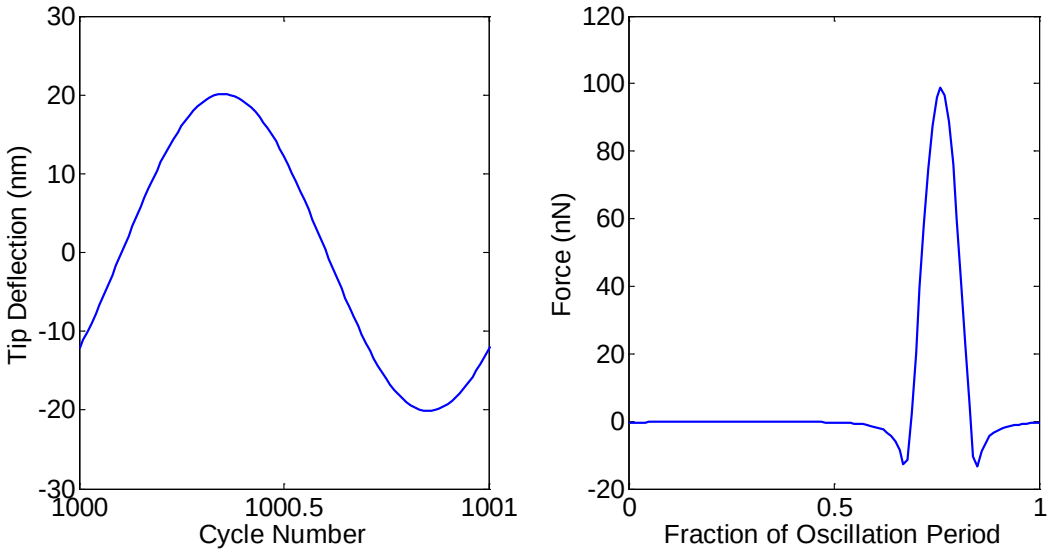

Figure 5.3.1.1: Changes in deflection and tip-sample force over two oscillation cycles with A = 20 nm, k = 50 N/m, β = 5.

The first term oscillating with amplitude a_o can be neglected based on a similar argument as before, leaving

$$z_{\min} = A_d \cos(\phi + t\omega) + q_o + z_o \tag{19}$$

Now we should note another important feature of tapping mode: the deflection amplitude is equal to z_o. We use this to replace z_o

$$z_{\min} = A_d + A_d \cos(\phi + t\omega) + q_o \tag{20}$$

It is trivial to note that this term is at the minimum when the A_d terms cancel out, i.e.:

$$z_{\min} = q_o \tag{21}$$

Substituting Equation 21 this into the solution for $\cos(\phi)$ and recalling that $z_o = A_d$ We then obtain:

$$\cos(\phi) = -\frac{A_d}{a_o} - \frac{2q_o}{a_o} + \frac{A_d\omega^2}{a_o\omega_o^2} \tag{22}$$

As shown earlier by Cleveland et al, the expression for *sin(ϕ)* can be obtained by considering the energy delivered by the excitation force $\langle E_{drive}\rangle$ over one oscillation cycle

$$\langle E_{drive}\rangle = < kq(t)[z_o + a_o\cos(\omega t)]' > = \frac{1}{2}ka_oA_d\sin(\phi)\omega \tag{23}$$

and the energy dissipated by the viscous force

$$\langle E_{dissV}\rangle = < bz'(t)z'(t) > \tag{24}$$

$$= \frac{ka_o^2\omega^2}{2Q\omega_o} + \frac{ka_oA_d\cos(\phi)\omega^2}{Q\omega_o} + \frac{kA_d^2\omega^2}{2Q\omega_o}$$

which can be truncated to the third term based on arguments used before, giving

$$\langle E_{dissV}\rangle \approx \frac{kA_d^2\omega^2}{2Q\omega_o} \tag{25}$$

The average energy dissipated by the tip-sample interaction, $<E_{diss}>$, will be then given by subtracting $\langle E_{drive}\rangle$-$\langle E_{dissV}\rangle$, yielding

$$< E_{diss} > = \frac{kA_d^2\omega^2}{2Q\omega_o} - \frac{1}{2}ka_oA_d\sin(\phi)\omega - \frac{kA_d^2\omega^2}{2Q\omega_o} \tag{26}$$

Solution for $sin(\phi)$is then obtained as

$$\sin(\phi) = \frac{2 < E_{\text{diss}} >}{ka_oA_d\omega} + \frac{A_d\omega}{Qa_o\omega_o} \tag{27}$$

which In the absence of energy dissipation in tip-sample interaction reduces to

$$\sin(\phi) = \frac{A_d \omega}{Q a_o \omega_o} \tag{28}$$

Solutions for $sin(\phi)$and $cos(\phi)$ can be now combined to find q_o, and, in accordance with Equation 9, the final expression for the average tip-sample force as a function of operating parameters:

$$< F_{\text{ts}} >= -\frac{kA_d}{2} + \frac{k\sqrt{Q^2 a_o^2 {\omega_o}^2 - A_d^2 \omega^2}}{2Q\omega_o} + \frac{kA_d\omega^2}{2\omega_o^2} \tag{29}$$

As shown below, through additional approximations valid for operation off resonance, this equation can be expressed in a particularly useful form which relates <F_{ts}> to the ratio $\frac{\Delta A}{A_o}$, where $\Delta A = A_o - A_d$ and $A_o$denotes the deflection oscillation amplitude far away from the surface (free oscillation amplitude).

For a high Q system the deflection oscillation amplitude away from the surface Ao can be approximated with the well-known solution for a driven damped harmonic oscillator

$$A_{\text{o}} = \frac{a_o \omega_o^2}{\sqrt{(\omega^2 - \omega o^2)^2 + \frac{\omega^2 \omega_o^2}{Q^2}}} \tag{30}$$

which in the limit $Q \to \infty$ can be solved for ω_o giving

$$\omega_o = \frac{\sqrt{A_o}\omega}{\sqrt{-a_o + A_o}} \tag{31}$$

Substituting this into the equation gives

$$< F_{\mathrm{ts}} > \approx \frac{1}{2}k\left(\frac{\sqrt{Q^2 a_o^2 {\omega_o}^4 - A_d^2 \omega^2 {\omega_o}^2}}{Q{\omega_o}^2} - \frac{a_o A_d}{A_o}\right) \tag{32}$$

Taking the limit $Q \to \infty$:

$$< F_{\mathrm{ts}} > \approx \lim_{Q\to\infty}\left[\frac{1}{2}k\left(\frac{\sqrt{Q^2 a_o^2 {\omega_o}^4 - A_d^2 \omega^2 {\omega_o}^2}}{Q{\omega_o}^2} - \frac{a_o A_d}{A_o}\right)\right] \tag{33}$$

$$= \frac{1}{2}k a_o \frac{\Delta \mathrm{A}}{A_o}$$

The above derivation confirms earlier results published by our group, where Equation 23 for average tip-sample force resulted from simulations of tapping mode imaging far below resonance [17].

Effective mass models emerge as approximations from contact mechanics. The model described in this paper is *ad hoc* in the sense that it lacks this background. However, it improves on the widely used model of Garcia et al. According to their model, the force would be dependent on the position of the tip, which is incorrect and leads to an extra term $k_c\langle z\rangle$ in the expression for the tip-sample force. By making the assumption that the average deflection is much smaller than the oscillation amplitude, this term becomes negligible, which gives the correct result, but is not necessarily true. Therefore, in the model described in this paper, deflection is considered instead of position.

Also, existing models, including the widely used model of Garcia et al., are usually restricted to the case of resonance. However, driving below resonance has a wide range of applicability (replacing active *Q* control, just to name one). Therefore, in the current work, zero energy dissipation is assumed in the derivation of *sin(ϕ)* instead. This assumption is reasonable

for high Q systems (e.g. imaging in tapping mode in air). Comparison with the results of the numerical simulations is shown in Figure 5.3.1.2.

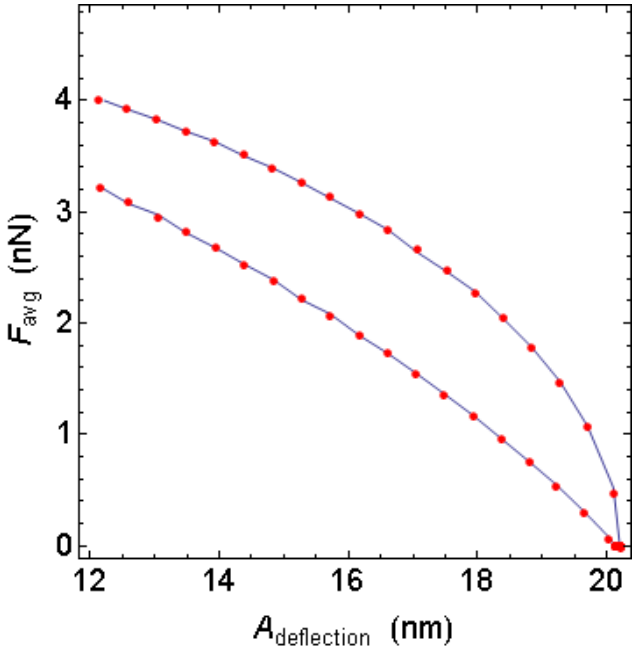

Figure 5.3.1.2: Comparison of the average force values given by the simulation (blue curves) and predicted by the analytical model (red dots) at k = 50 N/m and A = 10 nm, as a function of deflection amplitude, at $AH = 10^{-21}$J, on resonance and 10% below it. The upper curve shows the case of resonance; 10% below resonance the average force is already almost a linear function of the amplitude (lower curve).

The final expression for tip-sample force can be expressed in terms of set-point ratio $\alpha = \frac{A}{A_o}$ and reduced frequency β. As a starting point, we can use the solution for oscillation amplitude of a free damped oscillator:

$$A = \frac{a_o {\omega_o}^2}{\sqrt{\frac{\omega^2 \omega o^2}{Q^2} + (\omega^2 - {\omega_o}^2)^2}} \tag{34}$$

For operation on resonance, the value of this amplitude is a_oQ. Now let us define the frequency in terms of that value of parameter β for which the oscillation amplitude would be βA_{res}. Keeping that solution of the fourth-order equation that is physical for operation below resonance, the reduced frequency $\frac{\omega}{\omega_o}$ is given as

$$\omega_{\text{red}} = \frac{\sqrt{Q^2 - \frac{\beta + \sqrt{\beta^2 - 4Q^2(-1+\beta^2)}}{2\beta}}}{Q} \tag{35}$$

Substituting this into the final expression for the tip-sample force (Equation NUMBER) gives

$$F_{\text{ts}} \tag{36}$$
$$= -\frac{1}{4Q^2\beta} k(A_d(\beta + \sqrt{\beta^2 - 4Q^2(-1+\beta^2)})$$
$$- \sqrt{2}\sqrt{\beta}\sqrt{2{a_o}^2 Q^4 \beta + {A_d}^2(\beta - 2Q^2\beta a + \sqrt{\beta^2 - 4Q^2(-1+\beta^2)})})$$

Expressing the oscillation amplitude in terms of ratio α, with A_o equal to the free oscillation amplitude and substituting $\text{ao} = \frac{\text{Ao}}{Q\beta}$ for drive amplitude:

$$F_{\text{ts}} \tag{37}$$

$$= -\frac{1}{4Q^2\beta}k(A_o\alpha(\beta + \sqrt{\beta^2 - 4Q^2(-1+\beta^2)})$$

$$-\sqrt{2}\sqrt{\beta}\sqrt{\frac{2{A_o}^2Q^2}{\beta} + \mathrm{Ao}^2\alpha^2(\beta - 2Q^2\beta + \sqrt{\beta^2 - 4Q^2(-1+\beta^2)})})$$

For high quality systems, dividing out the common term dependent on cantilever properties and oscillation amplitude, $\frac{\mathrm{Ao}k}{Q^2}$, we get the normaliyed force, depending only on α and β:

$$F_{\text{ts}} = \frac{A_o k}{2Q}F_{\text{red}} \tag{38}$$

Where F_{red} is defined as

$$F_{\text{red}} = (-\alpha\sqrt{-1 + \frac{1}{\beta^2}} + \sqrt{-\alpha^2 + \frac{1}{\beta^2}}) \tag{39}$$

Far below resonance:

$$F_{\text{redOff}} = \frac{(1-\alpha)}{\beta} \tag{40}$$

And the tip-sample force:

$$F_{\text{tsOff}} = \frac{A_o k}{2Q}F_{\text{redOff}} \tag{41}$$

By substituting the expressions for α, β, and $A_{d,}$ it can be shown that this equation is identical to the one given before (Equation 33)

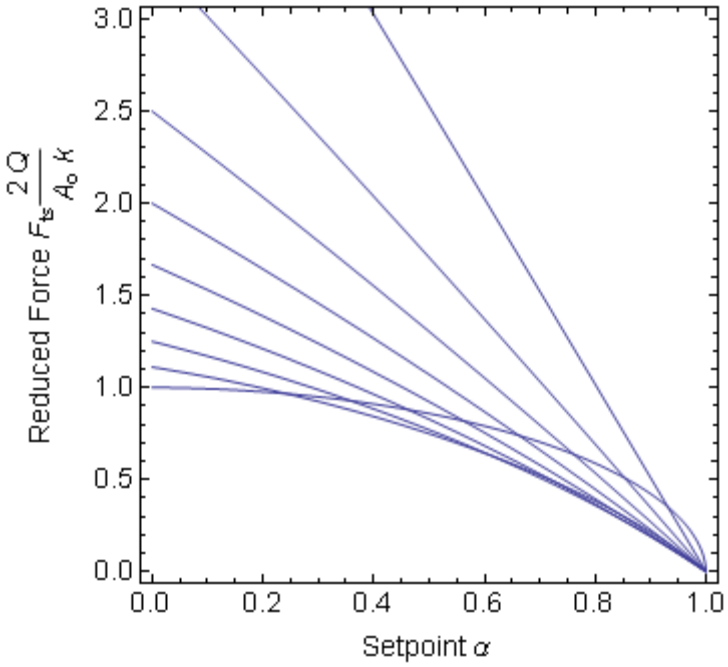

Figure 5.3.1.3: Reduced force as a function of setpoint for different values of reduced frequency.

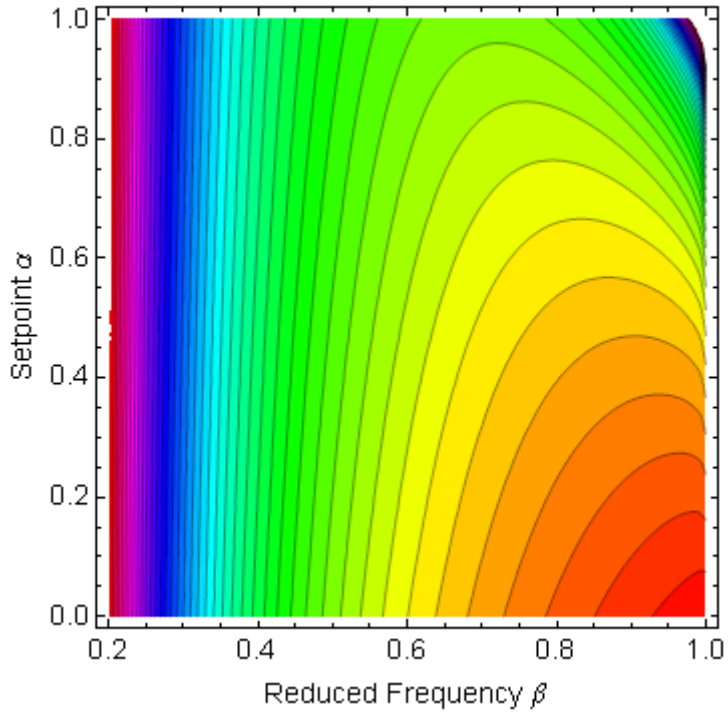

Figure 5.3.1.4: Effective cantilever stiffness as a function of setpoint and reduced frequency.

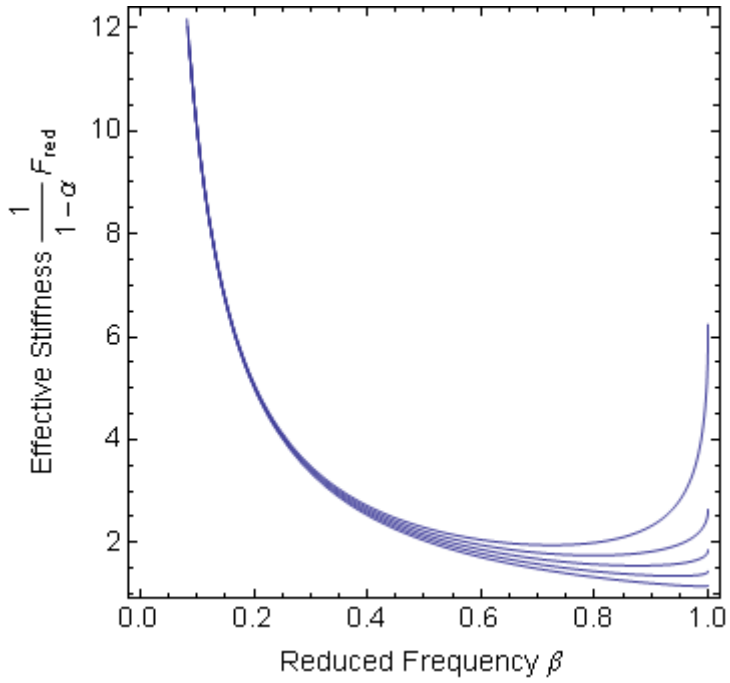

Figure 5.3.1.5: Effective stiffness $\frac{F_{red}}{1-\alpha}$ as a function of reduced frequency for different setpoint values.

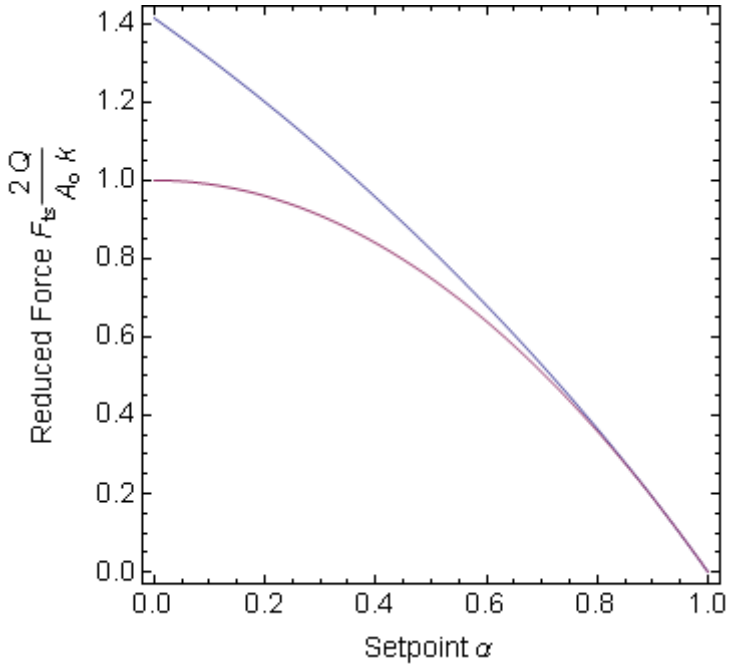

Figure 5.3.1.6: Reduced force at optimal coditions (minimal effective stiffness).

5.3.2 Numerical simulations

Numerical simulations were performed by solving Equation 1 numerically with MATLAB and SIMULINK (MathWorks Inc., Natick, MA). The tip-sample force was approximated based on the Derjaguin-Muller-Toporov (DMT) model [12,13]:

$$F_{\mathrm{ts}} = \begin{cases} -\frac{AHR_{\mathrm{tip}}}{6\,z^2} & z > a_{\mathrm{D}} \\ \frac{4}{3\pi\kappa_{\mathrm{eff}}}\sqrt{R_{\mathrm{tip}}}(a_{\mathrm{D}}-z)^{\frac{3}{2}} - \frac{AHR_{\mathrm{tip}}}{6\,{a_{\mathrm{D}}}^2} & z \le a_{\mathrm{D}} \end{cases} \quad (2)$$

In this model the tip is treated as a spherical nanoscopic object with radius R_{tip} , which for distances

$z > a_{\mathrm{D}}$ interacts with the surface through an attractive van der Waals force, the magnitude of which is governed by the Hamaker constant *AH* [14]. For distances $z \le a_{\mathrm{D}}$ the attractive term remains fixed, and the repulsive interaction is decribed using the Hertz indentation model for a spherical indenter with radius R_{tip} and the force proportional to the *(indentation depth)*$^{3/2}$, i.e. $(a_{\mathrm{D}}-z)^{\frac{3}{2}}$. Mechanical properties of the tip and the surface are accounted for by the term

$$\kappa_{\mathrm{eff}} = \frac{1-{\nu_t}^2}{\pi E_t} + \frac{1-{\nu_s}^2}{\pi E_s} \quad (3)$$

where E_t, ν_t and E_s, ν_s are, respectively, the Young's modulus and Poisson coefficient of the tip and the sample.

Equation 1 with such described tip-sample interaction was solved numerically using fixed step first order Runge-Kutta method, with the time step always chosen to be equal to 1/100th of an oscillation period $\frac{2\pi}{\omega}$, to facilitate comparison of results obtained for different frequencies. In each simulation run, the cantilever assembly was initially positioned away from the surface at base position z_0 chosen to be at least twice the target deflection amplitude, assuring that at the beginning of the simulation run the tip interaction with the surface was negligible. The cantilever base position z_0 was then lowered toward the surface at a constant rate, down to the height for which the oscillation amplitude decreased to zero. The direction of base height motion was then reversed, raising it back to the original position. Such simulation scheme directly corresponds to the so-called force curve (or more appropriately amplitude curve) experiment, used to calibrate the AFM cantilever deflection detector. The magnitude of the approach/withdrawal rate was chosen in such a way as to allow the transients arising from damping to decay away and reach the quasi-steady state. This was accomplished by setting the entire approach/withdrawal cycle to last for 10^5 oscillation cycles or 1 s, making it comparable with typical approach-withdraw rates used in tapping mode AFM calibration experiments.

To explore the role of cantilever oscillation frequency, the simulations were carried out for base oscillation frequencies ω which were chosen based on the condition $A_d(\omega) = \beta A_o(\omega_o)$, with A_d referring to „free" deflection oscillation amplitude, and the dimensionless „off resonance parameter" $0 < \beta \leq 1$ providing the measure of how far below resonance the oscillation was performed.

In order to investigate the role of deflection amplitude and cantilever spring constant, the calculations were performed for a range of k and A_0 shown in Table 1, which also shows the values

of other parameters, which were all chosen to correspond to the values encountered under typical AFM imaging conditions.

Parameter (unit)	Applied values
A_0 (nm)	20, 10, 5
k_c (N/m)	50, 20, 10, 5
β	0.1, 0.2, 0.3, 0.4, 0.5, 0.6, 0.7, 0.8, 0.9, 1.0
R_{tip} (nm)	50
E_{tip} (N/m^2)	$200*10^9$
E_{sample} (N/m^2)	$200*10^9$
ν_{tip}	0.3
ν_{sample}	0.3
a_D (nm)	0.4
Q	100
AH (J)	10^{-21}, $5*10^{-20}$

Table 5.3.2.1: Parameters used in the simulation.

The typical output of the simulation in the form of tip position trajectory *z(t)* is shown in Figure 5.3.2.1. Since the plot covers the time range shows the changes in the tip position over 300000 oscillation cycles and on this scale, single cycles cannot be resolved. The initial transient very first

portion of It is clear that after turning on the cantilever motion, the transient dies out very quickly. This indicates that the experiment was started sufficiently high above the surface, because the transient is expected to die out well before the cantilever comes into contact with the sample. This is a graphical representation of the oscillation cycle envelope, with the upper limit corresponding to tip position at the top of oscillation cycle, and the lower bondary corresponding to the lowest point. The distance betw these two remains nearly constant, which means that the position amplitude initially remains constant, then increases as a result of the attractive force between the cantilever and the surface, followed by a linear decrease caused by tip-surface repulsion. It is worth noting that the maximum is less pronounced for stiffer cantilevers. During the decrease, the tip position at the bottom of each oscillation cycle remains nearly fixed. In a real experiment, the tip-sample force might be high enough for the tip to indent deeper and deeper into the surface. However, in our simulations, a silicon tip and substrate was considered, and for such hard surfaces this indentation was barely noticeable. As a matter of fact, this linear decrease of oscillation amplitude is the basis of tapping mode, because it can be used to sense the proximity of the tip to the surface. Typical AFM operation involves setting this value to constant and scanning the surface ensuring that it remains constant (constant amplitude operation).

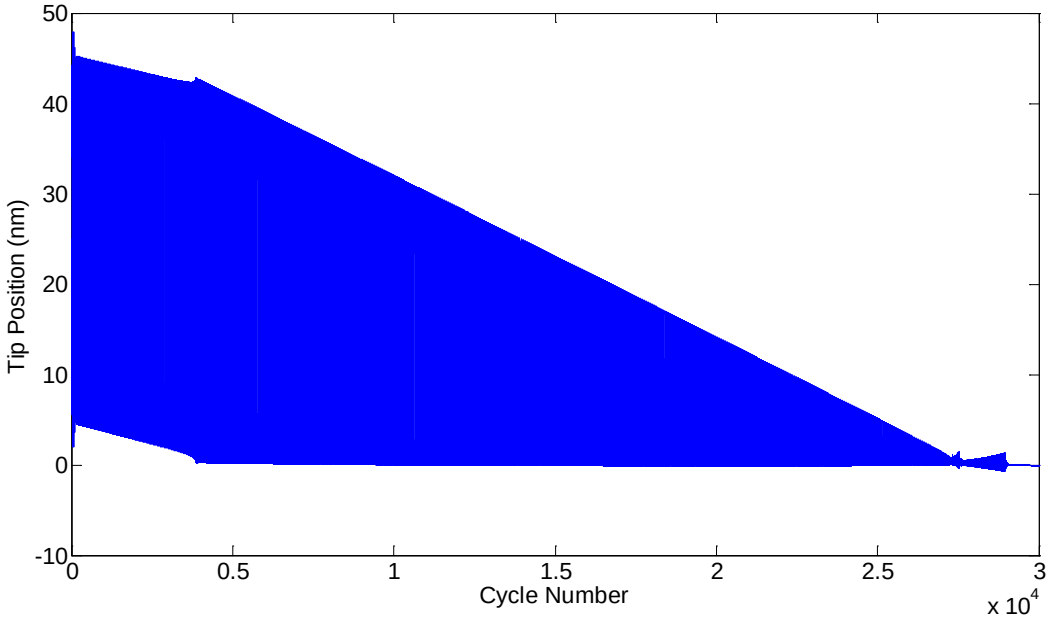

Figure 5.3.2.1: Changes in tip position over the first 30 000 cycles when driving the cantilever (k = 10 N/m) 40% below resonance, at A_d = 20 nm.

So far the system was considered in an external laboratory frame, to demonstrate how the tip is lowered to the surface. Switching to another coordinate system that moves along with the cantilever base, introduces an internal non-inertial frame in which cantilever motion is described in terms of deflection $q(t) = z(t) - [z_o + a_o \cos(\omega\, t)]$ rather than position (Figure 5.3.2.2). This choice of reference frame is more appropriate, since typical AFM detectors monitor cantilever deflection, and for the oscillating cantilever, the deflection amplitude.

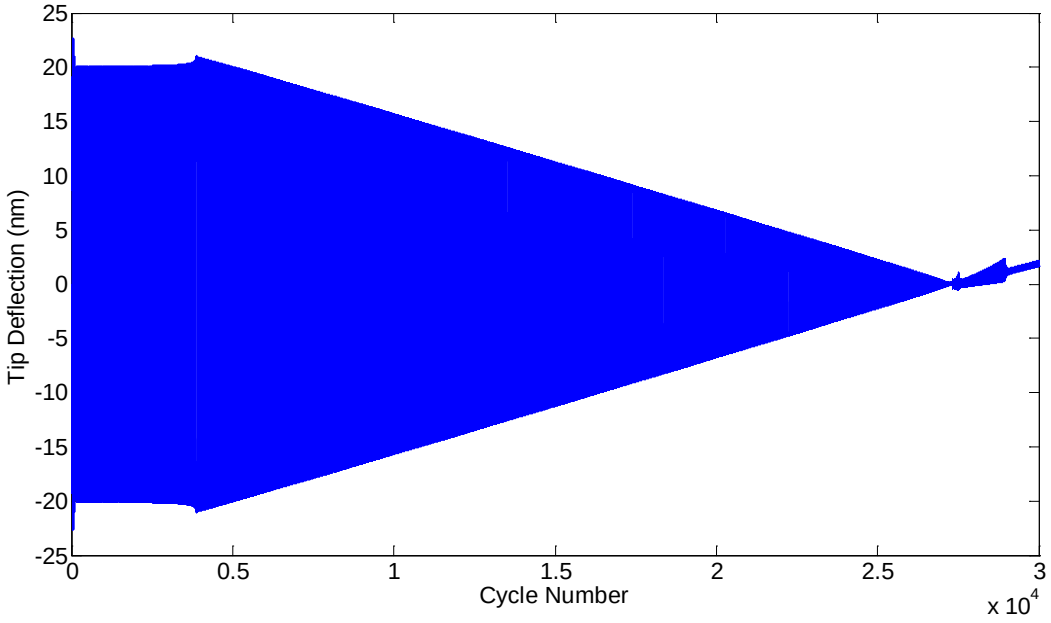

Figure 5.3.2.2: Changes in cantilever deflection over the first 30 000 cycles when driving the cantilever (k = 10 N/m) 40% below resonance, at A_d = 20 nm.

The average cantilever deflection amplitude A was computed using a sliding window as A_d=½ (q_{max}-q_{min}), where q_{max} and q_{min} are, respectively, the highest and lowest values of deflection within the window. The width of the window was set to be equal to one oscillation cycle, and the window was advanced by the same amounts eliminating any overlap.

The dependence of such calculated deflection amplitude on base position is plotted as a red trace in Figure 5.3.2.3**:** changes in tip position are shown over the first 30 000 cycles when driving the cantilever (k = 10 N/m) 40% below resonance, at A_d = 20 nm.

To illustrate the effect of deflection amplitude on the tip sample force, Figure 5.3.2.3 includes also the insets, which show the instantaneous tip-sample force F_{ts} for to different values of deflection amplitude indicated by the arrows. The leftmost inset shows the tip-sample force in purely non-

contact regime, before the tip begins to strike the surface. Within one oscillation cycle the force is purely attractive (negative), and its magnitude increases and then decreases as the tip moves toward and then away from the surface at the bottom of the oscillation cycle. Once the The forceIt can be seen that upon approach to the surface the force is initially purely attractive negativ Comparison of these insets points to the marked increase of tip-sample force with the decrease of A_d,in accordance with the general notion that decreasing the value of set-point amplitude A_d in tapping leads to „hard" tapping.

The insets also illustrate that prior to direct contact, the force is always attracitve, and the repulsive interaction comes into play on resonance.

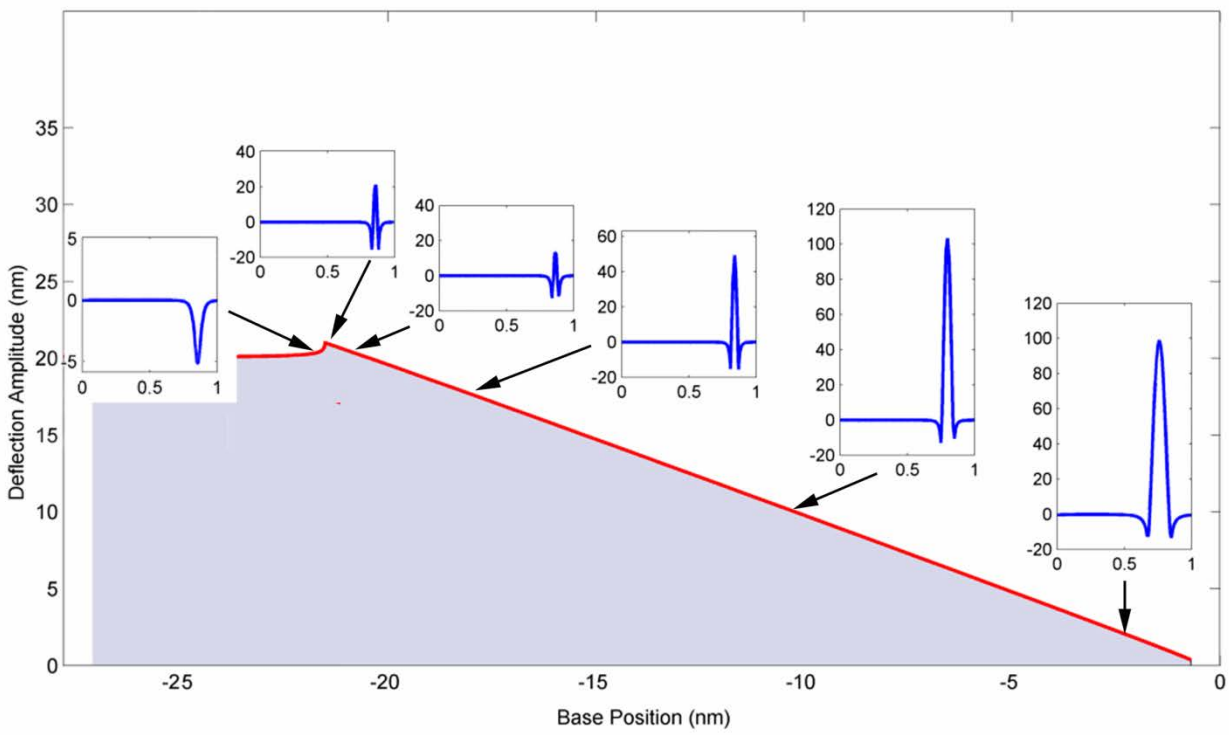

Figure 5.3.2.3: The red curve shows the dependence of deflection amplitude on base position when driving a cantilever of k = 10 N/m 40% below resonance, at A_d = 20 nm. The insets depict force plots over one oscillation period at different deflection amplitudes. Units of the force are

nm in each insets; the corresponding amplitude is given by the value of the red line at the spot shown by the arrows.

5.3.2.1 Dependence of the quality of Imaging on oscillation amplitude, cantilever stiffness and strength of tip-sample attraction

The average tip-sample force was calculated by first order numerical integration, using a sliding window similar to the one described above for the calculation of deflection amplitude.

Figure 6 depicts the normalized average force – set-point relationship in the case of driving the cantilever on resonance (β = 1), and 10% (β = 0.9), 20% (β = 0.8), 90% (β = 0.1) below resonance. For clarity, the results are plotted for every 50th cycle. Attractive force shifts the resonance peak towards lower frequencies. The softer the cantilever, the more substantial this shift becomes. Therefore, with the applied value of Hamaker constant (AH = 5 * 10^{-20} J, which is a typical value for van der Waals interactions), for cantilevers of low spring constant (k <= 10 N/m), the value of the average force on resonance might be negative, meaning that no tapping was performed. However, this is not an issue off resonance, because of the already mentioned increase in the performed work.

The force curves can be grouped together if the F_{avg} values are calculated and plotted as a function of amplitude (Figure 7). Farther off resonance, this dependence becomes *quasi* linear and can be approximated by a simple linear fit. When driving the cantilever on resonance, the force curves obtained by simulation can be approximated by the analytical model. Note that as the AFM measures root-mean-square deflection amplitude, the values used in the simulation might have to be multiplied by $\frac{\sqrt{2}}{2}$.

With low AH, for all spring constants and all oscillation amplitudes, the value of the normalized force falls on the same master curves. Only positive values are shown, signifying the region were the tip is in contact with the sample. Beta=0.1 is the one with highest slope (Figure 5.3.2.1.1).

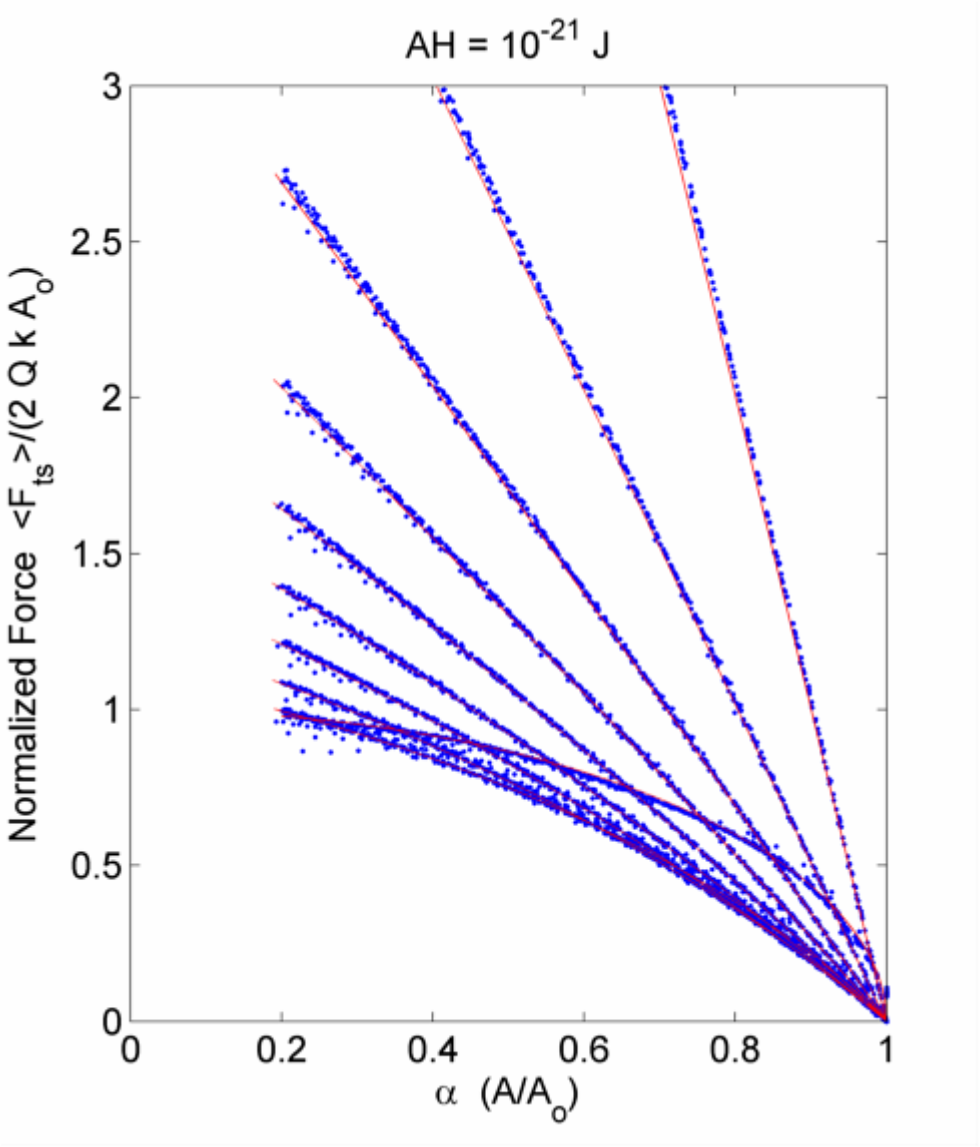

Figure 5.3.2.1.1: Normalized force as a function of set-point amplitude in the lack of attractive tip-sample force.

For larger AH, we can see much more scattering (Figure 5.3.1.2.2).

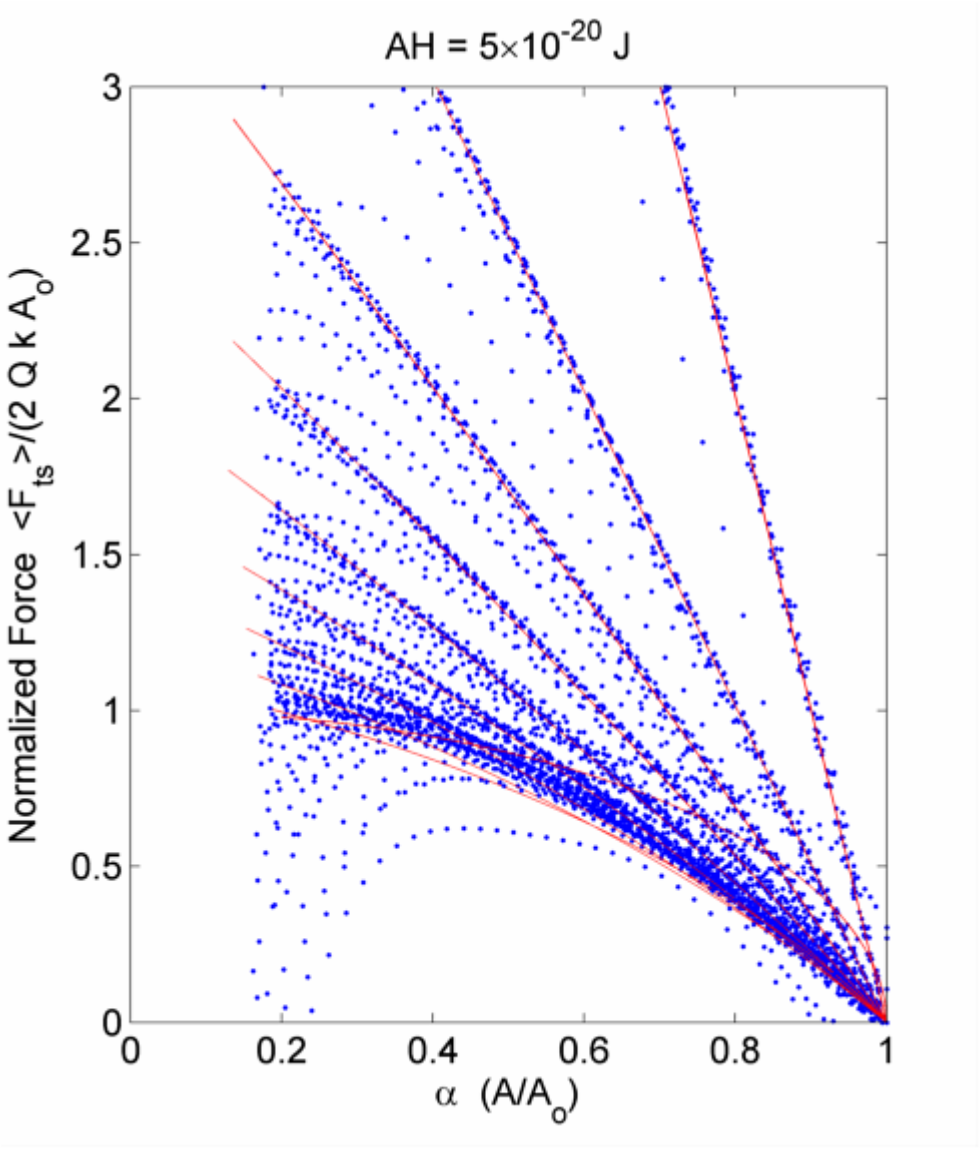

Figure 5.3.2.1.2: Normalized force as a function of set-point amplitude in the presence of attractive tip-sample force.

Another prediction was pointing to the existence of a shallow minimum in the effective cantilever stiffness graph (Figure 5.3.2.1.3). The trend in the results for stiffness is similar to the one observed for normalized force.

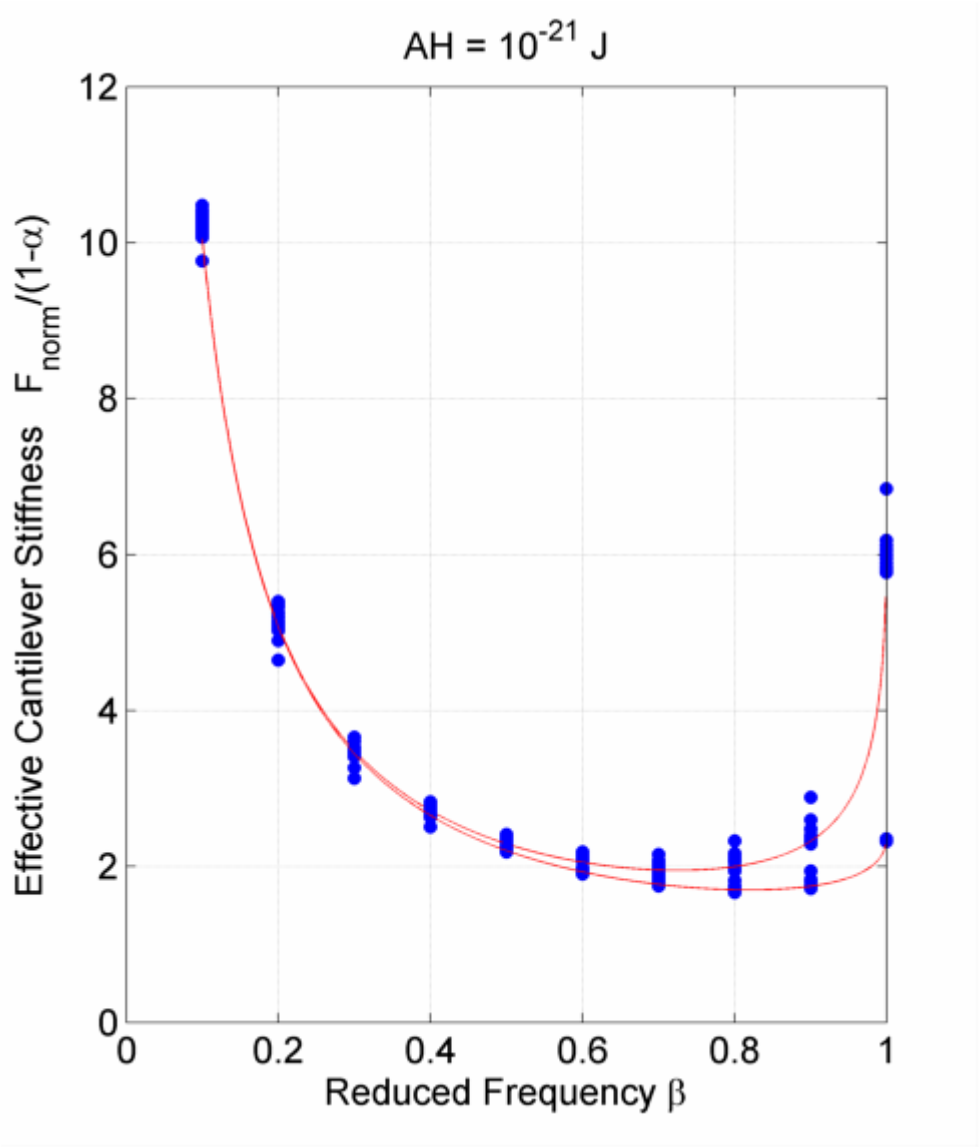

Figure 5.3.2.1.3: Effective cantilever stiffness as a function of off-resonance parameter in the lack of attractive tip-sample force.

Similarly to the force, at higher AH, the general trend is followed, but with much more scattering.

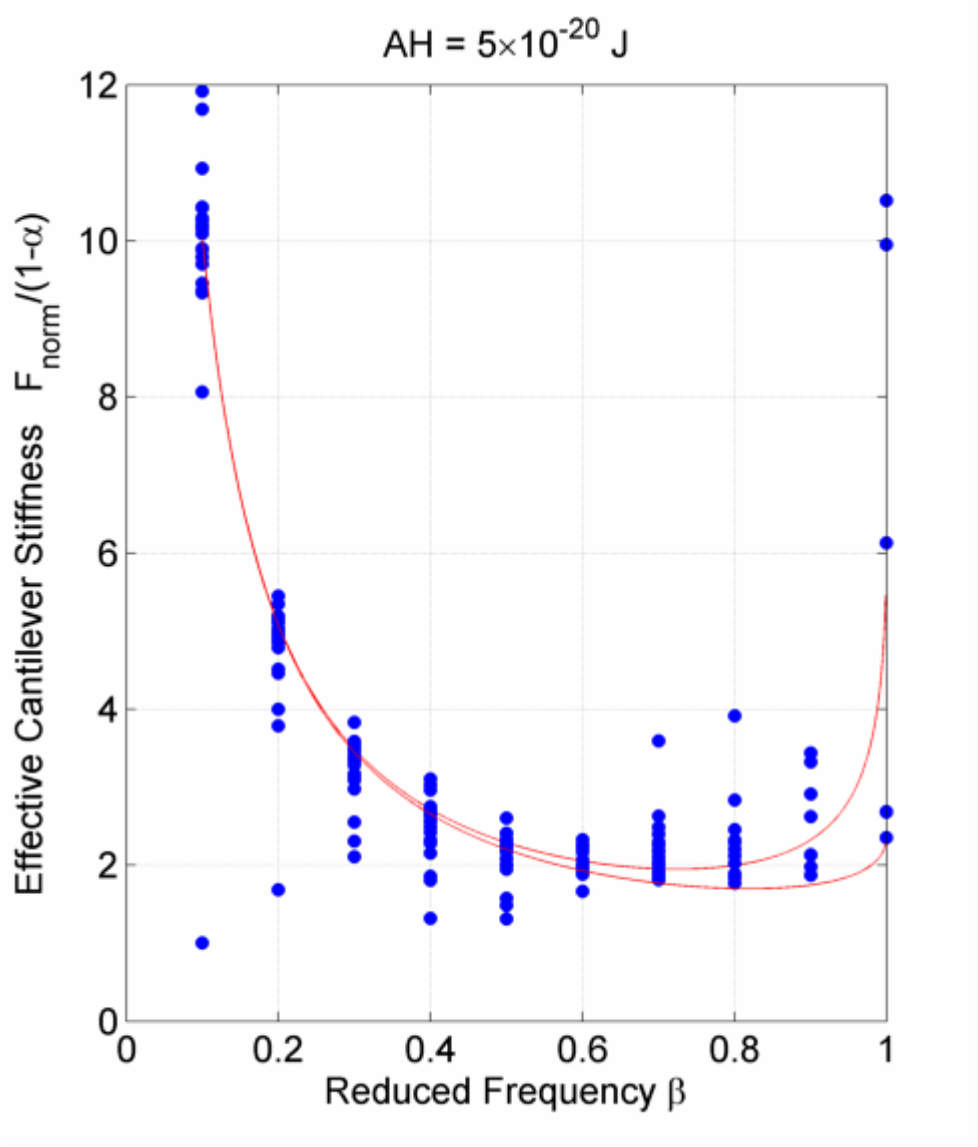

Figure 5.3.2.1.4: Effective cantilever stiffness as a function of off-resonance parameter in the presence of attractive tip-sample force.

Taking several force profiles like the ones depicted in the insets in Figure 5.3.2.1.1 and mapping them together, we can generate force maps (Figure 5.3.2.1.5). The force is plotted as a function of base position instead of the deflection amplitude, because this is a monotonic function of time. The width of each of the frames is one oscillatory cycle. The top of the frames corresponds to 1.2 A_d, the bottom to 2.2 A_d. The horizontal line on each subfigure shows the target amplitude, and the

changes in color correspond to the change of the phase (given by the position in one cycle). Off resonance (farther down the table) the phase changes more, and as the amplitude decreases (from left to right) the peak gets broader. In conclusion, the frequency and the amplitude influence the average tip-sample force.

In the case of softer cantilevers, there is a high likelihood for the tip not going into contact with the sample at all. With low oscillation amplitudes (light tapping), the probability of developing this regime increases. These cases have to be excluded form data analysis.

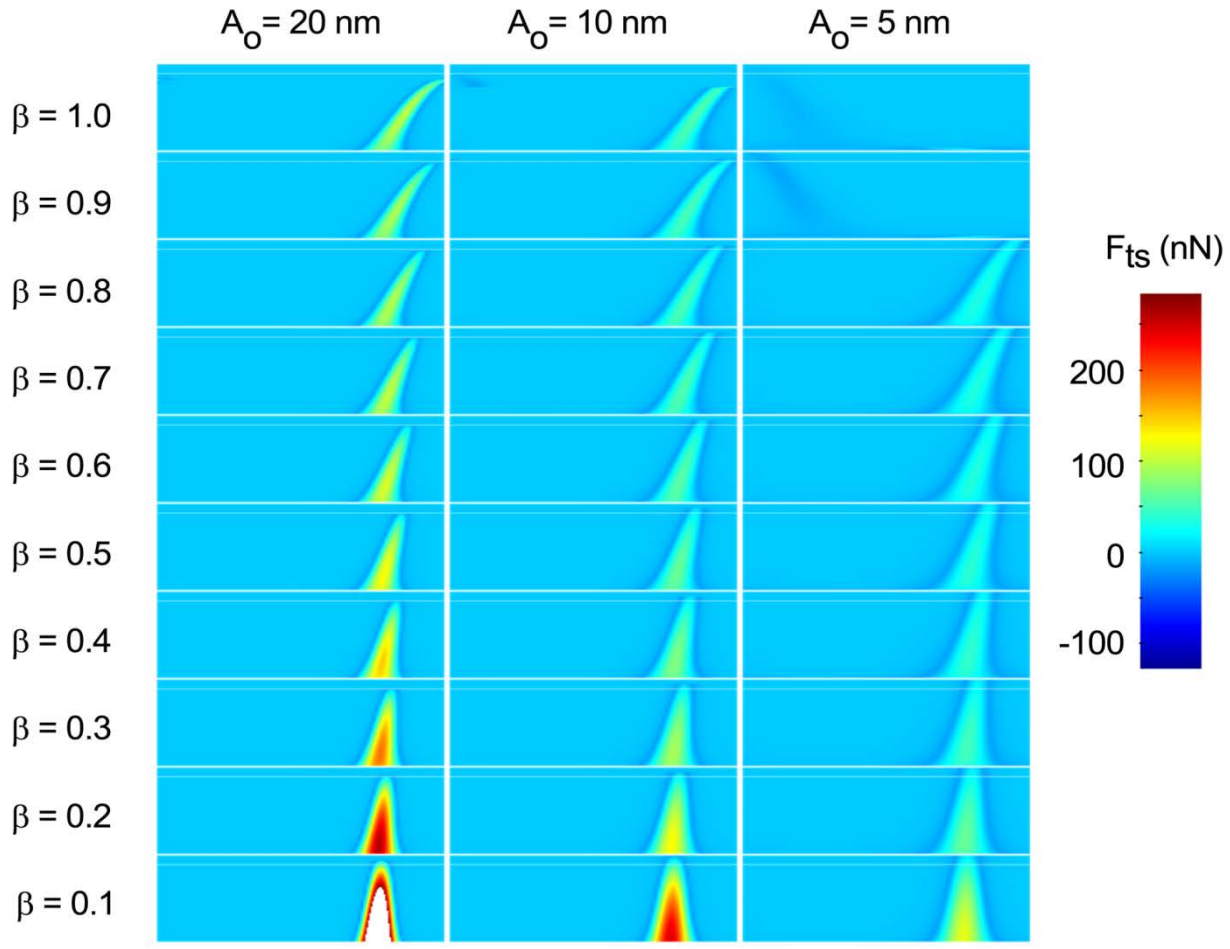

Figure 5.3.2.1.5: Force maps at k = 50 N/m. Frequency decreases from top to bottom (β = 1, 0.9, 0.8, 0.7, 0.6, 0.5, 0.4, 0.3, 0.2, 0.1), target amplitude decreases from left to right (20 nm, 10 nm, 5 nm).

A composite of all instantaneous force maps. For low AH: we always go into tapping, and the phase shift is always negative (Figure 5.3.2.1.6). The softer the cantilever, the narrower the range of real tapping.

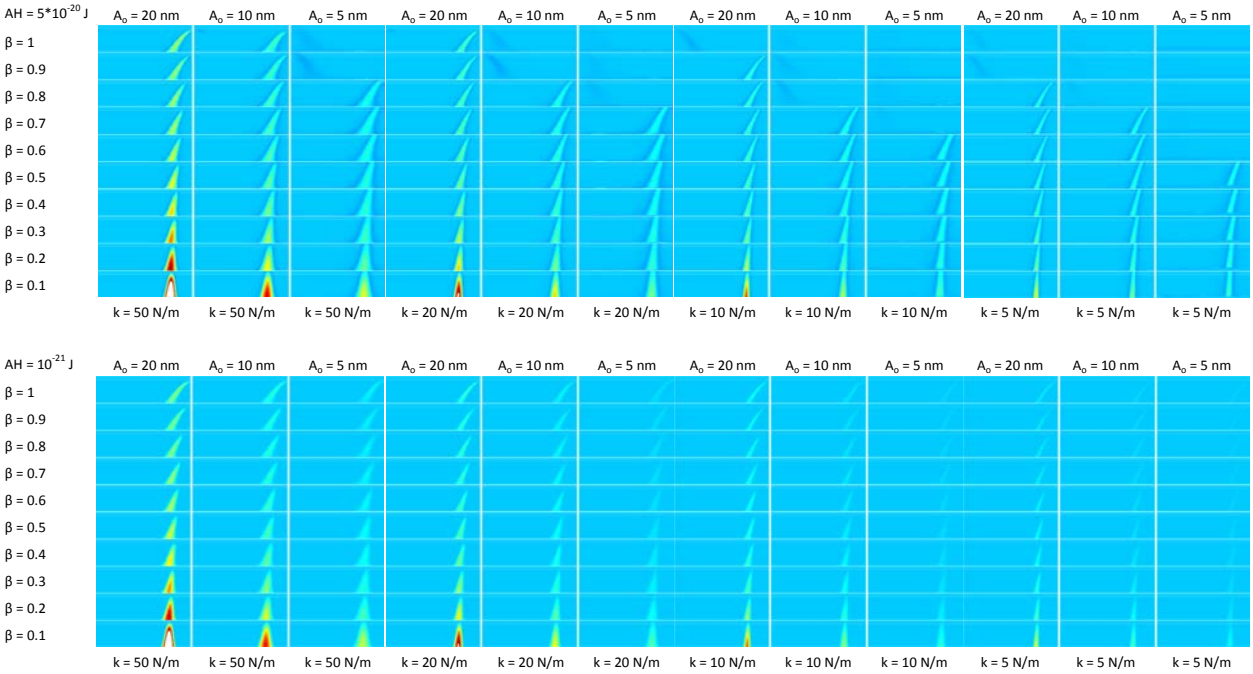

Figure 5.3.2.1.6: Force maps collected by running simulations with a wide range of parameter settings.

To quantify the results, the rms deviation of tip-sample force averaged over a wide range of set points from the mean force values were calculated and plotted. For low AH, we have found a very close agreement across a wide range of parameters. Relative error less than 1%, exept for the cases of low k and low A. For low k and low A, deviation from theory can be as much as 50%. However,

all this is genuine tapping. Deviations arise from transients, from chaotic oscillatory behavior due to perturbation of the system.

For high AH, the deviation from theory is much more substatnial, especially if we go to lower k, even after removal of non-contact scenarios.

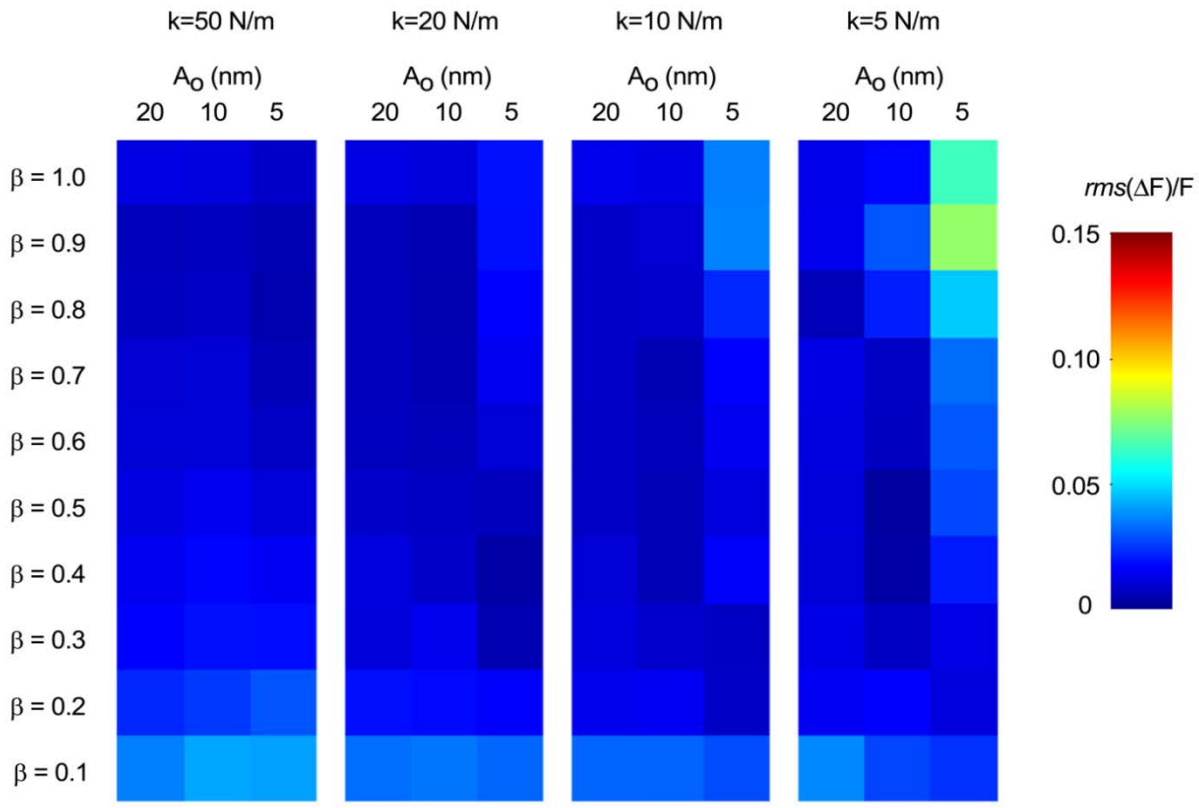

Figure 5.3.2.1.7: The error in the simulation experiments in the lack of attractive tip-sample force.

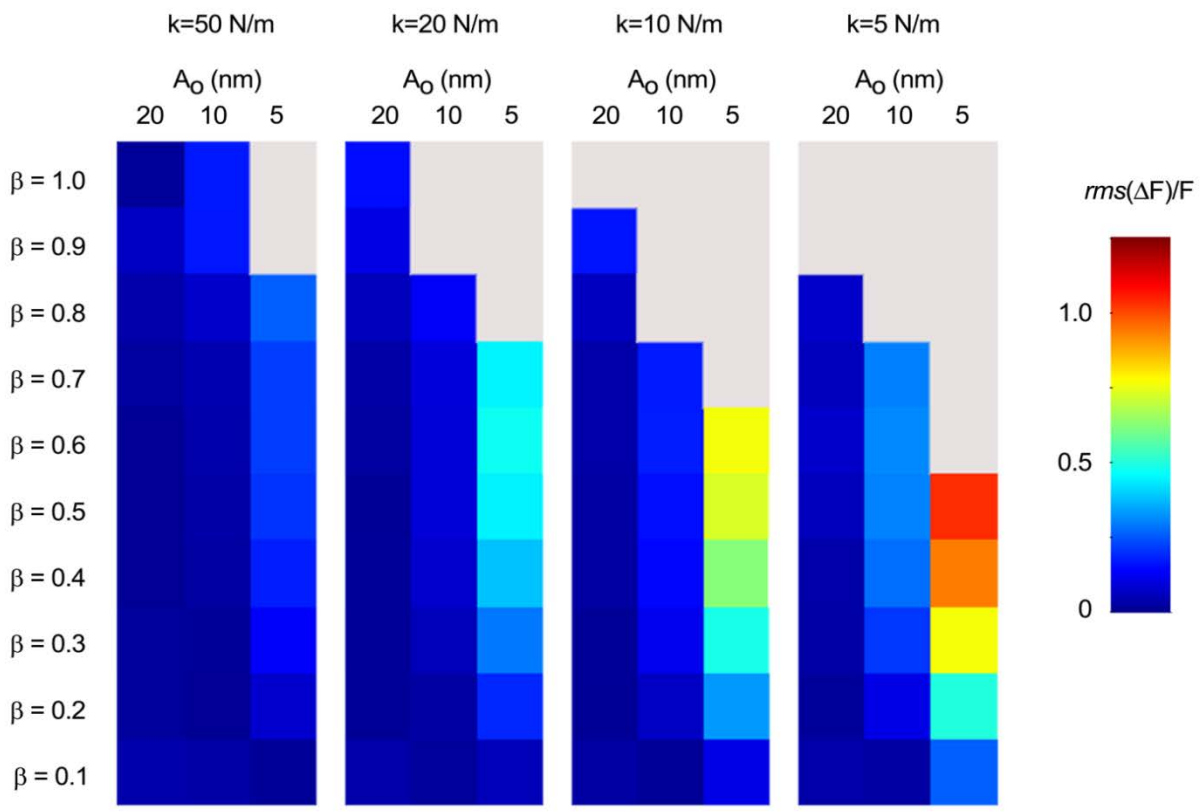

Figure 5.3.2.1.8: The error in the simulation experiments in the presence of attractive tip-sample force.

With higher set-points, the tip spends the entire oscillation period in the zone where the tip-sample attraction is very strong (close proximity of the sample or even pushing into it). Even at setpoint =1, the tip pushes into the surface of the sample at once. Under these conditions, indentation is more informative than tip-sample force.

In the absence of attractive force, the operation is determined by the geometrical effects, not the average attractive force. Cantilever bending is not important: as the set-point becomes lower and lower, the tip gets pushed into the sample. This indentation decreases the significance of frequency dependence, because the tip spends most of the oscillation period time in the vicinity of the surface.

In the presence of tip-sample attraction, the tip spends more time in the vicinity of the surface, which has two important consequences. First, the dependence of the net average force on oscillation amplitude is opposite to what we experience in the lack of attractive force. In the presence of attraction, the lower the tip amplitude, the higher the net average force. In the case of a soft sample, this effect is even more pronounced. Second, the behavior of the system becomes sample modulus dependent. If the sample's Young's modulus is high, once the tip gets into the close proximity of the surface, the attraction can pull it into the sample. The resulting indentation causes perturbation in the system, therefore, it makes sense to minmize the attractive force by pulling back the tip and tappin harder.

With settings of the simulation, the attractive force is small compared to the spring constant of the cantilever. Consequently, the indentation force is the same with k = 5 and k = 50, meaning that we can safely use a more rigid cantilever.

5.4 Conclusions

An expression for the average tip-sample force has been derived and compared with the finding of simulations. The derivation is based on the work of Cleveland et al. and Garcia et al., but with an important difference in the general equation of motion. Namely, in the proposed model, the tip-sample force depends on cantilever deflection, rather than on tip position.

The new model is superior to the existing ones in that those only contain information about the force on resonance. Driving the cantilever below resonance is of practical interest, due to decreased response time and increased oscillatory stability. Using this model, the A/A_d ratio can be used to carry out experiments at a given force.

Overall, the simulation results were in good agreement with the prediction of the theory. At higher AH, the attractive force might be strong enough to cause a significant shift in the resonance frequency. This shift can induce a chaotic behavior instead of reaching a steady state in the oscillations, and it is not guaranted that the tip goes into tapping. Lowering the oscillation amplitude decreases contact time. Also, the tip spends more time in the vicinity of a sample of high Young's modulus, causing more deviation from the behavior predicted by theory. Decreased contact time increases the likelihood of unpredictable behavior. The lack of tip-sample contact cause considerable scatter and in real-life experiments, these will act as noise, diminishing the imaging resolution. The usage of a stiff cantilever is generally not a good strategy, because the operation might be highly perturbed by attractive force. Instead, we recommend to use set point close to unity with either high oscillation amplitude or with driving the cantilever far below resonance.

5.5 References

(1) Garcıa, R. *Amplitude Modulation atomic Force Microscopy*; Wiley-VCH Verlag & Co. KGaA, Weinheim, Germany, 2010.

(2) Garcia, R.; San Paulo, A. *Phys. Rev. B: Condens. Matter Mater. Phys.* **1999**, *60*, 4961-4967.

(3) Cleveland, J. P.; Anczykowski, B.; Schmid, A. E.; Elings, V. B. *Appl. Phys. Lett.* **1998**, *72*, 2613-2615.

(4) Garcia, R.; Tamayo, J.; Calleja, M.; Garcia, F. *Appl. Phys. A: Mater. Sci. Process.* **1998**, *66*, S309-S312.

(5) Magonov, S. N.; Reneker, D. H. *Annu. Rev. Mater. Sci.* **1997**, *27*, 175-222.

(6) Noy, A.; Sanders, C. H.; Vezenov, D. V.; Wong, S. S.; Lieber, C. M. *Langmuir* **1998**, *14*, 1508-1511.

(7) Tamayo, J.; Garcia, R. *Appl. Phys. Lett.* **1997**, *71*, 2394-2396.

(8) Garcia, R. *Amplitude Modulation Atomic Force Microscopy*; John Wiley & Sons, 2010.

(9) Kowalewski, T.; Legleiter, J. *J. Appl. Phys.* **2006**, *99*, 064903/064901-064903/064905.

(10) Legleiter, J.; Kowalewski, T. *Applied Physics Letters* **2005**, *87*, 163120/163121-163120/163123.

(11) San Paulo, I.; Garcıa, R. *Phys. Rev. B* **2001**, *64*, 193411-193414.

(12) Derjaguin, B. V.; Muller, V. M.; Toporov, P.; Yu, C. *J. Colloid Interface Sci.* **1975**, *53*, 314-326.

(13) Kühle, A.; Sorensen, A. H.; Zandbergen, J. B.; Bohr, J. *Appl. Phys. A: Mater. Sci. Process.* **1998**, *66*, 889.

(14) Israelachvili, J. N. *J. Chem. Soc., Faraday Trans. II* **1973**, *69*, 1729-1738.

(15) Anczykowski, B.; Gotsmann, B.; Fuchs, H.; Cleveland, J. P.; V.B., E. *Applied Surface Science* **1999**, *140*, 376–382.

(16) Goldstein, H. *Classical Mechanics*; Addison-Wesley Publishing Company; Reading, Massachusetts, 1980.

(17) Kowalewski, T.; Legleiter, J. *J. Appl. Phys.* **2006**, *99*, 064903/064901-064903/064905.

(18) Clifford, C. A.; Seah, M. P. *Nanotechnology* **2005**, *16* 1666–1680.

(19) Garcia, R.; Gomez, C. J.; Martinez, N. F.; Patil, S.; Dietz, C.; Magerle, R. *Phys. Rev. Lett.* **2006**, *97*, 016103-016107.

(20) Raman, A.; Melcher, J.; Tung, R. *Nano Today* **2008**, *3*, 20-27.

Appendix

Chapter III

I ^{1}H NMR

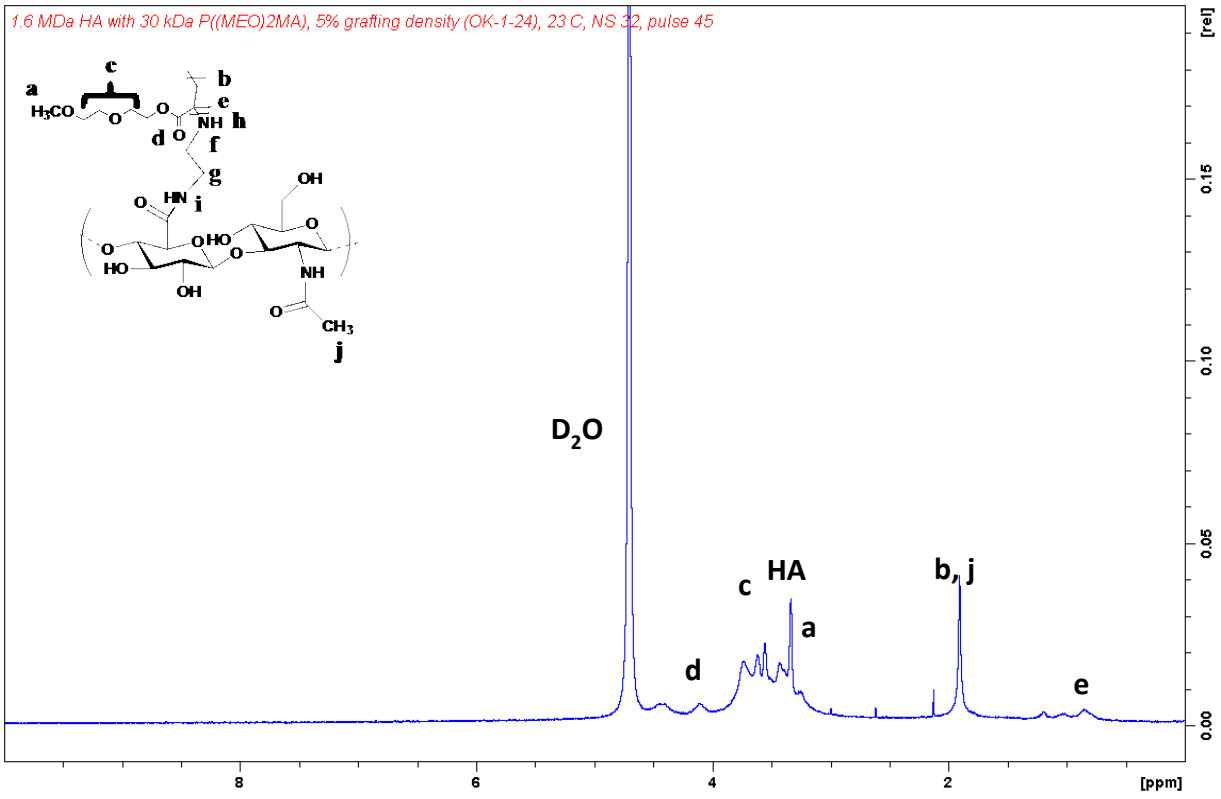

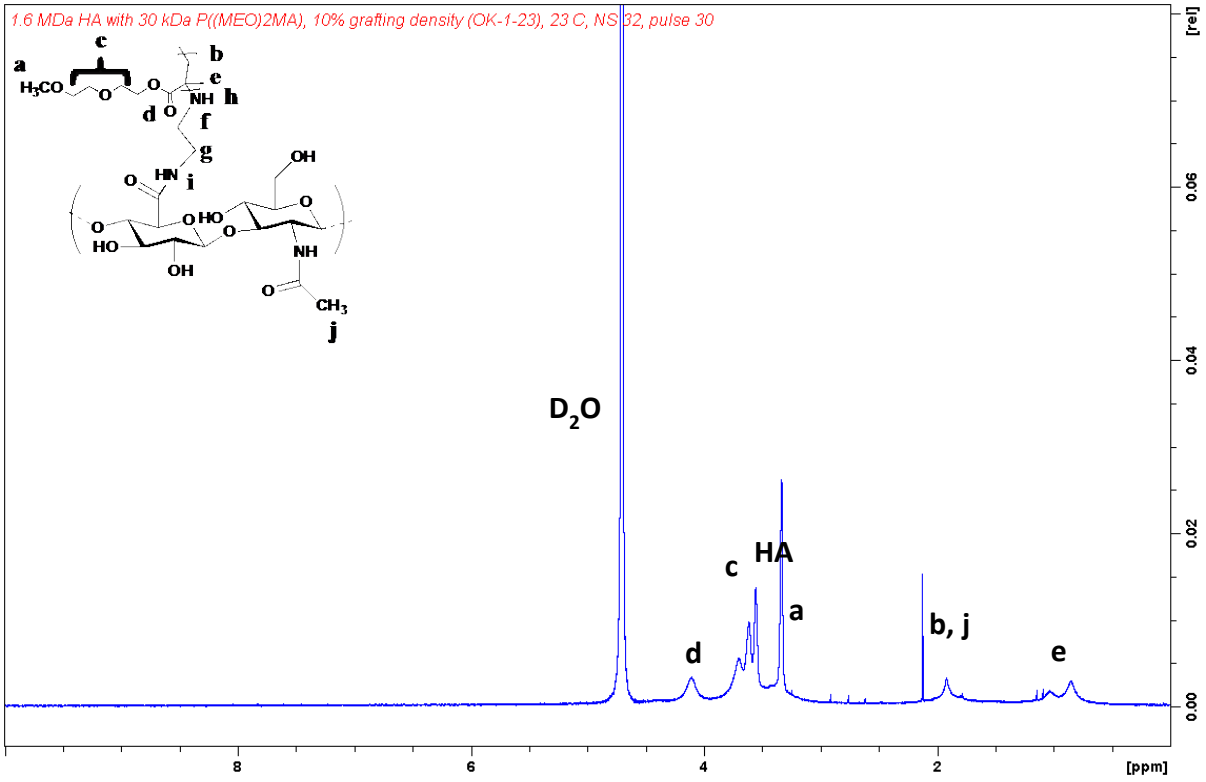
1.6 MDa HA with 30 kDa P((MEO)2MA), 10% grafting density (OK-1-23), 23 C, NS 32, pulse 30
D2O
HA
c
a
d
b, j
e
[rel]
[ppm]

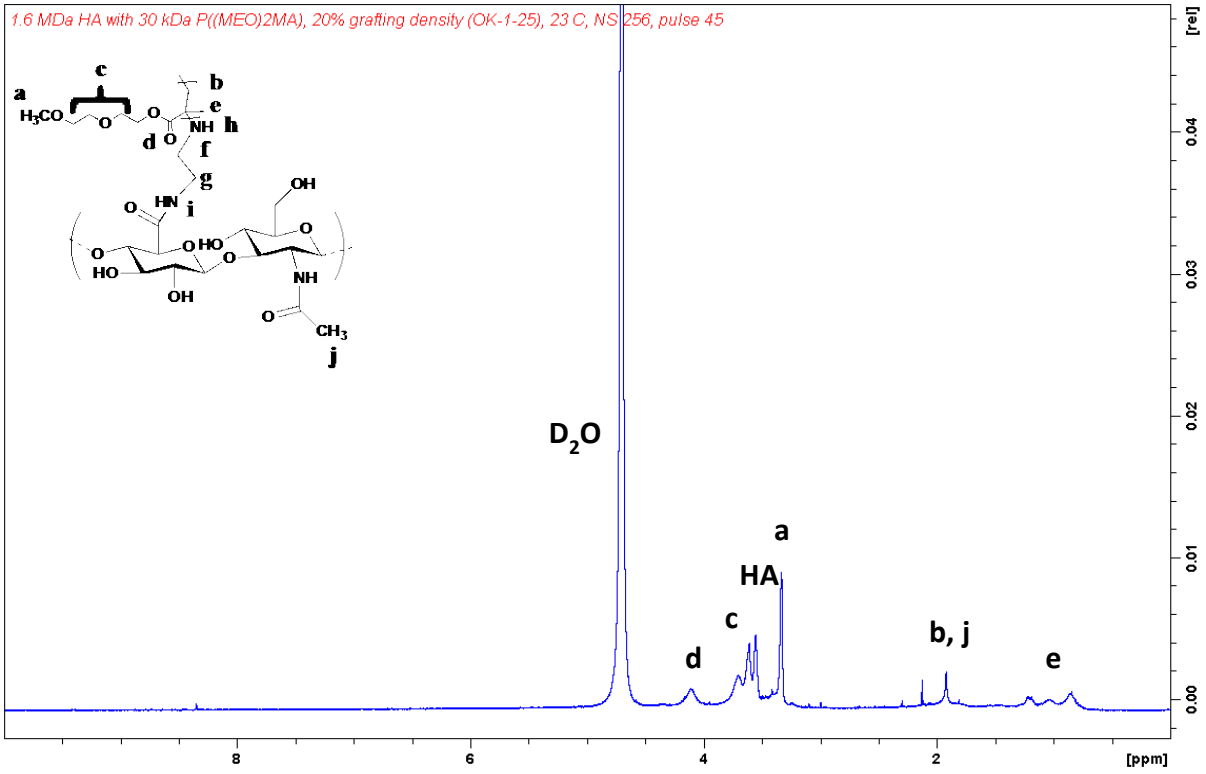
1.6 MDa HA with 30 kDa P((MEO)2MA), 20% grafting density (OK-1-25), 23 C, NS 256, pulse 45
D2O
a
HA
c
d
b, j
e
[rel]
[ppm]

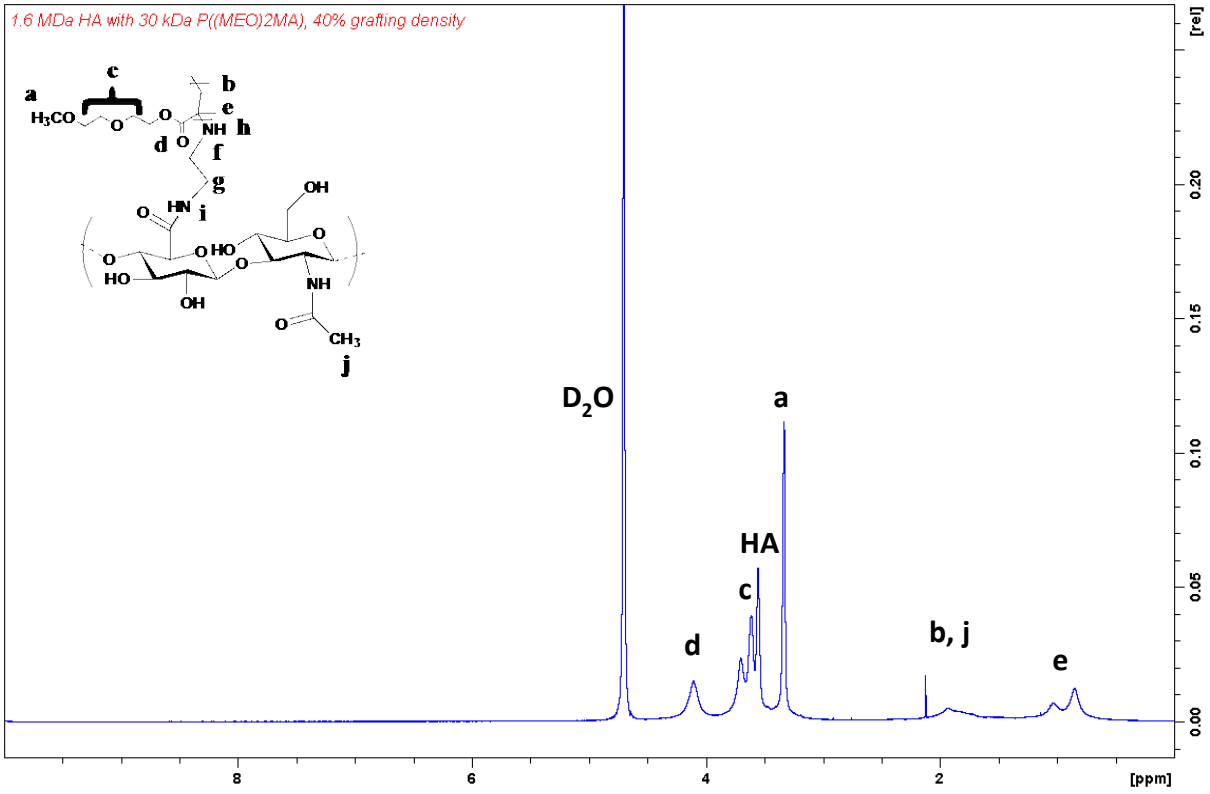

Samples with different length of grafted polymer

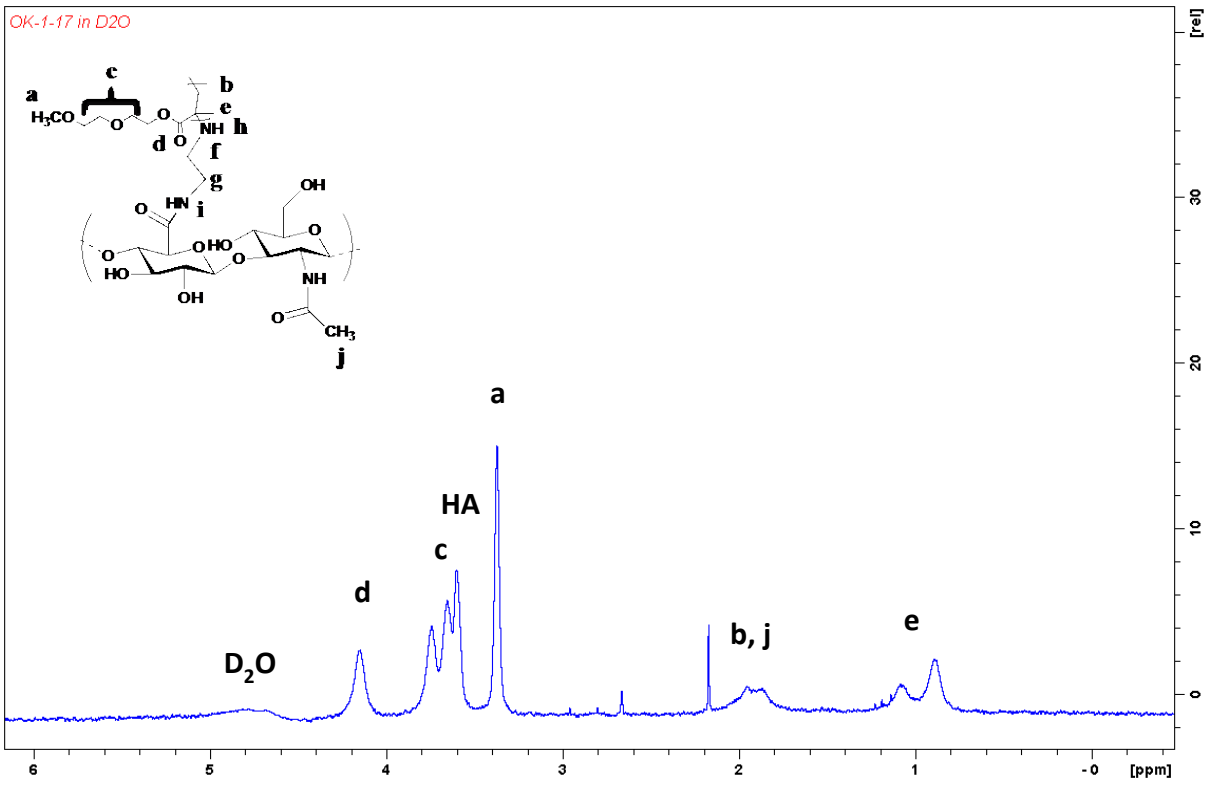
OK-1-17 in D2O
a
b
c
d
e
f
g
h
i
j
HA
D2O
b, j
[rel]
[ppm]

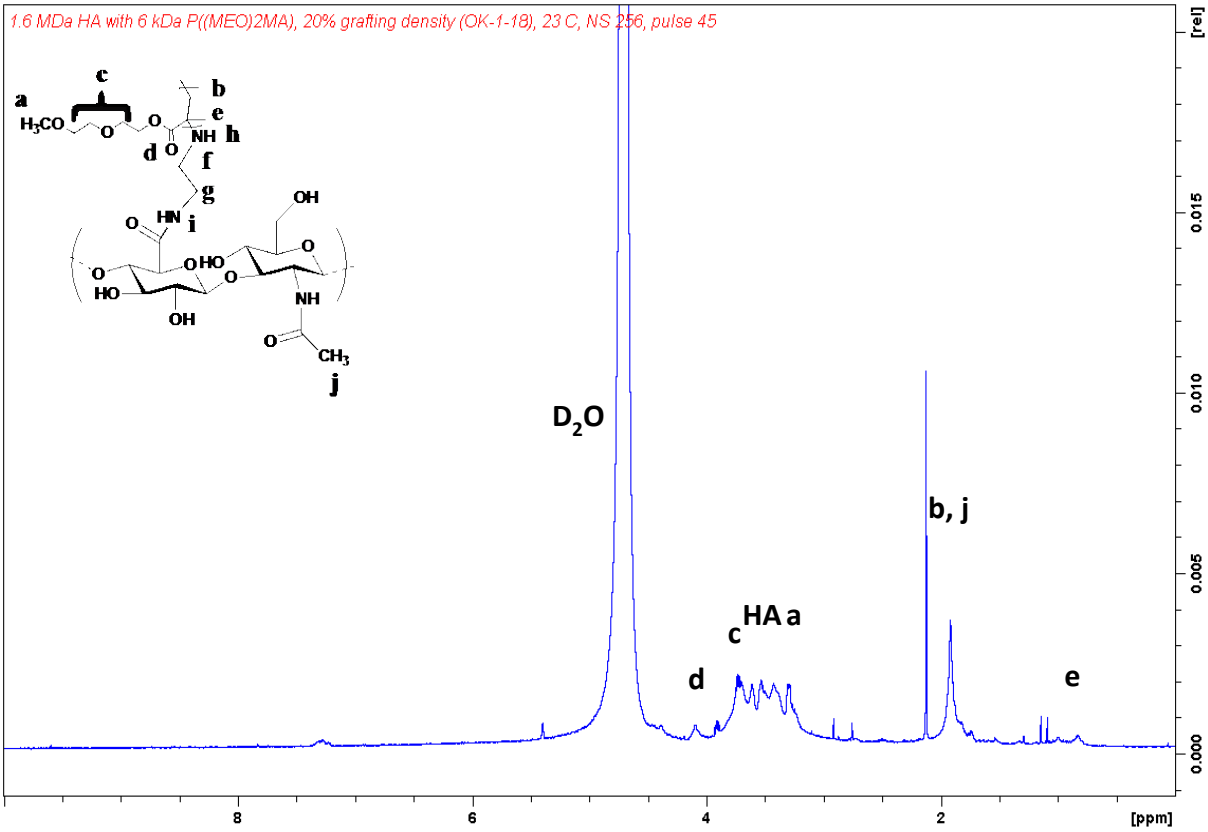
1.6 MDa HA with 6 kDa P((MEO)2MA), 20% grafting density (OK-1-18), 23 C, NS 256, pulse 45
a
b
c
d
e
f
g
h
i
j
D2O
b, j
HA a
[rel]
[ppm]

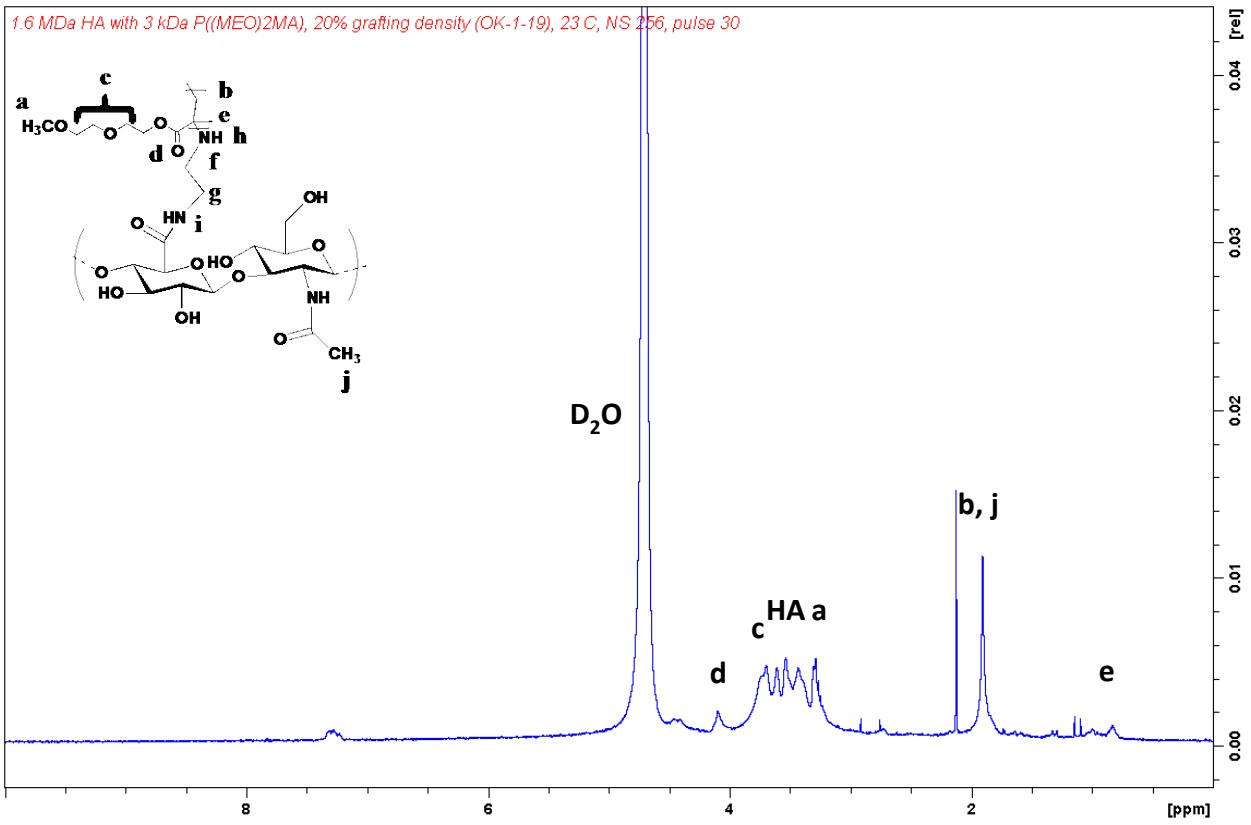

Approximate GD values based on integration:

Integration of peaks between 0-5 - 1.5 ppm was set to DP * 3p = 542,

where p=molar amount of polymer, and DP was determined to be 33991/188.22=180, based on monomer consumption in the ATRP of the polymer. P was taken to be 1, so that h will be given as relative compared to p.

The peak at 1.9 ppm was integrated and h was calculated from the equation integral = DP * 2p + 3h, and GD = 100%/h.

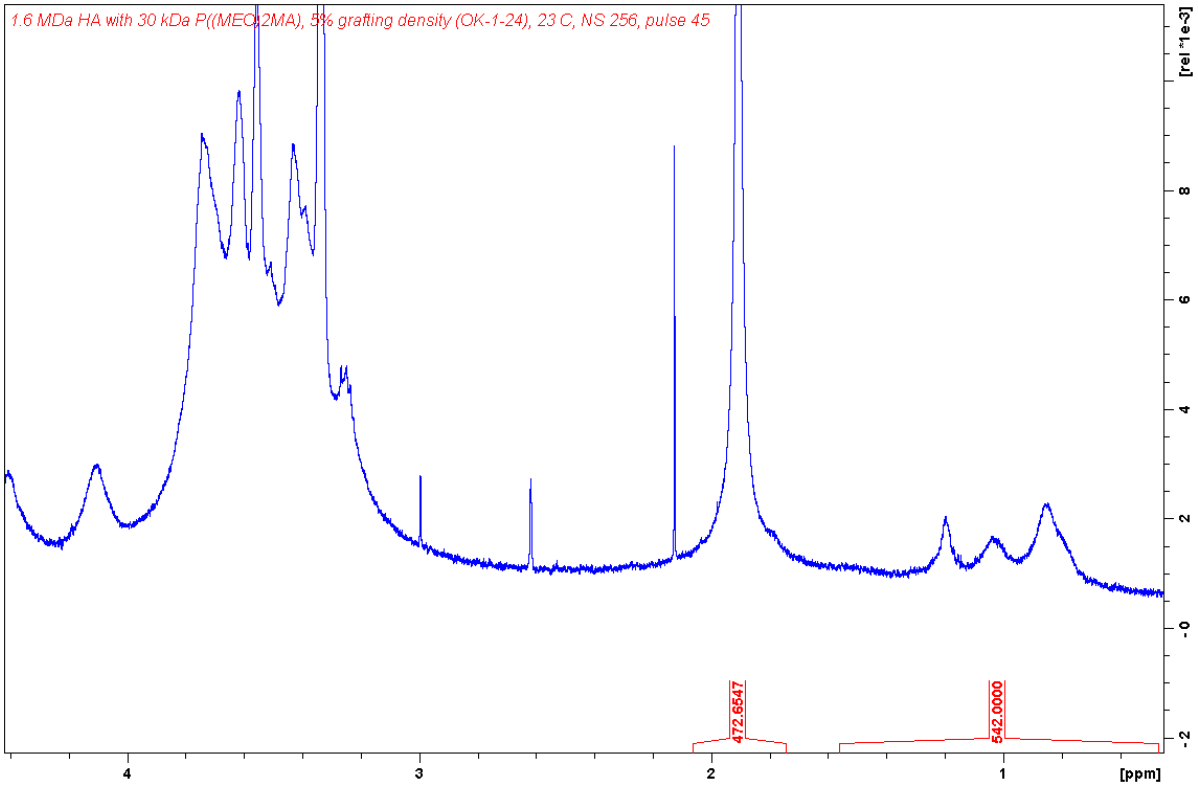

GD_NMR = 3% (GD_target = 5%).

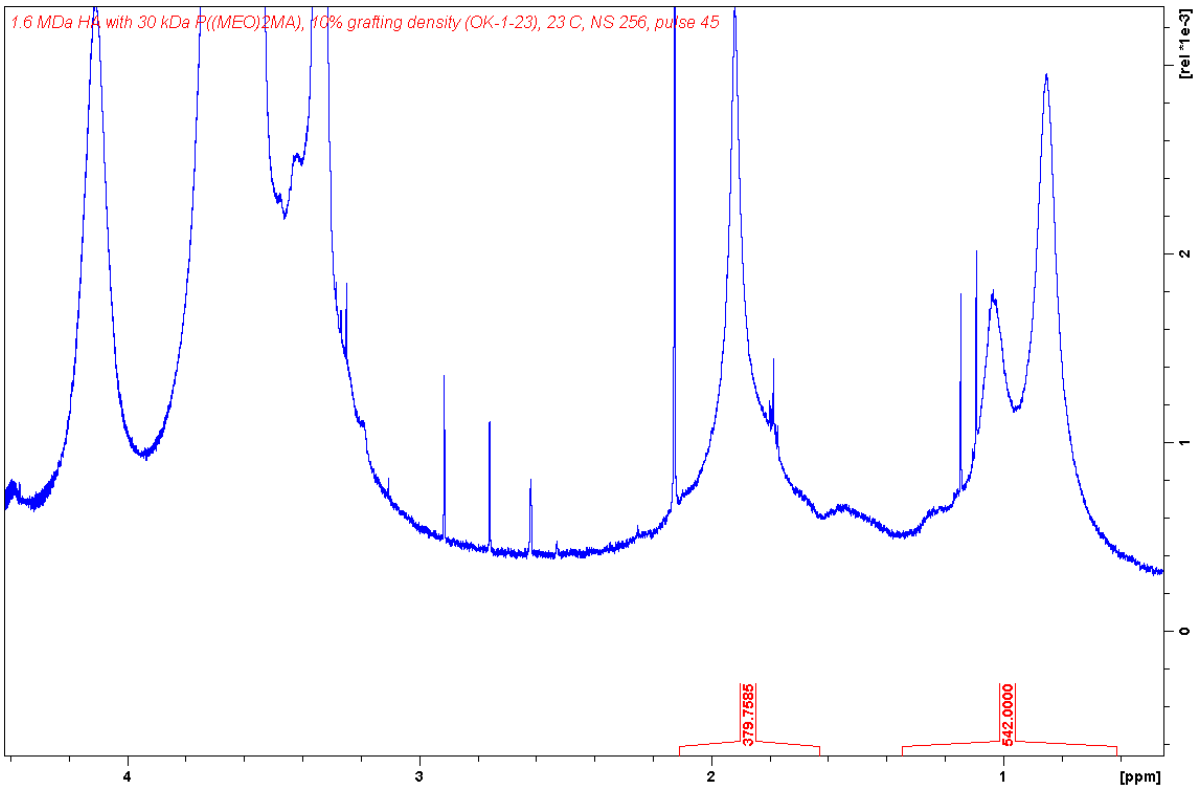

GD_NMR = 15% (GD_target = 10%).

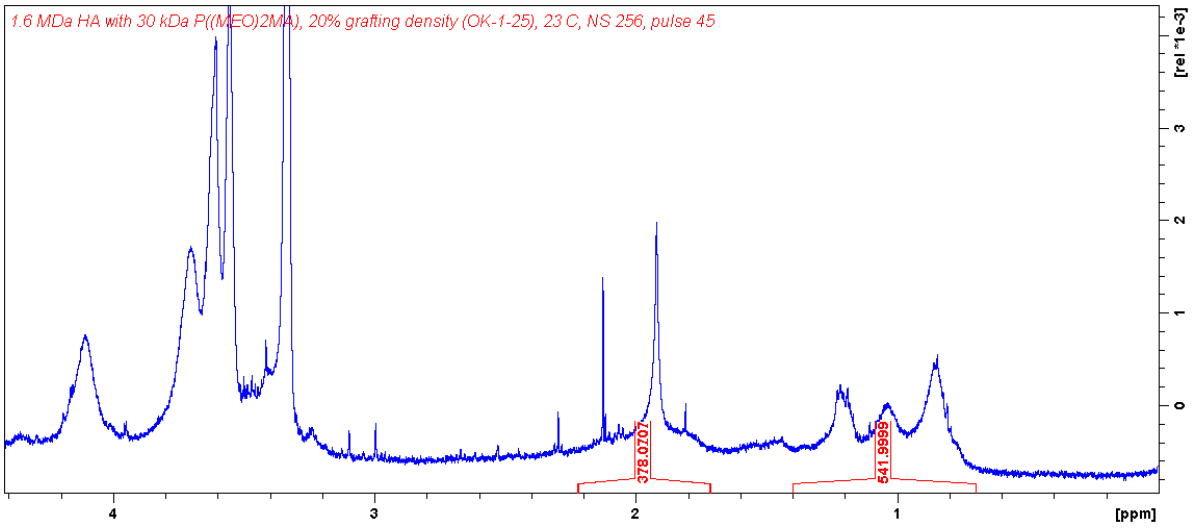

⇨ GD_NMR = 17% (GD_target = 20%).

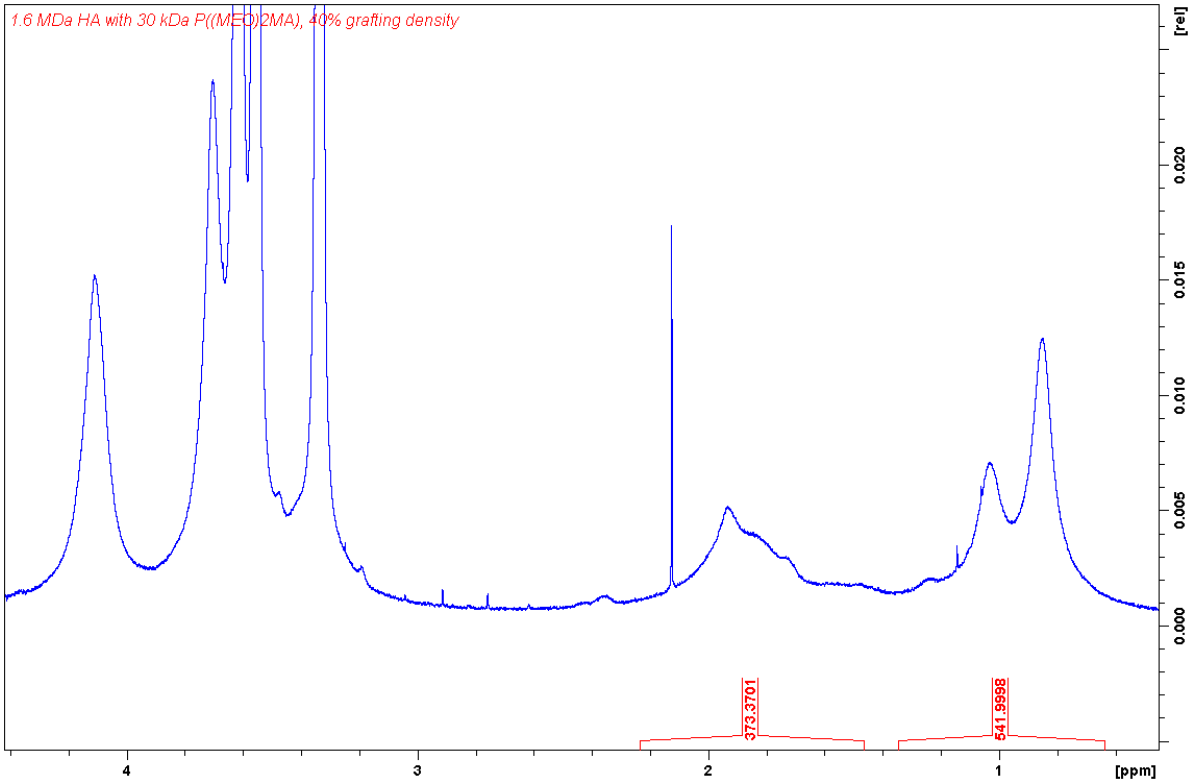

⇨ GD_NMR = 22% (GD_target = 40%).

A document with calculations for setting up reactions, monomer consumption, and NMR spectra of compounds that are not end products of the synthetic scheme is available for request.

II DLS

40 kDa polymer with GD 5%

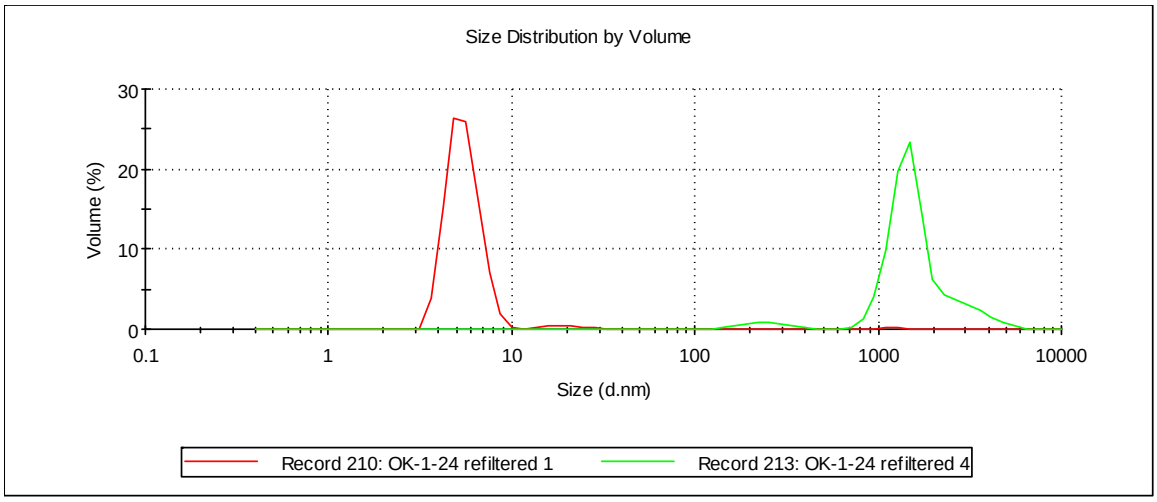

40 kDa polymer with GD 10%

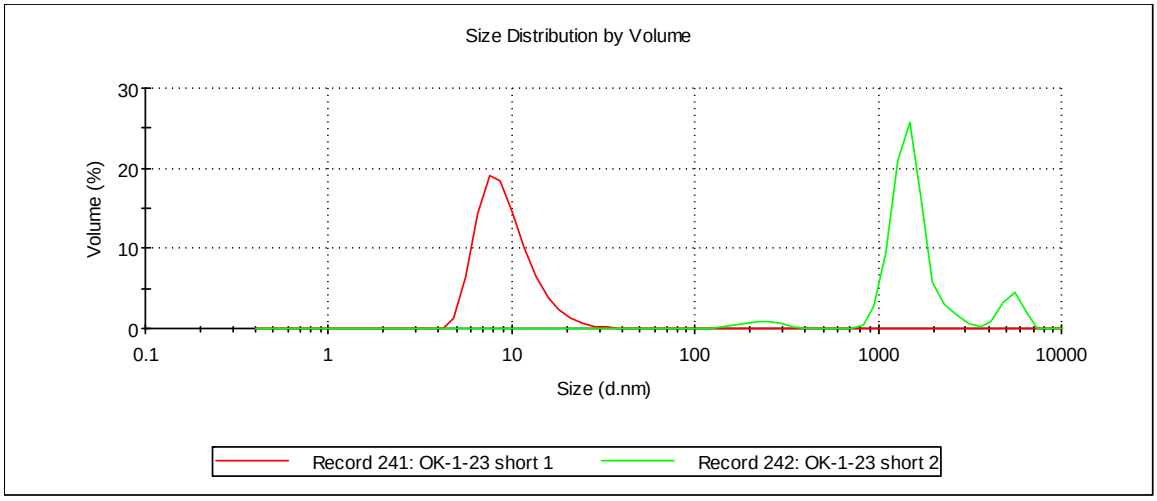

40 kDa polymer with GD 40%

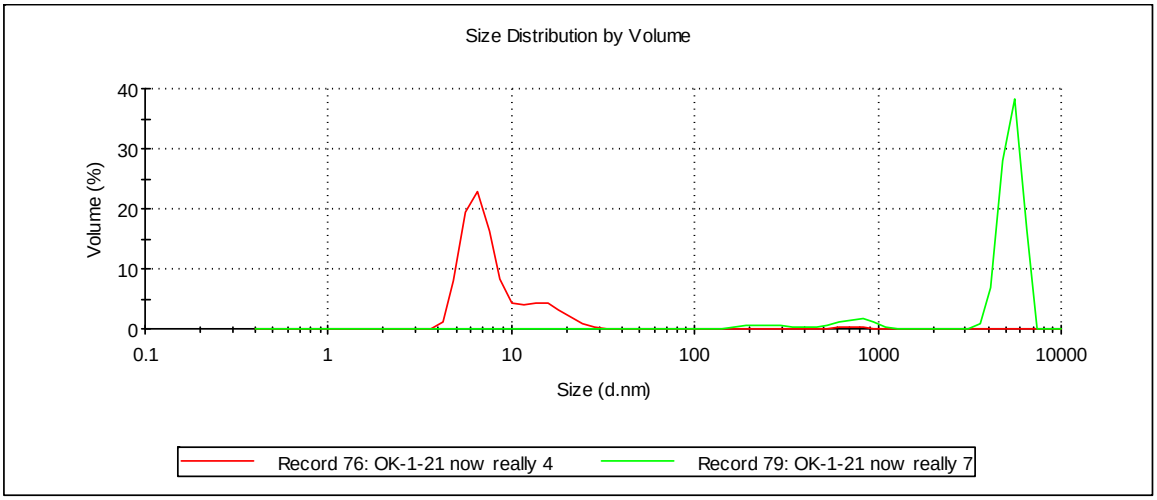

40 kDa pol w/ GD 0.3%

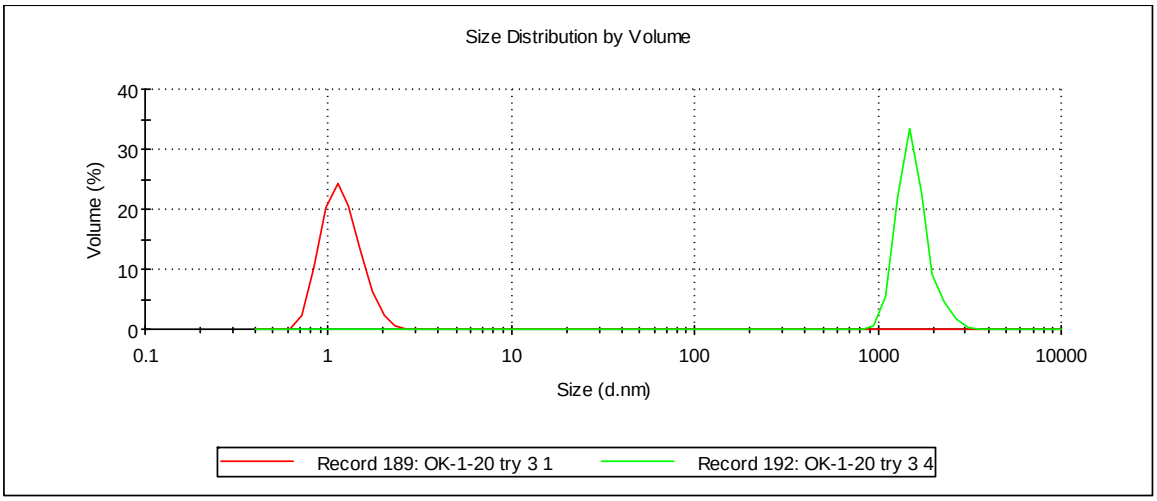

GD 20% w/ 28 kDa pol. (OK-1-17): No transition at 27 C, transition at 31 C:

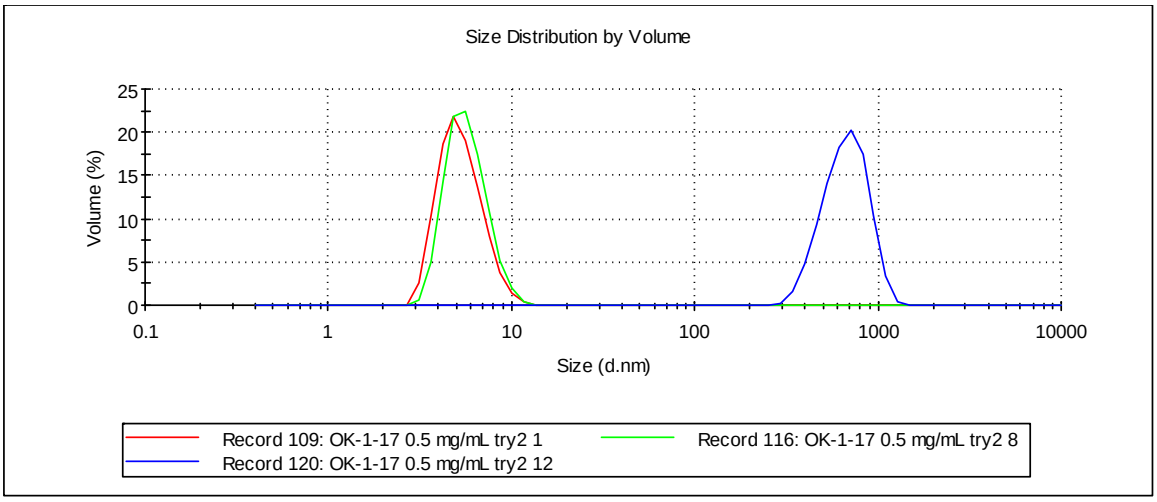

GD 20% w/ 6 kDa pol. (OK-1-18):

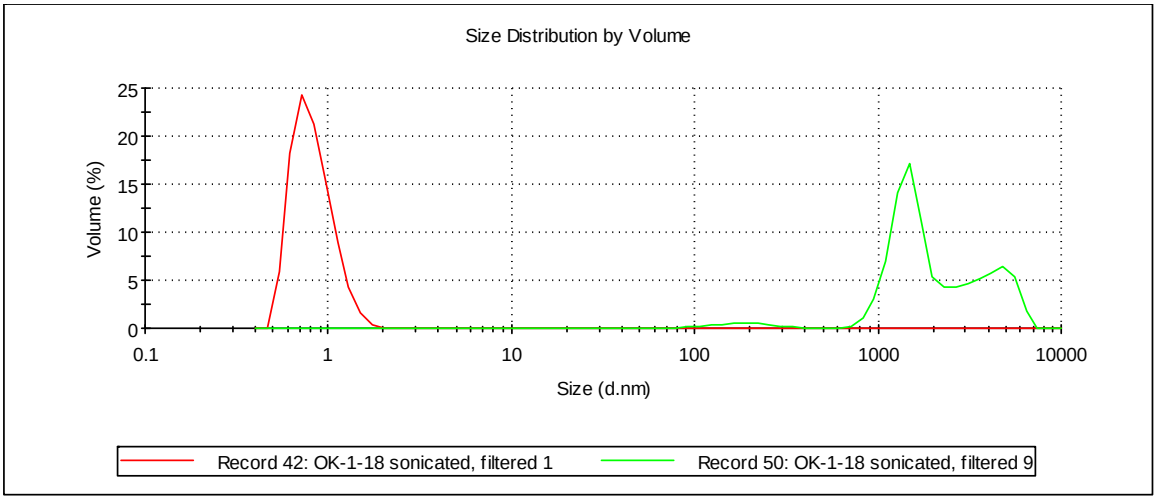

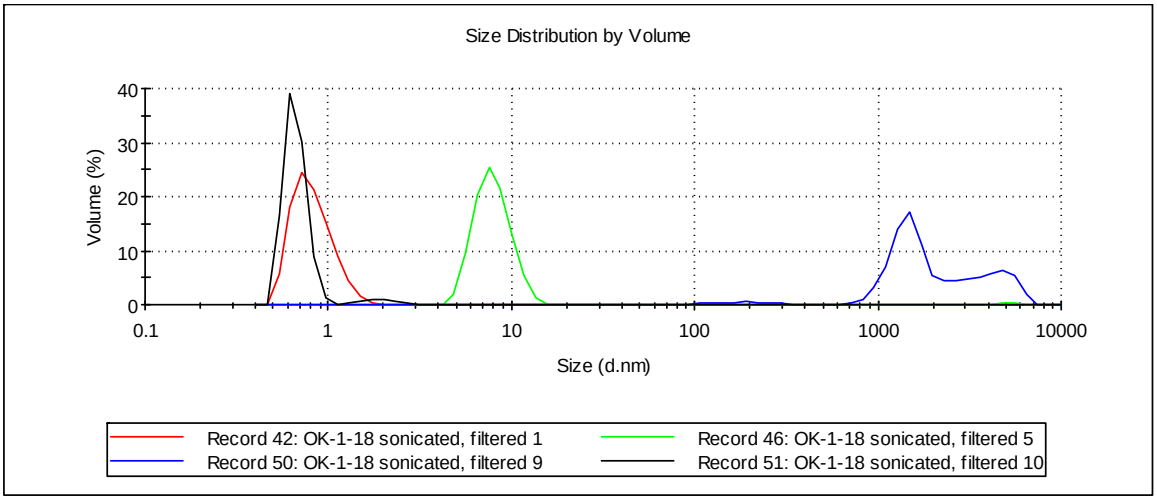

GD 20% w/ 3 kDa pol. (OK-1-19):

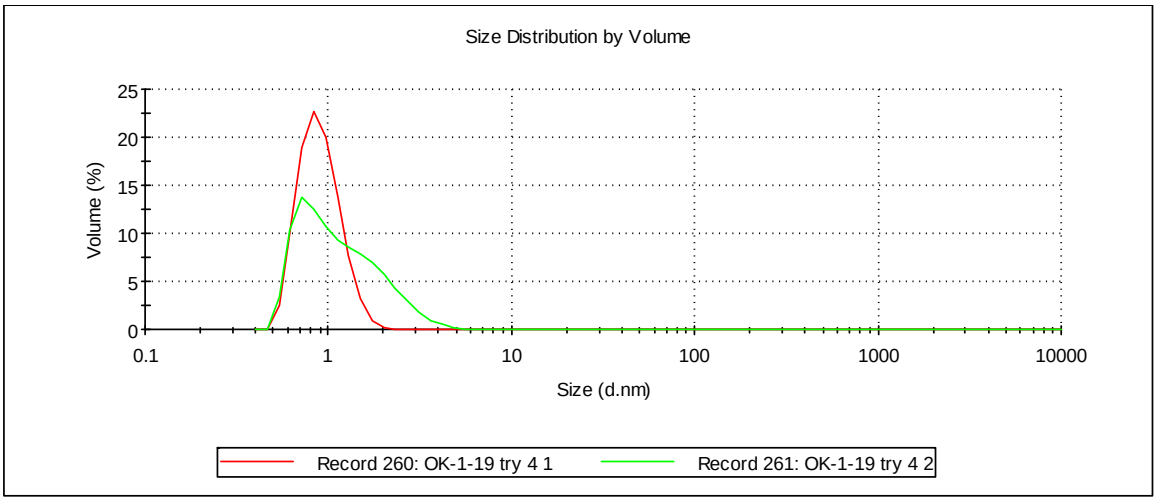

III QCM

Dissipaion changes as a function of time for all sampes are shown below. Time intervals with significant changes are circled in green.

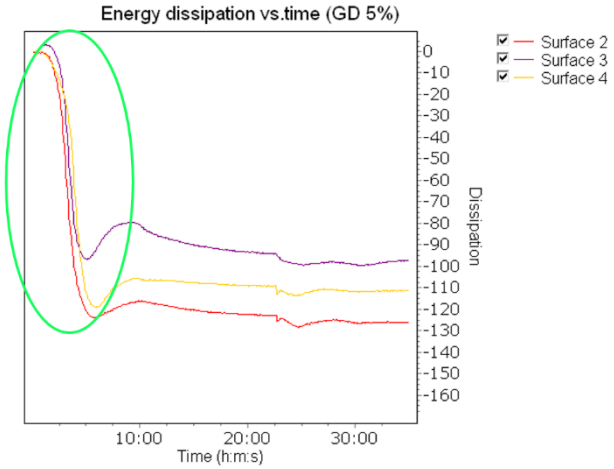

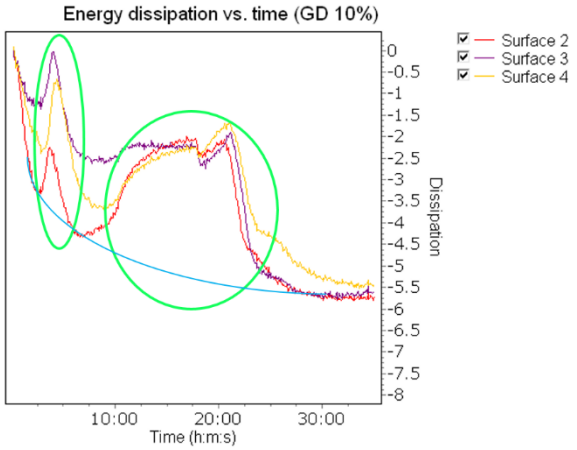
Energy dissipation vs. time (GD 10%)
Surface 2
Surface 3
Surface 4
0
-0.5
-1
-1.5
-2
-2.5
-3
-3.5
-4
-4.5
-5
-5.5
-6
-6.5
-7
-7.5
-8
Dissipation
10:00
20:00
30:00
Time (h:m:s)

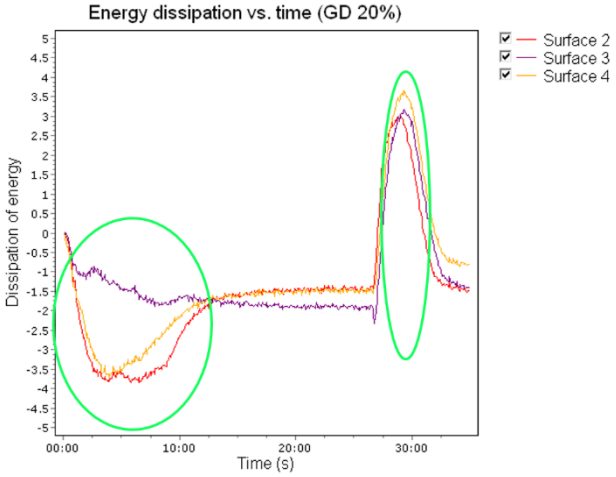
Energy dissipation vs. time (GD 20%)
Surface 2
Surface 3
Surface 4
Dissipation of energy
5
4.5
4
3.5
3
2.5
2
1.5
1
0.5
0
-0.5
-1
-1.5
-2
-2.5
-3
-3.5
-4
-4.5
-5
00:00
10:00
20:00
30:00
Time (s)

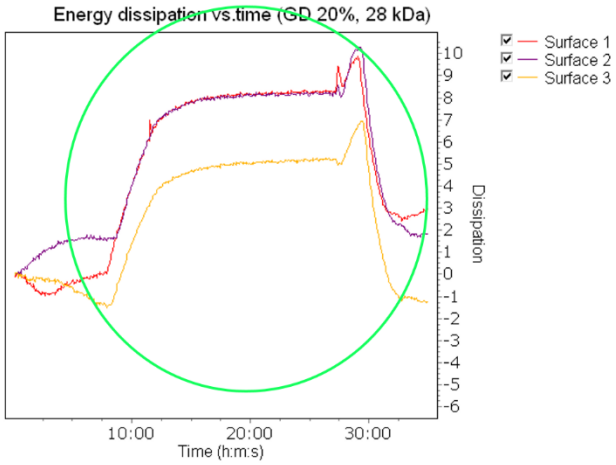
Energy dissipation vs.time (GD 20%, 28 kDa)
Surface 1
Surface 2
Surface 3
10
9
8
7
6
5
4
3
2
1
0
-1
-2
-3
-4
-5
-6
Dissipation
10:00
20:00
30:00
Time (h:m:s)

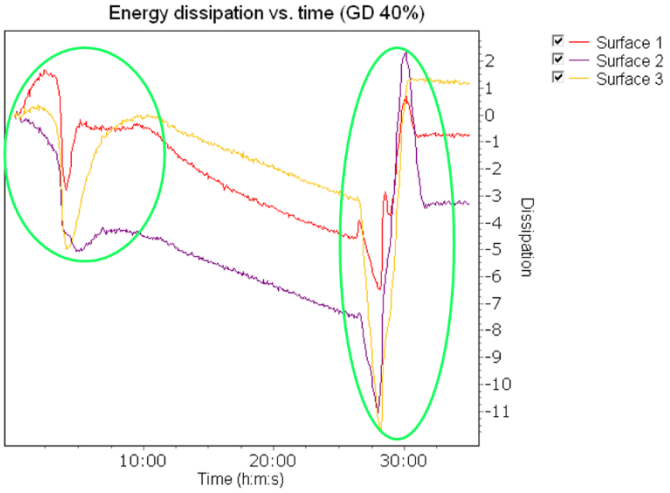

Note that these values are relative to the water control, therefore negative values are also physically meaningful. The curves belonging to the dissipation - time functions before subtraction of the control have similar shapes, as shown for two examples below.

Energy dissipation as a function of time after the introduction of the coating solution containing each samples, without the subtraction of the water signal:

dissipation vs. time (GD 10%), without control subtraction

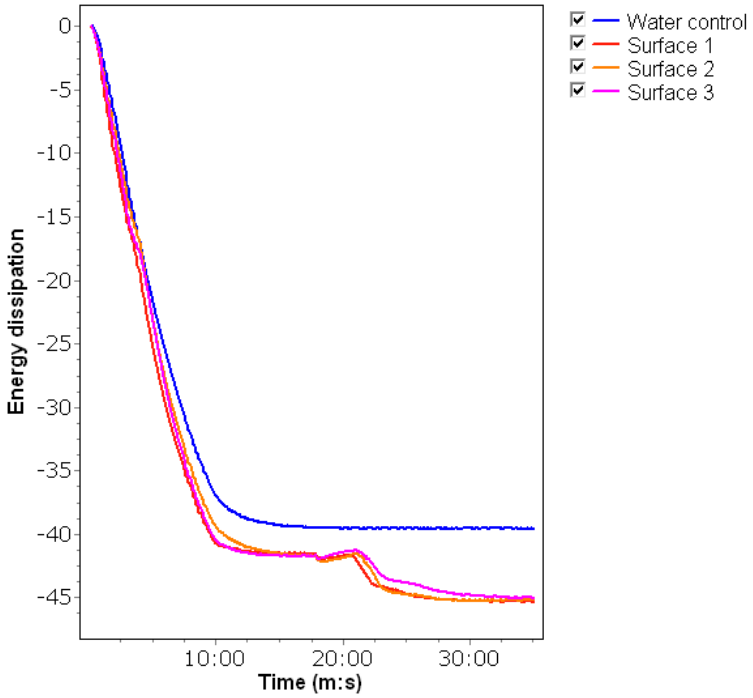

dissipation vs. time (GD 40%), without control subtraction

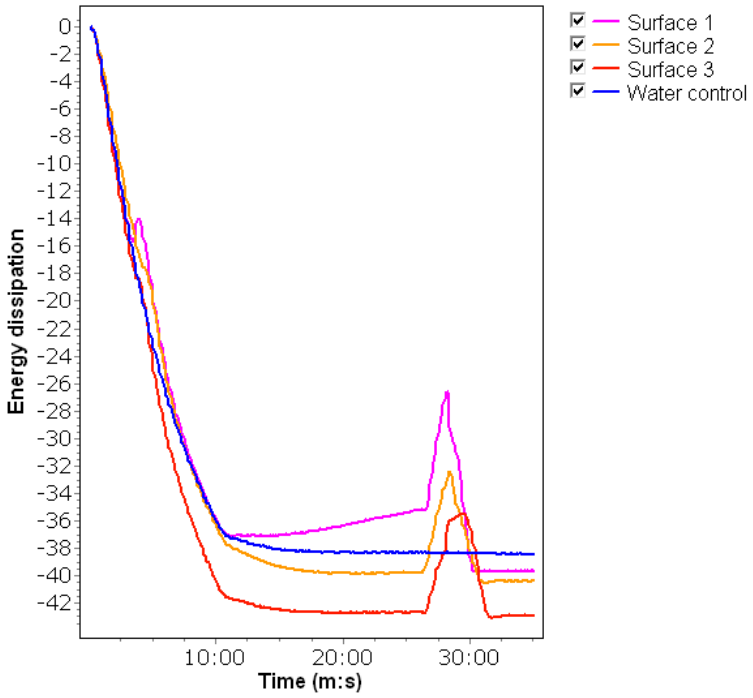

dissipation vs. time (GD 20%), without control subtraction

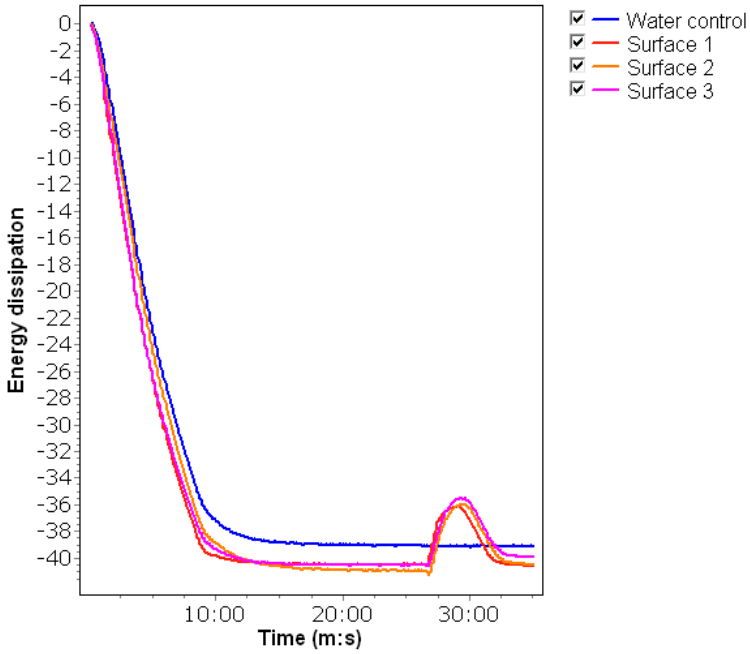

dissipation vs. time (GD 5%), without control subtraction

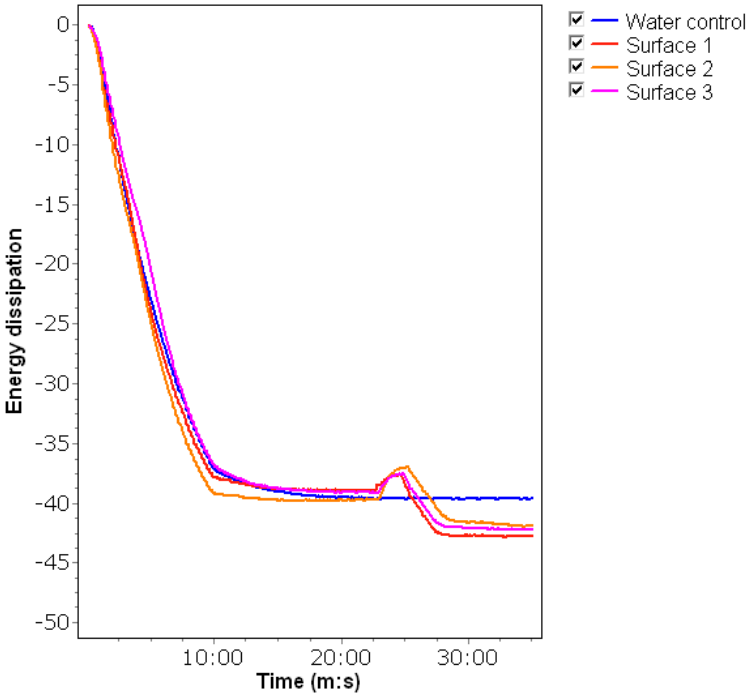

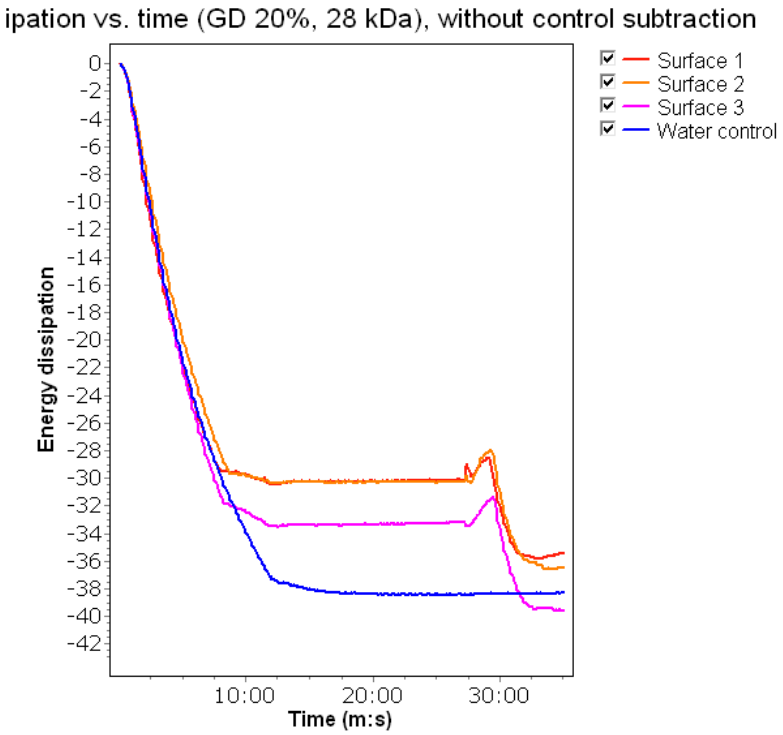

After the deposition, the values for the samples with good antifouling property are quite consistently below the water signal, at least until what we think corresponds to the rearrangement of the coating. Here there is an increase and in some cases the signal goes above that of the water control, but in some cases just approaches it, this is why sign of the signal that we get after control subtraction changes sign here for some samples, but not for all of them.

IV Goniometry

Images from which the WCA values were calculated are available for request; here they are not included because of their large number.

V UV-visible spectroscopy

Scan Analysis Report

Report Time : Thu 17 Jul 02:05:58 PM 2014

Method:

Batch: C:\ProgramData\Varian\Cary WinUV\Orsi\OK-1-25 24C.DSW

Software version: 4.20(468)

Operator:

Zero Report

Read	Abs(400.00)
Zero	0.0676

Sample Name: 24C1

Collection Time 7/17/2014 2:07:05 PM

Peak Table

Peak Style	Peaks
Peak Threshold	0.0100
Range	400.00nm to 200.00nm

Wavelength (nm)	Abs
212.00	1.530
205.00	10.000
202.00	0.721

Scan Analysis Report

Report Time : Thu 17 Jul 02:16:36 PM 2014

Method:

Batch: C:\ProgramData\Varian\Cary WinUV\Orsi\OK-1-25 25C.DSW

Software version: 4.20(468)

Operator:

Zero Report

Read	Abs(400.00)
Zero	0.0676

Sample Name: 25C

Collection Time 7/17/2014 2:16:44 PM

Peak Table

Peak Style Peaks

Peak Threshold 0.0100

Range 400.00nm to 200.00nm

Wavelength (nm)	Abs
212.00	1.513
205.00	10.000
202.00	0.775

Scan Analysis Report

Report Time : Thu 17 Jul 02:25:57 PM 2014

Method:

Batch: C:\ProgramData\Varian\Cary WinUV\Orsi\OK-1-25 26C.DSW

Software version: 4.20(468)

Operator:

Zero Report

Read	Abs(400.00)

Zero 0.0676

Sample Name: 26C

Collection Time 7/17/2014 2:26:11 PM

Peak Table

Peak Style Peaks

Peak Threshold 0.0100

Range 400.00nm to 200.00nm

Wavelength (nm)	Abs
212.00	1.604
205.00	10.000
202.00	0.952

Scan Analysis Report

Report Time : Thu 17 Jul 02:38:45 PM 2014

Method:

Batch: C:\ProgramData\Varian\Cary WinUV\Orsi\OK-1-25 27C.DSW

Software version: 4.20(468)

Operator:

Zero Report

Read	Abs(400.00)
Zero	0.0676

Sample Name: 27C

Collection Time 7/17/2014 2:38:51 PM

Peak Table

Peak Style Peaks

Peak Threshold 0.0100

Range 400.00nm to 200.00nm

Wavelength (nm)	Abs
213.00	2.263
207.00	2.356
205.00	10.000

Scan Analysis Report

Report Time : Thu 17 Jul 02:51:08 PM 2014

Method:

Batch: C:\ProgramData\Varian\Cary WinUV\Orsi\OK-1-25 28C.DSW

Software version: 4.20(468)

Operator:

Zero Report

Read	Abs(400.00)
Zero	0.0676

Sample Name: 28C

Collection Time 7/17/2014 2:51:13 PM

Peak Table

Peak Style Peaks

Peak Threshold 0.0100

Range 400.00nm to 200.00nm

Wavelength (nm) Abs

214.00	2.594
212.00	2.628
207.00	10.000

Scan Analysis Report

Report Time : Thu 17 Jul 03:02:48 PM 2014

Method:

Batch: C:\ProgramData\Varian\Cary WinUV\Orsi\OK-1-25 29C.DSW

Software version: 4.20(468)

Operator:

Zero Report

Read	Abs(400.00)
Zero	0.0676

Sample Name: 29C

Collection Time 7/17/2014 3:02:54 PM

Peak Table

Peak Style Peaks

Peak Threshold 0.0100

Range 400.00nm to 200.00nm

Wavelength (nm)	Abs
215.00	2.810
213.00	2.754
210.00	2.585
208.00	2.304
205.00	10.000

Scan Analysis Report

Report Time : Thu 17 Jul 03:13:37 PM 2014

Method:

Batch: C:\ProgramData\Varian\Cary WinUV\Orsi\OK-1-25 30C.DSW

Software version: 4.20(468)

Operator:

Zero Report

Read	Abs(400.00)
Zero	0.0676

Sample Name: 30C

Collection Time 7/17/2014 3:13:45 PM

Peak Table

Peak Style Peaks

Peak Threshold 0.0100

Range 400.00nm to 200.00nm

Wavelength (nm)	Abs
215.00	2.845
212.00	2.817
209.00	2.551
207.00	2.275
205.00	10.000
202.00	1.351

Scan Analysis Report

Report Time : Thu 17 Jul 03:28:15 PM 2014

Method:

Batch: C:\ProgramData\Varian\Cary WinUV\Orsi\OK-1-25 31C.DSW

Software version: 4.20(468)

Operator:

Zero Report

	Read	Abs(400.00)
Zero		0.0676

Sample Name: 31C

Collection Time 7/17/2014 3:28:23 PM

Peak Table

Peak Style Peaks

Peak Threshold 0.0100

Range 400.00nm to 200.00nm

Wavelength (nm)	Abs
352.00	1.601
217.00	2.883
215.00	2.988
211.00	2.744
208.00	10.000
206.00	10.000

Scan Analysis Report

Report Time : Thu 17 Jul 03:43:24 PM 2014

Method:

Batch: C:\ProgramData\Varian\Cary WinUV\Orsi\OK-1-25 32C.DSW

Software version: 4.20(468)

Operator:

Zero Report

Read	Abs(400.00)
Zero	0.0676

Sample Name: 32C

Collection Time 7/17/2014 3:43:32 PM

Peak Table

Peak Style Peaks

Peak Threshold 0.0100

Range 400.00nm to 200.00nm

Wavelength (nm)	Abs
351.00	1.674
216.00	2.977
213.00	3.239
210.00	3.120
208.00	10.000
206.00	1.758
203.00	10.000

All spectra from 24-32 °C:

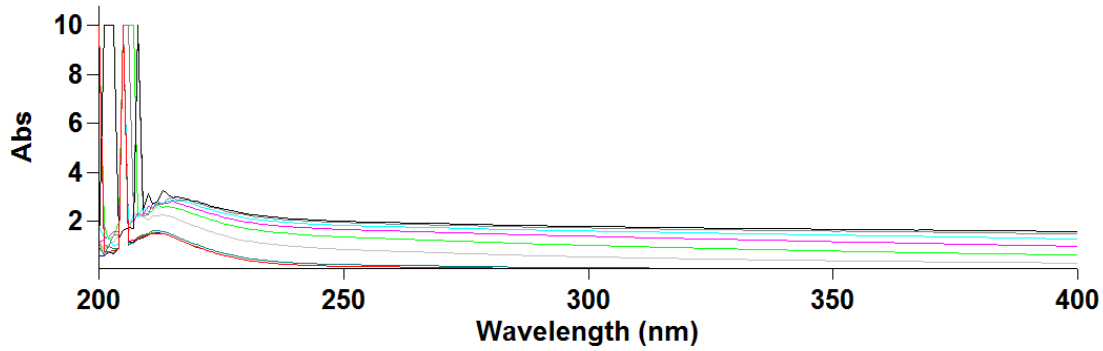
Abs
10
8
6
4
2
200
250
300
350
400
Wavelength (nm)

28 °C and 32 °C:

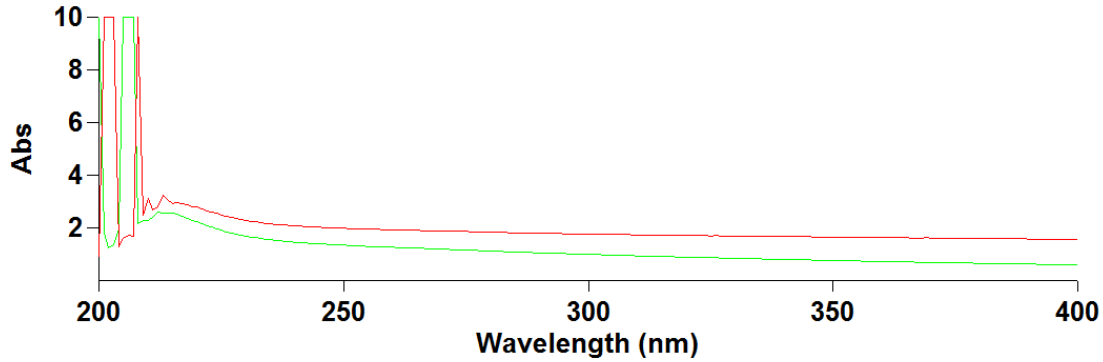
Abs
10
8
6
4
2
200
250
300
350
400
Wavelength (nm)

Supporting Information for:

Self-assembly of Covalently bond Fibers by Zipper-like Driven Aggregation

Experimental

Materials. PEO-OH (10 kDA), *N*,*N*,*N'*,*N"*,*N"*-pentamethyldiethylenetriamine (PMDETA, 98%), CuSO4-5H2O, propargyl bromide, sodium ascorbate and dichloromethane were purchased from Sigma. Water used was ultrapure high resistivity water purified using a Barnstead nanopure water purification system. L-4-azidophenylalanine (pN_3F) was purchased from Bachem. DH10B cells, and *pBadA* were purchased from Invitrogen.

Instrumentation. Particle size was measured using a Zetasizer Nano from Malvern Instruments. Confocal microscopy was carried out using a Carl Zeiss LSM 510 Meta NLO Confocor 3 Inverted Spectral Confocal Microscope using an argon laser with an excitation at 488 nm. Samples were dropped onto a glass coverslip and imaged. Tapping mode atomic force microscopy (AFM) experiments were carried out using a Nanoscope III system (Veeco 2 Instruments). The tapping mode AFM measurements were performed in air, using commercial silicon cantilevers with a nominal spring constant and resonance frequency respectively equal to 75 N/m and 350 kHz.

Expression and purification of GFP-azide.

DH10B *E. coli* cells co-transformed with one *pBad* vector and pDule1-pCNF. The pDule1-pCNF plasmid has been shown to have high fidelity and efficiency for site specifically incorporation of a variety of unnatural amino acids including pN_3F(*1*). The *pBad-sfGFP-134TAG,150TAG* vectors were used for producing GFP-135,150pN_3F respectively. The co-transformed cells were used to inoculate 5 mL of non-inducing medium (Table 1) containing 100 μg/mL Amp and 25 μg/mL Tet. The non-inducing medium culture was grown to saturation with shaking at 37 °C, and 5.0 mL was used to inoculate 0.5 L autoinduction medium with 100 μg/mL Amp, 25 μg/mL Tet, and 1 mM pN_3F (0.5 L of media grown in 2 L plastic baffled flasks). After 40 hours of shaking at 37 °C, cells were collected by centrifugation.

The protein was purified using BD-TALON cobalt ion-exchange chromatography. The cell pellet was resuspended in wash buffer (50 mM sodium phosphate, 300 mM sodium chloride, pH 7) containing 1 mg/mL chicken egg white lysozyme, and sonicated 3 × 1 min while cooled on ice. The lysate was clarified by centrifugation, applied to 6-9 mL bed-volume resin, and bound for 30 min. Bound resin was washed with >50 volumes wash buffer.

Protein was eluted from the bound resin with 2.5 mL aliquots of elution buffer (50 mM sodium phosphate, 300 mM sodium chloride, 150 mM imidazole pH 7) until the resin turned pink and the color of the eluent the column was no longer green. The elusions concentrations were check with a Bradford protein assay. The protein were desalted into PBS using PD10 columns and concentrated with 3000 MWCO centrifuge filters.

SI Table 1. Components for autoinducing and non-inducing mediums(*1*), for final volume of 500 mL.

	A) Autoinduction medium	**B)** Non-inducing medium
5% aspartate, pH 7.5	25 mL	25 mL
10% glycerol	25 mL	-
25× 18 amino acid mix	20 mL	20 mL
50× M	10 mL	10 mL
leucine (4 mg/mL), pH 7.5	5 mL	5 mL
20% arabinose	1.25 mL	-
1 M $MgSO_4$	1 mL	1 mL
40% glucose	625 µL	6.25 mL
Trace metals	100 µL	100 µL

PEO Dialkyne: To a solution of α, ω-dihydroxy PEO (M_n = 10000, 10 g, 1 mmol) in 200 ml of THF, 0.6 g of propargyl bromide (5 mmol) and 0.20 g of NaOH (5 mmol) were added. The mixture was refluxed under nitrogen atmosphere over night before cooled to room temperature. The insoluble solid was filtered out and the solvent was removed under reduced pressure. The residue was redissolved in dichloromethane and washed with brine and water. After removing most of the solvent, large amount of cold ethyl ether was added to precipitate the product, which was dried in vacuum to constant weight. Yield 900 mg (90 %). ^{1}H NMR ($CDCl_3$) *ô*: 4.22 (d, 4H, *J* = 2.4 Hz, -OC*H*$_2$C≡CH), 3.66-3.61 (m, -OC*H*$_2$C*H*$_2$-), 2.46 (t, 2H, *J* = 2.4 Hz, -OCH$_2$C≡C*H*).

GFP-fiber Synthesis: p(GFP2-PEO$_{1k}$dialkyne)

To a 10 ml round bottom flask 970μL of 20.1 mg/ml 134/150-GFP-diazide (GFP2) (19.6 mg, 7*10^{-4} mmol) was added. PEO$_{10k}$dialkyne (7 mg, 7*10^{-4}mmol) dissolved in 200 μL of 0.1M PBS buffer (pH= 7.4) was added to the GFP solution. PMDETA (1.307 μL, 9.1*10^{-3} mmol) was complex with $CuSO_4$□5H_2O (1.74 mg, 7*10^{-3}mmol) in 100μL PBS buffer and added to the reaction mixture while stirring. The reaction mixture was capped with a rubber stopper and degassed by bubbling with nitrogen for 5 minutes and sodium ascorbate (1.525 mg, 7.7*10^{-3}mmol) in 50 μL of PBS buffer was injected to start the polymerization. The reaction was protected from light and stirred under nitrogen for 5 days. The reaction mixture was centrifuged to isolate the GFP-fibers. The supernatant liquid discarded and the pellet was washed an additional two times with PBS to remove unreacted reagents. The pellet was analyzed using DLS, confocal microscopy and AFM.

A control reaction was conducted in the exact same manner as the polymerization but the sodium ascorbate was added to the reaction mixture. No pellet was observed and analysis using DLS (Figure S1) showed that only one peak at ~5 nm. This indicates that only native GFP is present post reaction.

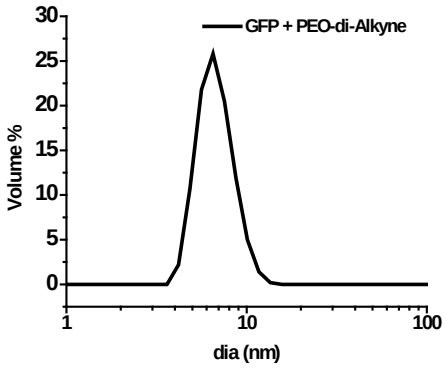

SI Figure 1: Synthesis and characterization of GFP-fibers prepared by the "click" step-growth polymerization of GFP-diN_3 and PEO1k-dialkyne *sans* sodium ascorbate (i.e. control reaction). Size distribution analysis using DLS of control reaction for GFP-fibers experiment.

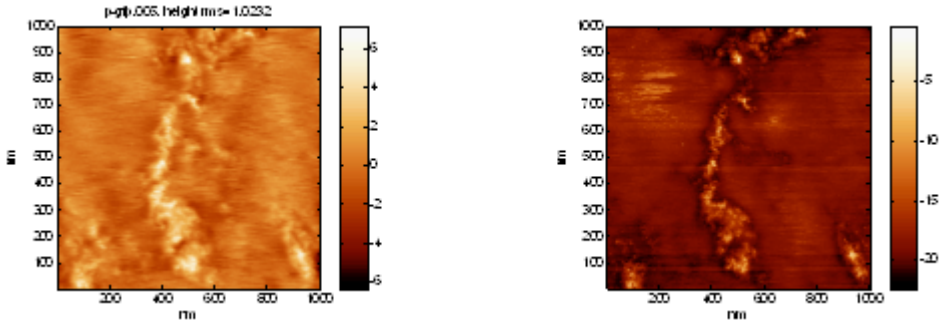

SI Figure 2: AFM images acquired in the presence of 2 nM $CaCl_2$, substrate: mica. Left: height, right: phase.

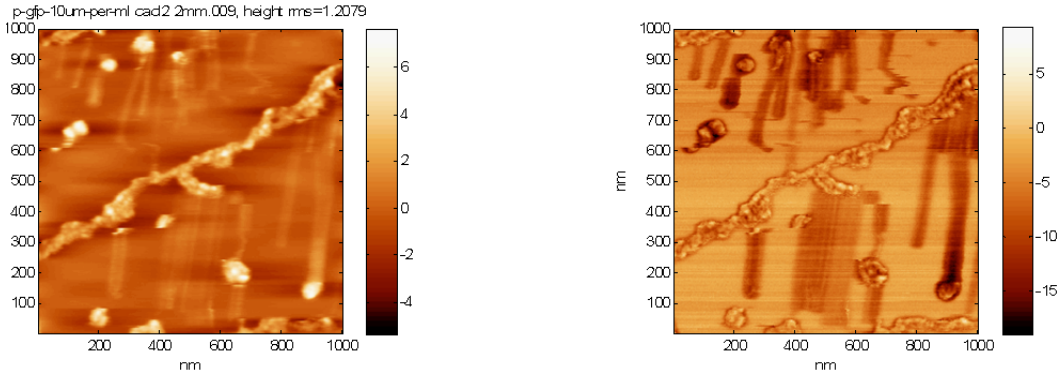

SI Figure 3: AFM images acquired in the presence of 2 nM $CaCl_2$, substrate: HOPG. Left: height, right: phase.

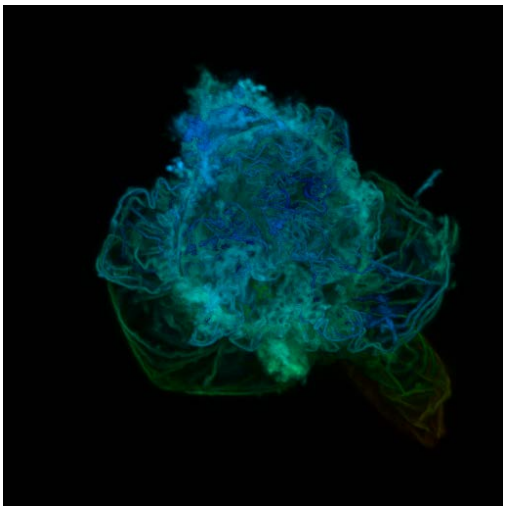

SI Figure 3: 3D fluorescent image of GFP fibers. The fluorescent images were analyzed and displayed in 3D by using Zeiss LSM 510 Image Browser.

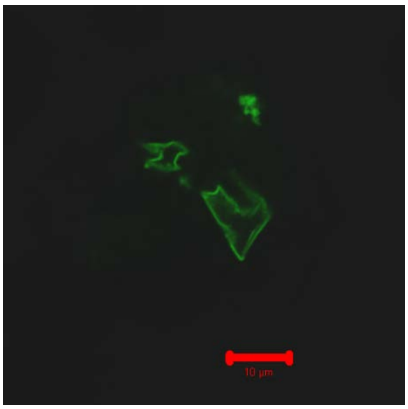

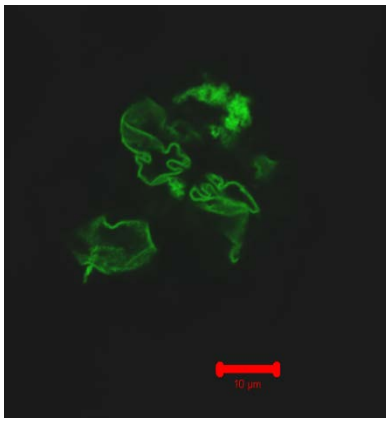

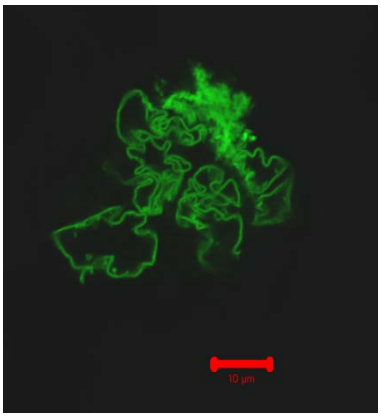
10 µm

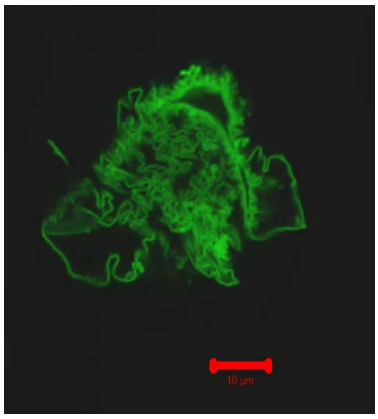
10 µm

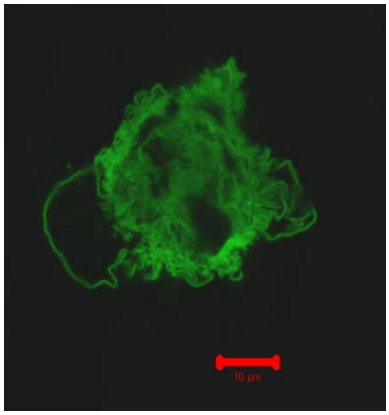
10 µm

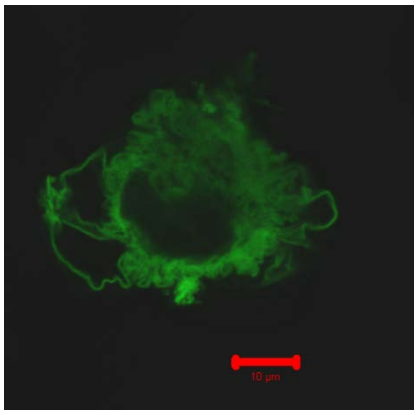
10 µm

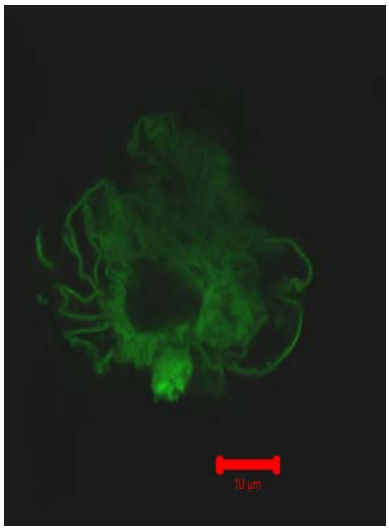
10 µm

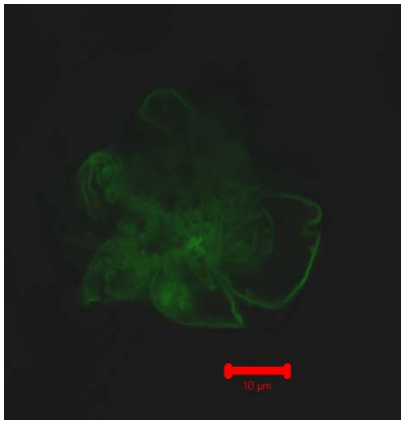
10 µm

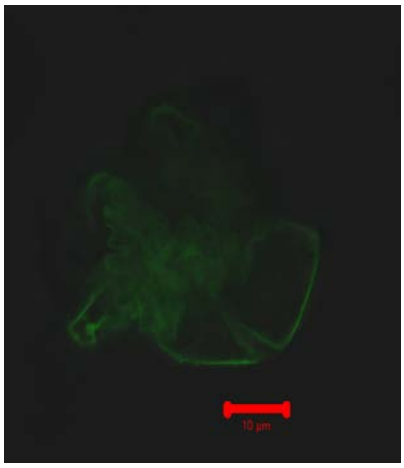
10 µm

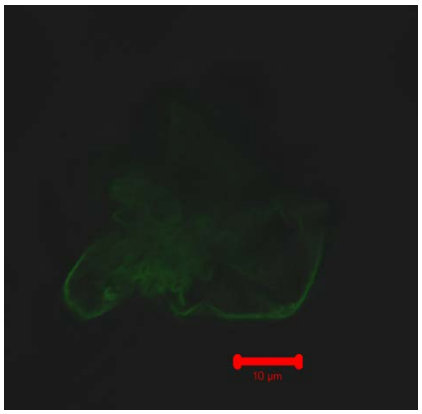
10 µm

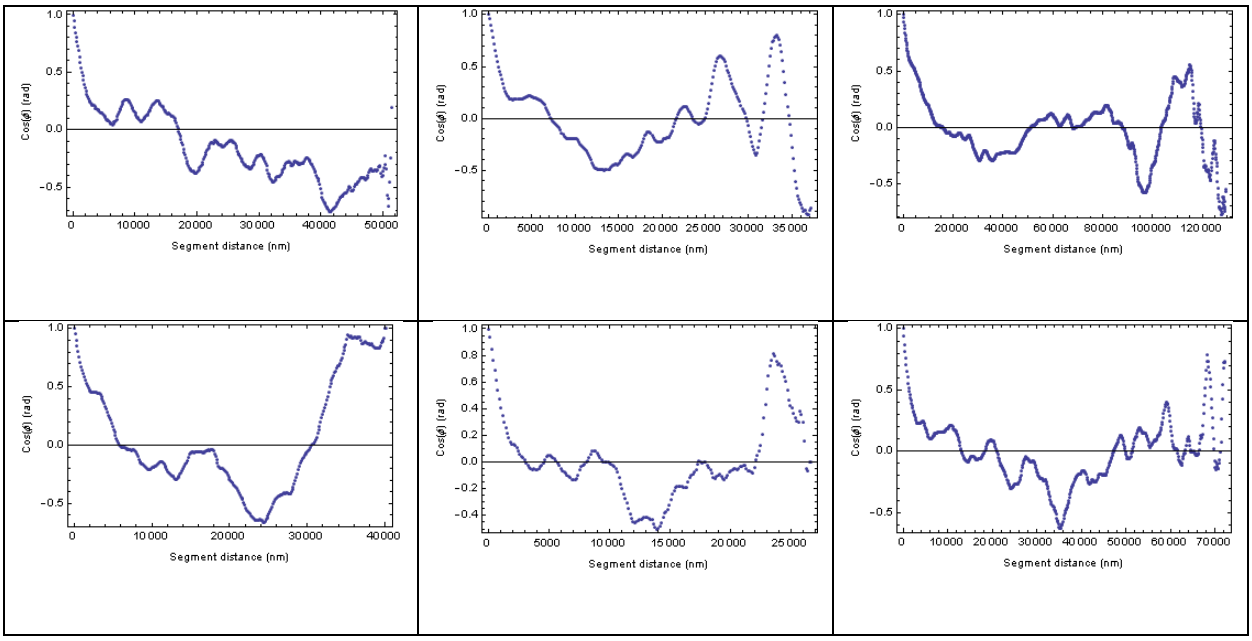
Cos(φ) (rad)
Segment distance (nm)

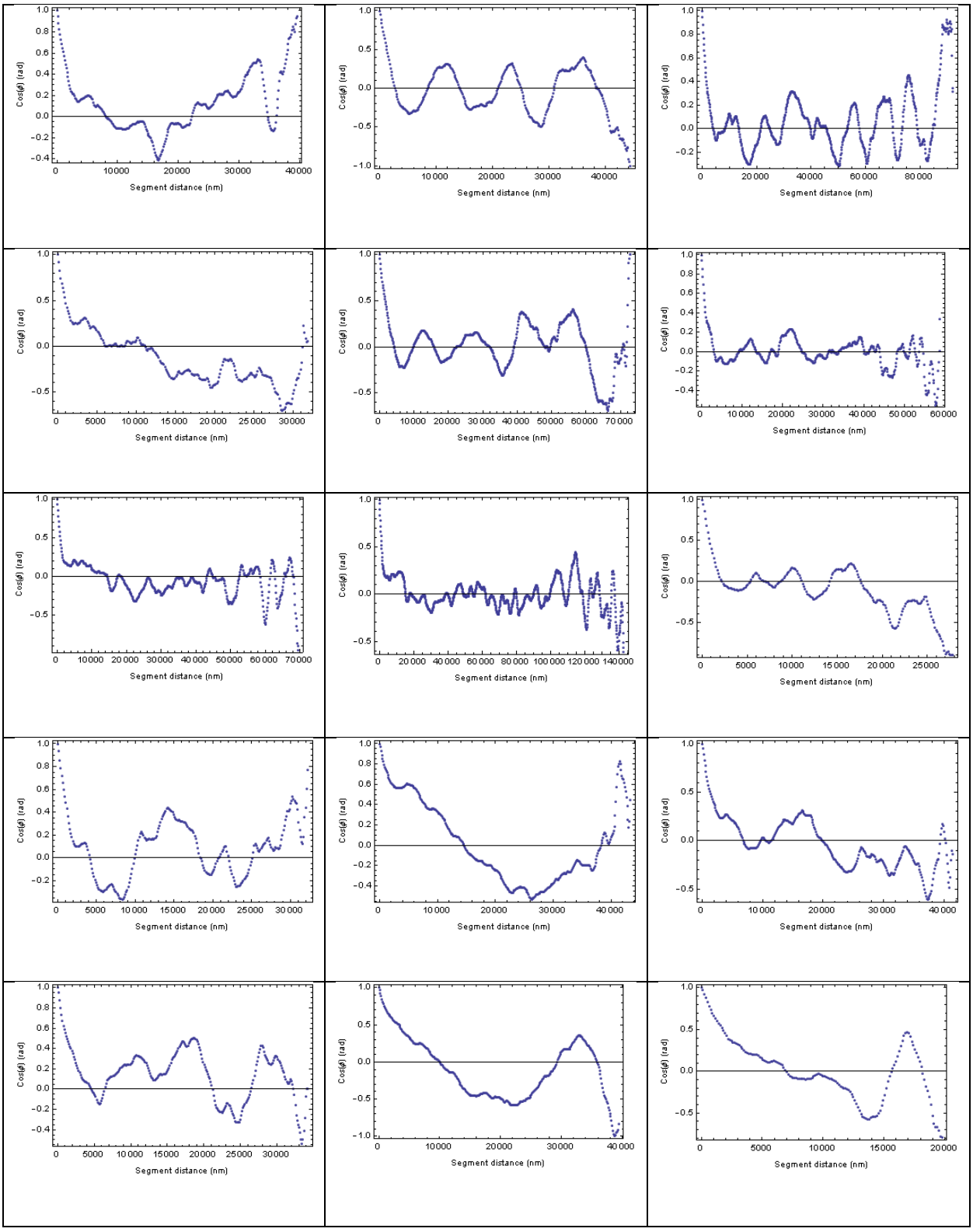
Cos(φ) (rad)
Segment distance (nm)

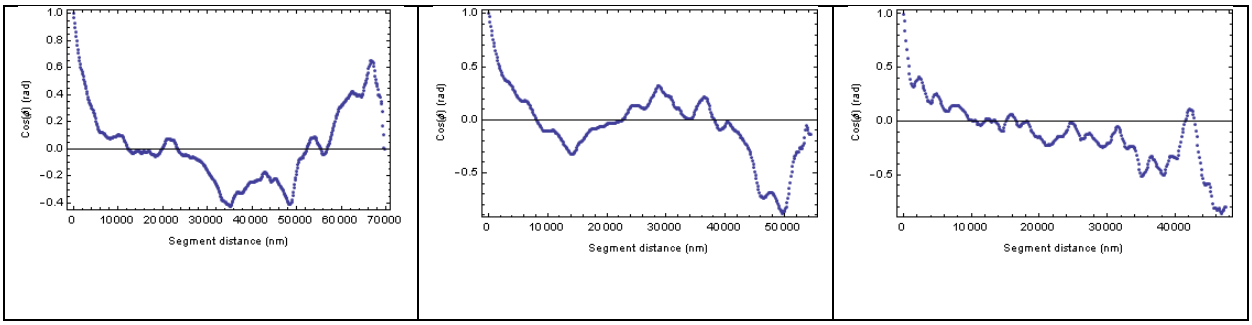

SI Table 1. Change of cos(θ) with increasing segment distance for 24 slices. Slices were tracked on the fluorescent images; Θ is the angle between two segments. The plots show an initial exponential decay, followed by oscillations around the origin, as expected.

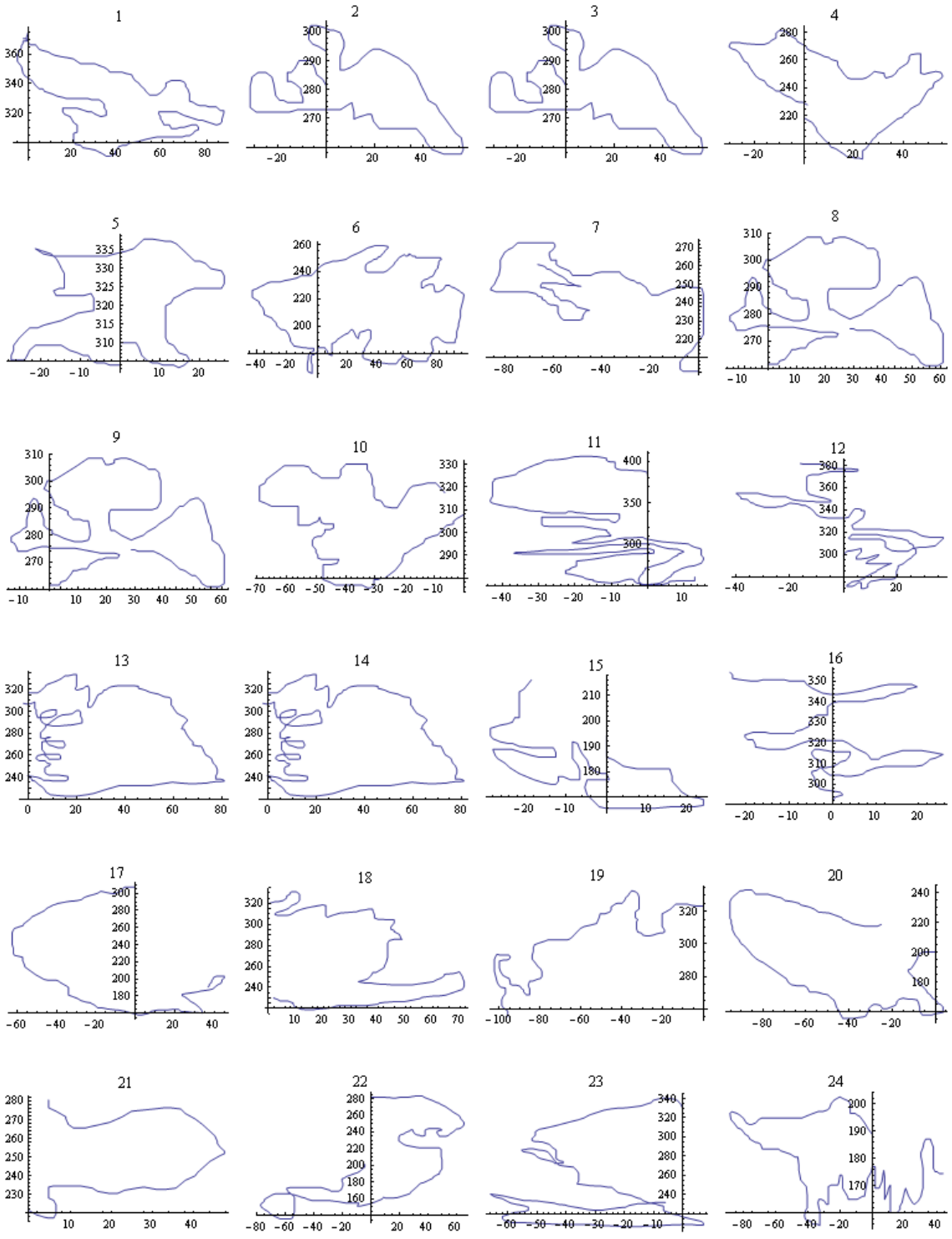

SI Table 2. Examples of the tracked chains.

AFM images were processed with a homemade Matlab R2012 (MathWorks Inc., Natick, MA) function. Persistence length calculations were carried out in Mathematica 9 (Wolfram Inc.). Modification sites in GFP were visualized using Pymol version 1.4.1with Python version 2.7.

Electrostatic potential was calculated using Rasmol version 2.7.5, from the Protein Databank file for GFP (available at www.rcsb.org), using Coulomb's law taking the charge field to be the charge associated with that atom. Using a dielectric constant value of 10, the following color scheme was assigned to the potential values.

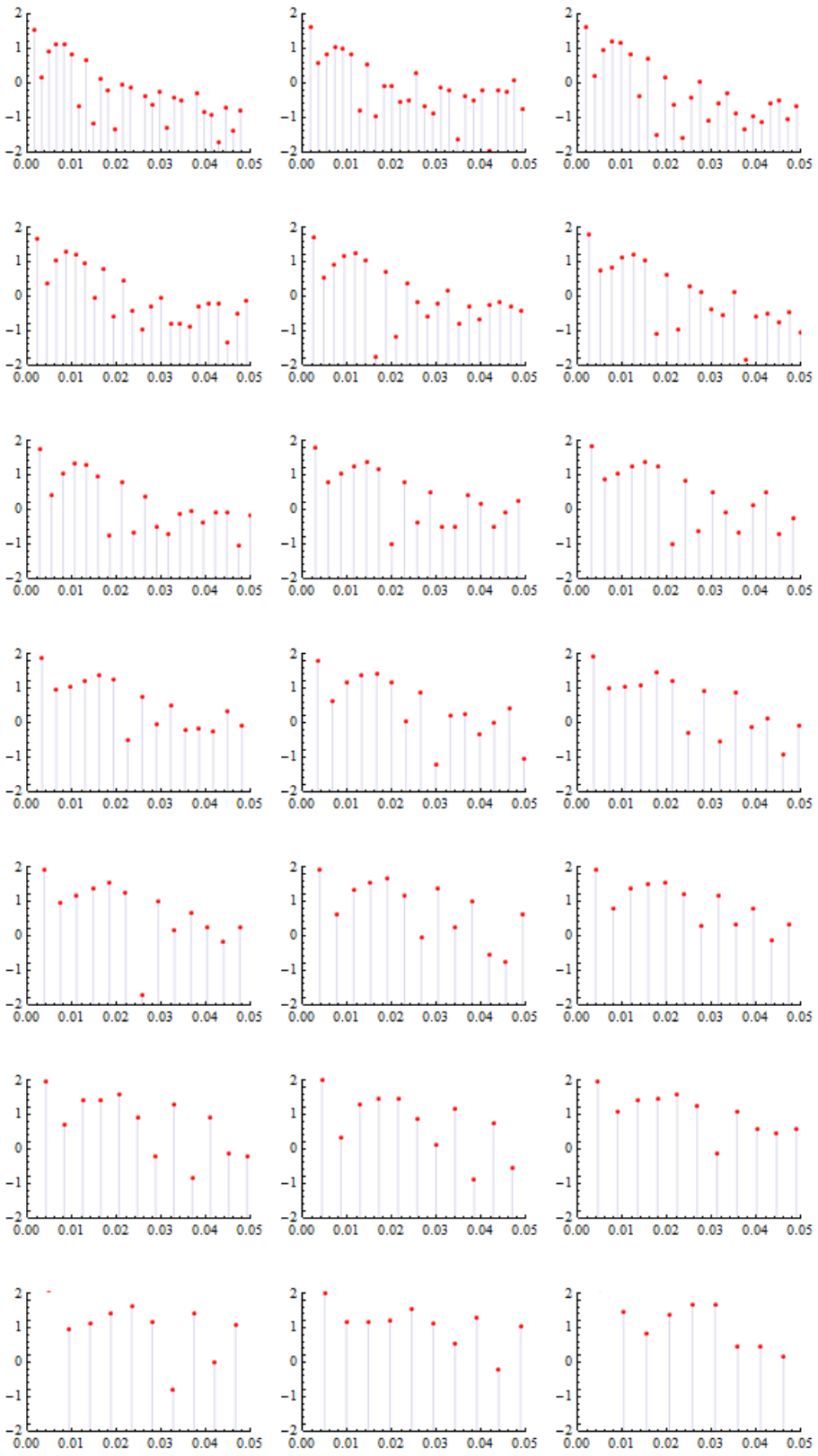
2
1
0
−1
−2
0.00
0.01
0.02
0.03
0.04
0.05

SI Table 3. Fourier transform of the height images at different cross-sections (axes as in Figure 2.3 left).

1. . Miyake-Stoner, S. J., Miller, A. M., Hammill, J. T., Peeler, J. C., Hess, K. R., Mehl, R. A., and Brewer, S. H. (2009) Probing Protein Folding Using Site-Specifically Encoded Unnatural Amino Acids as FRET Donors with Tryptophan, *Biochemistry 48*, 5953-5962.

Chapter V

Supporting Information File 1

(A = 20 nm for all figures.)

For k = 5:

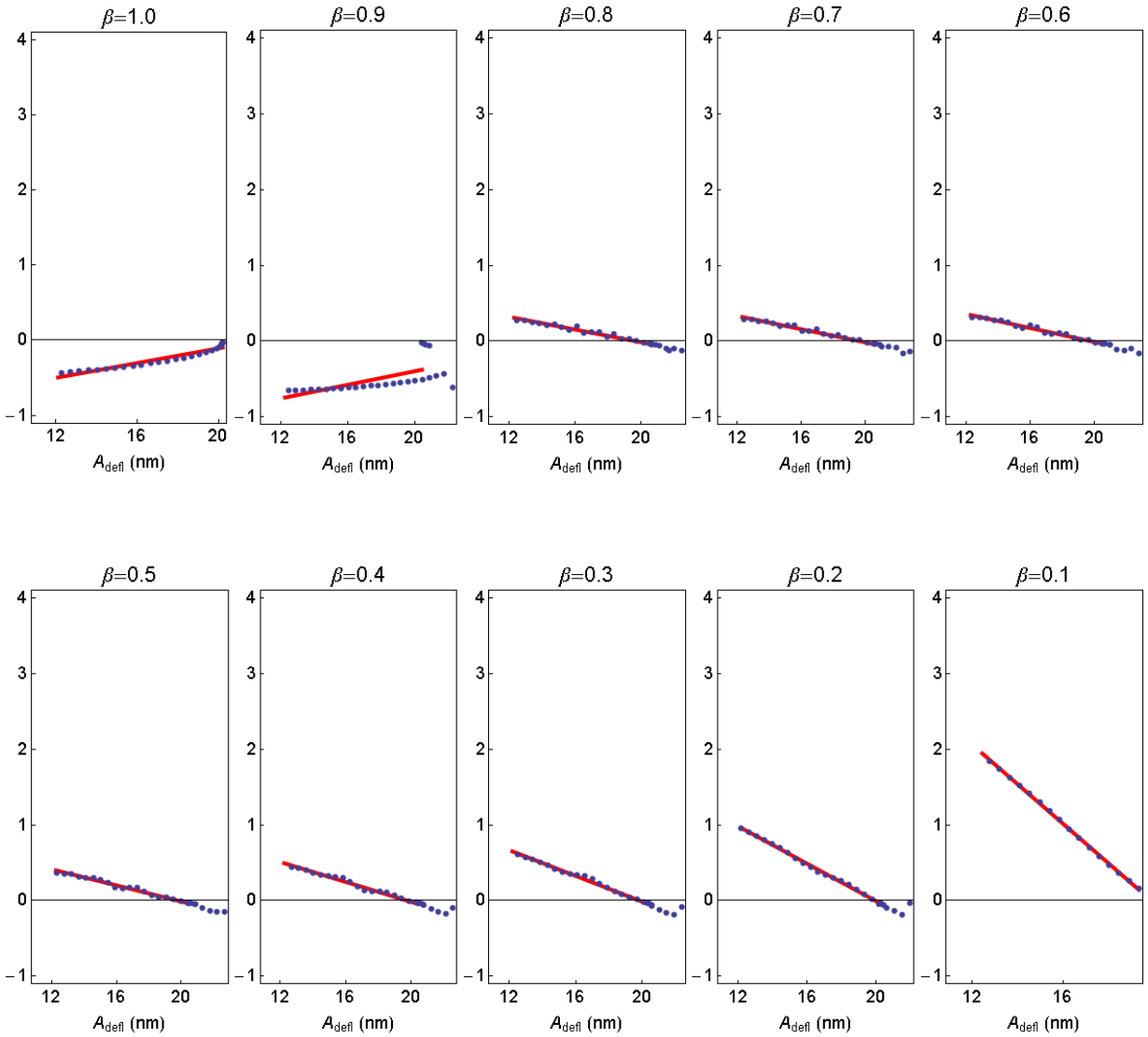

For k = 20:

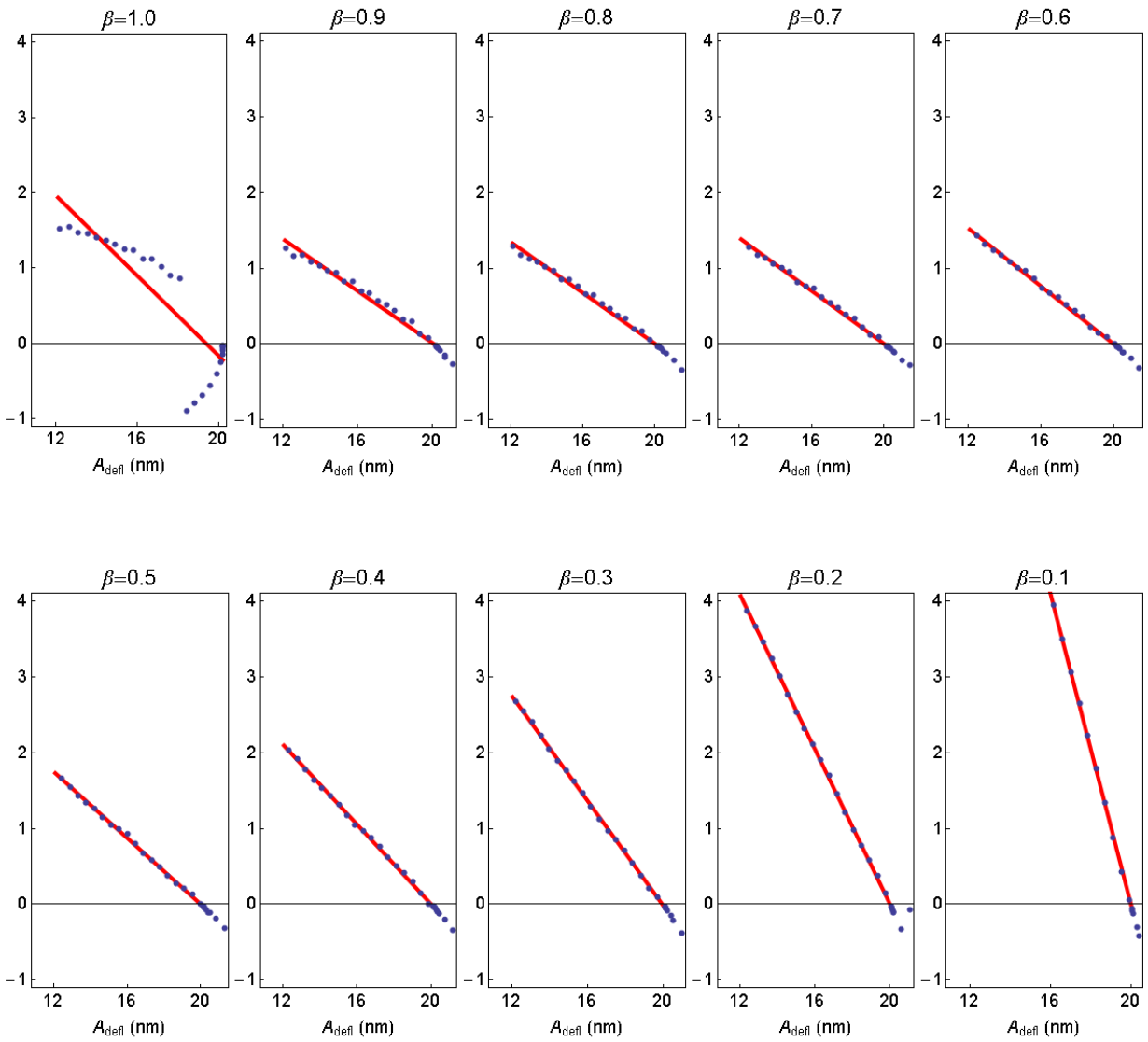

For k = 50:

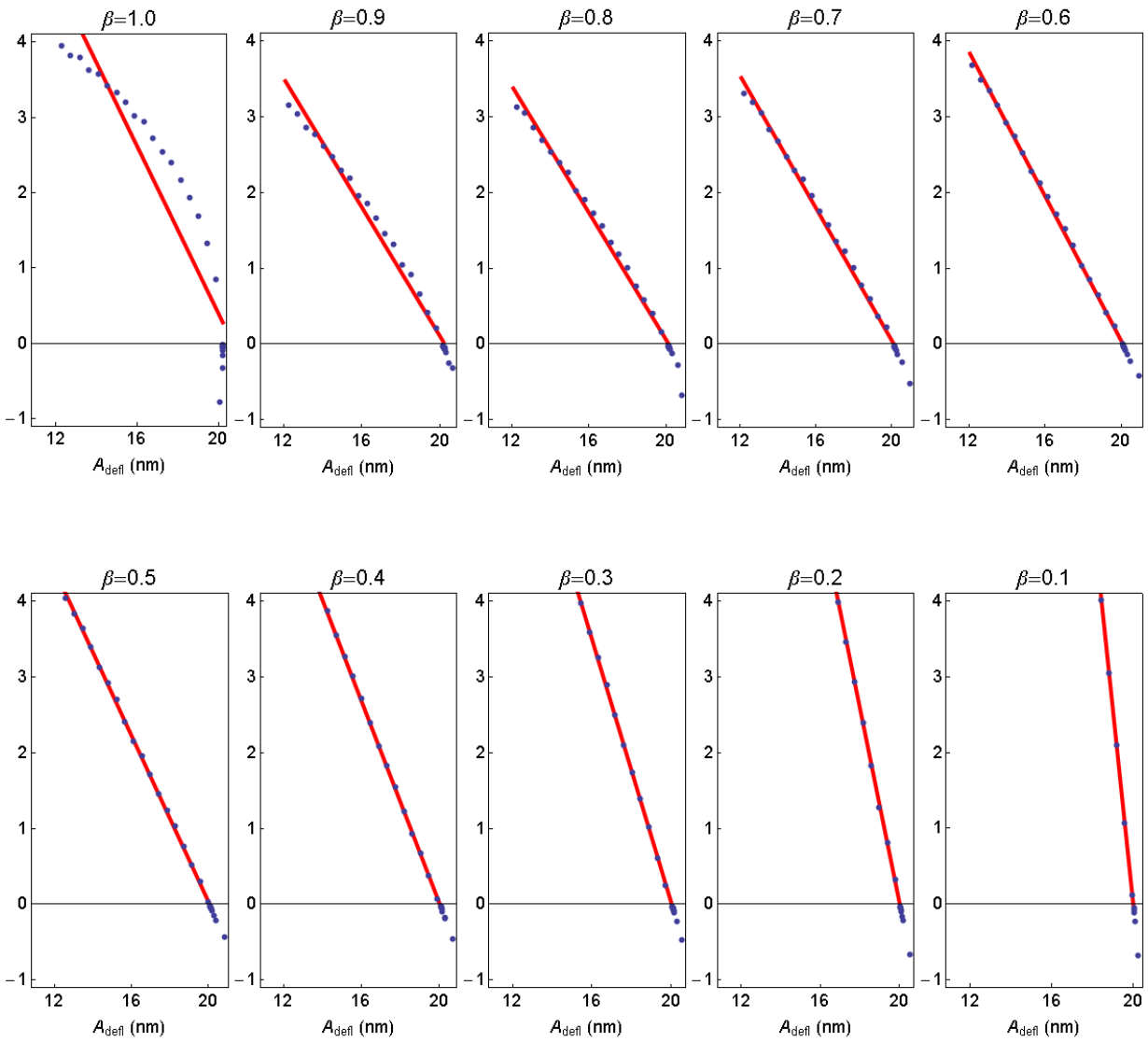
β=1.0
β=0.9
β=0.8
β=0.7
β=0.6
β=0.5
β=0.4
β=0.3
β=0.2
β=0.1
A_defl (nm)
12
16
20
4
3
2
1
0
−1